

https://dspace.org/

Performance improvement of vacuum arc thrusters

Lun, Jonathan

2016-03-16
http://hdl.handle.net/10539/20101

Downloaded from a DSpace repository. https://dspace.org/

Performance Improvement of Vacuum Arc Thrusters

Jonathan Lun

A thesis submitted to the Faculty of Engineering and the Built Environment at the University of the Witwatersrand, Johannesburg, in fulfilment of the requirements for the degree of Doctor of Philosophy.

School of Mechanical, Industrial and Aeronautical Engineering

Johannesburg, 2015

Declaration

I declare that this thesis is my own original work. It is being submitted to the Degree of Doctor of Philosophy to the University of the Witwatersrand, Johannesburg. It has not been submitted before for any degree or examination to any other university. The knowledge contained in this thesis was obtained while under the employment of the South African National Space Agency, Space Science Directorate. Sponsorship for this work was provided for by the National Research Foundation.

Signed: .....

on this day: .....

Copyright © 2015 University of the Witwatersrand, Johannesburg
All rights reserved.

Publications

Below is a list of journal articles, conference papers and provisional patents produced prior to publication of this work:

- Lun, J. & Law, C. (2014). Influence of Cathode Shape on Vacuum Arc Thruster Performance and Operation, December 2014 Special Issue on Plasma Propulsion, IEEE Transactions on Plasma Science, DOI: 10.1109/TPS.2014.2361439.
- Lun, J. (2014). Improvements in vacuum arc thrusters, SA Provisional patent application no. 2014/06500.
- Lun, J. (2014). Pulsed vacuum arc thrusters, SA Provisional patent application no. 2014/06501.
- Lun, J. (2014). Anode switching systems, SA Provisional patent application no. 2014/06502.
- Lun, J. & Law, C. (2014). Direct thrust measurement stand with improved operation and force calibration technique for performance testing of pulsed micro-thrusters. Measurement Science and Technology, 25(9), 095009.
- Lun, J. & Law, C. (2013). Influence of Cathode Shape on Vacuum Arc Thruster Performance and Operation. In 33rd International Electric Propulsion Conference, IEPC–2013–177. Washington, DC.

Abstract

Vacuum arc thrusters (VATs) hold great promise as an attractive pulsed plasma micropropulsion technology for satellites. To reach their full potential as practical devices, substantial efforts must be made to explore and better understand the intricacies of VAT design and operation. This body of work contributes to this effort by studying a number of new thruster designs, operational modes and cathode fuels that may lead to performance improvement of the VAT. These include (1) the use of millisecond-long arc pulses lengths as a new form of thruster operation, (2) the use of conical cathode shapes, (3) the novel use of carbon and graphite-based materials as cathode materials, and (4) novel heat management using the discrete anode switching technique. Detailed and extensive experimental measurements of thrust, cathode erosion rate, ion current and plasma jet ICDD profiles were undertaken in order to characterise the behaviour and performance of VAT prototypes. Testing was accomplished with the development of a μN-level direct thrust measurement stand, a Faraday Cup probe, a two-axis thruster rotation system, an ion collector and various data collection and processing systems.

In a number of cases, new thruster designs and operations were found to (1) enhance ion production rates, (2) reduce the cathode erosion rate by improving cathode spot motion, and (3) tailor the plasma jet shape towards favourable performance. As a result, several VAT prototypes demonstrated significant increases in thrust production and specific impulse values of up to 100% ($\sim$ 400 μN/A) and 250% ($\sim$ 1000 s) respectively over typical baseline VAT designs ($\sim$ 200 μN/A, 400 s). Several previously unexplored relationships and interactions between VAT performance and thruster parameters such as arc current, arc pulse length, cathode surface geometry, cathode microstructure and thermal prop-

erties, plasma jet shape, and cathode spot dynamics were recognised and characterised. The role of the arc pulse length, spot motion and erosion coverage were highlighted as key elements which profoundly impacted on VAT design and performance. This work opens up new areas of VAT design, whilst posing new questions about the fascinating nature and utility of vacuum arc spots for efficient and effective plasma jet production.

Acknowledgements

To my supervisor, Craig Law – thank you for having the faith in me to take on such an ambitious project. Your guidance and suggestions provided clarity and depth on many technical issues and I appreciated your rigorous approach to academic writing. Your valuable feedback over the many months and years has challenged and grown me.

To Phil Ferrer – I am forever indebted to you for opening up your laboratory space to me and being willing to share your resources to making the Wits Space Propulsion Research laboratory possible. Our partnership was a fine and adventurous example of interdisciplinary collaboration and friendship. Thanks for being a listening ear whenever I needed to bounce ideas off someone.

To Wits University technical and workshop staff – Shaun Rieckert, Marius Van Wyk, Lionel Claassen, Bootie Mgwenya, John Augustine, Vincent Govender and Gerrard Peters, thank you for putting in so many hours towards building (and fixing!) all the equipment and tools I needed for this project. Your high-standard of work, patience and kindness was instrumental to my success.

To Kamil Midor – thank you for generously lending me so much equipment for such a long time and saving my budget!

To Prof. Ivan Hofsajer and Michael Grant – thank you for always being willing and cheerful whenever I came around to ask for help on electric pulse circuits. The anode switching system would not have been possible without you, Ivan.

To Dr Lee-Anne McKinnell and staff at SANSA Space Science – thank you for taking such a huge risk with me and believing that I could accomplish my work to a standard that would make SANSA proud. The tireless and warm assistance from the administrative and finance staff (in particular, Sylnita, Phemelo, Priscilla and Sandra) was much appreciated.

To the National Research Foundation – thank you for providing the crucial funds needed to make this project possible and allowing me to focus on my work without worrying about finances.

To my colleagues and friends – thank you for keeping me sane and reminding me that there was life outside the lab.

To my family, Vincent, Lorraine, Stanley, Alison, Rebecca & Jonah, Stephanie, Daniel L. and Daniel S. – thank you for your endless patience with me and for being a constant source of encouragement and support when things got tough.

To my dearest wife, Maryke – thank you for being by my side through it all. You were always understanding and never once complained about the endless long nights or my work frustrations. We made it! It's been quite a journey and I can't wait to start the next phase of our lives together.

Dedication

To my family, for always encouraging me to dream and to help create a better world.

Contents

Declaration **i**

Publications **ii**

Abstract **iii**

Acknowledgements **v**

Dedication **vii**

Nomenclature **xxxv**

Acronyms **xxxix**

1 Introduction **1**

1.1 Background 2

1.1.1 Micro-propulsion in the South African and international context . . 2

1.1.2 Why study the vacuum arc thruster? 3

1.1.3 What are vacuum arcs? 4

1.1.4 History of the vacuum arc thruster 7

1.2 VAT design theory 8

1.3 VAT design practice 9

1.3.1 Choice of cathode geometry 10

1.3.2 Choice of cathode material 11

1.3.3 Choice of arc pulse characteristics 12

1.3.4 Cathode erosion and the production of macroparticles 16

1.3.5 Performance enhancement of VATs 19

1.4 Motivation 20

1.5 Objectives 20

1.6 Outline 21

2 Method **22**

2.1 Experimental versus theoretical approach 22

2.1.1 The experimental approach 22

2.1.2 The theoretical approach 23

2.1.3 Findings and conclusion 25

2.2 Use of a baseline thruster design 26

2.3 Measurement strategy 27

2.3.1 Performance metrics 27

2.3.2 Scope of Measurement 31

2.3.3 General approach to data handling and presentation 33

3 Experimental apparatus & test setup **35**

3.1 Introduction 35

3.2 Vacuum chamber and high-vacuum pump system 36

3.3 Pulsed power circuit 37

3.3.1 Description of circuit development and performance 37

3.3.2 Arc pulse waveforms 40

3.4 Direct thrust measurement stand 46

3.4.1 Background 46

3.4.2 Thrust stand description 48

3.4.3 Analytical model and analysis of beam response 52

3.4.4 Commissioning and quantifying thrust accuracy 55

3.4.5 Final thrust stand performance 59

3.4.6 Design and performance summary 60

3.5 Faraday cup probe 61

3.5.1 Background 61

3.5.2 Probe description 63

3.5.3 Probe operation, behaviour and performance analysis 67

3.5.4 Performance summary 75

3.6 Two-axis rotation system 76

3.6.1 Background 76

3.6.2 Description of ICDD capture system 79

3.6.3 Commissioning & verification 83

3.6.4 ICDD data capture & analysis 85

3.6.5 Performance summary 90

3.7 Ion collector 90

3.7.1 Background 90

3.7.2 Description 90

3.7.3 Signal measurement and verification 91

3.8 Erosion rate measurement 92

3.8.1 Background 92

3.8.2 Description of erosion measurement technique 94

4 Thruster design, behaviour & performance evaluation 96

4.1 Introduction 96

4.2 Thruster description 96

4.2.1 Electrode design 96

4.2.2 Arc initiation mechanism 99

4.2.3 Choice of reference cathode materials 103

4.3 Thruster characterisation, validation and verification 104

4.3.1 General operation of VAT prototypes 104

4.3.2 Thruster performance tests 104

4.3.3 VAT plume distribution 115

4.3.4 Comparison with empirical performance model 117

4.4 Summary 119

5 Pulse length study 121

5.1 Introduction . . . 121

5.2 Method . . . 121

5.3 Results & discussion . . . 122

5.3.1 Erosion tests . . . 122

5.3.2 ICDD measurements . . . 126

5.3.3 Ion current . . . 132

5.3.4 Thrust tests . . . 133

5.3.5 Proposed mechanism for enhanced ion and thrust production rates . 136

5.3.6 Overall performance . . . 137

5.3.7 Comments on surface contaminants and gas absorption . . . 138

5.4 Summary . . . 139

6 Cathode shape study **141**

6.1 Introduction . . . 141

6.2 Method . . . 141

6.2.1 Cathode design . . . 141

6.2.2 Choice of arc pulse characteristics . . . 142

6.2.3 Test setup . . . 143

6.3 Results & discussion . . . 144

6.3.1 Arc pulse behaviour . . . 144

6.3.2 Erosion rate . . . 145

6.3.3 ICDD and thrust correction factors . . . 148

6.3.4 Thrust production . . . 152

6.3.5 Overall performance . . . 155

6.3.6 Possible explanations for enhanced thrust . . . 156

6.4 Summary . . . 159

7 Carbon cathode study **161**

7.1 Introduction . . . 161

7.2 Method . . . 161

7.2.1 Material list . . . 161

7.2.2 Operating conditions and performance tests . . . 162

7.3 Results & discussion . . . 163

7.3.1 Overall behaviour and thrust production . . . 163

7.3.2 Erosion rate . . . 170

7.3.3 ICDD measurement . . . 172

7.3.4 Overall performance . . . 173

7.3.5 Comparison with literature . . . 175

7.4 Summary . . . 178

8 Discrete anode switching technique **180**

8.1 Introduction . . . 180

8.2 Description of anode switching setup . . . 181

8.2.1 Anode design . . . 181

8.2.2 Switching patterns and times . . . 183

8.2.3 DAS control system . . . 184

8.3 Test method . . . 185

8.4 Results & discussion . . . 187

8.4.1 Erosion behaviour across different cathode materials . . . 187

8.4.2 Switching limits . . . 189

8.4.3 Effect of DAS with varying arc pulse length . . . 190

8.4.4 Thrust . . . 192

8.4.5 Overall performance . . . 193

8.5 Summary . . . 194

9 Synthesis **195**

9.1 Overview . . . 195

9.2 The use of long arc pulse lengths . . . 195

9.3 The key role of cathode spot motion & coverage . . . 196

9.4 Effect of cathode material on C_T . . . 197

9.5 Combined use of DAS and conical cathodes . . . 198

9.6 Overview of VAT specific impulse performance gains . . . 200

10 Conclusion **202**

10.1 Overview . . . 202

10.1.1 Arc pulse length . . . 203

10.1.2 Cathode shape . . . 203

10.1.3 Carbon cathodes . . . 204

10.1.4 Discrete anode switching . . . 204

10.2 Recommendations 205

References **206**

Appendices **217**

A Empirical VAT performance table **218**

B Derivation of thrust correction factor **220**

C Vector problems in ICDD measurement **224**

C.1 Determining the thrust vector from ICDD data 224

C.2 Finding the true TARS thruster orientation angle 226

D Additional experimental data **228**

D.1 Pulse length study 228

List of Figures

1.1 Schematic illustrating basic elements (cathode, anode, insulator, PFN) and features (cathodic arc, cathode spots, plasma jet, macroparticles) of a typical VAT. 2

1.2 Schematic of single cathode spot surface and near-cathode regions with major particle interactions of neutral and electron emission, electron and ion return, ionisation and ion acceleration. Source from Lun (2009). 5

1.3 Map of arc operating conditions (peak arc current and arc pulse length) for several published VAT designs. Approximate areas identifying extreme (Regions A–D) and desirable (Region E) operating limits are shown. A previously untested region of VAT operation within Region E is highlighted. . . 14

3.1 Test ring vacuum chamber and high-vacuum pump system at the Wits Space Propulsion Research laboratory, School of Physics. 36

3.2 Schematic of VAT baseline inductive pulse circuit with typical component specifications. 38

3.3 Typical arc current and arc voltage pulse waveforms measured at the pulse circuit output (shown here filtered and averaged over 20 samples). In this example, an iron cathode was used. Pulse charging occurs at time $t < 0$ μs; arc initiation occurs at $t = 0$ μs and the arc discharge occurs at $t > 0$ μs. . . . 39

3.4 Photograph of Mark I and II VAT inductive energy storage pulsed power circuits. 39

3.5 Process flow chart of automated LABVIEW data capture control system . . . 41

3.6 Typical waveform traces of captured (a) arc current and (b) arc voltage (peaks beyond 1 ms indicate arc termination). In this example, a Bi cathode was used (50 A peak arc current, 2138 μs median pulse length, 75 sampled traces). 42

3.7 Typical waveform traces of captured (a) ion current and corresponding (b) arc current. In this example, a Fe cathode was used (50 A peak arc current, 529 μs median pulse length, 20 sampled traces). 43

3.8 Normal probability plots for processed results of average arc current, average arc voltage and arc pulse length. In this example, a Bi cathode was used (50 A peak arc current, 2138 μs median pulse length, 75 sampled traces). . . 44

3.9 Normal probability plots for processed results of average arc current, average arc voltage and arc pulse length. In this example, an Al cathode was used (50 A peak arc current, 233 μs median pulse length, 175 sampled traces). 44

3.10 Histograms of untransformed and Box-Cox transformed pulse length data from Figure 3.9. Probability plot shows that transformed data is well fit to a Log-Normal distribution. 45

3.11 Normal probability plot for processed results of ion-to-arc charge ratio. In this example, a Fe cathode was used (50 A peak arc current, 529 μs median pulse length, 20 samples). 46

3.12 Thrust stand: (a) Overall schematic, (b) Electrostatic calibration system (ECS) with 5 degree of freedom linear positioning system, (c) Experimental test setup inside the vacuum chamber 49

3.13 Detailed view of gallium pot power interface as installed on thrust stand. The interface can currently support up to a total of nine (9) power and/or data conduits. 50

3.14 Typical beam displacement response to a 12.5 s long repetitively-pulsed thrust firing from a VAT with an iron cathode. A comparison of the measured and analytical beam response shows good agreement. Value of x_s is found by measuring the average displacement several seconds after initial thruster firing or start-up. 54

3.15 Typical calibration result showing relationship between beam displacement and the applied force on the beam 55

3.16 (a) Schematic force diagram and (b) photograph of calibration setup verifying ECS force generation. 57

3.17 Comparison of theoretical electrostatic force and force generated by the ECS system 57

3.18 Comparison of sources of thrust error over the 0–40 μm displacement range truncated to a maximum error limit of 10%. 60

3.19 Schematic of Faraday Cup probe and circuit. Ion collector is negatively biased to -118 V and connected to ground via a terminating resistor. In the setup depicted here, the resistor value was set at 2.48 $\pm$0.01 MΩ for ICDD measurements in this study. An additional -60 V bias plate was installed for further repulsion of plasma electrons. 64

3.20 Photograph and engineering drawings of Faraday Cup probe 65

3.21 Comparison of normalised arc discharge waveform and ion current signals taken directly in front of VAT (Fe cathode) from a distance of z = 230 mm. Arc pulse characteristics are I = 50 and 120 A, $t_p \sim 500$ μs. 68

3.22 Measurement of ion current signal from baseline VAT at various drift lengths to the FC probe (z = 150, 230 and 300 mm) . Ion current drops according to $1/z^2$. 68

3.23 Measurement of FC ion current signal from baseline VAT taken at various bias collector voltages from −118 V to +20 V. Negative ion current signals at 0 and +20 V clearly depicts non-repulsion of plasma electrons. 69

3.24 Observed increase of peak ion current location with peak ion current magnitude. Ion signals taken directly in front of VAT with Fe cathode. 70

3.25 Plot of peak ion current location against peak ion current magnitude with observed linear trend. Captured ion current samples obtained from tests with Al, Fe and Bi cathodes, peak arc currents of 50 and 100 A and pulse lengths 200–3000 μs long. Drift length z = 230 mm and R = 2.48 MΩ. 70

3.26 Comparison of ion current signals taken with two different terminating resistor values. Note the different response times of the two resulting signals, where the lower resistor value gives a faster response. Waveforms are averaged over 40 samples. Calculated charge of ion pulses are within 10% of each other. Drift length z = 230 mm. 71

3.27 Measured FC ion current signals against varying bias plate voltages over the range −60 V to +60 V. A baseline VAT with an Fe cathode (I = 50 A pk, t_p = 2.7 ms) was used. FC probe drift length z = 230 mm. 73

3.28 Vector diagram of thrust vector comprised of yaw and pitch components. . 79

3.29 Photograph of ICDD capture system with TARS rig and Faraday cup probe. VAT prototype is centrally mounted to TARS frame. 80

3.30 Schematic side view of ICDD measuring setup with TARS and Faraday cup probe arrangement as used in this work. 80

3.31 Process flow chart of TARS stepper motor control system 81

3.32 Functional diagram of ICDD measuring system 82

3.33 Range of alignment errors over (a) yaw and (b) pitch angles for worse-case scenario TARS thruster assembly positions. Data curves best fit to sinusoidal function. Pitch error due to gearbox teeth play is not shown here. . . 83

3.34 Surface fit of ICDD test data with various distribution fits shown for comparison. Test data shown here is for a baseline VAT operating with a Fe cathode (50 A pk, 2.7 ms, 3 Hz, 7.5 W) and a FC probe distance of z = 230 mm. Twenty samples per pitch and yaw angle were taken. Best fit is a Gaussian distribution of spread factor w = 1.197 ±0.032 (R^2 = 0.982, RMSE = 0.012). . 87

3.35 Problem geometry and variable definitions used for calculating C_T. Adapted from Sekerak (2005). 89

3.36 Sectioned view of ion collector enclosure for measuring total ion-to-arc current ratio. Enclosure is suspended and isolated from vacuum chamber with plastic blocks (not shown here). Thrusters are positioned in the centre of the enclosure to ensure total and uniform collection. 91

3.37 Measurement of ion current signal emitted from a baseline VAT taken at various ion collector bias voltages from −60 V to +20 V. Negative ion current signal at +20 V clearly depicts non-repulsion of plasma electrons. 92

4.1 Illustrated matrix of (a) rod, (b) tube and (c) annular VAT electrode designs in both coaxial and planar format (based on Lun (2009)). 97

4.2 (a) Engineering model drawings and (b) photographs of baseline/reference VAT design. 100

4.3 Exploration of different film manufacturing techniques such as (a) & (b) silver paint, (c) & (d) cold spray copper films, and (e) & (f) graphite coatings used to manufacture the thin conducting film for triggerless arc initiation. . 101

4.4 Close-up views of Al and Fe VAT prototypes firing inside the vacuum chamber with visible plasma jet plume emanating outward from the cathode surface – (a) Al plasma generally exhibits a purple glow, whilst (c) Fe plasma exhibits a blue glow. Macroparticle emission in each respective VAT is observed in (b) and (d) as radiating incandescent particles from the cathode region (highlighted with arrows). 105

4.5 Thrust stand setup with three VATs mounted for lifetime testing. Cathode materials used were Al, Fe and Bi. Lifetime test duration of 1–5 $\times 10^4$ pulses. 106

4.6 Typical averaged arc current and arc voltage pulse waveforms for Al, Fe and Bi during lifetime thrust tests. Data shown here after n = 3000–4000 pulse firings. 108

4.7 Used thrusters after lifetime and verification thrust tests. Note the differences in cathode erosion patterns for each thruster. 109

4.8 Measured arc pulse current, voltage and median pulse length over duration of lifetime test on baseline VATs with Al, Fe, and Bi cathodes. Data fluctuation and error bars are indicative of the noisy behaviour of the vacuum arc pulses. Lifetime test duration is expressed in terms of number of pulses fired.110

4.9 Growth of median pulse length error bound values over time for Fe cathode lifetime test. Vertical axis represents the lower and upper bound values as a percentage of the median pulse length value. 111

4.10 (a) Measured thrust against arc current for baseline VATs with Al, Fe, and Bi cathodes with observed linear trends of thrust against current; (b) shows change in thrust production per input arc current over thruster lifetime. . . 112

4.11 (a) Measured average thrust against average arc power and (b) average impulse bits against average pulse energy for baseline VAT tests using Al, Fe, and Bi cathodes. A wide range of thrust and impulse production performance across all materials is demonstrated. General increases in thrust and impulse with increasing thruster power and energy levels are also observed. 114

4.12 Ion current plume distributions along (a) pitch and (b) yaw axes for baseline VATs using Al, Fe and Bi cathodes. I = 50 A pk and average pulse lengths for Al, Fe and Bi are 309, 506 and 3421 μs respectively. Measured deviation angles along pitch and yaw axes have been corrected to produce centred ICDDs for comparison purposes. Vertical axis is the ion charge collected by the Faraday cup probe divided by the arc pulse charge. 116

5.1 Comparison of erosion uniformity between short (250–500 μs) and long (2000–3000 μs) pulses on (a) Bi and (b) Al cathodes. Majority of erosion extends up to 1 mm from cathode edge when using short pulses, whilst long pulses produce near-uniform erosion. Peak arc current I = 50 A. 123

5.2 Erosion rate results for baseline VATS operating at various pulse lengths for (a) Al, Fe, Cu and (b) Bi cathodes. Peak arc currents in the 15–100 A range are studied. 125

5.3 ICDD results for baseline VATS operating at various pulse lengths using (a) Al, (b) Fe and (c) Bi cathodes. Peak arc currents I = 50 A for (a)–(c) and I = 100 A for (d). For conciseness, only pitch data is shown in detail here. 127

5.4 Growth of peak ion charge ratios along thruster centreline with pulse length. Cathode materials Al, Fe and Bi each show different growth behaviour. Peak ICDD test data taken from Figure 5.3 (a)–(c) where peak I = 50 A. 129

5.5 Thrust correction factor results for baseline VATS operating at various pulse lengths using (a) Al, (b) Fe and (c) Bi cathodes. Peak arc currents of 50 A and 100 A are studied. 131

5.6 Average thrust per current results for baseline VATs using Al, Fe, Cu and Bi cathodes operating at 50 A peak arc current at various pulse lengths. All thrust data here is shown for VATs firing up to no more than a total cumulative arc pulse charge of ~80 C. Error bars have been omitted for visual clarity. 134

5.7 Average thruster per current results for baseline VAT with Fe cathode operating at 50 A peak arc current at various pulse lengths. A linear fit (for visual purposes and appropriate within the range and scope of study) through 50 A data shows an increase in average thrust production with increasing pulse length from 216 μN/A at 500 μs to 262 μN/A at 2000 μs (21.3% increase).135

6.1 Illustration of thruster geometry used in this study with (a) flat and (b) concave cathode surface profile defined by cone angle α. VATs with conical cathodes prepared for testing are shown in (c). 142

6.2 Growth of average arc voltage for decreasing cone angle α. Each data point represents combined average of arc voltage test data. 145

6.3 Shortening of arc pulse with decreasing cone angle α. Each data point represents combined average of median arc pulse length. 145

6.4 Measured cathode erosion rates at selected cone angles of α = 180°, 120° and 90°. Results are normalised to flat cathode result (baseline). Normalised surface area of cathode rod head against cone angle is also included for comparison. 146

6.5 View of eroded conical Fe cathode (α = 120°) in (a) unaltered and (b) highlighted views. Radial grooves or "spokes" are highlighted with red lines. Grooves in segment 1 are spaced roughly 80° apart, whilst grooves in segment 2 are spaced roughly 60° apart. 147

6.6 Ion current density distribution results for (a) Bi, (b) Fe and (c) Al cathodes at α = 180° (□), 135° (△), 120° (○), and 90° (◇) cone angles along pitch and yaw axes. Data corrected for thrust vector deviation in both pitch and yaw to aid visual comparison. 149

6.7 Comparison of weighted C_T' values for a conical cathode design against approximated C_T values for a flat cathode design at the same arc pulse length (number in brackets, milliseconds). Flat cathode designs being compared are baseline (0.5 mm recessed) and equivalently recessed to the same depth as a conical cathode design (135° → 0.65 mm, 120° → 0.91 mm, 90° → 1.58 mm). 150

6.8 Thrust correction factors for conical cathode designs normalised against baseline flat cathode design (α = 180°). Test data taken from Figure 6.7. Pulse lengths used are in the 1.4–5.1 ms range. 151

6.9 Thrust measurements (T/I) measured at various cathode cone angles (α = 90°, 120° and 135°). Each data point is an average of 16 thrust tests run up to $\sum Q \approx 50$ C. Trend lines shown represent average thrust per arc current for baseline flat cathodes tested in this study as presented in Figures D.1–5.7 and D.3. 152

6.10 Measured thrust per arc current for various cathode cone angles (α = 90°, 120° and 135°) normalised against baseline average thrust trend lines. Test data taken from Figure 6.9. 153

6.11 Consolidated average T/I values for various cathode cone angles (α = 90°, 120° and 135°) and materials normalised against baseline average thrust trend lines. Test data taken from Figure 6.10. 154

6.12 Simplified four-quadrant outcome on plasma jet shape and thrust production as a function of cathode cone angle and arc pulse length. 155

7.1 Photographs of cathode erosion for Glassy carbon (GC) and AF-5, EDM-3 and EDM-200 pure carbon graphite rods. 164

7.2 Measured thrust per arc current (left vertical axis) and thrust-to-power ratios (right vertical axis) over test duration for pure carbon cathodes. Materials include (a) GC, (b) AF-5, (c) EDM-3 and (d) EDM-200. Total cumulative pulse charges range from 80 to 120 C. Lines through data points are for visual aid only. 165

7.3 Photographs of cathode erosion for TTK-4C, C-3 and C-200 copper-impregnated carbon graphite rods. 167

7.4 Measured thrust per arc current (left vertical axis) and thrust-to-power ratios (right vertical axis) over test duration for copper-impregnated carbon cathodes. Materials include (a) TTK-4C, (b) C-3, and (c) C-200. Total cumulative pulse charges range from 80 to 120 C. Lines through data points are for visual aid only. 168

7.5 Comparison of thrust per arc current behaviour over test duration for pure graphite and copper-impregnated carbon graphite compounds. Materials shown are paired as (a) EDM-200 and C-200, and (b) EDM-3 and C-3. Differences in starting thrust levels and converged thrust levels at the end of the test are highlighted with arrows. 169

7.6 Measured erosion rate results for carbon cathodes in this study. Typical pulse characteristics used are I = 50 A peak, f = 10–20 Hz, $\bar{P}$ = 2–10 W. 170

7.7 Relationship between material properties and (long-pulsed) erosion rates for (a) pure carbon and (b) copper-impregnated graphite cathodes. Average particle size and electrical resistivity of each material is indicated. 171

7.8 Measured ICDD of cathode material C-3 in a baseline VAT. Typical pulse conditions are I = 50 A peak, t_p = 1.4 ms, f = 2 Hz. 173

8.1 Anode designs used in this study on a baseline VAT: (a) standard ring and (b) six discrete segments. 182

8.2 Close up of a semi-built segmented anode VAT with graphite film installed on three equally spaced anodes. Once graphite film construction was completed, the cathode rod and remaining anodes were mounted with final film touch up. 182

8.3 Schematic of anode switching patterns. Black dots and arrows represent cathode spot(s) and their expected forced motion over the surface at various stages in the anode switching sequence according to (a) triangular motion with three active and inactive (or "dead") anodes used, or (b) cross-shaped motion with three active anode pairs. 183

8.4 Schematic circuit diagram of DAS switch control system comprised of three switching subsystems (one for each anode) incorporated into the VAT pulse circuit. Each subsystem is comprised of an optocoupler to receive Arduino commands, a floating voltage source, a gate driver and a dedicated IGBT switch to control a discrete anode. 186

8.5 Anode signal switching timeline for each anode signal (**S1**, **S2** and **S3**) where T_1 is the anode active switching time (45, 120 and 520 μs), T_2 is the transition time (20 μs) and ΔT is the dedicated anode activation time (5, 80 and 480 μs). 187

8.6 Erosion patterns on (a) Al, (b) Fe and (c) Bi cathodes subjected to discrete anode switching (120 μs switching time, crossed pattern). Levels of erosion are labelled according to severity. A high-contrast image of each cathode provides an approximate visual indication of cathode spot erosion coverage. Pulses characteristics are I = 50 A peak and t_p = 300–400 μs long. 188

8.7 Erosion patterns on (a) AF-5 and (b) C-3 graphite cathodes subjected to discrete anode switching (120 μs switching time, crossed pattern). Levels of erosion are labelled according to severity. A high-contrast image of each cathode provides an approximate visual indication of cathode spot erosion coverage. Pulses characteristics are I = 50 A peak and t_p = 300 μs long. . . . 188

8.8 Erosion rate results demonstrating lower limits of operation and switching times of DAS technique applied to baseline VAT design with Fe cathode. Pulse characteristics are I = 25 A peak, t_p = 200–330 μs pulse lengths and 1–2 W average thruster power. Anode triangular switching pattern was used. 190

8.9 Erosion rate results for different switching times as a function of arc pulse length. Tests performed on Fe cathode running at I = 50 A peak. Erosion results for the baseline VAT operating with the standard anode ring is included for comparison. 191

8.10 Direct thrust measurements for Fe cathode operating in long-pulsed mode with and without DAS implementation. Baseline thrust data was obtained from Figure 5.7 with error bars omitted for visual clarity. DAS-enhanced VAT operating conditions were I = 50 A peak, f = 6 Hz, 45 μs switching time (crossed pattern) run up to a total charge of $\sum Q$ = 92.5 C. 192

9.1 Simplified network interaction of factors influencing cathode erosion rate. Spot motion and coverage is seen as a central influence. 197

9.2 Relationship between material boiling point and average thrust correction factor. Data taken from baseline VAT tests operating at I = 50 A peak in both short (500 μs) and long pulses (1000–1500 μs) – see Table 5.3 and Figure 7.8. 198

9.3 Summary and comparison of prototype VAT performance levels (specific impulse) measured within this study. The list includes carbon-based cathode materials and metal cathodes operating in long- (L) and short-pulsed (S) modes. Performance of conical (120°) and DAS-enhanced (45 μs) Fe cathodes are also shown. Each element type is colour-grouped for visual aid.200

B.1 Problem geometry and variable definitions used for calculating C_T. Adapted from Sekerak (2005). 221

C.1 Vector diagram of thrust vector comprised of yaw and pitch components. . 225

C.2 Geometric representation of thruster orientation angle problem using a tetrahedron 226

D.1 Average thrust per current results for baseline VAT with Al cathode operating at 50 A and 100 A peak arc current at various pulse lengths. A linear fit through 50 A data shows an increase in average thrust production with increasing pulse length from 141 μN/A at 500 μs to 172 μN/A at 2000 μs (22.0% increase). 228

D.2 Average thrust per current results for baseline VAT with Cu cathode operating at 50 A peak arc current at various pulse lengths. A linear fit through 50 A data shows an increase in average thrust production with increasing pulse length from 197 μN/A at 500 μs to 246 μN/A at 2000 μs (24.9% increase).229

D.3 Average thrust per current results for baseline VAT with Bi cathode operating at 50 A and 100 A peak arc current at various pulse lengths. A linear fit through 50 A data shows an increase in average thrust production with increasing pulse length from 364 μN/A at 500 μs to 404 μN/A at 2000 μs (11.0% increase). 229

List of Tables

1.1 List of typical arc current per spot values for several cathode materials, based on work by Djakov & Holmes (1971), Lafferty (1980), Beilis et al. (1997) and Boxman et al. (1995). 6

1.2 Some published VAT designs or tests in approximate chronological order with varying cathode materials, sizes and geometry (where available). Specified operating pulse characteristics are also listed. 10

3.1 Range of VAT pulse circuit performance parameters 38

3.2 Range of expected space-charge-limited ion currents for all materials used in this study based on revised analysis of Child-Langmuir Law by Bridges et al. (1965) 74

3.3 Comparison of ICDD capture methods using Faraday probes 77

3.4 Surface fitting results for the example shown in Figure3.34. Spread factors, pitch and yaw absolute deviation angles, and goodness-of-fit indicators for each distribution type are listed. The Gaussian distribution is shown to be the best fit in this example (highlighted in grey). 87

3.5 Range of typical values and uncertainties for f, Δt and Δm in this work's erosion studies and their effect on final E_r uncertainty 95

4.1 Major VAT design requirements and constraints 98

4.2 Material properties of Al, Fe, Cu and Bi cathode samples used in this study. Thermophysical data from Incropera & DeWitt (2002). 103

4.3 Summary of total weighted-averaged arc pulse characteristics, total charge transferred and total pulse firings for baseline VAT lifetime tests for Al, Fe and Bi cathode materials 106

4.4 Comparison of measured and predicted erosion rates of baseline VATs with published literature. Measured cathode mass loss in brackets. 109

4.5 Overall performance results of baseline VAT tests with Al, Fe and Bi cathodes. Values of T/I and T/P are averaged over the entire data set for each cathode material. 115

4.6 Specifications of fitted plume distributions (type, spread factor, goodness-of-fit indicators) and thrust vector deviation angles for baseline VAT designs with Al, Fe and Bi cathodes. Resulting thrust correction factors for each case are also listed. 117

4.7 Empirical values used for predicting baseline VAT performance of Al, Fe and Bi cathodes 118

4.8 Comparison of weight-averaged measured and empirically predicted performance results for baseline VAT tests using Al, Fe and Bi cathodes. Predicted results are in brackets. 118

5.1 Comparison of selected erosion rate results for Al, Fe, Cu and Bi cathode materials in a baseline VAT design operating with long and short pulses. Peak arc current is I = 50 A. 123

5.2 Trend fit specifications for peak ion charge ratios $\bar{J}$ (μC/C) against median pulse length t_p (μs) as shown in Figure 5.4. 129

5.3 Test parameters and results (distribution type, spread, goodness-of-fit, thrust correction factor) for ICDD measurements at various arc pulse lengths. Data from Figure 5.3 is included. 130

5.4 Comparison of averaged ion-to-arc current ratio results for Al, Fe and Bi cathode materials in a baseline VAT design operating with long and short pulses. Peak arc current is I = 50 A. 132

5.5 Comparison of thruster performance for selected baseline VAT designs for Al, Fe, Cu and Bi cathodes operating with short and long pulses. Peak arc current at I = 50 A. 137

6.1 Comparison of average erosion rates of baseline (180°) and conical VATs for selected cone angles (120° and 90°). For additional context, weight-averaged pulse lengths (in milliseconds) during each E_r measurement are included in brackets. 146

6.2 Comparison of VAT performance for selected conical and equivalent baseline VAT designs operating with Al, Fe and Bi cathodes at I = 50 A. Thrust and erosion rate data taken at similar millisecond-range pulse lengths for each case pair. 156

7.1 List of grades and properties of carbon rod materials tested in this study (data obtained from suppliers' websites). Carbon materials are grouped according to their composition, namely that of (1) pure carbon and (2) copper-impregnated graphite compounds. Materials are arranged in order of increasing average particle size. 162

7.2 Summarised performance test results for long-pulsed baseline VATs with carbon-based cathodes. Thrust per arc current, thrust-to-power ratio and impulse per pulse energy results are weight-averaged against delivered charge per test sample for a total population sample from $\sum Q$ = 0 to 80 C. Fe baseline performance as measured in Chapter 4 is provided for comparison. . . 174

7.3 Comparison of averaged measured carbon VAT thrust and erosion performance against empirical model and published literature. Note that model assumes ϵ = 0.19 (in brackets). EDM-200's lowest measured thrust per arc current level (occurring at $\sum Q$ = 67 C) is included in brackets directly underneath the total test average. Ion-to-arc current ratios for AF-5 and C-3 are averaged over 200 samples taken at I = 50 A peak, t_p = 1.5–2 ms, f = 2 Hz.176

8.1 Typical electrical resistances of interelectrode junctions of the segmented anode VAT design 181

8.2 Comparison of thruster performance for three selected Fe VATs operating with (1) short pulses (baseline design), (2) long pulses (baseline design) and (3) long pulses and DAS implementation. Peak arc current at I = 50 A. 193

9.1 Comparison of erosion rate results for selected conical and baseline (flat) cathode shapes with and without DAS implementation. Peak arc current I = 50 A. Cathode material is Fe. 199

A.1 Empirical VAT properties and performance for various pure metal cathode materials. The top five performing materials in each category of specific impulse I_{sp}, thrust-to-power ratio T/P and efficiency η are highlighted in grey. 219

Nomenclature

Roman Letters

A	Area (m^2), thrust vector yaw component magnitude (N)
a	Electrostatic force coefficient (N/V^2)
B	Thrust vector pitch component magnitude (N)
C	Particle density coefficient $(Am)^{-1}$, thrust vector magnitude (N)
C_T	Thrust correction factor
D	General function
d	Diameter (m)
E_i	Ion erosion rate (μg/C)
E_j	Pulse energy (J)
E_k	Kinetic energy (eV)
E_r	Total erosion rate (μg/C)
e	Electron, electron charge (C)
F	Force (N)
f	Frequency (Hz)
g	Gravitational acceleration (m/s^2)
H_o	Heavyside step function
I	Arc current (A)
I_{bit}	Impulse bit (Ns)
I_i	Ion current (A)
I_m	Mass moment of inertia (kgm^2)
I_{sp}	Specific impulse (s)

i	Ion
J	Current density (A/m^2)
$\bar{J}$	Ion-to-arc charge ratio
K_b	Boltzmann constant (J/K)
k	Exponential distribution spread factor
k_{eff}	Effective beam stiffness (N/m)
L	Inductance (H)
L_{mfp}	Mean free path (m)
M, m	Mass (kg)
N	Pulse number
n	Sample number, particle density (1/m^3)
P	Power (W)
P_r	Probability
p	Pressure (Pa)
Q	Charge (C)
R	Resistance (Ω), Fitness coefficient
R_o	Oscilloscope resistance (Ω)
r	Radius (m)
r_a	Thrust stand moment arm, anode radius (m)
r_c	Cathode radius (m)
s	Spacing, gap distance (m)
T	Thrust (N)
T_1	Anode switching time (s)
T_2	Anode switch transition time (s)
T_b	Boiling point (K)
T_r	Temperature (eV or K)
t	Time (s), Student's number
t_{off}	Length of time that a thruster is off (s)
t_{on}	Length of time that a thruster is on (s)
t_p	Pulse length (s)
V	Arc voltage (V)
V_0	Bias voltage (V)
V_{fc}	Voltage drop across FC circuit terminating resistor (V)

v	Velocity (m/s)
w	Gaussian distribution spread factor
x	Distance along X-axis co-ordinate, translational displacement (m)
x_s	Steady state beam displacement (m)
y	Distance along Y-axis co-ordinate (m)
$\bar{Z}$	Average ion charge state
z	Distance along Z-axis co-ordinate, drift length (m)

Greek Symbols

α	Cone angle
β_p	Thrust vector pitch component angle (deg)
β_y	Thrust vector yaw component angle (deg)
β_T	Thrust vector angle (deg)
γ	Parabolic distribution spread factor(s)
Δ	Difference, uncertainty
ΔD	Final uncertainty of function D
Δm	Cathode mass loss (kg)
ΔT	Single anode activation time (s)
Δt	Total firing time (s)
ΔX	Uncertainty of dependant variable
δ	Damping term
δ_c	Duty cycle (%)
ϵ	Ion-to-arc current ratio
ϵ_o	Permittivity of free space (C^2/Nm^2)
ζ	Damping coefficient
η	Thruster efficiency (%)
θ	Angle, angular displacement (rad)
λ_D	Debye length (m)
λ_k	Thermal conductivity (W/mK)
ρ	Density (kg/m^3)

σ	Standard deviation
τ	Time term
ϕ	Ion incidence or plume divergence angle (rad)
ϕ_e	Deviation of ϕ to the normal axis (rad)
ω_n	Natural frequency (Hz)

Subscripts

b	Beam
cl	Space charge limit
e	Electron
ecs	Electrostatic calibration system
i	Ion
ip	Captured probe signal
p	Plasma
T	Thrust
th	Theoretical
$true$	True, actual
tot	Total
z	Distance along the normal direction of the thruster or cathode surface (m)

Acronyms

AASC	Alameda Applied Sciences Corporation
CEX	Charge Exchange Collisions
CPUT	Cape Peninsula University of Technology
CSD	Charge State Distribution
DAS	Discrete Anode Switching
DC	Direct Current
ECS	Electrostatic Calibration System
EDM	Electric Discharge Machining
EMI	Electromagnetic Interference
EP	Electric Propulsion
FC	Faraday Cup
FEEP	Field Emission Electric Propulsion
GC	Glassy Carbon
HV	High Voltage
ICDD	Ion Current Density Distribution
IEPC	International Electric Propulsion Conference
IGBT	Insulated-Gate Bipolar Transistor
JPL	Jet Propulsion Laboratory
LBNL	Lawrence Berkeley National Laboratory
LDVT	Linear Variable Differential Transformer
LTE	Local Thermal Equilibrium
MP	Macroparticle
NASA	National Aeronautics and Space Administration

PFN	Pulse Forming Network
PIC	Particle-In-Cell
PPT	Pulsed Plasma Thruster
RMSE	Root Mean Square Error
SANSA	South African National Space Agency
SCS	Switch Control System
TARS	Two Axis Rotation System
TOF	Time Of Flight
VAT	Vacuum Arc Thruster

Chapter 1

Introduction

The vacuum arc thruster (VAT) is a small space propulsion system that produces plasma jets by means of a vacuum arc pulse between two electrodes separated by an insulator (Schein et al. 2002a). The schematic shown in Figure 1.1 depicts the basic elements and features of a typical VAT. The action of the vacuum arc forms hot microscopic cathode spots on the cathode surface, which emits vapourised cathode material. This material becomes ionised within the arc region and expands outward as a dense high-speed plasma, achieving velocities as high as 20 km/s. The vacuum arc pulses within the VAT are generated by a power circuit comprised of a network of capacitors and inductors called a pulse-forming network (PFN). Typical thrust values from a VAT are on the order of a few mN per pulse, where pulses are usually 50–500 μs in length and fired at a rate of 1–50 Hz. Typical impulses (or impulse bits) are in the μNs range.

The VAT falls under the category of a *microthruster*, which is a propulsion system that gives small satellites (typically 1–100 kg mass) the ability to perform orbital manoeuvres, drag compensation and station-keeping. These capabilities are highly attractive because they allow a satellite to orient itself at will, perform orbit positioning and greatly extend mission lifetime. A large variety of microthrusters exist and continue to be developed to address the technical challenges of miniaturising propulsion systems. Examples include Pulsed Plasma Thrusters (PPT), Field Emission Electric Propulsion (FEEP), Laser Abla-

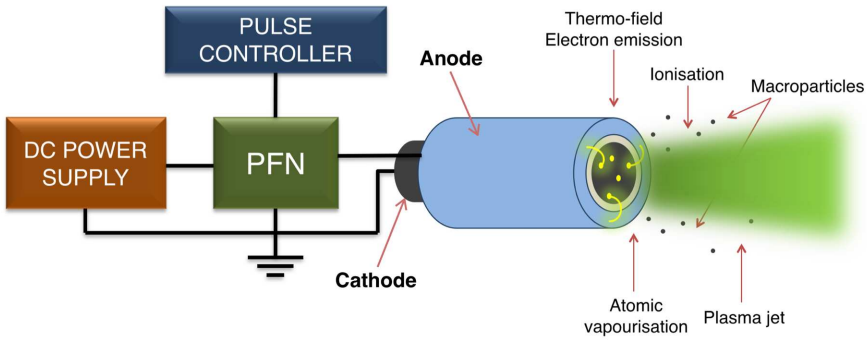

Figure 1.1: Schematic illustrating basic elements (cathode, anode, insulator, PFN) and features (cathodic arc, cathode spots, plasma jet, macroparticles) of a typical VAT.

tion Thrusters, micro-Ion Thrusters, micro-Resistojets and micro-Cold Gas Thrusters. Readers may consult Mueller (1997) and Micci & Ketsdever (2000) for a general overview of micro-propulsion options for satellites.

1.1 Background

1.1.1 Micro-propulsion in the South African and international context

In the last decade, the South African government has recognised the socio-economic, scientific and technological benefits that space and satellite technology can provide to its citizens. As a result, the newly-formed South African National Space Agency (SANSA) has been mandated to develop practical applications of space technology in areas such as remote sensing, earth observation, space weather monitoring and research, asset tracking and telecommunications (SANSA 2013). One of the ways SANSA plans to achieve this mandate is the development of space system technologies, particularly for small-sized satellites. This comes at an opportune time when the local and international space community has taken an increasing interest in the application of small satellites to allow lower cost access to space and with shorter development times (Smallsat 2014). In particular, the number of satellite missions utilising the CubeSat architecture is growing, a recent example being the local development and successful launch of South Africa's first CubeSat ZACUBE-1 (now called *TshepisoSat*) in November 2013 (CPUT 2014).

South Africa's small satellite engineering subsystem expertise currently include electronic and power subsystems, attitude control & determination, structures and thermal. However, South Africa's experience with satellite propulsion systems is limited at best, where nearly all systems previously developed (in the 1980's and 1990's) were chemically-based and applicable only to relatively large spacecraft. To date, there are no locally-developed and flight-qualified propulsion systems or microthrusters available to satellite designers. Recent satellite propulsion system research has generally been limited to theoretical and early laboratory prototypes (Weyer et al. 2004, Lun 2009, Ferrer & Tchonang 2011). This limitation is due to the demanding operation, performance, size and mass requirements expected of small satellite propulsion systems, the lack of diagnostic tools and infrastructure required for thruster testing, as well as a general lack of knowledge about thruster design and manufacturing. This is particularly true for electric or plasma propulsion systems, which promise higher performance in a smaller package volume over chemical propulsion, but at the expense of lower maximum thrust, the requirement of a power source and the presence of complex electromagnetic and plasma behaviour. This body of work aims to address some of these issues by expanding current knowledge of the VAT's design and operational aspects.

1.1.2 Why study the vacuum arc thruster?

The VAT is attractive as a potential microthruster due to its low overall system mass (< 1 kg), flexible and low average power usage (1–100 W), use of relatively low cost materials or manufacturing techniques, the generation of quasi-neutral plasma (no neutraliser unit is required) and the ability to use any electrically-conductive solid material as propellant. The use of relatively safe and inert solid propellent also eliminates the requirement for, and failure modes associated with, propellant tanks, valves and piping. Additionally, intricate and potentially hazardous propellant handling procedures are avoided and VATs pose little to no risk of catastrophic failure to a satellite. These powerful and potential benefits of VATs have been recognised by several research groups, which had been or are presently developing VAT propulsion system hardware for space flight (IEPC 2013, priv. comm.). However, in practice, the VAT generally only provides modest specific impulse values (300–600 s) and thrust-to-power ratios (5–10 μN/W) compared to other

plasma thrusters. Additionally, the VAT is still a relatively new propulsion technology compared to many other commercial systems such as the PPT, which has almost 50 years of development and flight heritage. With that in mind, there exists much opportunity to enhance, optimise and mature VAT technology in order to achieve its wider acceptance by the small satellite community as an attractive and viable propulsion solution.

1.1.3 What are vacuum arcs?

The term *vacuum arc* is used to describe a current-driven arc discharge that exists between a pair of anode and cathode electrodes within a vacuum environment. A characteristic feature of the vacuum arc is that the cathode electrode is *a source of both electron emission and plasma production* (Anders 2008). The mechanism for the creation and emission of plasma is achieved through the formation of small arc spots on the cathode surface. These *cathode spots* are microscopic in size and are initially formed by intense thermo-field emission at several micro-protrusions on the surface where the electric field (10^9 V/m) is highly concentrated. The high power density present in these areas is sufficient to heat, vapourise and eject cathode material, which collides with the electron cloud to form highly ionised quasi-neutral plasma consisting of single- and multiply-charged ions travelling on the order of 10–20 km/s (see Figure 1.2). The surprisingly large amount of ion momentum (thrusting force) that is generated by the vacuum arc plasma is presently considered to be primarily due to the ion pressure gradient (gas-dynamic expansion) and electron-ion coupling/friction (fast-moving electrons imparting momentum to slower-moving ions) (Weickert 1987, Hantzsche 1991, Yushkov et al. 2000). A conventional model of the process of cathodic plasma generation is shown in Figure 1.2, which contains simplified regions dominated by emission, ionisation and diffusion. Ions from this plasma jet expand outward, with a portion of ions returning to the cathode surface. The bombardment of returning ions assists in sustaining heating of the cathode spot surface until the vacuum arc de-stabilises and re-initiates a new spot at a suitable nearby location. This continued behaviour during the arc gives the impression of spot motion. Each arcing event leaves one or more small surface craters, dynamically altering the surface structure and its conditions for the next arcing event. More detailed descriptions of cathodic arc physics can be found in a number of sources (e.g. (Boxman

et al. 1995, Anders 2008)). The reader is also welcome to read a previous article written by the author on the development of a vacuum arc cathode spot model (Lun et al. 2010).

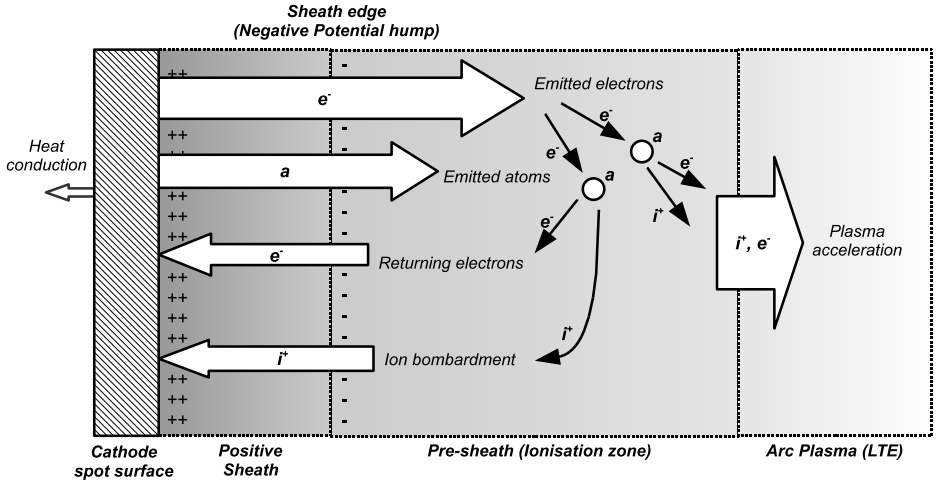

Figure 1.2: Schematic of single cathode spot surface and near-cathode regions with major particle interactions of neutral and electron emission, electron and ion return, ionisation and ion acceleration. Source from Lun (2009).

Remarkably, many of these vacuum arc processes occur on extremely small time scales (ns to μs), making their observation highly challenging. Vacuum arcs can exist over a wide range of operating conditions, such as low- or high-temperature electrodes, the presence of a gas or magnetic fields, from 10 A to 10 kA arc current levels and in different arc modes (Anders 2008). In this work, we deal primarily with cathodic arcs (a subset of vacuum arcs) where the arc operates in high vacuum on low-temperature cathodes and typically forms non-stationary cathode spots. Cathodic arcs were found to be the most common arc mode of choice in literature for operating vacuum arc thrusters.

The structure of cathode spots have been a subject of much controversy over the decades. Initially, each spot was assumed to be a singular micro-sized area of surface heating and plasma generation (Boxman et al. 1995). A spot was reported to generally carry no more than a fixed amount of arc current, whereby an increase in total cathode arc current resulted in “spot splitting” and the formation of additional spots (Djakov & Holmes 1971, Lafferty 1980). Spot splitting was found to be material-specific and related to the cathode’s thermal properties. Table 1.1 lists typical arc current per spot values reported for several cathode materials. Once a sufficiently large number of spots becomes present during higher arc currents (kA range), grouped spot behaviour occurs, often influenced

by the self-magnetic fields of the cathode spots' plasma jets (Boxman et al. 1995). Thus, the choice of cathode material and arc current used will jointly influence the overall behaviour and operation of the VAT.

Table 1.1: List of typical arc current per spot values for several cathode materials, based on work by Djakov & Holmes (1971), Lafferty (1980), Beilis et al. (1997) and Boxman et al. (1995).

Material	**Arc current per spot** (A)
Bismuth	3–5
Aluminium	30–50
Copper	75–100
Chromium	30–50
Iron	60–100
Titanium	70
Carbon	200
Tungsten	250–300

As the spatial and temporal resolution of spot observations improved over the years, researchers soon discovered that the cathode spot itself was comprised of a collection of ever-smaller structures, commonly referred to as spot fragments or cells (Barengolts et al. 2003). Ultimately, a fractal approach to cathodic arcs was proposed by Anders (2008), arising out of Mesyats's (1995) concept of the smallest emission site possible within a cathode spot (called "ectons"). Presently, the most essential definition of the cathode spot can be considered to be

> "...an assembly of emission centers showing fractal properties in spatial and temporal dimensions."
>
> — Anders (2008, p. 128)

Vacuum arcs as a phenomena were studied as early as the 19th Century as part of the emerging interest in electricity and arc discharges at that time. Since then, vacuum arc research was extensively expanded through the development and use of vacuum switches/tubes and thin film deposition in the 20th Century. Today, vacuum arcs continue to play an important role in the production of thin films and coatings (Sanders & Anders 2000), as ion sources (Brown 1994) and in the production of carbon nanotubes and graphene (Keidar et al. 2011). Popular and comprehensive texts on vacuum arcs

and cathodic arcs have been written by Lafferty (1980), Boxman et al. (1995) and Anders (2008).

1.1.4 History of the vacuum arc thruster

The earliest published studies on vacuum arc thrusters were performed by Dethlefsen (1968), and Gilmour & Lockwood (1972). They tested a variety of cathode materials and pioneered the use of an axial magnetic field to focus the ejected plasma jet. It was soon recognised that operating the thruster in a pulsed fashion enabled the required production of high power densities within the arc whilst maintaining low average power usage and small system size. However, the problem of delivering an adequate power supply to spacecraft systems meant that the VAT and many other electric propulsion systems of that era did not develop further for small satellites until much later in the 20th Century. Eventually, the miniaturisation of electronic components and the widely-adopted use of solar panels allowed the vacuum arc thruster to become a more attractive form of small satellite propulsion. VAT research was revitalised over the period 1998–2005 as result of a collaboration between Alameda Applied Sciences Corporation (AASC), NASA/Caltech Jet Propulsion Laboratory (JPL) and the Lawrence Berkeley National Laboratory (LBNL) (Qi et al. 1998, Tang et al. 2005, Polk et al. 2008). During that time, a number of important developments were made such as the development of the inductive energy storage circuit (Schein et al. 2002a), which incorporates the triggerless arc initiation technique (Anders et al. 1998) and the integration of a compact magnetic coil to collimate and accelerate the plasma (Tang et al. 2005, Keidar et al. 2005). Additionally, Qi et al. (1998) considered the vacuum arc thruster as a potential ion source for an electrostatic ion engine. An early engine prototype was developed using a bismuth cathode, which demonstrated good specific impulse levels as high as 3000–4000 s. AASC is the only company currently offering the VAT commercially (AASC 2011).

The first in-flight testing of a VAT system was attempted in 2006, where a simple VAT propulsion system was designed for the Illinois Observing Nanosatellite, a student-built satellite developed at the University of Illinois at Urbana-Champaign. Unfortunately, the launch rocket failed to reach orbit and the satellite was lost (Takker & Dabrowski 2006).

Currently, other researchers are developing VATs for use as CubeSat propulsion subsystems. This includes work by the University of Federal Armed Forces in Germany on the UWE-4 nanosatellite (Pietzka et al. 2013), Kyushu Institute of Technology development on HORYU nanosatellites (Fuchikami et al. 2013) and George Washington University's participation in the PhoneSat Project at NASA Ames Research Center (Keidar et al. 2013) and the US Air Force BRICSat-P CubeSat (Haque 2014). These groups intend to launch their satellites in the 2014–2015 time frame.

There are many practical aspects of VAT design that require further attention. These include safe and reliable arc triggering and cathode feed mechanisms, minimal thermal stresses, electromagnetic compatibility, consistent operation and performance, and extended operating lifetimes. These issues continue to pose serious challenges for researchers and engineers alike and must be addressed with innovative thruster designs (IEPC 2013, priv. comm.).

1.2 VAT design theory

Developing a complete and accurate theory of vacuum arc thrusters remains unfinished and is highly challenging because vacuum arcs can exist over a wide range of operating conditions, scales and modes. The cathode spots exhibit highly dynamic and complex behaviour which depend not only on ever-changing cathode surface conditions, but also on the plasma itself. Only in the last decade or so has the explosive and fractal nature[1] of these arc spots begun to be fully appreciated by the wider scientific community (Mesyats 1995, Hantzsche 2003, Anders 2008).

To make the problem more tractable, current VAT models have limited themselves to a number of gross simplifications of cathode spot behaviour and processes, e.g. one-dimensional domains, ignored secondary energy processes, and broad or averaged spot

[1] There are a wide range of cathode spot characteristics that support the fractal school of thought (e.g. see Anders (2008)). For example, cathode spots have been found to not be homogenous, but comprised of ever-smaller self-similar substructures (subspots, cells). Another example is the noise of the arc voltage, which can be shown to follow brown noise. Other self-similar qualities include cathode spot motion and creation (tree-like structures) and macroparticle size distribution (follows a power law).

and plasma behaviour. The first set of VAT theoretical performance models were developed during the early 21st century. Statom (2003) used published vacuum arc empirical data and a basic energy balance to convert electrical energy to kinetic energy in order to roughly estimate VAT thruster performance. Sekerak (2005) and Polk et al. (2008) developed a semi-empirical model based on the magneto-hydrodynamic equation of motion to more accurately determine VAT performance for a wide range of cathode materials. In so doing, they were able to identify some important design considerations for VAT electrodes and provided recommendations for cathode material options. To reduce some dependence on empirical data, Lun et al. (2010) developed a hybrid model combining a cathode spot model with Polk et al.'s (2008) semi-empirical model to predict thruster performance.

Unfortunately, present VAT models still require empirical data input from vacuum arc experiments, which currently only exists for certain operating conditions, electrode sizes and geometries. This makes present models applicable to only certain cathode shapes (small coaxial rod or tube, e.g. 3–6 mm diameter) and narrow arc pulse conditions (80–300 A, $\sim 250\mu$s). To improve VAT modelling and understanding, a great need exists to increase the amount of available experimental data across much wider performance envelopes, operating conditions and thruster geometries. This work aims to help address this lack of available data.

1.3 VAT design practice

A summary of several VATs that were previously designed, built and tested are listed in Table 1.2. It is immediately apparent that VATs can be operated across a wide range of fuels, cathode sizes, arc current levels and pulse lengths. It should be noted, however, that not all of these designs were necessarily optimised for peak performance. The most common VAT design and operating condition to date has been a coaxial electrode arrangement with a cylindrical 1/8 inch diameter cathode rod of Titanium, firing pulses of 10–200 A peak arc current and 250–500 μs in length. An assessment of these common design choices can provide some insight into VAT design philosophy and heritage.

Table 1.2: Some published VAT designs or tests in approximate chronological order with varying cathode materials, sizes and geometry (where available). Specified operating pulse characteristics are also listed.

Ref.	Cathode properties			Pulse characteristics	
	Material	**Dia./size** (mm)	**Geometry**	**Peak arc current** (A)	**Pulse length** (μs)
a	Zn, U, Mg, Ti	3.18	Rod	200	50–500
b	W, Ti	3.18	Rod	10	100
c	Cr, Y		Rod	10–25	250–500
d	Ti	3.18	Rod	14, 510	1500, 100
e			Multi-rods	25	600
f	Ti	50	Cylinder	1500–2000	400–500
g	Cu, Al	30	Rod	50–250	20000–DC
h	Al	10 × 2 (face)	Planar	200–800	0.4
i	Ti	6.35 (outer)	Annular tube	40	400
j	Cu	~ 4 (outer)	Rod, tube	10–50	250–400

[a]Gilmour & Lockwood (1972), [b]Schein et al. (2002a), [c]Schein et al. (2002b), [d]Sekerak (2005), [e]Tang et al. (2005), [f]Neumann et al. (2009), [g]Marks et al. (2009), [h]Lun (2009), [i]Zhuang et al. (2009), [j]Pietzka et al. (2013) and Kronhaus et al. (2013)

1.3.1 Choice of cathode geometry

The two most common cathode electrode designs used and studied in VATs are the small rod and tube shape (see Table 1.2). These designs are largely based on vacuum arc research heritage and provide a simple and convenient means of cathode manufacture and installation. A small-sized cathode also allows for the cathode face to approximate a point source for precise thrust pointing. As such, these cathode designs have been well studied both experimentally and theoretically (Anders & Yushkov 2002*a*, Sekerak 2005, Keidar et al. 2005). However, no VAT studies have been previously published on cathode surface shapes other than a flat rod or tube face. In other research areas such as laser ablation, plasma focus and nuclear fusion, concave or conical surface geometries were predicted and demonstrated to significantly affect the production of plasma jets over a wide range of plasma properties, and spatial and temporal scales (Lebedev et al. 2002, Luna et al. 2007, Yeates et al. 2011, Gambino et al. 2013). Some of those plasma conditions are not too dissimilar to that present within vacuum arcs. Experimental measurements by Miernik & Walkowicz (2000) also showed that the profile of the cathode surface can have a significant effect on the spatial distribution of emitted macroparticles from a vacuum arc. Hence, the effect of a conical cathode surface on vacuum arc plasma production

and expansion will be initially explored in this work for its effects and potential benefit towards thrust generation.

Sekerak (2005) measured the ion current density distribution (ICDD) of VAT plumes from titanium cathode rods and found that the spatial distribution of the plasma jet generally follows an Exponential or Gaussian distribution. He also found that thrust was highly influenced by the plume's divergence, the electrode geometry and electrode arrangement. For example, a theoretical analysis of the "standard" VAT electrode design (that is, flush coaxial) found that roughly two-thirds of the ejected ion momentum produced thrust in the desired normal direction. Subsequent performance studies and models have since assumed this behaviour for all cathode materials in this electrode arrangement (Polk et al. 2008). However, this assumption should be re-examined with additional experimental testing on other cathode shapes and materials, which may exhibit different plasma jet characteristics.

1.3.2 Choice of cathode material

Given that any solid conductive material can be used as propellant in a VAT, metals are generally well suited to this task due to their high density, good electrical and thermal conductivities, high melting and boiling points, and relatively low electronic work function. Therefore, nearly all VATs tested so far have used pure metallic elements as fuel (see Table 1.2). The popular use of Titanium is speculated to be largely due to familiarity with prior art, its established use in industrial applications and good performance (see Appendix A).

Although Polk et al. (2008) and Lun et al. (2010) were able to successfully predict VAT performance for a wide range of periodic elements, it remains a challenging task to fully explain why one cathode material performs better over another. Part of the frustration lies in the fact that each material possesses a unique combination of thermophysical and electrical properties. Additionally, these properties are liable to fluctuate and change depending on (1) the state of the cathode surface, (2) the presence of macroparticles and (3) its interaction with the dynamic, self-regulating vacuum arc (Anders 2008). Thus, it

is quite possible that better-performing cathode materials (pure, compounds or alloys) exist that have not yet been measured, properly predicted or merely overlooked.

The assumption that pure metals make the best fuel source also needs to be tested. For example, one class of non-metallic materials which have not been considered for use in VATs despite their extensive study in literature (e.g. Kandah & Meunier (1996), Beilis (1999)) and use in industry (Boxman et al. 1995, Anders 2008), are the carbon or graphite-based group of materials. Noteworthy characteristics of carbon are that it has high temperature resistance, it sublimates instead of melting, and its resistance decreases with increasing temperature (contrary to metals). Indeed, varying micro-structural, electrical, and thermophysical characteristics across several carbon allotropes and grades can be considered sufficient to regard each type of carbon as a unique material with different vacuum arc features. These material properties highlight carbon and other graphite-based materials as potentially interesting candidates as VAT fuels. Indeed, experimental evidence has indicated that carbon may possess significantly higher ion production rates (Anders et al. 2005) and a wide range of erosion rates (Kimblin 1973, Kandah & Meunier 1996) compared to their metallic counterparts. This study aims to explore and characterise some of these new and previously untested materials that may be beneficial to VAT performance.

1.3.3 Choice of arc pulse characteristics

Most VATs operate within a narrow "standard" region of 10–200 A of peak arc current and 50–500 μs pulse lengths (see Table 1.2). This operational choice was heavily influenced by the pioneering work of Gilmour & Lockwood (1972) and LBNL's extensive investigation of vacuum arcs, e.g. see Brown (1994). One well-known feature of VATs is that thrust is linearly proportional to the arc current delivered to the thruster. This is because the ions originate from micro-sized cathode spots, which tend to regulate their number depending on the amount of arc current present. In other words, as the arc current level increases or decreases, so do the number of plasma-emitting spots on the cathode surface. This behaviour enables thrust production to be achieved without loss of efficiency across a wide range of arc current or pulse charge levels (current-time integral).

However, the practical choice of arc pulse characteristics is often largely limited by the capability of the pulsed power circuit. The small size, volume and low average power consumption of the circuit places severe constraints on the designer and this has resulted in some VAT systems for nano-satellite platforms like the CubeSat to presently restrict themselves to very short pulse lengths (≤ 250 μs) and low arc currents (10–40 A) (IEPC 2013, priv. comm.).

There are a number of property changes that occur in a VAT plasma when operating within the realm of short pulses, all of which relate to the violent processes present in the initial and early stages of the vacuum arc pulse. The first change to consider is the average charge state of the ions being ejected by the VAT. Anders (1998) found that the average ion charge state of vacuum arc ions was highest near the beginning of the vacuum arc pulse (10's of μs) and tended to decrease towards a minimum asymptotic limit over time (100's of μs). This has been attributed to the gradual increase of charge exchange collisions (CEX) occurring between the highly charged ion species and the lesser charged species and neutrals as the arc pulse progresses in time (Anders & Yushkov 2007). For a number of metal cathodes, the average ion charge state was found to approach this lower limit after a pulse length of 200–300 μs (Anders 1998).

The second change is in the average ion energy of the plasma. Anders & Yushkov (2002*b*) and Anders et al. (2007*a*) also found that the most likely ion energy followed a similar pattern of behaviour as the average ion charge state – highest near the start of the pulse and decreasing to a lower asymptotic limit. This is also attributed to the increase of charge exchange collisions with neutrals over time. At first glance, it appears that higher ion energies at very short pulses should improve ion momentum and hence thrust. However, the value of the average ion charge state was pointed out by Polk et al. (2008) to have an inversely proportional effect on thrust production, i.e. high ion charge states resulted in lower thrust. Therefore, the changes in both the average ion energy and ion charge states may be such that they roughly cancel out their effects on overall thrust. In summary, operating at very short pulses may offer no or possibly even negative effects on VAT thrust production.

Thirdly, each arc initiation event generates significant amounts of neutrals and macropar-

ticles. By operating at very short pulses, there is greater likelihood of producing additional macroparticles and increasing the erosion rate (Boxman et al. 1995). Studies on sub-microsecond arc pulses have produced some evidence in agreement with this view (see Lun (2009) and list of sources by Boxman et al. (1995, p. 124, 126)). Using an increased number of arc triggering events to deliver the same amount of total impulse could also accelerate degradation of the insulator and interelectrode gap conditions required for stable arcing. This can have a significant effect on VAT performance, especially over the long-term. In conclusion, operating vacuum arc pulses of at least 200 μs length is recommended in VATs to ensure maximised thrust production and avoid increases in macroparticle emission.

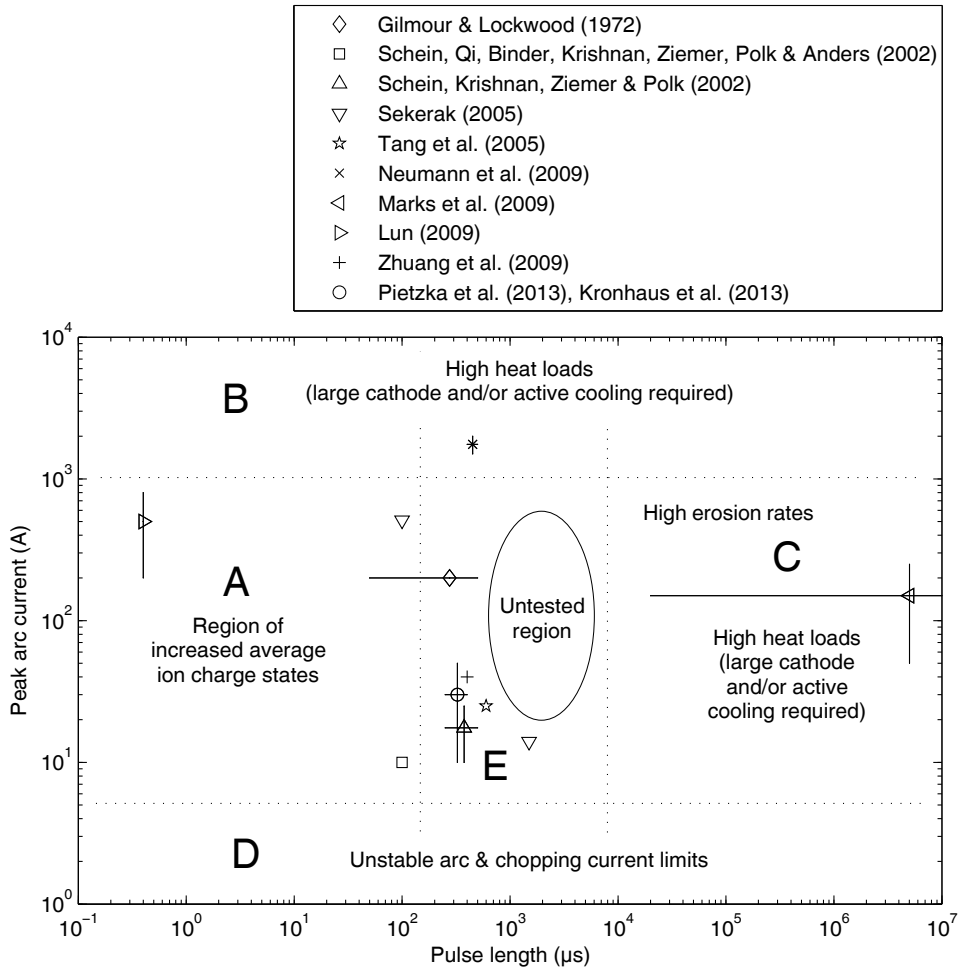

Figure 1.3: Map of arc operating conditions (peak arc current and arc pulse length) for several published VAT designs. Approximate areas identifying extreme (Regions A–D) and desirable (Region E) operating limits are shown. A previously untested region of VAT operation within Region E is highlighted.

Using data from Table 1.2, a map summarising arc pulse conditions previously tested in VATs is presented in Figure 1.3. Several regions highlighting some general restrictions placed on VAT design are identified. These regions are not strict and merely serve as guidelines for the designer.

Region A indicates increased average ion charge states, ion velocity and potentially higher erosion rates for pulse lengths < 200 μs. Region B indicates high heat loads due to large arc current levels (in the kA range). Region C very roughly indicates high heat loads from very long pulse lengths beyond 10 ms (the next section gives further discussion to heat management). Region D is a lower limit for arc currents such that arc stability and existence is possible. Region E is an area of VAT operation that is generally desirable within the requirements of a VAT space propulsion system with good performance. Most VAT designs exist within this area, with at least one extreme design presented in each of the outer regions (A, B and C).

Although numerous gaps are present on the map, Figure 1.3 identifies a specific operating region within Region E where almost no measurement or knowledge of VAT performance and behaviour exists, that of vacuum arcs running at pulse lengths 1–10 ms long and at low to medium arc current levels. Up to now, experimental evidence has shown that the thrust generated by the VAT is linearly proportional to the arc current or pulse charge, provided gross cathode melting does not occur. By extension, an assumption long held has been that the thrust from a VAT operating at a given average arc current should also be linearly proportional to the arc pulse length. While this has been generally shown to hold true for most VATs tested to date, there is very little evidence showing that this also holds true for VATs operating in the millisecond range. The notion that pulse lengths beyond 500 μs do not have an effect on ion properties and ion production rates also needs to be examined. The purpose of this study was to further explore and characterise vacuum arc thruster performance in this previously untested region.

1.3.4 Cathode erosion and the production of macroparticles

Cathode erosion occurs due to the production and ejection of plasma, neutrals and macroparticles. Macroparticles (MP's) can contribute as much as 20–50% of the total mass loss, but produce little momentum in the normal direction despite being relatively large in mass compared to ions. To illustrate this, assume typical VAT operating conditions where equal amounts of cathode material are converted to ions and macroparticles, the average ion velocity is 10 km/s, and the average MP velocity is 500 m/s. By direct comparison, the ratio of MP momentum to ion momentum is only 500/10000 = 5%. In reality, this ratio is much smaller because the majority of MPs are directed at large angles to the normal thrust direction (see next paragraph). In addition, a portion of MPs are intercepted by nearby surfaces, which further reduces their momentum contribution. Thus, it is reasonable to estimate that MPs contribute a negligible 1% or less of the total thrust level in a VAT.

Unfortunately, MP production makes a negative impact on the thruster's specific impulse because fuel that would have been available for ionisation (and thrust) is wasted as (low momentum) liquid droplets instead. The presence of macroparticles can also increase the likelihood of contaminating surrounding satellite components such as solar panels or optics. Daalder (1976) found that most MP's are ejected at peak shallow angles of 10°–30° to the cathode surface. This means that a VAT design can significantly reduce the amount of macroparticles being ejected outward by recessing the cathode within the thruster. However, care should be taken to not significantly reduce thrust by doing so (Polk et al. 2008). Rysanek & Burton (2008) studied both theoretically and experimentally the nature of MP's emitted by a VAT in terms of their charge, velocity and size distributions. They found that macroparticles can be positively charged and the charge state of a macroparticle is roughly proportional to the square of its diameter. They therefore proposed the use of externally applied electric fields as a possible filtering mechanism. However, no VAT design has tested this technique as of yet.

Daalder (1975) found that the arc current level, cathode size and arc pulse length made a significant impact on the erosion rate and MP production of copper vacuum arcs. Shalev et al. (1986) also found that MP production strongly depended on the cathode tempera-

ture. In other words, the hotter the cathode is, the higher the severity of cathode melting and macroparticle production. Thus, the thermal state of the cathode needs to be carefully managed. Active cooling systems such as water cooling are typically seen in industrial pulsed and direct current (DC) vacuum arc setups. However, this option is not attractive for VATs which need to be small in size and consume low levels of power. In practice, VATs typically operate by limiting the pulse's peak arc current and the firing frequency. A rough guideline is to run the VAT at ≤1% duty cycle (Brown 1994, Schein et al. 2002a), where duty cycle δ_c is a function of the time periods that the thruster is on (t_{on}) and off (t_{off}) during overall operation (Anders 2008, p. 244). Duty cycle can also be calculated as the product of pulse length t_p and pulse frequency f, i.e.

$$\delta_c = \frac{t_{on}}{t_{on} + t_{off}} \equiv t_p f \tag{1.1}$$

The choice of cathode material also impacts cathode heating and melting. Generally, cathode materials with a low melting point tend to erode more and therefore produce a larger amount of macroparticles compared to materials with high melting points. Other than practical experience, there does not currently exist any comprehensive study or design theory published on heat management in VATs. Practical limits on erosion rates for various power heating levels, cathode materials and sizes have also not yet been fully determined.

Apart from reducing macroparticle production, uniform cathode erosion is also important for the VAT to ensure consistent and reliable thruster operation. This can be achieved in a number of ways. General practise in vacuum arc research has been the delivery of relatively large arc currents (100's of A) in the 200–500 μs range for small cathodes (3–6 mm diameter) (e.g. Brown (1994)) or > 1 kA for larger cathodes sizes (30–50 mm diameter) (e.g. Neumann et al. (2009)). The high arc current level produces a large number of cathode spots, which tend to repel one another and spread out over the surface. An improvement to good spot surface coverage was further explored by Neumann et al. (2009), who used a centrally-triggered cathode design and a high current "sawtooth" arc current pulse shape to power the arc. This created the effect of a few cathode spots near the centre of the cathode and many spots near the cathode edge to achieve uniform spot spacing and distribution. This resulted in greatly improved erosion uniformity.

Unfortunately, many VAT designs are practically limited to using much lower arc current levels to ensure good heat management and low average power consumption. The resulting low number of cathode spots (sometimes only one spot is present) can create problems for uniform cathode erosion. This was recently experienced by Pietzka et al. (2013), who used pulses of 10–50 A peak arc current and 250–400 μs in length on a copper cathode rod. They found that erosion only occurred on the circumference of the rod where arc triggering took place, whilst the central portion of the rod remained untouched. This meant that the single cathode spot was unable to reach the rod centre before extinguishing. To address the problem of uneven erosion, Pietzka et al. (2013) installed a tubular cathode instead of a rod to ensure uniform cathode erosion at the tube edge. An in-depth study of pulse length effects on cathode erosion in VATs is lacking in present literature.

The degree and location of cathode erosion can also be controlled by steering the cathode spots. Generally increasing the motion of cathode spots over the cathode surface tends to reduce local cathode temperatures because the spots do not reside over a particular area long enough to induce gross melting (Daalder 1975). A common method used in industrial film deposition and vacuum arc interrupter devices is to use magnetic fields to force spot motion or disrupt the arc altogether (Boxman et al. 1995, Anders 2008). This technique has been well studied over the decades and recently applied by Zhuang et al. (2009) in a VAT, who used an axial magnetic field to both focus the plasma jet and cause the cathode spot to rotate along the cathode tube's circumference.

There may exist other techniques to help direct cathode spot motion across the cathode surface. For example, in an industrial film deposition application, Vergason et al. (2001) used several discrete anodes positioned around the cathode. During operation, each anode was electrically switched at a desired frequency, forcing the cathode spots to move along with the presently active anode(s). This caused a significant reduction in both the cathode's surface roughness and deposited macroparticle content on target substrates. No literature has been found on the use of discrete anode switching in a VAT. Further study is required to assess if this technique is feasible, applicable and beneficial to the operation of VATs.

1.3.5 Performance enhancement of VATs

Magnetic “nozzles” and plasma confinement are considered established areas of study in plasma physics and general electric propulsion, with widespread use in Ion thrusters, Hall thrusters and Magnetohydrodynamic thrusters. To date, axial magnetic fields have been successfully demonstrated to enhance the performance of VATs by causing the ejecting plasma jet to collimate and accelerate in the desired thrust direction (Gilmour & Lockwood 1972, Keidar et al. 1996, Keidar et al. 2005). In one thruster design, AASC used a magnetic coil formed as part of the pulse circuit to produce a 50% thrust increase without significantly increasing the overall system mass (Tang et al. 2005). Present engineering issues for magnetically-enhanced VATs has been system integration and implementation within very demanding mission size, volume and mass constraints. Another vital issue is mitigating the increase of VAT operating arc voltage due to the presence of the diverging axial magnetic field. This can occur in a coaxial cathode rod electrode configuration where the orientation of the magnetic field lines can impede electron flow from the cathode to the anode, forcing a rise in arc voltage (and thus arc power) to sustain the vacuum arc (Keidar et al. 1997).

Given the significant amount of research already done in this area, the scope of this work was purposefully limited to exclude comprehensive studies on magnetically-enhanced VATs. Instead, this study recognises and explores alternative means of enhancing VAT performance and operation, some of which have been discussed in previous sections. Adopting a step-by-step strategy, the primary goal of this work is to first show and understand how the proposed new VAT designs can influence VAT performance in their own capacity. Only then, can an extra layer of complexity be added and their combined use with axial magnetic fields explored. For practical limitations on scope, only the first exploration step is considered, with a focus on VAT designs that exclude the use of an externally-applied axial magnetic field.

1.4 Motivation

Whilst key design improvements such as the inductive energy storage circuit and the axial magnetic field have improved the VAT's potential as a propulsion system, there exist a number of alternative thruster designs, operating conditions and aspects that remain unexplored in literature and which may further benefit VAT performance and an understanding of their behaviour. In addition, some of the present assumptions in vacuum arc science and VAT design philosophy need to be re-examined. At present, four clear gaps in the current literature have been identified that suggest potential areas of greater understanding of VAT operation and performance improvement. These are: (a) the use of longer arc pulse lengths beyond the present state-of-the-art, (b) the use of cathode profile shapes other than a flat surface, (c) the study of previously untested cathode materials such as graphite, and (d) techniques such as anode switching to manage cathode erosion.

1.5 Objectives

There are many features of vacuum arc thruster design and operation that need to be studied and expanded upon. This study will investigate the following areas with the overall goal of improving the performance of vacuum arc thrusters:

1. Study the effect of operating parameters such as arc pulse length on VATs;
2. Expand cathode design knowledge through the use of new or untested materials and new electrode shapes; and
3. Better understand cathode erosion and cathode heat management in VATs using the discrete anode switching technique.

1.6 Outline

An outline of this work is as follows: Chapter 2 explains the method and strategy used to perform this study. Chapter 3 provides a detailed description of the test setup, measuring apparatus and techniques developed for this work. Chapter 4 provides a detailed description of thruster prototype development, behaviour and performance. Chapters 5–8 presents the test method and results of each of the areas of study, that is, the effects of arc pulse length (Chapter 5), cathode shape (Chapter 6), the novel use of carbon-based cathodes as fuel (Chapter 7), and the use of the discrete anode switching technique (Chapter 8). A synthesis and overall summary of results is presented in Chapter 9. Finally, conclusions and recommendations are given in Chapter 10. Appendices containing empirical VAT performance data, mathematical derivations, geometric solutions and additional experimental results are also included.

Chapter 2

Method

2.1 Experimental versus theoretical approach

2.1.1 The experimental approach

Historically, research on VAT performance has been largely experimental. The greatest advantage with this approach are that VAT prototypes can be feasibly developed and operate in a manner where all relevant environmental and internal influences are present. In other words, experimentation can provide stronger evidence on the effect of new thruster designs and changes to operations. Also, the design changes and new techniques proposed in this study are easier to implement and test through well-understood and established experimental techniques, rather than developing complex and untested theoretical models for each design change.

It is generally difficult to experimentally measure plasma properties of the vacuum arc close to the cathode region due to the intense conditions and small spatial and temporal scales present. Another significant problem is the physical presence of plasma probes, which can affect the plasma itself. Thus, the probe must be (a) small in size and able to function for a brief period of time before being damaged, or (b) positioned far from the

plasma source such that it has a small influence on overall plasma behaviour.

Another concern with experimentation is to ensure consistent and accurate test conditions. Undesirable changes can and do occur to the thruster during tests, such as wear and tear, uncontrolled cathode spot motion, changes in the cathode's surface properties and features, and variation in the interelectrode surface and regional gap properties (topology, composition and electrical conductivity). Thus, great care should be taken to ensure identical initial thruster conditions prior to testing, minimising disturbance on measurements, and applying appropriate statistical analysis on test data. Experimentation also requires significant investment in the development of thruster diagnostics equipment and high-vacuum test facilities, much of which did not exist in sufficient capacity at Wits University (or the country for that matter) prior to this work.

2.1.2 The theoretical approach

A review of current literature indicates that vacuum arc thruster models are still in the early stages of development. To date, there are a number of useful theoretical approaches available for predicting VAT performance over a limited range of VAT design and operating conditions. These include analytical (Beilis 2008), empirical (Polk et al. 2008), hybrid (Lun et al. 2010), and numerical (Keidar et al. 2005) methods. Many of these models require empirical data to function correctly and may be performed singly or in conjunction with other models to describe the entire cathode surface-to-plasma jet region. For example, Keidar et al. (2005) numerically modelled a magnetically-enhanced plasma jet ejected from a VAT, but relied on an analytical cathode spot model and some empirical data to generate boundary conditions for the plasma simulation. Despite giving reasonably good estimates of general VAT performance and behaviour, VAT models remain unverified for a large range of thruster designs, cathode materials and thruster operating conditions.

Ideally, the advantage of a theoretical modelling approach is in its potential to predict and discover new and optimum thruster designs and operating regimes according to specified design parameter inputs. Theoretical modelling can also predict VAT perfor-

mance and behaviour for test conditions or designs that are difficult to replicate in the laboratory. However, considerable theoretical development is still required to make this a practical reality. This is because the vacuum arc itself is a highly complex phenomenon.

In an effort to better model vacuum arc processes, increasingly descriptive and complex models are being pursued. Most recently, Beilis (2014) began work towards developing a time-dependant and mathematically closed model of the cathode spot applicable to the VAT. However, considerations must still be made for dynamic initial conditions, the presence of macroparticles and cathode surface topology. To address this, it is foreseeable that future vacuum arc models will be predominantly numerical in nature. Multi-physics simulation models may hold the potential to incorporate the entire spectrum of physical interactions, and include the multi-phase, spatial and temporal processes on the micro and macroscopic scale. Recent models by Timko (2011) and others are a step in this direction.

One popular method used in many plasma thruster simulations has been particle-in-cell (PIC) numerical models. These models break the plasma domain down into small discrete cells and apply the relevant particle force interactions and continuity equations to each cell (much like the well-established iterative discrete models of Finite Element Analysis and Computational Fluid Dynamics). PIC models often have several constraints or assumptions about the plasma in question. For instance, a Maxwellian distribution of electrons is often used, models are practically limited (in memory size and computing time) to medium-level plasma densities ($\sim 10^{16}$–10^{18} m^{-3}) or a small physical test region.

Unfortunately, these simplifications are generally unsatisfactory in VAT-related problems. This is because electron behaviour in the near cathode spot region is not stable and highly dynamic (non-Maxwellian). There also exists a transition from non-thermal to thermal equilibrium plasma conditions within the local near-cathode region, which introduces added difficulty in modelling broad plasma behaviour. The high range of plasma densities across the cathode spot domain and very small time scales (ns) in which vacuum arc processes function also force adequate PIC models to incorporate very small time steps and cell sizes. The PIC model must be able to model plasma conditions in the near-cathode spot region at the micron level right up to the centimetre-sized scale of the

plasma jet, including interactions with adjacent spots, nearby surfaces and the plasma itself. A significant issue is the constantly varying initial conditions and feedback mechanisms of the plasma and cathode spot region(s), which introduce large uncertainties in many types of modelling. Ultimately, proper consideration of the spatial and temporal dynamics of the vacuum arc thruster will require considerably larger computational resources and software development compared to many other more traditional plasma thruster models.

Finally, the validation and verification of theoretical models is limited by the range of available empirical data. This limits what can be done in these models, where the full range of vacuum arc behaviour and physical processes is not yet sufficiently understood to produce high confidence in model results.

2.1.3 Findings and conclusion

Very few breakthroughs in thruster design were expected to be accomplished from a purely theoretical approach at this stage of thruster development. It was also seen to be too ambitious to develop sufficient advances in modelling plasmas arc discharges within a single project without prior experience in plasma simulation. Coupled with a 3–4 year time frame to accomplish the scope of work, computational simulation was not recommended. In terms of the study objectives, experimentation offered a more attractive path over the theoretical approach because new thruster designs, materials and operating conditions could be more easily implemented, and their effects more strongly validated using test data taken in a real world environment. At the same time, experimental data is more useful to the micropropulsion community, generating results that can be used to further evaluate existing theoretical VAT models and provide interesting and useful test cases for improving those models. Therefore, an experimental approach to this study was primarily adopted.

2.2 Use of a baseline thruster design

In order to generate repeatable and comparable experimental results, the development of a baseline or reference thruster prototype was considered a crucial element in this study. The baseline thruster design has a number of features:

1. The design, operation, behaviour and performance of the baseline thruster should be broadly typical to that of other VATs within literature. This ensures that the initial (and subsequent) prototypes are functioning correctly and that comparisons of this work's results with previously published data on both VATs and relevant vacuum arc research can be more easily made. The measured performance of the baseline thruster can also be used to validate and verify thruster diagnostic equipment.

2. The baseline thruster contains flexible and modular features that can accommodate different electrode designs, mounting configurations and add-ons.

3. The performance of the baseline thruster provides a foundational result for comparing the effects of any design or operational modifications that are being studied. The strength of this approach is that any biases and external factors (uncontrolled or inherent) that are present in test studies can be generally compensated for by also measuring the baseline thruster under the same conditions.

The focus of this study was to examine the design and performance aspects of VATs within the size & mass (≤500 g total system mass), supply voltages (≤ 100 V) and power limits (1–20 W) typically desired of a microthruster system for small satellites (as mentioned in Chapter 1). Therefore, the operation of all VAT prototypes tested in this project was limited to relatively low arc currents (up to 100 A peak; most tests at 50 A peak) and low power levels (typically within 1–30 W average power). These limits were largely governed by practical issues such as thermal load management of the small-sized VATs and the performance capabilities of the present pulse circuit.

The baseline thruster was designed with the ability to easily use different cathode materials of varying thermophysical and electric properties. Each material delivers different levels of performance and affects thruster operation in its own way, which aids thruster performance characterisation over a wide operating space. However, only a single cathode diameter was studied based on commercial availability and cost of materials, and to limit the test matrix to a more manageable size.

2.3 Measurement strategy

2.3.1 Performance metrics

To assess a VAT design or any thruster for that matter, a set of quantifiable performance metrics needs to be defined. These criteria are usually formulated from a combination of different thruster input and output variables. Over the years, a few key thruster performance and qualification metrics have gained acceptance within the general propulsion and specialised micro-propulsion literature. They include *specific impulse*, *thrust-to-power ratio*, *power efficiency*, *total impulse*, *impulse bit*, *nominal thrust* and *nominal power usage*. Parameters such as thrust, thrust-to-power, impulse per joule, efficiency and specific impulse are the de facto method of characterising general performance by space thruster designers. These parameters also give system engineers and mission planners a useful indication of propulsion system performance in relation to the overall satellite system. More specialised parameters such as ion erosion rate and ion mass fraction are more commonly used in vacuum arc science to describe ion production rates. These parameters are useful in the context of VATs because they allow test runs to be compared in generic terms for their ability to produce ions (and hence thrust) for a given amount of input energy or fuel mass. By using widely accepted methods of characterising vacuum arcs, VATs and microthrusters in general, this study provides data that is more compatible and accessible to the overall research effort on vacuum arcs, VATs and the micro-propulsion systems.

According to Polk et al. (2008), a number of thruster performance metrics specifically

tailored to VATs can be formulated as follows:

Thrust (in the normal direction) is defined as

$$T = C_T \dot{m}_i \bar{v}_i = C_T \left(m_i \frac{I_i}{e\bar{Z}} \right) \bar{v}_i \tag{2.1}$$

where m_i is the ion mass, I_i is the ion current, e is electron charge, $\bar{Z}$ is the average ion charge state, $\bar{v}_i$ is the average ion velocity, and C_T is a correction factor to account for a reduction in normal thrust due to plume divergence as well as the presence of the anode electrode intercepting part of the plume jet. A detailed description and derivation of C_T can be found in Appendix B. The value of C_T was generally found to be 0.64 for a coaxial flush electrode configuration (Polk et al. 2008). This means that only 64% of the total ion momentum provides thrust in the normal direction of the cathode surface.

Note that the term in brackets is the ion mass flow rate $\dot{m}_i$. The ion current can also be conveniently described as a ratio of the arc current, i.e. $I_i = \epsilon I$. The parameter ϵ is known as the ion-to-arc current ratio. This value is typically between 7–10% of the arc current and is generally found to be constant over a wide range of arc conditions and current levels.

The impulse bit is defined as

$$I_{bit} = \int_0^{t_p} T\,dt \approx T\,t_p \tag{2.2}$$

where t_p is the pulse duration or length.

Specific impulse is a measure of how much force a thruster produces using a given amount of fuel and is defined as

$$I_{sp} = \frac{T}{I E_r g} \tag{2.3}$$

where I is the arc discharge current and g is gravitational acceleration. The total erosion rate E_r is defined here (and commonly in vacuum arc science) as the fraction of net mass

eroded Δm per total sum of arc pulse charges fired by the thruster $\sum Q$ and is normally depicted in units of μg/C

$$E_r = \frac{\Delta m}{\sum Q} \tag{2.4}$$

Each pulse charge is the product of average arc current I over pulse length t_p

$$Q = I t_p \tag{2.5}$$

The total sum of arc pulse charges can be calculated by counting the total number of pulses such that

$$\sum Q = QN \equiv Q(f\Delta t) \equiv I t_p f \Delta t \tag{2.6}$$

where N is the total number of pulses fired, Δt is the total operating time of the thruster, f is the pulse frequency and the term $t_p f$ defines the duty cycle of the thruster (e.g., a 10% duty cycle means that the thruster fires for an equivalent time of 0.1 s for every second of operation).

The arc power is the product of arc current I and arc voltage V

$$P = IV \tag{2.7}$$

Accordingly, average input power is

$$\bar{P} = P(t_p f) \tag{2.8}$$

The pulse energy is the product of arc power P and pulse length t_p

$$E_j = P t_p \tag{2.9}$$

Finally, the thruster efficiency is the ratio of thrust power to input power

$$\eta = \frac{T^2}{2PIE_r} \tag{2.10}$$

Other metrics

In addition, many authors such as Anders & Yushkov (2002*b*), Anders et al. (2005), Polk et al. (2008), Beilis (2008), Lun et al. (2010) and Neumann et al. (2012) introduced or adopted a variety of other VAT-specific lower-level performance metrics to more easily compare results across different cathode materials. These include:

1. Ejected mass of ions per input charge (also known as *ion erosion rate* or $\dot{m}_i$)
2. Ion mass fraction (ratio of ion-to-total erosion rate)
3. Thrust per arc current, T/I
4. Thrust-to-power ratio, T/P
5. Impulse (or momentum) per ion particle, $m_i \bar{v}_i$
6. Impulse per ejected mass of ions
7. Impulse per eroded volume of cathode material
8. Impulse per joule of input energy (numerically equivalent to thrust-to-power ratio)

Only items 1, 3, 4 and 8 will be implemented here and used to provide particular insights into general cathode material performance. The ratio T/I is particularly useful as a metric because it allows thrust production to be conveniently compared across a wide range of arc current (and hence power) levels, thruster designs and operating conditions. It also acknowledges the physically-observed linear relationship between arc current and thrust. Item 2 can be useful since it provides an indication of how effectively the thruster converts fuel into thrust-producing particles versus wasted material. However, only rough estimates of the ion-to-erosion rate ratio can be made because finding the ion

mass flow rate requires knowledge of the average ion charge state, which could not be directly measured in this study (measuring ion charge was initially considered at the start of the study, but it was eventually decided that other parameters were of greater practical benefit, given the limited time available and difficulty in performing such a task). Fortunately, specific impulse (which can be calculated) gives a more holistic and meaningful indication of thrusting efficiency.

Note on the calculation of specific impulse

Some comments should be made on the calculation of specific impulse. It has been noted in literature that some researchers in the micropropulsion community report the value of specific impulse merely as a function of the average ion velocity, i.e. $I_{sp} = v_i/g$. This definition of I_{sp} is misleading because it ignores (1) the divergence of the plume, (2) the effect of thruster geometry on the ion flux and (3) the emission of neutral particles which do not contribute to thrust, but contribute to the fuel mass consumed. For VATs in particular, this error can be significant due to the large amount of macroparticles ejected from the cathode. The result is that I_{sp} values for VATs are sometimes erroneously reported to be within the range of 1000–3000s, when in fact *true* I_{sp} values lie within 300–600 s. Therefore, this work adopts the definition of specific impulse made by Polk et al. (2008) (as seen in Equation 2.3), which correctly accounts for all the above-mentioned issues.

2.3.2 Scope of Measurement

Outline

In order to construct the performance metrics listed above, a number of variables were measured, namely *thrust* (T), *cathode mass loss* (Δm), *arc pulse length* (t_p), *arc current* ($I(t)$), *arc voltage* ($V(t)$) and *pulse frequency* (f). In addition, microscopic imaging and other thruster parameters such as the *ion current density distribution* (for characteris-

ing the plasma jet's shape) and *ion current* were also measured to complement thruster studies. Due to resource and time constraints, detailed and adequate measurements of ion energies, ion charge states and MP production could not be assessed in this study. These measurements should be made in future work to add to the body of knowledge introduced by this study. Some additional comments on specific parameter measurements are made below.

Thrust measurement

It was decided early on in the project that direct measurement of thrust would provide far more accurate and reliable results than relying on measurements of its four dependant variables (C_T, I_i, Z, v_i) to calculate thrust indirectly. Thus, only direct thrust measurement methods were considered for this study. Measuring the progression of thrust over time was also seen as an important element of VAT diagnosis and performance analysis.

Ion current density distribution measurement

Previous vacuum arc studies measured the peak ion currents signals captured by an ion probe to determine the ion current density distribution (ICDD). However, there are some weaknesses with this approach. For example, the physical properties of the ion detection probe and its circuitry can produce distortions of the captured ion signal due to stray capacitance and transmission effects due to the presence of grids in the probe. This can introduce errors such that the ion current cannot be easily or correctly compared to the arc current. One possible option to mitigate these errors is to instead consider the charge of the collected ion signal. In this way, the problem of current signal distortions is avoided.

To implement this approach, this work introduces a new dimensionless ion diagnostics parameter called the *ion-to-arc charge ratio*, which is a ratio of the ion-to-arc current pulse charge collected by an ion probe at a set distance from the thruster. One important feature of this ratio is its constancy regardless of whether charge Q, current I or current

density J is being compared. This allows the results of this work to still be easily compared to literature, which generally reports in terms of current or current density values. In other words,

$$\bar{J} = \frac{Q_{ip}}{Q} \equiv \frac{I_{ip}}{I} \equiv \frac{J_{ip}}{J} \tag{2.11}$$

where subscript ip refer to the ion current signal captured by the ion probe. The ion-to-arc charge ratio $\bar{J}$ is useful because any variation in arc current between individual data samples within a test run is compensated for, greatly improving the accuracy of test results. Another advantage of $\bar{J}$ is that it allows ion production to be easily compared across arc current levels, cathode materials and thruster designs for a given ion probe and capture setup. However, individual information about ion charge states and ion current cannot be made by measuring $\bar{J}$ alone since both quantities affect the charge being collected. Additional diagnostics tools will be required to measure these specific plasma properties. It should also be noted that comparing different datasets of $\bar{J}$ is only valid provided the ICDD setup is identical (e.g. probe drift length, cathode material) for the test cases involved.

2.3.3 General approach to data handling and presentation

Given the fluctuating and noisy behaviour of the vacuum arc, appropriate treatment of the data is required to make fair representation and observation of thruster behaviour and performance. This usually entails statistically sound strategies such as capturing an acceptable number of test samples, quantifying the data and its distribution using variables such as *mean*, *median* and *standard deviation*, and appropriate calculation of data confidence bounds or uncertainties (Student's t-distribution, Order Statistics, Monte Carlo simulation).

Uncertainties

Unless otherwise stated, all uncertainties in this work for presented test data and results are set to within 95% confidence bounds. Propagation of uncertainties from processed

results towards higher-level parameters and metrics was generally dealt with by using the variance formula below:

$$\delta D = \sqrt{\left(\frac{\partial D}{\partial X_1}\right)^2 \delta X_1^2 + \left(\frac{\partial D}{\partial X_2}\right)^2 \delta X_2^2 + \ldots} \tag{2.12}$$

where $D = f(X_1, X_2, \ldots)$, and δD, δX_1, δX_2, etc. are the uncertainties of their respective measured variables.

Outliers

Outlier detection was only applied to select cases. For example, ICDD measurements required data gathering from individual thruster firing shots, a few of which might significantly fluctuate depending on the noisy behaviour of the vacuum arc pulse. In contrast, thrust measurements did not undergo outlier analysis because the test rig would sample a grouped set of thrust firings and measure an averaged thrust result, which inherently smoothed out thrust outliers. Outlier detection and elimination was performed with Peirce's Criterion (Peirce 1852), a more rigorous tool than Chauvenet's Criterion in detecting and eliminating multiple outliers (Ross 2003).

Data consolidation and fitting

Summaries of data to produce representative values such as arc current, arc voltage or average thrust was accomplished by using weighted averages based on the test duration or total delivered arc charge of each sample over the entire relevant dataset. Uncertainties of weighted-average values were determined by applying Student's t-distribution method across the dataset.

The linear least squares method was used to fit data to general trends and for fitting calibration data in measurement systems such as the thrust measurement stand. Non-linear least square fits for complex curve and surface fits (e.g. ICDD data) were accomplished with numerical implementation of the Levenberg-Marquardt algorithm.

Chapter 3

Experimental apparatus & test setup

3.1 Introduction

This chapter provides descriptions of the development and performance of test facilities (Section 3.2), thruster pulsed power circuits (Section 3.3) and thruster diagnostic tools and equipment used in this work. Each section provides some background on the tool, its function, design specifications and an assessment of its performance and ability to accomplish this work's study objectives. Major test equipment included the direct thrust measurement stand (Section 3.4), Faraday Cup probe (Section 3.5), two-axis rotation system (Section 3.6), ion collector (Section 3.7) and erosion rate measurement technique (Section 3.8).

All commissioning and experimental testing was performed at the newly-built Wits Space Propulsion Research laboratory at the School of Physics. The construction and considerable upgrading of the laboratory and high-vacuum systems was accomplished under collaboration with the staff at the School of Physics. Manufacturing of all thruster diagnostics systems was performed by the workshop of the School of Mechanical, Industrial and Aeronautical Engineering.

3.2 Vacuum chamber and high-vacuum pump system

All experimentation was performed in a stainless steel ring vacuum chamber with internal dimensions 760 mm diameter × 200 mm height and sealed with a semi-hemispherical lid. A mechanical hoist allowed for safe manipulation and access through the vacuum lid. Anti-vibration pads and feet on the vacuum chamber and frame provided mechanical isolation of the entire structure. VACOM multi-pin and high-voltage (HV) electrical feedthroughs were fitted onto chamber ports to allow power and data signal transfer. The pump system was comprised of a water-cooled oil diffusion pump (Leybold-Heraeus) and a roughing pump (Alcatel 2012A). Contact between the chamber frame and the roughing pump was minimized to avoid transfer of pump vibrations to the vacuum chamber. Pressure readings were taken by a low-vacuum Edwards PK-10 Pirani gauge (atm–10^{-3} mbar abs.) and a high-vacuum Leybold-Haraeus PM41 Penning Gauge (10^{-2}–10^{-9} Torr). Although the vacuum chamber system was capable of achieving a baseline pressure of 10^{-6} Torr, all testing in this work was performed between 1–5 $\times 10^{-5}$ Torr in order to reduce turn-around times between tests.

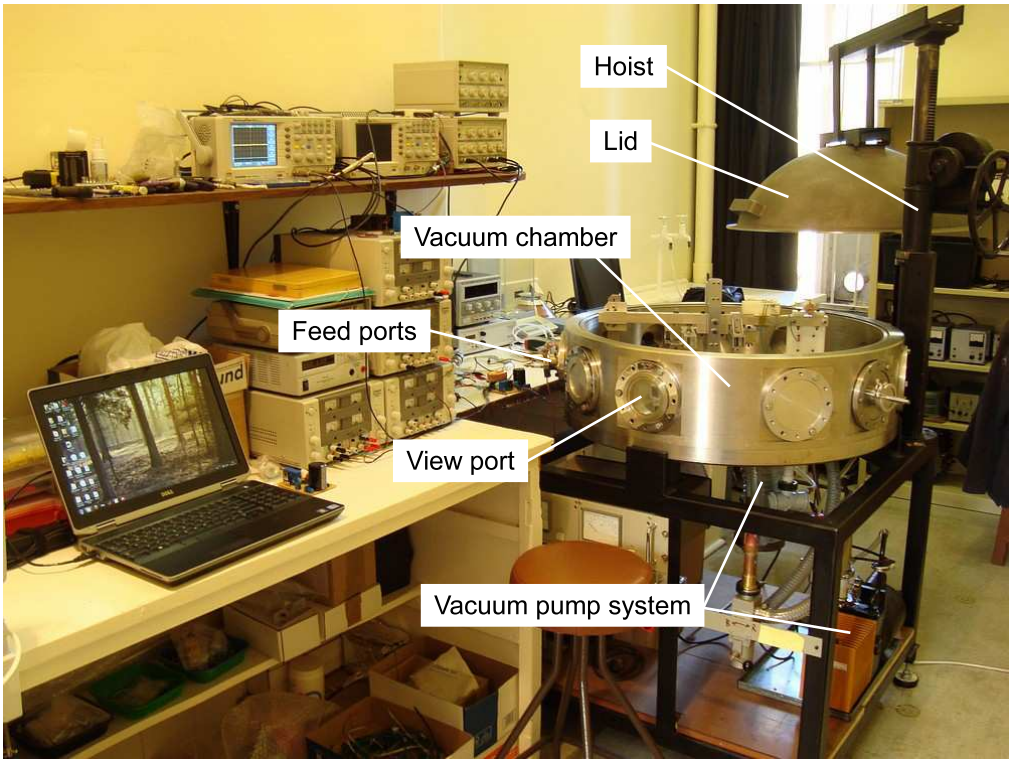

Figure 3.1: Test ring vacuum chamber and high-vacuum pump system at the Wits Space Propulsion Research laboratory, School of Physics.

Using kinetic theory, the mean free path of the air molecules in the chamber can be estimated with

$$L_{mfp} = \frac{k_B T_r}{\sqrt{2}\pi d^2 p} \tag{3.1}$$

where $k_B \approx 1.3806 \times 10^{-23}$ J/K is the Boltzmann constant, T_r is the temperature, d is the diameter of the gas particles and p is the pressure. Assuming room temperature (300 K), $d \approx 3 \times 10^{-10}$ m for the air molecule size and $p = 0.005$ Pa $\approx 5 \times 10^{-5}$ Torr, the mean free path of air is roughly 2 m in length. Therefore, the vacuum levels at which tests were performed was deemed acceptable because the mean free path of the air molecules was much larger than the chamber dimensions at that pressure.

3.3 Pulsed power circuit

3.3.1 Description of circuit development and performance

Vacuum arc pulses were created in thruster prototypes by means of an inductive energy storage circuit design based on Schein et al. (2002a). A schematic of the pulse circuit is shown in Figure 3.2. A stack of standard laboratory power sources supplied an adjustable DC voltage **V1** of 20–180 V to the circuit. The pulse circuit operates by storing energy in an inductor **L1** and releasing that energy into the thruster at a desired firing rate. Using a fast-acting Insulated-Gate Bipolar Transistor (IGBT) switch, the charging time of the circuit could be controlled. At the desired arc current level, the switch opens, causing a high-voltage potential (up to 1200 V) to form across the VAT in response to the fast change in current flow across the inductor ($V = L.dI/dt$). The HV pulse initiates the vacuum arc, causing arc current to flow out of the circuit and drive the VAT. During the arc, the arc voltage regulates itself such that a conductive path for the current is maintained. The arc current decays over time and extinguishes once it reaches a level too low for the arc to sustain itself (also known as the chopping current level). The switch closes again and the inductor charges up for the next pulse firing.

The pulse switching frequency and duration of the IGBT was controlled by a gate driver,

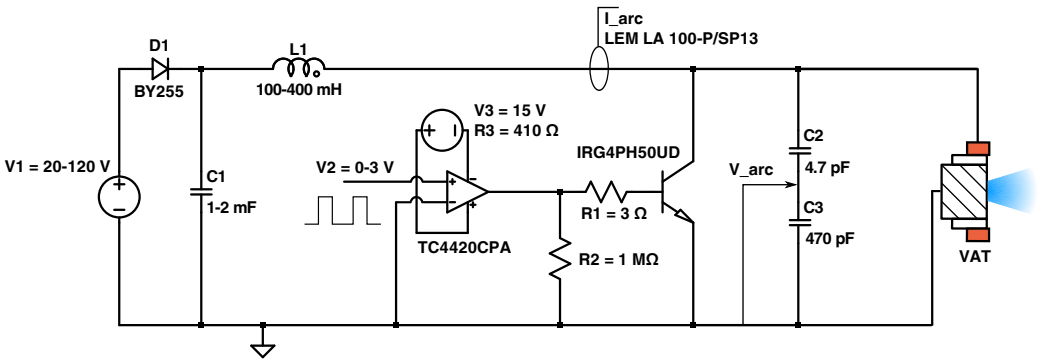

Figure 3.2: Schematic of VAT baseline inductive pulse circuit with typical component specifications.

which received pulse signals from a pulse generator. VAT firing pulse trains of a few seconds to several minutes were controlled by a Labview DAQ card computer interface system. As illustrated in Figure 3.3, similarly triangular-shaped arc charging and discharge profile were usually produced, which indicated relatively efficient energy transfer from the circuit to the thruster. The height and length of the pulse profile could be adjusted by a careful balance between the supply voltage, inductor size (one to several hundred mH) and switching time of the IGBT. This provided some flexibility in the choice of peak arc current and pulse length. The ~40 W arc power limit of the pulse circuit was dictated by the IGBT specification and inductor wire's heat dissipation limit. However, it was found that thruster parts made of UHMWPE material situated near the thruster head experienced structural warping when exposed to arc power loads greater than 30 W. Consequently, the VATs used in this work were typically fired at a maximum of 10–50 Hz for short pulses and 1–10 Hz for long pulses in order to not exceed an average arc power of 30 W. Table 3.1 summarises the performance capabilities of the VAT pulse circuit.

Table 3.1: Range of VAT pulse circuit performance parameters

Parameter	Min	Max
Supply voltage (V)	20	180
Arc voltage (V)	10	120
Peak arc current (A)	5	100
Avg. arc current (A)	10	50
Pulse length (μs)	50	5000
Pulse frequency (Hz)	1	50
Avg. arc power (W)	0.01	30

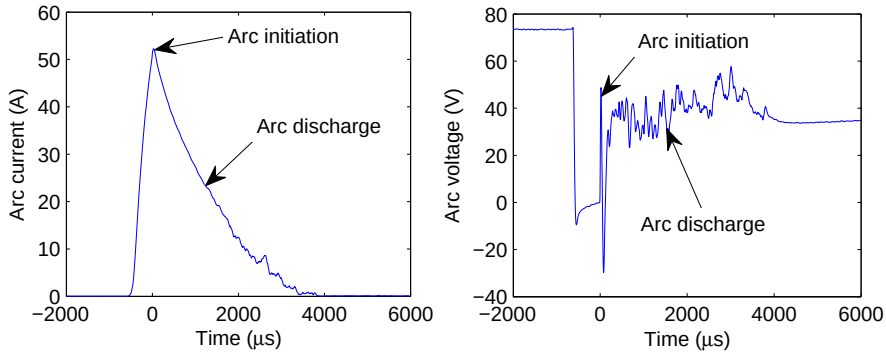

Figure 3.3: Typical arc current and arc voltage pulse waveforms measured at the pulse circuit output (shown here filtered and averaged over 20 samples). In this example, an iron cathode was used. Pulse charging occurs at time $t < 0$ μs; arc initiation occurs at $t = 0$ μs and the arc discharge occurs at $t > 0$ μs.

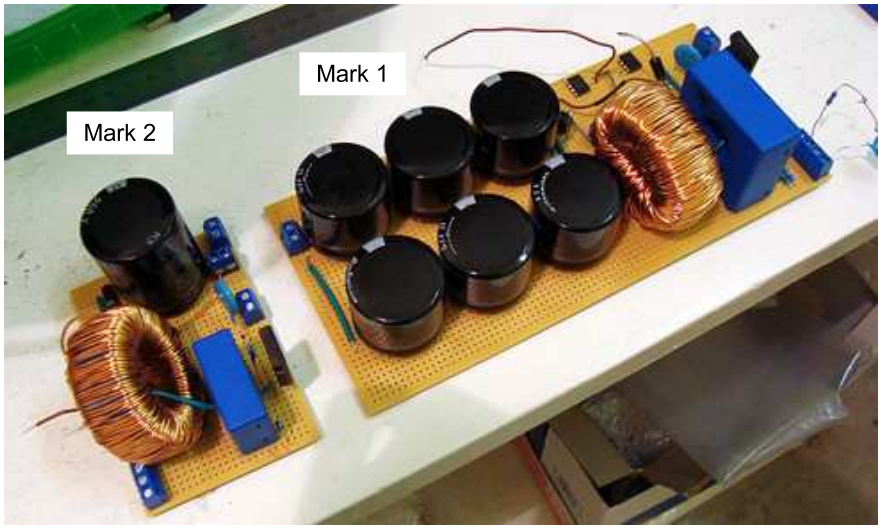

Figure 3.4: Photograph of Mark I and II VAT inductive energy storage pulsed power circuits.

Two versions of the VAT pulsed power circuit were built and used throughout this study as shown by Figure 3.4. The first design (Mark I), with a mass of roughly 400 g, was conservatively sized and can operate at supply voltages of up to 350 V. The second design (Mark II) was a revision over the Mark I, both in terms of size (one-third the volume of Mark I) and mass (~ 200 g), but has a lower supply voltage limit (200 V). Both circuits had the same peak arc current capacity since they both used the same model of IGBT switch.

Large ferrite cores were used in the construction of the inductors. Further investigation later in the project showed that a more efficient HI-FLUX powder core could be used instead to greatly reduce the inductor's size and weight. The improved inductor core also reduced the inductance required by the circuit and the circuit resistance (lowering the in-

put supply voltage levels needed and thus improving circuit power efficiency). However, it was difficult to reproduce arc pulses of the desired triangular shape and long pulse durations with the more efficient inductor cores. Thus, for the scope of this study, the less efficient ferrite cores were chosen for their ability to produce desirable arc pulse characteristics. Further detailed analysis and design improvements to the pulse circuit are required to address these performance issues and trade-offs within the VAT pulse circuit design.

3.3.2 Arc pulse waveforms

Data capture

Circuit diagnostics included a 100:1 capacitive voltage divider for monitoring voltage across the IGBT as well as a LEM hall current transducer ($\geq \pm 160$ A, DC–200 kHz bandwidth) for monitoring current through the inductor. The installation locations of these sensors are shown in Figure 3.2. Converted sensor voltage signals were subsequently sent to two high-speed digital oscilloscopes (ISO-TECH IDS 8064, 60 MHz 1Gs/s) for real-time monitoring and test data capture of repetitively-fired arc pulses.

Due to the noisy nature of the vacuum arc, two filtering stages were applied to the sets of arc current, arc voltage and ion current data:

1. An analogue first-order low pass RC filter with a cut-off frequency of roughly 0.5 MHz was installed at the arc current transducer's signal output.
2. A digital second-order Butterworth low-pass filter with a cut-off frequency of 6.25–62.50 kHz (depending on the sampling rate) was further applied to each current, voltage and ion waveform sample to further smooth noisy arc data and reject electromagnetic interference (EMI) noise bursts present at the start and end of each arc pulse.

An automated data collection and archiving program (process flow chart in Figure 3.5)

was developed in LABVIEW to capture and organise data from the oscilloscopes. The sampling rate of waveform data was adjusted from a few hundred milliseconds to several seconds between samples, depending on test conditions. Although sample sizes of 15–30 waveforms were typically used for most test runs, up to 100–300 waveform samples were captured and stored for some erosion rate tests. Used in conjunction with an additional control program, features such as timed remote firing of the thruster, automated data file organization and saving of input test parameters could be accomplished. Command signals were sent from the user's PC to a National Instruments data acquisition module (NI USB-6009), which delivered a voltage trigger signal to the pulse generator to charge and fire the VAT as desired. Presently, the VAT test and control system requires manual setting of the pulse firing frequency on the pulse generator.

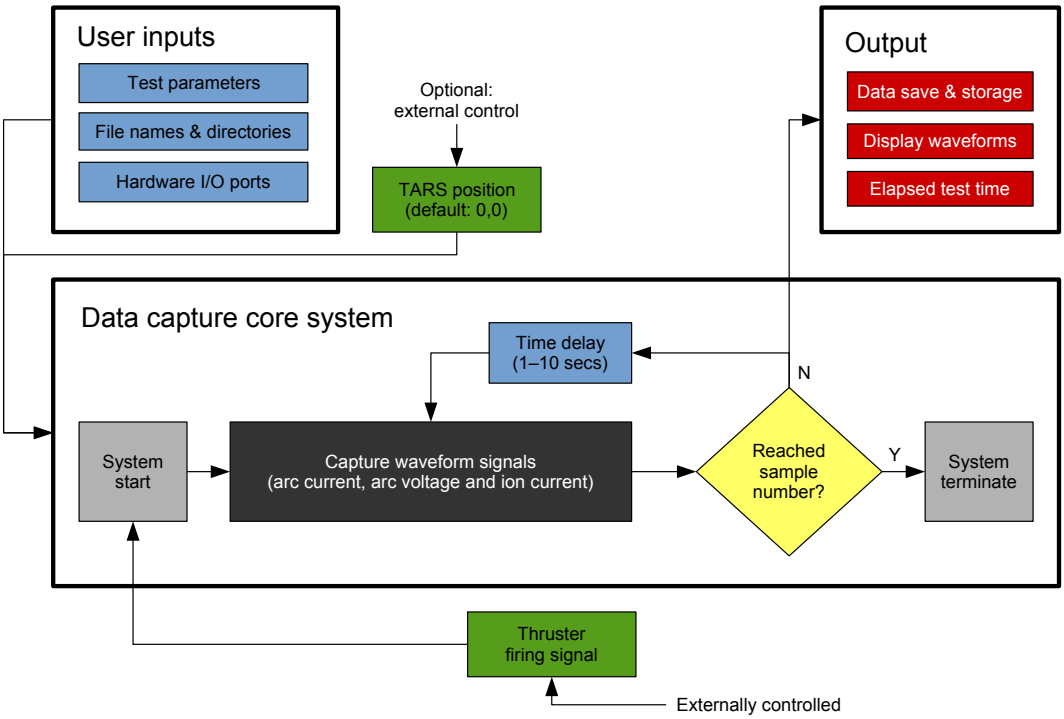

Figure 3.5: Process flow chart of automated LABVIEW data capture control system

Data processing, reduction and analysis

Once the captured raw data was filtered, further waveform processing was performed in MATLAB to convert data into a usable format and extract key parameters for each pulse

waveform sample:

1. Peak arc (discharge) current (I peak), i.e. the maximum arc current at the beginning of the arc pulse.

2. Arc pulse length (t_p), i.e. the time duration of the arc pulse from initiation to termination. Arc termination is assumed to occur when the arc current decays down to 1% of its initial peak value.

3. Average (or mean) arc (discharge) current (I), i.e. the arc current value averaged over the arc duration (arc pulse length).

4. Mean arc discharge voltage (V), i.e. the arc voltage value averaged over the arc pulse length.

5. Ion-to-arc charge ratio ($\bar{J}$), i.e. the ratio of the collected ion and arc current over the arc pulse length, i.e. ratio of current-time integrals.

Examples of a typical set of arc current, arc voltage and ion current sampled traces are shown in Figures 3.6 and 3.7 respectively. Current and voltage traces showed considerable fluctuations due to the present limitations of the pulse circuit and arc triggering method to produce and control vacuum arc pulses (explained in further detail below). To address this, statistical treatment of arc waveform data was used to extract meaningful arc properties and quantify the effect of fluctuations on data accuracy.

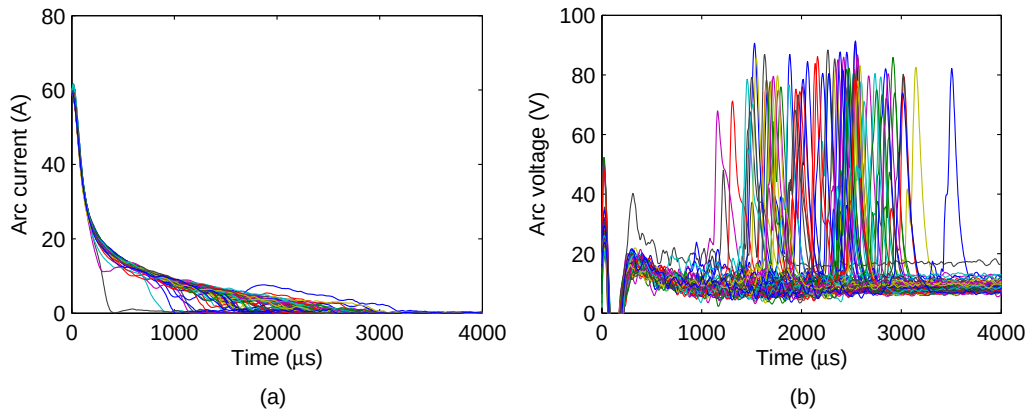

Figure 3.6: Typical waveform traces of captured (a) arc current and (b) arc voltage (peaks beyond 1 ms indicate arc termination). In this example, a Bi cathode was used (50 A peak arc current, 2138 μs median pulse length, 75 sampled traces).

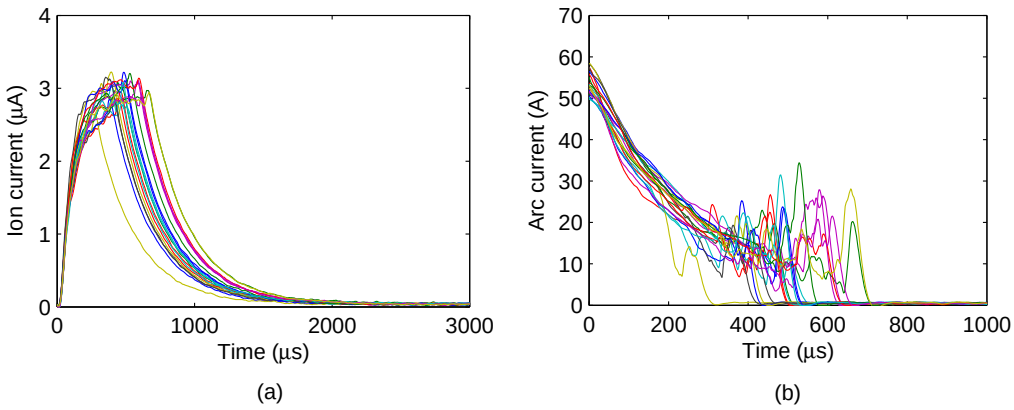

Figure 3.7: Typical waveform traces of captured (a) ion current and corresponding (b) arc current. In this example, a Fe cathode was used (50 A peak arc current, 529 μs median pulse length, 20 sampled traces).

Statistical analysis of arc waveform sampled traces within a typical test run or test set (such as in Figures 3.6 or 3.7) revealed that most parameters could be loosely considered to fit a Normal distribution, that is, a random spread of data (see dataset examples taken at long and short pulses in Figures 3.8–3.11 respectively). However, many of the plots do not show a good fit at their extreme values. A particular note is made of the arc pulse length tested at short pulses (Figure 3.9), which appeared to fit a Normal distribution rather poorly. Further investigation revealed that the arc pulse length distribution could be better fit to a Log-Normal distribution instead (seen under a Box-Cox transformation of pulse length data as shown in the example of Figure 3.10). A comparison of transformed pulse length data to a Normal distribution (mean $\mu = 5.5$, standard deviation $\sigma = 0.8$ in this example) using the Mann-Whitney-U test verified that the Log-normal distribution gave a reasonable fit at $P_r \approx 0.78$–0.99.

There are at least two reasons for the non-Normal behaviour of the arc pulse length as well as other arc parameters such as the arc voltage in some cases. The first reason is that these parameters have a natural limit of zero, causing their distributions to be skewed towards positive values. The second (and more influential) reason relates to the inherent nature of the vacuum arc, where each arc initiation and cathode spot event produces an irreversible change to the local conditions of the interelectrode region and cathode surface. This in turn has an influence on the formation of subsequent arcing events. Thus, the "memory" of the interelectrode region and cathode surface causes each vacuum arc pulse to never be independent of previous pulses. Test observations indicated that, when

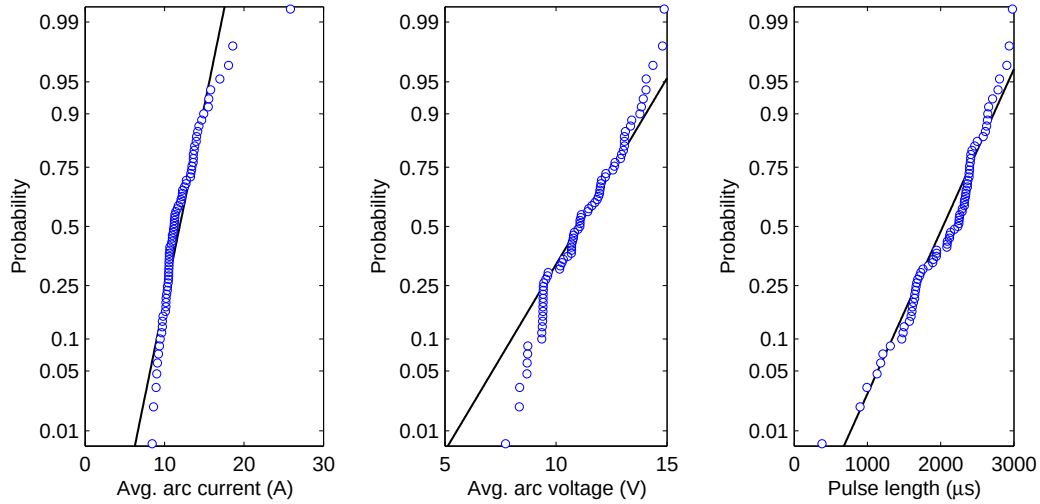

Figure 3.8: Normal probability plots for processed results of average arc current, average arc voltage and arc pulse length. In this example, a Bi cathode was used (50 A peak arc current, 2138 μs median pulse length, 75 sampled traces).

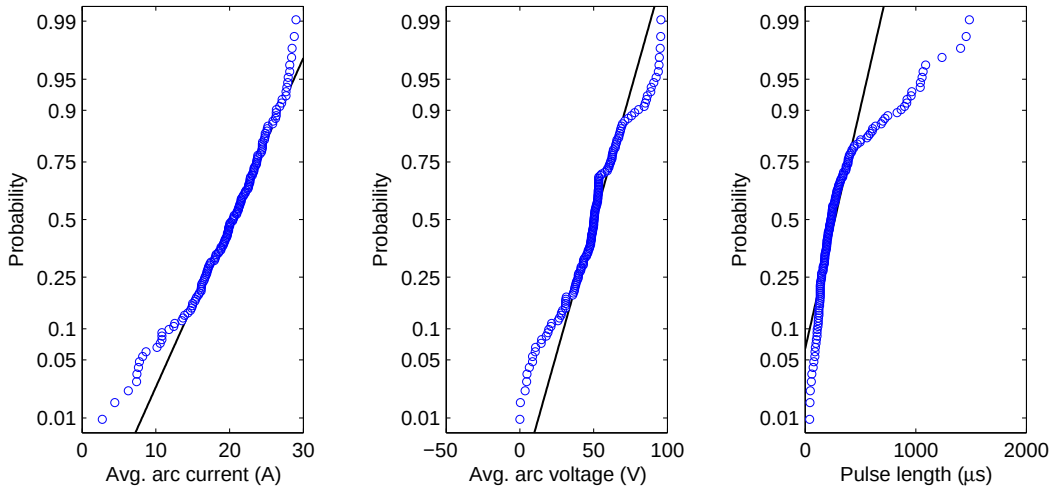

Figure 3.9: Normal probability plots for processed results of average arc current, average arc voltage and arc pulse length. In this example, an Al cathode was used (50 A peak arc current, 233 μs median pulse length, 175 sampled traces).

left to their own natural formation, arc parameters such as pulse length were most visibly affected by this characteristic of the vacuum arc and were therefore required to be handled in a statistical manner different to truly random behaviour because of it.

Based on these findings, all waveform parameters within this study were aggregated and statistically treated in a non-parametric manner (that is, independent of statistical distribution) by using the *median* of all the parameters. This was considered an overall more

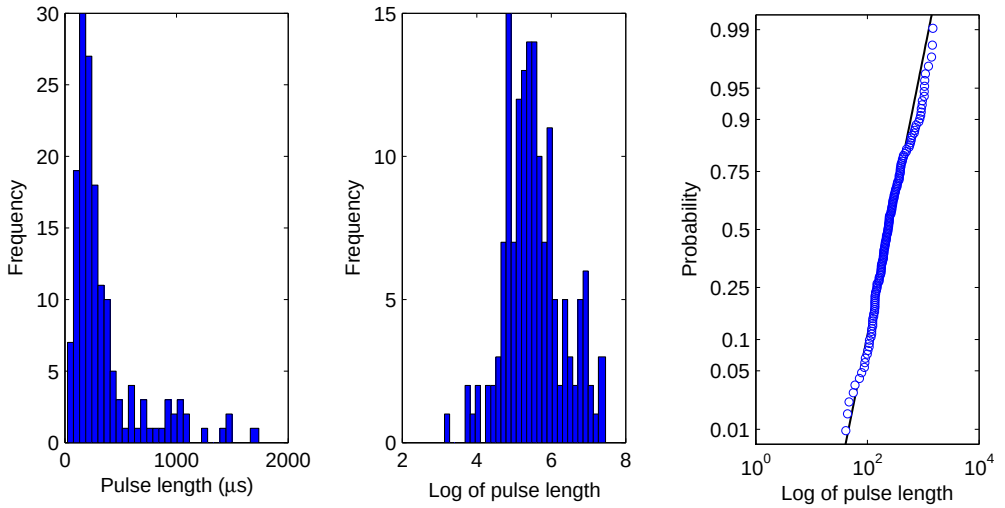

Figure 3.10: Histograms of untransformed and Box-Cox transformed pulse length data from Figure 3.9. Probability plot shows that transformed data is well fit to a Log-Normal distribution.

conservative and robust method of determining representative or more likely values of arc pulse properties rather than merely using the *mean* value. Order Statistics were then used to estimate 95% confidence upper and lower bounds for all waveform parameters.

An exception was made for ion-to-arc charge ratio data, which was able to take into account the noisy fluctuations of vacuum arc behaviour. This occurs because any temporal variation in plasma production at the thruster source is detected by the ion detection probe. Thus, the ion-to-arc current ratio, by its own definition, effectively "cancels out" fluctuations in ion production from the final result. This is demonstrated by $\bar{J}$'s excellent probability plot fit to a Normal distribution in the example of Figure 3.11. Therefore, ion-to-arc charge ratio data in this study was treated as Normally distributed. Confidence bounds on aggregated sample data were obtained using Student's t-distribution method.

It is important to note that the resulting confidence bounds (uncertainties) calculated for various arc pulse parameters as outlined here are indicative of arc stability for a given set of captured arc pulse data. By propagating these uncertainties over to thruster performance parameters such as T/I, T/P, $\bar{J}$, C_T and E_r, the effect of arc stability on the uncertainty within final thruster performance results can be confidently and conveniently expressed.

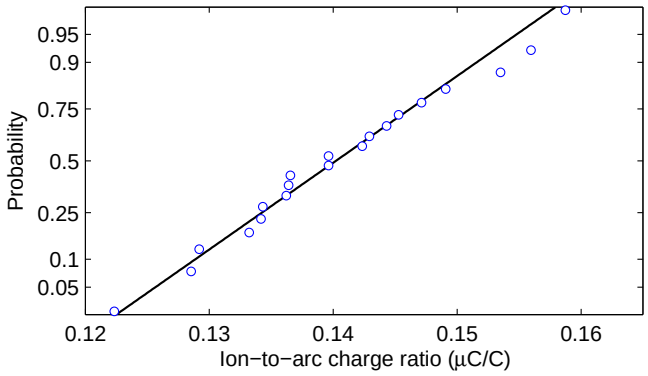

Figure 3.11: Normal probability plot for processed results of ion-to-arc charge ratio. In this example, a Fe cathode was used (50 A peak arc current, 529 μs median pulse length, 20 samples).

3.4 Direct thrust measurement stand

3.4.1 Background

Thrust from plasma thrusters can be measured with two kinds of approach: (1) indirect, or (2) direct measurement. The indirect approach (Gessini et al. 2007, Grubišić & Gabriel 2010) is generally simpler to implement and is used where the thruster or propulsion system is large in size or mass. The thruster remains fixed to the test chamber and thrusts against a freely-moving capture apparatus or impingement plate. Indirect techniques are very sensitive to small thrust forces, but must be carefully designed to ensure that as much of the ejected particles are captured by the plate and are not reflected off, giving incorrect thrust results. In addition, knowledge of the thrust plume's spatial distribution is required to correctly resolve the thrust.

The direct measurement approach (Ziemer 2001, Polzin et al. 2006, Xu & Walker 2009) is more desirable from an accuracy point of view since knowledge of the plume distribution and its interaction with the test rig is not required. However, direct thrust measurement systems are more complex to design and build. The deflections experienced by direct systems are generally much smaller than indirect systems due to the greater inertia that must be displaced, hence thrusters need to be as small and light as practically possible to maximise the measurement resolution of the system.

The most common means of direct impulse bit measurement from pulsed micro-thrusters has been to resolve thruster firings with a pendulum mechanism that can detect rig displacements at the micron or sub-micron level. The most challenging aspects of a direct thrust stand design are: (1) the use of a low-stiffness pendulum joint, (2) the use of high-resolution displacement sensors, (3) the elimination or minimization of friction, hysteresis and external disturbances, (4) operating in a high-vacuum environment (10^{-5} Torr or greater) of limited size, and (5) operating in the presence of electromagnetic noise generated by the micro-thrusters under study (Sovey et al. 1989). A number of alternative design and measurement techniques have been explored by the propulsion community to avoid or address the need to measure increasingly smaller impulse bits with greater sensitivity down to the sub-μNs range; for example, firing several pulses to create an equivalent single larger impulse (Ziemer 2001), the use of amplifying lever arms (Polzin et al. 2006), firing at the stand's resonant frequency (Lake et al. 2003) and using laser interferometry (Cubbin et al. 1997, Canuto & Rolino 2004).

Established thrust stand design elements include the flexural pivots, magnetic dampers and μm to nm-resolution displacement sensors (capacitive, magnetic, optical, etc.). However, it is still technically challenging to implement stable, reliable and accurate μN-level force calibration that is also simple. Many calibration techniques such as gas calibration (Selden & Ketsdever 2003), electrostatic combs (Selden & Ketsdever 2003, Pancotti et al. 2012), impact hammers (Ziemer 2001, Koizumi et al. 2004) and magnetic solenoids (Rocca et al. 2006) are either complex to design, manufacture and handle, require extensive and highly accurate support equipment or rely on numerical simulation for operation and characterization.

The ability to transfer power and data signals to and from the thrust stand with minimal stiffness, friction or hysteresis has also remained a persistent challenge. Many thrust stands use thin wires for power transfer, but the presence of the wires introduces possible errors from thermal expansion due to joule heating, plastic deformation and the presence of added stiffness to the overall system.

3.4.2 Thrust stand description

The stand that was developed for this work is shown in Figure 3.12 and is based on the torsional pendulum concept used by a number of authors (Ziemer 2001, Gamero-Castaño 2003, Koizumi et al. 2004, D'Souza & Ketsdever 2005). A thruster is fixed on a mounting assembly at one end of a 600 mm long beam, which is centrally pivoted about the vertical axis by two hinges above and below the beam. To reduce weight, the beam is made of aluminium. An adjustable counterweight is installed at the other beam end to ensure the beam undergoes as pure a horizontal rotation as possible. When the thruster fires, the beam undergoes a small rotational displacement. The thrust stand is designed to accommodate thrusters up to a maximum total mass of 10 kg (with a 10 kg counterweight).

Thrust measurement approach

A new operating technique for measuring impulsive thrust developed by Wong et al. (2012) was adopted in this work, where thrust pulses are fired repeatedly at a set frequency. Initially, the displacement response is similar to that for a single-fired impulse and appears chaotic, but the displacement quickly stabilizes to a constant value. It was found that this stable displacement is linearly proportional to the average impulse bit delivered to the thrust stand. For a pulse micro-thruster like the VAT, this is controlled by pulse frequency and pulsed thrust level.

The advantages of this method are: (1) the thruster can be tested over a wide range of pulse frequencies; (2) the variability of average thrust production over long operating times can be measured; (3) the method is immune to the displaced beam's initial conditions prior to the thruster firing; (4) the relatively stable displacement voltage signal is inherently easier to measure to a high sensitivity compared to a dynamic signal. However, this measurement technique is unable to quantify any pulse-by-pulse variation of impulse bits during a single firing sequence and only considers average thrust production.

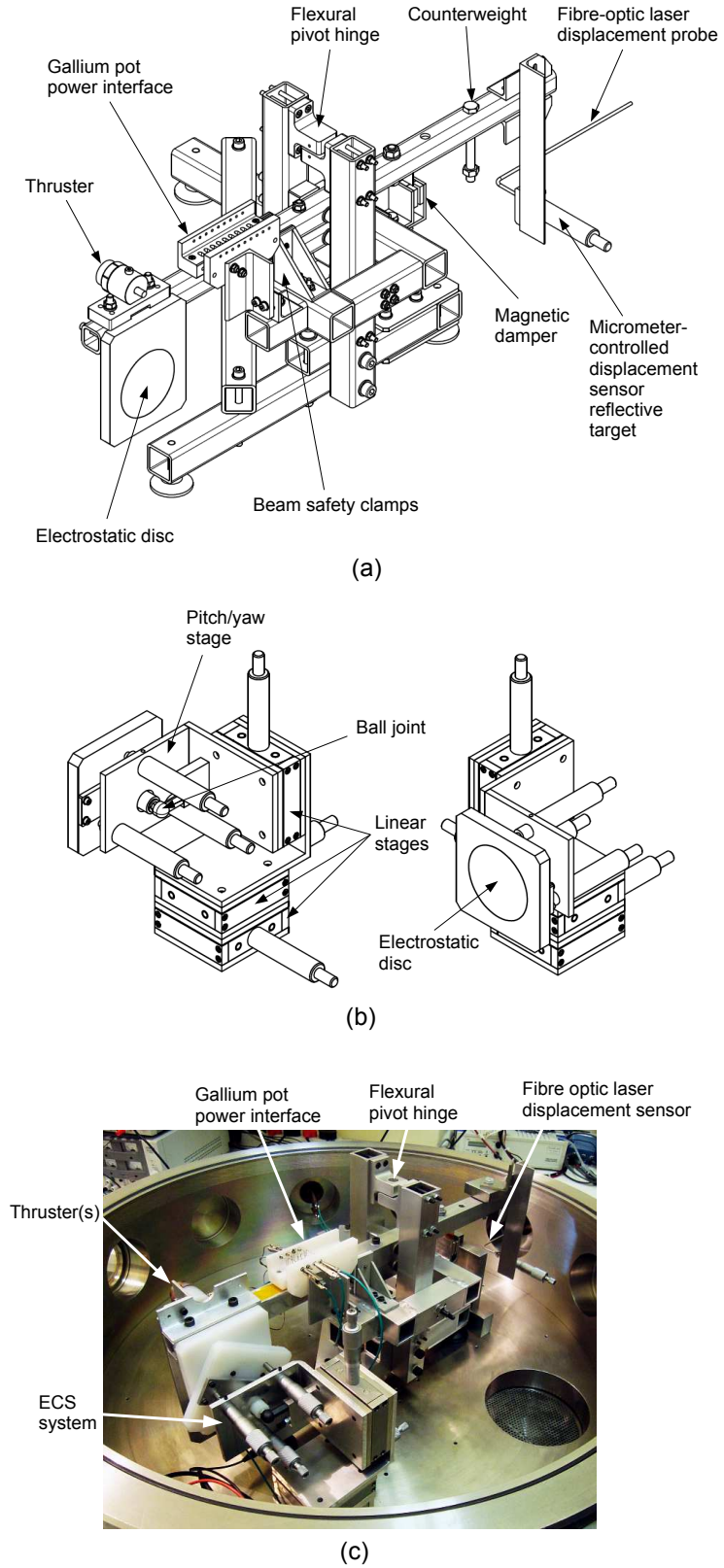

Figure 3.12: Thrust stand: (a) Overall schematic, (b) Electrostatic calibration system (ECS) with 5 degree of freedom linear positioning system, (c) Experimental test setup inside the vacuum chamber

Friction elimination/minimization

The beam hinges consist of two flexural pivots (Riverhawk model 5016-800), which provide a low-stiffness frictionless hinge solution that can operate (within a safe limited angle range of ±2°) without lubrication in vacuum for an unlimited lifetime.

Stiffness, friction and hysteresis from power cabling was successfully eliminated by the use of liquid metal pots, which act as an interface between the freely moving and static portions of the thrust stand. This solution was based on the work of Polzin et al. (2006), which used liquid gallium pots to transfer power to their stand for mN-level force measurement. Gallium is well suited to this application as it exists in liquid form at room temperature, is less toxic compared to Mercury, and has a very low vapour pressure. This work demonstrates for the first time that the liquid metal pot interface can be successfully implemented in the μN force and μm displacement operating regime of thrust stands.

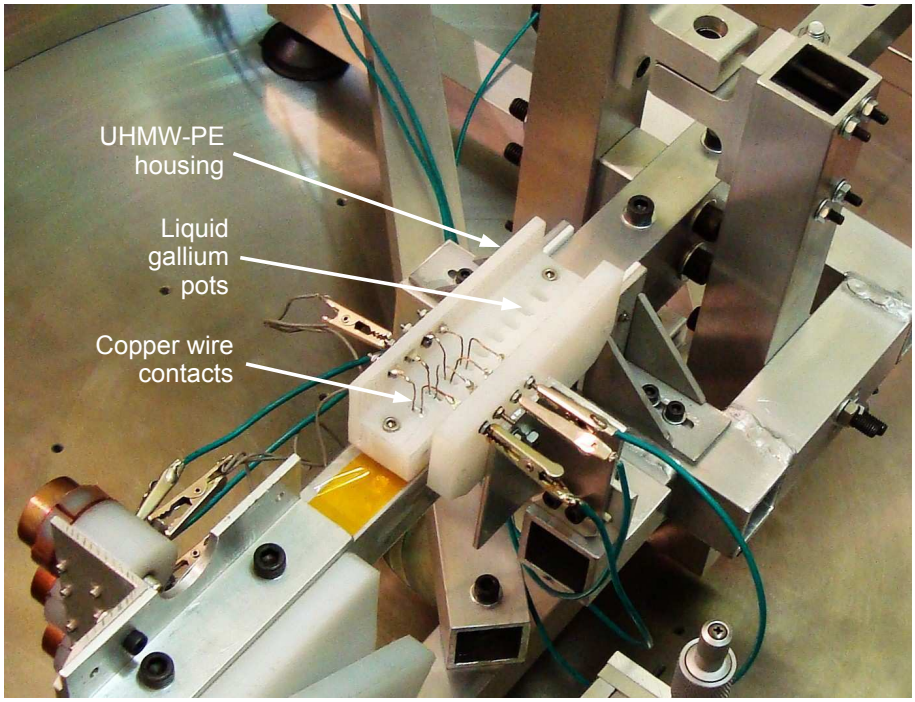

Figure 3.13: Detailed view of gallium pot power interface as installed on thrust stand. The interface can currently support up to a total of nine (9) power and/or data conduits.

A damper is usually added to provide non-contact damping of the beam due to disturbances or impulse firing of the thruster in a frictionless environment (e.g. see Polzin et al.

(2006)). The damper may be passive (permanent magnets) or active (electromagnets), where a control system can be used to increase damping effectiveness. For simplicity, a passive damper made of six 20 × 10 × 5 mm rare-earth neodymium magnets was installed at a fixed point under the beam with a 2 mm gap between the magnets. The 20 mm wide, 0.9 mm thick copper plate damps the motion of the beam as it passes between the magnets due to eddy-current formation within the plate. These eddy currents produce an opposing magnetic force to the magnets which counteracts the plate's motion and converts kinetic energy into thermal energy. Care was taken to produce a sufficiently under-damped response that allows for a reasonably short settling time without reducing the amount of displacement. In a typical test, the beam was observed to have a natural frequency of ω_n = 0.2–0.26 Hz, a damping coefficient of $\zeta \approx 0.27$ and an initial response rise time of 1.5–2 s to the application of a steady-state force.

Instrumentation

Linear Variable Differential Transformer (LDVT) sensors are often used as displacement measurement sensors due to their high-resolution (≤ 1 μm) and reasonable cost (Ziemer 2001, Koizumi et al. 2004, Pancotti et al. 2012). However, optical fibre sensors also have successfully demonstrated use due to their immunity to EMI, e.g. see Gamero-Castaño (2003). For this project, the beam end displacement was measured by a Philtec D63 fibre optic displacement sensor which remained fixed to the vacuum chamber. The sensor probe operates by emitting an infra-red laser beam from its tip, which reflects off a small target on the beam end. The sensor unit outputs a voltage signal between 0–5 V depending on the target's reflectivity and the gap distance between the target and the sensor tip. For greatest sensitivity, the target was made of aluminium foil (~80% reflectivity) and the gap distance set between 0.1–0.3 mm, that is, within the linear operating range of the sensor. The displacement sensor is immune to EMI, compatible with high-vacuum and capable of resolving displacements as low as 0.4 μm with a sensitivity of 2.75 mV/μm. The sensor voltage output was sent to a National Instruments 14-bit Data Acquisition Module (NI USB-6009) for data capture. All displacement data (uncertainty of ±1 mV) was sampled at a sufficiently high sample rate of 300 Hz and smoothed with a low-pass filter of 2.5 Hz, which is roughly an order of magnitude larger than the beam's natural

frequency (safely meets Nyquist sampling limit). Filtering is done in order to mitigate sensor noise and possible EMI from the thruster. In this way, the beam's response was sufficiently captured and suitably processed for displacement analysis.

Calibration system

Calibration of the thrust stand is performed using an Electrostatic Calibration System (ECS) similar to that of Gamero-Castaño (2003). Two 70 mm diameter flat polished stainless steel discs are positioned in close proximity to one another and an electrostatic force is generated by creating a known potential difference between the discs. The advantages of this method are that (1) a non-contact force can be applied to the thrust stand; (2) the production of the electrostatic force can be controlled from a remote location; (3) a wide range (μN's to mN's) of forces can be applied; and (4) once prepared correctly, the calibration procedure can be performed under vacuum conditions just prior to thruster testing.

For the ECS to function correctly, however, its two discs need to be accurately and reliably positioned for consistent calibration. This required a five-degree of freedom (5 DOF) linear positioning system that was designed and built to accurately align a stationary disc, to its twin which is attached to the freely-rotating beam (see Figure 3.12c). The X, Y and Z position of the fixed disc is controlled by a custom-designed spring-loaded micrometer-actuated linear stage system, and the disc's pitch and yaw is adjusted by three circularly-positioned micrometers on an L-bracket. The ECS system has a positional accuracy of $\pm$10 microns for each axis and a disc angular tolerance of $\pm 0.009^{\circ}$.

3.4.3 Analytical model and analysis of beam response

The displacement response of the thrust stand can be described analytically based on the derivation of the linear displacement response of an under-damped pendulum to a repetitive impulsive force (Wong et al. 2012). Converting the response to an angular

displacement results in the following equation:

$$\begin{aligned}\theta(t) = \frac{x(t)}{r_a} &= \sum_{i=0}^{N}\left[\frac{\bar{I}_{bit} r_a}{I_m \omega_n \delta}\exp\{-\omega_n \zeta \tau\}\sin\{\omega_n \delta \tau\}\right] H_o \tau \\ &+\theta(0)\exp(-\omega_n t\zeta)\left[\frac{-\zeta\sin(\omega_n t\delta)}{\delta}+\cos(\omega_n t\delta)\right] \\ &+\left[\frac{\dot{\theta}(0)+2\theta(0)\omega_n\zeta}{\omega_n\delta}\right]\exp(-\omega_n t\zeta)\sin(\omega_n t\delta) \end{aligned} \tag{3.2}$$

where

$$\begin{aligned}\delta &= \sqrt{1-\zeta^2} \\ \tau &= t-\frac{i}{f}\end{aligned}$$

and $\theta(t)$ and $x(t)$ are the angular and linear displacement as a function of time t respectively, r_a is the moment arm from the thruster to the pivot hinge, $\bar{I}_{bit}$ is the average impulse bit, I_m is the effective rotating system's moment of inertia, ω_n is the natural frequency of the system, ζ is the damping coefficient ($\zeta < 1$), f is the pulsing frequency, N is the total pulse number, $x(0)$ and $\dot{x}(0)$ are the system's initial displacement and velocity and H_o is the Heavyside step function. Equation 3.2 is capable of modelling the system's response to an arbitrary number of repetitive pulses, including a single pulse ($N = 1$).

The average impulse bit and force from the thruster are found using:

$$\bar{I}_{bit} = T\bar{t}_p \tag{3.3}$$

$$\bar{F} = \bar{I}_{bit} f = F\bar{t}_p f \tag{3.4}$$

where F and $\bar{t}_p$ is the pulsed thrust and pulse duration.

The natural frequency of the thrust stand beam is defined as

$$\omega_n = \sqrt{\frac{k_{eff}}{M}} \tag{3.5}$$

where k_{eff} is the effective stiffness of the system and M is the system mass.

During quasi-steady state, the beam displacement follows Hooke's Law such that

$$\bar{F} = k_{eff} x_s \tag{3.6}$$

where x_s the steady-state displacement response of the beam to a repetitively-pulsed force.

Thus, the pulsed force produced by a thruster is found using a combined expression of Equations 3.4 and 3.6:

$$F = \frac{k_{eff} x_s}{\bar{t}_p f} \tag{3.7}$$

Equation 3.2 shows that a smaller ω_n and M will result in a larger beam displacement. Hence, a thrust stand should be designed to have as low a stiffness and moment of inertia as practically possible based on Equations 3.5 and 3.7.

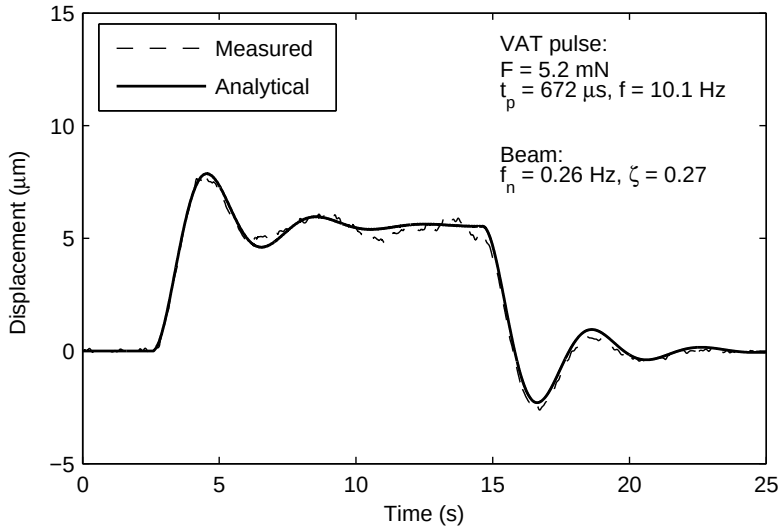

Figure 3.14: Typical beam displacement response to a 12.5 s long repetitively-pulsed thrust firing from a VAT with an iron cathode. A comparison of the measured and analytical beam response shows good agreement. Value of x_s is found by measuring the average displacement several seconds after initial thruster firing or start-up.

Comparison with a sample experimental measurement as shown in Figure 3.14 demonstrates relatively good agreement between measured displacement data and Equation 3.2 for the calculated beam properties.

Based on test observations, a recommended minimum thrust firing duration of at least 12 s (15–20 s preferred) was found to produce an acceptably stable displacement measurement of x_s, which was determined by averaging the steady state response of the beam. A similar amount of waiting time was also used in calibration-related activities to allow sufficient time for the system beam response to stabilise.

3.4.4 Commissioning and quantifying thrust accuracy

Thrust calibration takes into account the physical and dynamic characteristics of the beam, calibration, and sensor systems. These system characteristics will differ slightly whenever a new thruster design is mounted onto the thrust stand for testing or when any part of the thrust stand system is moved or modified. Thus, whenever testing a thruster design in a new configuration, a calibration procedure must be undertaken. Before calibration, a disc alignment exercise was performed, where the fixed disc was manually aligned parallel to the free disc and then positioned at a set gap distance. The gap distance was defined as the average distance between the two discs. To generate an electrostatic force on the beam, the fixed disc was charged to a steady electric potential using a stack of standard laboratory power supplies, whilst the free disc was connected to the grounded thrust stand. A range of electrostatic forces was generated and the displacement response of the beam recorded. A typical set of results is shown in Figure 3.15 over the 0–30 μm range.

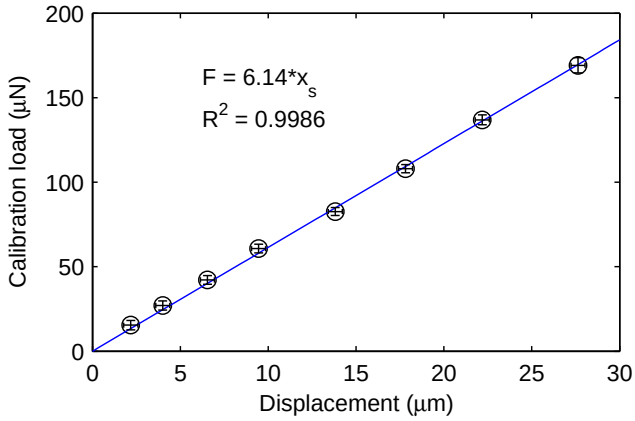

Figure 3.15: Typical calibration result showing relationship between beam displacement and the applied force on the beam

The calibration procedure was shown to be of sufficiently high accuracy and no hysteresis was observed when removing the calibration loads. A linear least squares method was used to fit a curve through the data, revealing the linear relationship between force and displacement (in this example, see Figure 3.15 where $F = 6.14x_s$, $R^2 = 0.9986$). This result verifies that the thrust stand behaves consistently and correctly as a spring element of predictable stiffness. The force-displacement expression was then used to directly relate the average force on the beam to the deflection measured by the displacement sensor. In this work, the thrust stand spring stiffness typically ranged from k_{eff} = 4–7 N/m depending on beam loading.

Before the thrust stand can be implemented, however, the accuracy of the ECS system needs to be characterised. The three main sources of error in the system that are expected are: (1) the accuracy of measuring and applying the calibration loads, (2) changes in the plate gap when larger electrostatic forces are applied, and (3) the accuracy and repeatability of aligning the ECS discs to one another. Assessment and verification tests for these system errors is described below.

Accuracy of ECS force generation

To calibrate and verify the accuracy of the electrostatic force generated by the ECS system, the beam's position at zero load (neutral or null position) was recorded. Based on work by Lafleur (2007), a set of small calibration masses (m = 25–250 ± 0.1 mg) were then hung via a thin thread arrangement as shown in Figure 3.16 so as to apply a load to the thrust stand beam along the line of action of the thruster. Friction is eliminated from the setup through the use of Lami's theorem, where the horizontal force acting on the beam is

$$F_1 = mg\cot(\theta) \tag{3.8}$$

and θ is the angle between thread F_2 to the horizontal (between roughly 50°–70° in this work) and g = 9.786 is the gravitational acceleration constant of the local test facilities. This expression holds true provided changes in θ are very small, which is the case here.

Measurements of θ were taken with a digital level meter (user error accuracy of $\pm 0.5^{\circ}$).

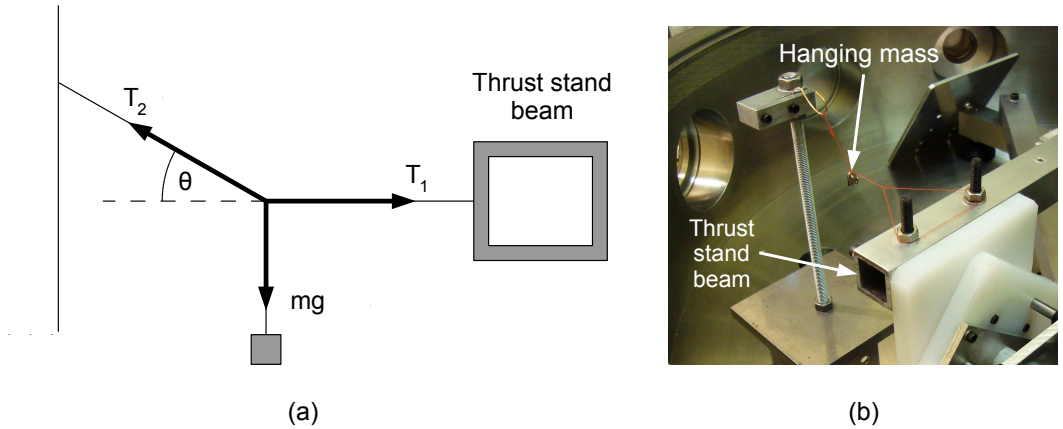

Figure 3.16: (a) Schematic force diagram and (b) photograph of calibration setup verifying ECS force generation.

An electrostatic force F_{ecs} was then applied to bring the beam back to its null position, exactly balancing the load due to the calibration mass. This ensured that the desired gap between the discs remained constant throughout the calibration process. The electrostatic force between the two finite circular discs can be theoretically described by:

$$F_{ecs,th} = \frac{\epsilon_0 A V_{ecs}^2}{2s^2}\left(1 + \frac{2s}{d}\right) \tag{3.9}$$

where ϵ_0 is the permittivity of free space, A is the disc area, V_{ecs} is the voltage, s is the spacing between the plates and d is the plate diameter. Figure 3.17 shows the results of the ECS force generation tests in comparison to the predicted force for a desired plate gap of $s = 2$ mm.

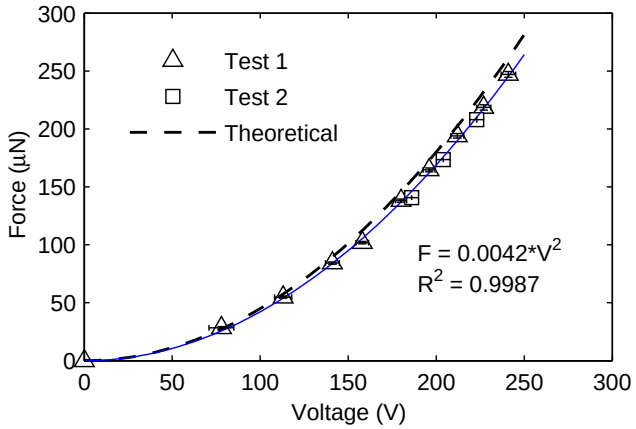

Figure 3.17: Comparison of theoretical electrostatic force and force generated by the ECS system

Applying a quadratic curve fit across all test data results in the following relationship between the voltage applied and the force generated by the ECS:

$$F_{ecs} = aV_{ecs}^2 \tag{3.10}$$

where coefficient $a = 4.2 \pm 0.045 \times 10^{-3}$ N/V^2. For the ECS parameters used in this test, the theoretical electrostatic force can be shown to bear the following relation to the voltage: $F_{ecs,th} = 4.5 \pm 0.044 \times 10^{-3} V_{ecs}^2$. Thus, the force deviation from the theoretical case is just over 7%. For the initial runs (Test 1) the force generated by the ECS system was slightly less than predicted by the theoretical model (Equation 3.9). Test runs (Test 2) were repeated at a different thread angle, after realignment of the ECS and produced similar results as shown in Figure 3.17. Another calibration exercise was repeated a year later and still produced a coefficient of $a = 4.2 \pm 0.065 \times 10^{-3}$ N/V^2, demonstrating the excellent long-term stability of the measurement and calibration systems. This confirmed that the calibration system is highly accurate and repeatable, and that the deviation from the theoretical model was an inherent characteristic of the ECS. The most likely cause of this deviation was found to be slight misalignment of the discs within their respective plastic housings, which produced a greater gap than expected depending on the disc's roll position. Hence, changes to the disc's roll position were avoided once the ECS was calibrated to maintain reliable force generation.

Accuracy of ECS Plate Gap

When steady electrostatic forces are applied by the ECS for calibrating a thrust test, the displacement of the beam will cause the plate gap to become smaller. This will have the effect of slightly amplifying the force generated. Analysis of Equation 3.9 reveals that the force error grows by an estimated 0.097% per 1 μm of gap reduction for small displacements. Thus, over the 0–40μm displacement range, the error due to the plate gap increases from 0% to 3.8% of the force applied.

Accuracy of ECS Disc Alignment

ECS disc alignment accuracy was assessed by hanging a single ~340 mg mass on the thrust stand beam. An electrostatic potential was applied to the discs such that the static mass load was cancelled out and the beam was in the null position. A plate gap of s = 2 mm was chosen for this and all subsequent tests to limit plate edge effects, whilst still keeping the uncertainty of the gap distance small (≈0.5%). The load test was repeated n = 10 times where the load was re-hung, and the ECS realigned from an initial position each time. Thus, the variability of the sampled voltages takes into account all system uncertainties and variability within the preparation of each test run. To minimize the effect of the displacement sensor's resolution on the results, a relatively large mass and hence a large electrostatic potential was chosen for this exercise.

A Goodness of fit test indicated that the voltage data had a good fit to a normal distribution (mean V_{ecs} = 772 V, std dev. σ = 13 V, Chi-square test P_r = 0.63–0.99). Based on the assumption of a normal distribution and using Student's t-distribution, it can be shown that the uncertainty of the applied voltage is $\Delta V = t\sigma/\sqrt{n}$, where n is the number of alignment runs. For t = 3.25 (99% confidence) and n = 10, the result is ΔV = 13.4 V. Hence it can be shown that the applied voltage uncertainty, which represents the accuracy of ECS disc alignment is 1.7% with 99% confidence level. An additional alignment test a year later demonstrated an ECS alignment error as low as 1.1 % at the same confidence level. This result further verifies the repeatability and reliability of the ECS positioning system.

3.4.5 Final thrust stand performance

Based on system resolution limits and verification tests performed, the thrust stand force error due to different sources over the 0–40 μm displacement range is summarized in Figure 3.18. The interpretation of this analysis is that the thrust stand accuracy is dominated by the resolution limit of the displacement sensor output signal in the 4–20 μm displacement range (2–10% error). Above 20 μm, the ECS plate gap error dominates in

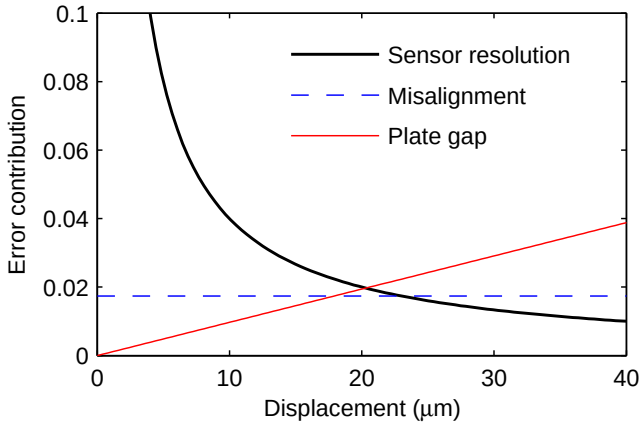

Figure 3.18: Comparison of sources of thrust error over the 0–40 μm displacement range truncated to a maximum error limit of 10%.

the 20–40 μm range (2–3.8% error). Thus, the optimal range of thrust measurement accuracy occurs between 15–25 μm of beam displacement. The thrust stand error analysis also shows that the error due to ECS disc misalignment and force generation does not play a significant role in the final thrust error in the present thrust stand configuration.

3.4.6 Design and performance summary

The ECS system and *in situ* calibration method in this work has demonstrated a number of attractive features, namely that (1) the force generated can be adequately predicted by a simple analytical description of the electrostatic force without the need for an electromagnetic simulation model, (2) electrostatic forces can be regularly and accurately verified by calibration masses whilst keeping the test-rig intact, (3) an impulsive excitation from a pulse circuit is not required to calibrate the stand for pulsed thrust, and (4) the ECS system is stable over a long period of time.The disc gap error which was of previous concern (Selden & Ketsdever 2003) with regards to the electrostatic disc calibration technique was demonstrated to not play as significant a role in the total error, provided deflections were not too large. However, the error due to the electrostatic disc gap in the ECS system at larger displacements can be eliminated by replacing the calibration discs with an electrostatic comb system (Pancotti et al. 2012) instead. However, there is the trade-off of greater manufacturing and handling complexity of the electrostatic fin arrangement.

The possible range of impulse bits that the present thrust stand setup is capable of resolving can be estimated using the above error limits. Based on a 10% error limit, the minimum and maximum displacement that can be measured is 4–100 μm. This translates to an average force of 27–600 μN. Assuming thruster pulse limits of 1–100 Hz, the measurable impulse bit range is thus 0.27–600 μNs, which covers four orders of magnitude.

These performance results compare favourably with other previously mentioned stands in literature (Gamero-Castaño 2003, Koizumi et al. 2004). However, the stand's sensitivity was intentionally limited from a practical implementation point of view taking into account the size of the test chamber, the cost of the displacement sensor, and EMI generation from the VAT. The chosen design solution favours simple calibration, operation, and maintenance. The flexural pivots' stiffness, fibre-optic displacement sensor's resolution and the short beam arm length are the main limiting factors to thrust sensitivity. This could be addressed by (1) installing pivots of lower stiffness value, which will improve sensitivity at the cost of lower load limits; (2) upgrading the sensor, which will improve sensitivity at the lower range of displacements; and (3) optimizing the beam by reducing its mass to reduce system inertia and further increase sensitivity. Care should be taken that the resulting increase in the natural frequency of the stand should not be too close to the tested thruster's operating pulse frequency to avoid resonance effects.

3.5 Faraday cup probe

3.5.1 Background

Ion measurements are an important diagnostic tool for characterization of plasma sources. Depending on the study, a variety of diagnostic probes can be used to measure specific plasma properties such as the amount and rate at which ions are produced (Faraday probe), ion energies (Retarding Field Energy Analyser), charge state distribution of the ions (Mass Spectrum Analyser) and electron properties (Langmuir probe).

Ion current or the ion flow rate is commonly measured with a Faraday probe (plate, cup or gridded form). The probe consists of an ion collector that is impacted by incoming positive ions and becomes charged as a result. In response, electrons flow from ground to the collector to exactly neutralize the charge imbalance. This current flow can be determined by measuring the voltage drop across a terminating resistor positioned between the probe and ground, hence capturing the ion current impacting the probe collector. It is important to note that only a partial amount of the total ion current emitted by the thruster is measured by the probe due to the limited surface or orifice area of the probe collector. Hence, results may be presented as ion current densities (A/m^2), which acknowledges the presence of this finite area. Probe surface area also determines the spatial resolution of the current density, where a larger probe area produces smoother ion current density data.

One feature of vacuum arc plasmas is that the ion charge states and velocities approach stable values soon after leaving the cathode surface ($\leq$ 1 mm travel distance) as described by Anders (1997) and Weickert (1987). Used together with measurements of ion current density, these ion properties can be used to find the particle density of the plasma and observe how it decreases over distance as the jet travels further away from the thruster. Indeed, Anders (2008) reports that during plasma expansion, a quadratic drop in plasma density along the normal direction occurs and can be described by the following empirical expression:

$$n_p = C\frac{I}{z^2} \tag{3.11}$$

where n_p is the plasma particle density, C is a constant depending on the cathode material ($\sim 10^{13}$ $(Am)^{-1}$ for copper), I is the discharge arc current and z is the normal distance (or drift length) from the vacuum arc source in space.

One advantage of measuring ion flow with a Faraday Cup (FC) probe is that the ion current coming off the thruster at different ejection angles can be measured by adjusting the orientation of the FC probe with respect to the thruster head (Sekerak 2005). Combining this set of data gives a measure of the ion current density distribution (ICDD). This ion distribution is important because of its direct relation to the thrust plume distribu-

tion; given that the ions contribute most, if not all of the thrust. Therefore, the ICDD provides knowledge of the shape of the thrust-producing jet and how it affects thruster performance.

FC probes can be used to find the most likely ion velocity using the Time-of-Flight method. This is achieved by measuring the peak-to-peak delay in ion signal from when the arc discharge is created to when the plasma is detected by a probe, a set distance away. Various forms of this technique have been used in both vacuum arc science (Anders 1998, Yushkov et al. 2000, Anders & Yushkov 2002*b*) and VAT studies (Sekerak 2005, Zhuang et al. 2009).

The FC probe alone is unable to distinguish between different ion species. Instead, a mass spectrum analyser is commonly used to separate the different ion components in order to find the ion charge state distribution, e.g. see Bugaev et al. (2000). Alternatively, an electrostatic ion acceleration grid system was developed by Brown et al. (1987) to accelerate different ion species present in the vacuum arc plasma to different velocities. After a long drift length, the individual ion species would arrive at an FC probe at sufficiently varied times, stratifying the ion charge state distribution (CSD) into its respective components. However, this system required a complex set of fast gates and ion optics to control and focus the plasma jet towards the FC probe as well as a large chamber size to achieve a long ion drift length.

3.5.2 Probe description

A FC probe with a cup design was developed and built to measure the ion current in the plasma jet emitted from the thruster. The current flow produced by incoming ions is measured by reading the voltage change across the terminating resistor R in the probe circuit as illustrated in Figure 3.19. The ion collector is negatively biased to repel plasma electrons and only allow the positive ion charges to be collected.

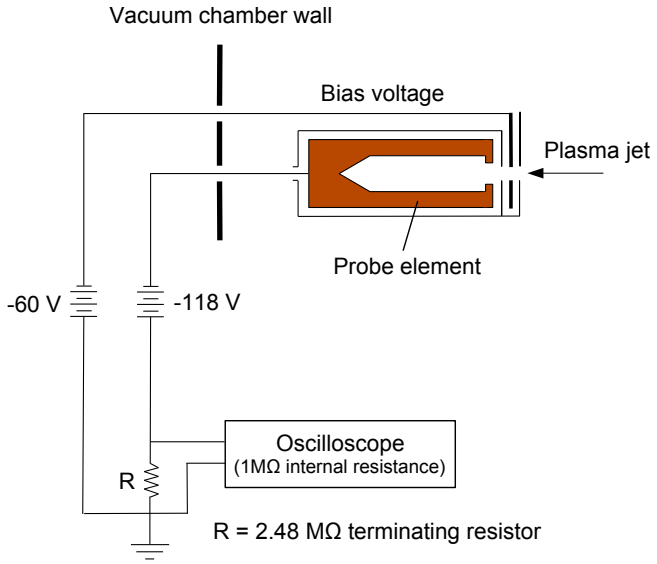

Figure 3.19: Schematic of Faraday Cup probe and circuit. Ion collector is negatively biased to -118 V and connected to ground via a terminating resistor. In the setup depicted here, the resistor value was set at 2.48 ±0.01 MΩ for ICDD measurements in this study. An additional -60 V bias plate was installed for further repulsion of plasma electrons.

Probe circuit design

A schematic of the probe circuit shown in Figure 3.19 includes a shielded pack of 9 V batteries to act as a floating negative bias power supply for the ion collector as well as a standard laboratory power supply to charge the negative bias plate to −60 V in front of the FC probe. BNC cabling and connectors were used to connect various portions of the FC probe and circuit inside and outside the chamber as well as to the digital oscilloscope for data capture. A digital oscilloscope (ISO-TECH IDS 8064, 60 MHz 1Gs/s) measured the voltage drop across a shielded terminating resistor in the circuit to measure the ion current signal. However, the resistance of the oscilloscope in parallel must also be taken into account if a large terminating resistor value is used. Therefore, the true terminating resistance is

$$R_{true} = \frac{R_o R}{R_o + R} \tag{3.12}$$

where R_o = 1 MΩ is the oscilloscope resistance and R is the terminating resistance. To ensure a good range of signal strengths, terminating resistor values may range from kΩ to MΩ to convert the detected ion current into a sufficiently detectable and accurate

voltage drop.

Hence, the ion current captured by the FC probe I_{ip} is simply

$$I_{ip} = \frac{V_{fc}}{R_{true}} \tag{3.13}$$

where V_{fc} is the voltage drop measured by the oscilloscope across the terminating resistor.

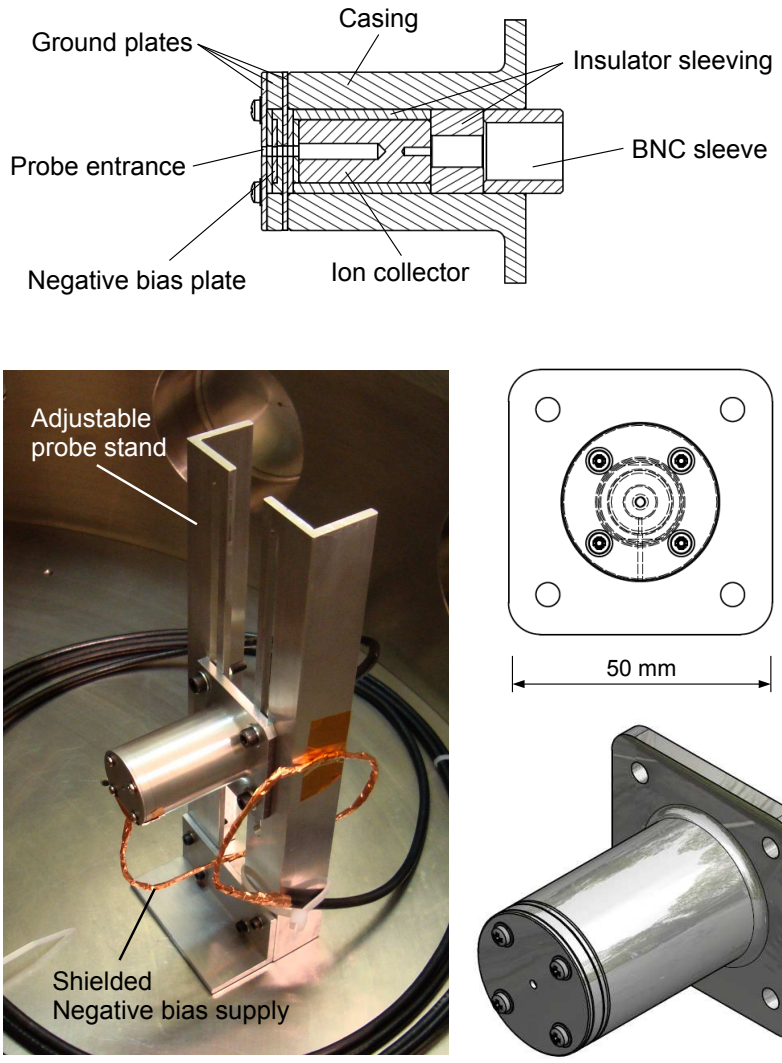

Figure 3.20: Photograph and engineering drawings of Faraday Cup probe

Probe design

Design specifications for the FC probe as depicted in Figure 3.20 are as follows:

1. The ion collector component of the FC was made of copper and designed to have a deep inner cup (or orifice) length-to-diameter ratio of 5:1 (15 mm deep and 3 mm diameter) to ensure successful ion capture and reduce the likelihood of escape of any secondary electron emissions caused by collision of ions with the collector material. The end of the collector orifice was conical in shape to ensure any reflection of ions and secondary electrons would be intercepted by the inner wall of the collector orifice. A 0.9 mm thick copper ring with a 2 mm diameter hole is located directly in front of the collector.

2. A negative bias of -118 V was used for the ion collector to ensure the rejection of plasma electrons.

3. The probe entrance and plate holes were made as small as possible to reduce the possible shielding effect of the plasma sheath on the negative bias plate. However, the smallest hole diameter was limited to 1.8 mm for reasons of accurate manufacturing and limits on the smallest ion current signal that could be practically measured by the setup.

4. An additional 0.9 mm thick copper plate of negative bias -60 V was installed in front of the ion collector to further repel plasma electrons. Aluminium ground potential plates are located on either side of the bias plate to cancel out the effect of the electric field generated by the bias plate (the ions are accelerated toward the plate, then decelerated past the plate). Cabling supplying the negative bias was shielded with copper foil at the interface with the probe.

5. Insulation rings (0.9 mm thick) and sleeves made of UHMW-PE plastic were used to separate the collector, bias and grounded components from each another.

6. A casing for housing and shielding FC probe components was machined out of aluminium. The casing also allows for the probe to be mounted on an adjustable vertical stand for positioning the probe.

7. A BNC connector at the back of the probe sends the ion current signal through a shielded BNC vacuum connection and feedthrough to the probe circuit outside the chamber.

3.5.3 Probe operation, behaviour and performance analysis

Validation and verification checks

The following checks and verifications on the functioning of the FC probe were performed:

1. The probe's ion signal was visually confirmed to have a similar waveform profile to the arc current discharge profile and maintained its shape despite the arc current level (see Figure 3.21) . Peak ion current was also shown to be in correct proportion to the arc current level for similar arc pulse conditions.
2. Practically zero incoming signal was measured by the probe when firing a VAT prototype against a blanked off probe entrance. This result confirmed that no leakages were present within the shielding of the probe, cabling and circuitry.
3. Measurement of ion current signals at various drift lengths (150, 230 and 300 mm) demonstrated that the ion current signal (and by inference, plasma density) correctly drops according to $1/z^2$ as described by Equation 3.11 (see Figure 3.22). The slight deviation at $z = 300$ mm is likely due to the nearby presence of the chamber wall affecting the plasma's expansion into the surrounding vacuum.
4. Varying the bias voltage for the ion collector over a range from -118 V to $+20$ V revealed that the FC was correctly repelling electrons from a bias voltage of at least -40 V (see Figure 3.23).
5. A measurement of ion current at different ejection angles to the VAT produced an Exponential or Gaussian-shaped ion current density distribution. This behaviour is in agreement with observations by Sekerak (2005), further validating the behaviour of the FC probe.

6. Errors due to terminating resistor values, oscilloscope arc current and time sampling resolution limits (±0.4%, ±1% and ±0.025% respectively) were small enough to be considered negligible in comparison to the uncertainty of average charge of the ion arc current signals, which were typically ≥ ±5% (due to the noisy nature of vacuum arc pulses).

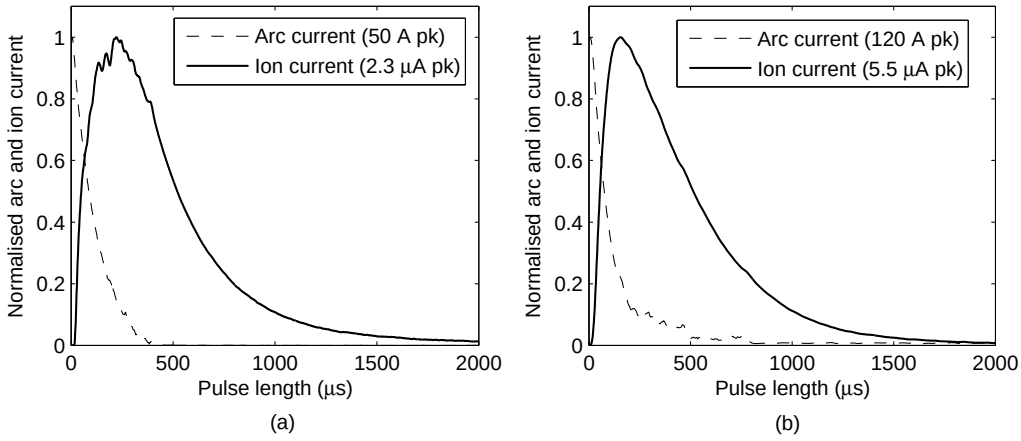

Figure 3.21: Comparison of normalised arc discharge waveform and ion current signals taken directly in front of VAT (Fe cathode) from a distance of $z = 230$ mm. Arc pulse characteristics are $I = 50$ and 120 A, $t_p \sim 500$ μs.

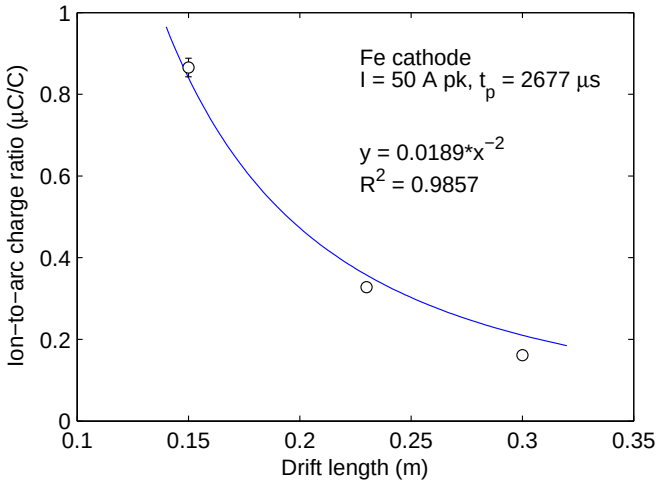

Figure 3.22: Measurement of ion current signal from baseline VAT at various drift lengths to the FC probe ($z = 150$, 230 and 300 mm) . Ion current drops according to $1/z^2$.

Circuit effects

In any given test, some persistent differences in shape between the ion current and arc current waveforms were observed (Figure 3.21 is an example of this). The first observed

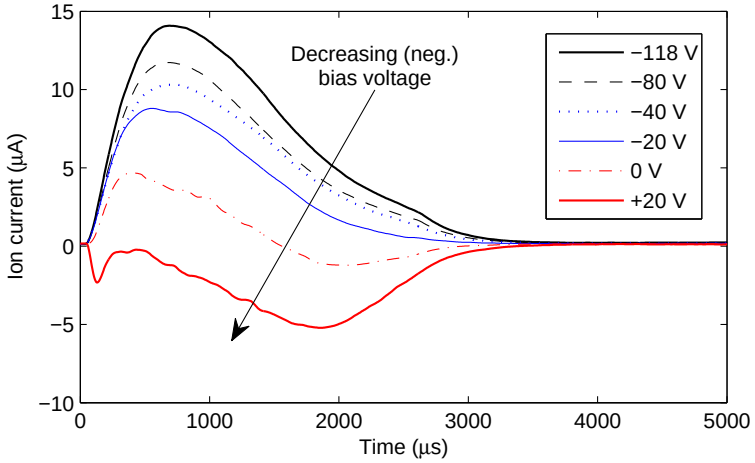

Figure 3.23: Measurement of FC ion current signal from baseline VAT taken at various bias collector voltages from −118 V to +20 V. Negative ion current signals at 0 and +20 V clearly depicts non-repulsion of plasma electrons.

difference was the delayed initial response rise time of the ion signal, which gave the waveform a more spread out "hill-shape" compared to the triangular shape of the arc discharge. The peak of the ion current tended to occur much later in time after the discharge (about 100–200 μs as seen in the example) and could not be attributed to the finite ion velocity, which would only cause a 10–20 μs time delay over a ~200 mm drift distance. The second observed difference was in the overall duration of the waveforms, where the ion current signal took roughly 1 ms longer than the arc current pulse to dissipate. This was observed regardless of arc current level or pulse length.

The damped nature of the ion current signal was further characterised by noting the increasing change in peak ion current location with increasing peak ion current magnitude, that is, the larger the ion signal, the greater the rise time of the ion signal as demonstrated in Figure 3.24.

An additional plot of several peak ion current signal locations and magnitudes over a variety of arc pulse conditions and cathode materials reveals a general linear trend (see Figure 3.25). This trend signifies the maximum capable dI/dt response (or "inertia") of the FC probe and circuit. The relatively constant value of dI/dt means that the FC system dampens the ion signals by the same measure, i.e. the electrical characteristics of the system are fixed across all tests with the same setup.

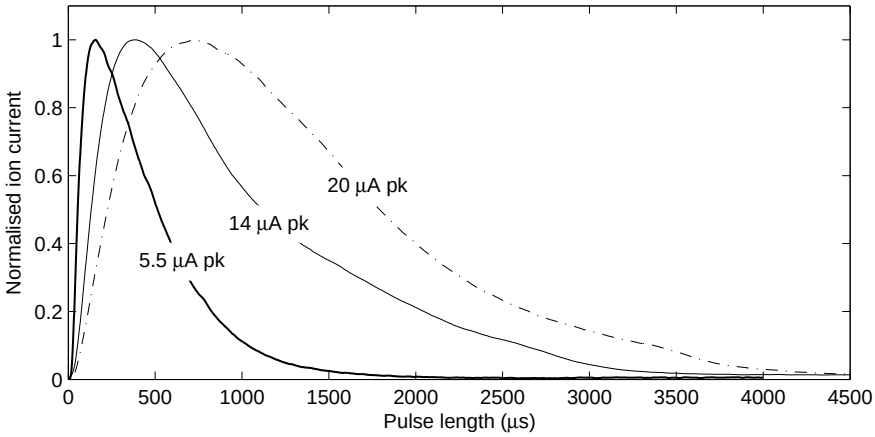

Figure 3.24: Observed increase of peak ion current location with peak ion current magnitude. Ion signals taken directly in front of VAT with Fe cathode.

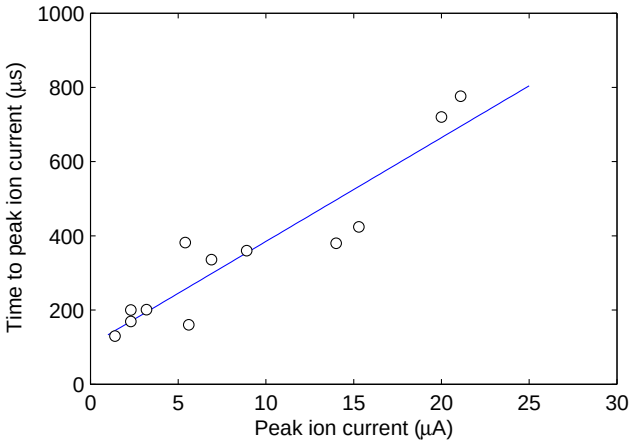

Figure 3.25: Plot of peak ion current location against peak ion current magnitude with observed linear trend. Captured ion current samples obtained from tests with Al, Fe and Bi cathodes, peak arc currents of 50 and 100 A and pulse lengths 200–3000 μs long. Drift length z = 230 mm and R = 2.48 MΩ.

All these findings suggest that it is not the ions alone that determine the circuit response, but the FC system also. Measurement of ion current with two differently-sized resistors (65.5 kΩ and 2.48 MΩ) revealed that the terminating resistor value significantly affected the damped response of the ion current signal (Figure 3.26). The larger terminating resistor was used in this study to ensure a better signal-to-noise ratio with a compromise on signal response time. To overcome this distortion on the data, a measurement of integrated ion current over time (charge of ion pulse signal) was used instead as a measure of ion production (see discussion in Section 2.3.2). Additional, but likely minor culprits of ion current signal damping include capacitance and inductance effects in the cabling and batteries.

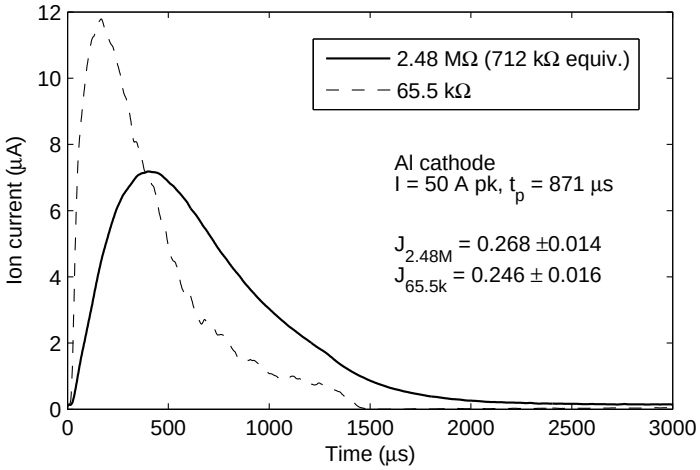

Figure 3.26: Comparison of ion current signals taken with two different terminating resistor values. Note the different response times of the two resulting signals, where the lower resistor value gives a faster response. Waveforms are averaged over 40 samples. Calculated charge of ion pulses are within 10% of each other. Drift length $z = 230$ mm.

Secondary electron emission

One of the potential errors experienced in FC probes is the production of secondary electrons caused by the ions hitting the collector surface. The emission of these electrons is such that they contribute to the current flow in the probe circuit. Thus, a larger-than-actual ion current measurement can be erroneously made. Typical vacuum arc plasma contains ions species with charges ranging from +1 to +3 with energies ranging from 20–150 eV (Anders 2008, p. 203). These relatively low ion charge states and energies (sub-keV range) are such that secondary electrons produced by the ions hitting the collector surface were not expected to pose a significant error in ion current measurement (Anders et al. 2004). Nevertheless, a deep cup length aids the re-absorption of any secondary electrons within the collector.

Debye shielding

The effectiveness of the FC probe to reject plasma electrons can be estimated by finding the Debye length of the plasma at the probe entrance. The Debye length is a characteristic measurement of a plasma and indicates the extent to which the electric field from a charged object immersed inside the plasma is screened out by the attraction of like-

charged particles (also known as a Debye shield or sheath). This behaviour is important in FC probe design, because the hole size of the ground and bias plates must be small enough to not allow the ions from the plasma to shield out the bias plate and thus render it ineffective in repelling plasma electrons.

The Debye length can be estimated using the following formula:

$$\lambda_D = \sqrt{\frac{\epsilon_0 k_B T_e}{n_e e^2}} \tag{3.14}$$

where $\epsilon_0 \approx 8.854 \times 10^{-12}$ F/m is the permittivity of free space, k_B is the Boltzmann constant, T_e is the electron temperature within the plasma, n_e is the electron particle density and $e \approx 1.6 \times 10^{-19}$ C is the electron charge.

To find the electron (particle) density, the ion density can be first estimated using Equation 3.11, where typically $C \sim 10^{13}$ (Am)$^-1$ for copper (Anders 2008). For a measuring probe distance of 200 mm from the thruster operating with an arc current of $I = 50$ A peak, $n_p \approx 1.25 \times 10^{16}$ m^{-3}.

Assuming quasi-neutral plasma and based on the Zero-Order Model of the interelectrode plasma (Boxman et al. 1995, p. 293), the plasma and electron densities can be estimated:

$$\begin{aligned} n_p &= n_i + n_e \\ n_e &= \bar{Z} n_i \end{aligned}$$

Hence

$$n_e = \left(\frac{\bar{Z}}{\bar{Z}+1}\right) n_p \tag{3.15}$$

Assuming a typical electron temperature of 3 eV based on literature (Boxman et al. 1995, p. 286–288), and combining Equations 3.11, 3.14 and 3.15 results in a Debye length of roughly 140 μm. General practice recommends a probe hole or aperture size of ≤ 2 Debye lengths, which for this example requires a probe hole diameter of 280 μm or smaller. Therefore, the above analysis shows that the significantly larger hole size in the FC probe

presently causes the negative bias plates to be shielded by the incoming plasma and not repel plasma electrons. This means that nearly all of the electron repulsion is primarily due to the negative bias of the ion collector alone. Experimental measurements at various bias plate voltages from −60 V to +60 V confirmed that the bias plate had a weak effect on the ion current signal. However, a bias of −60 V begins to shows a small but measurable decline in ion signal.

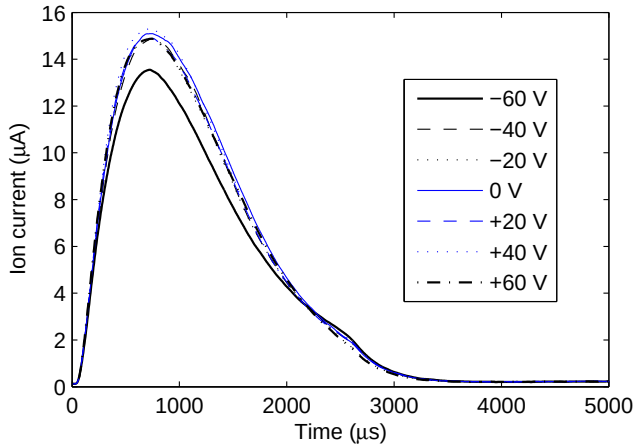

Figure 3.27: Measured FC ion current signals against varying bias plate voltages over the range −60 V to +60 V. A baseline VAT with an Fe cathode (I = 50 A pk, t_p = 2.7 ms) was used. FC probe drift length z = 230 mm.

Space-charge-limited ion current

An upper space charge limit exists for how much ion current the FC probe collector is able to capture based on the Child-Langmuir Law. For a negatively biased collector wall, the space charge limit can found with (Forrester 1988):

$$J_{cl} = \frac{I_{cl}}{A} = \frac{4}{9}\epsilon_0 \left(\frac{2e}{m_i}\right)^{1/2} \frac{V_0^{3/2}}{s^2} \tag{3.16}$$

where J_{cl} is space-charge current density limit, A is the area of the collector orifice back end face exposed to the plasma, m_i is the ion mass, V_0 is the bias potential between the anode (ground plate) and cathode (ion collector) and s is the distance between the two electrodes. Rearranging Equation 3.16 and assuming a Bi ion of mass of 208.98 amu $\equiv 3.47 \times 10^{-25}$ kg, and V_0 = 118 V, $A = \pi d^2/4$, where d = 3 mm is the orifice diameter and

s = 15.9 mm gives a worse-case scenario value of I_{cl} = 0.14 μA.

However, this value is highly pessimistic because Equation 3.16 is only applicable to the one-dimensional case of two infinite parallel electrodes spaced a fixed distance apart. For the more realistic case of a two- or three-dimensional finite electrode configuration and domain, the actual current limit has been shown in literature to be significantly larger than the one-dimensional case. For example, Bridges et al. (1965) numerically calculated the increased space-charge-limited current for a hollow tube geometry, where the plasma was constrained to travel along a drift tube between two planar electrodes and the tube walls were included as conducting elements. Extrapolating their results to the dimensions of this study's ion collector orifice hole, electrode gap and depth suggests that more realistic values of at least $I_{cl} \approx$ 33–38 μA for Bi should be expected. Table 3.2 lists revised I_{cl} results for all material elements in this study. In practice, experimentally measured peak ion currents in this work were typically found to reach nominal values of 5–10 μA and a maximum of 25 μA for extreme cases. Thus, nearly all data in this study can be safely considered to fall within space-charge-limited current values.

Table 3.2: Range of expected space-charge-limited ion currents for all materials used in this study based on revised analysis of Child-Langmuir Law by Bridges et al. (1965)

Element	**Bi**	**Cu**	**Fe**	**Al**	**C**
Mass (amu)	208.98	63.55	55.85	26.98	12.01
I_{cl} (μA)	33–38	59–69	63–73	91–106	136–158

Ion velocity measurements

Preliminary TOF tests with I = 25 A peak, 200 μs long vacuum arc pulses on a copper cathode resulted in a measured average ion velocity of 13.8 ±2 km/s, a close comparison to 13.2 km/s as measured by Anders & Yushkov (2002*b*). However, measurement difficulties experienced due to ion signal distortions and a short drift length of 200–300 mm (the largest practical drift length for the vacuum chamber) gave a measurement uncertainty of at least 15%. Furthermore, these challenges became untenable when long arc pulses were used, because the resolution limits of the oscilloscope sample were similar to or even larger than the travelling time of the plasma. Therefore, whilst basic ion velocity

measurements could be demonstrated and shown to generally agree with literature, the present FC probe and vacuum setup was found to be unsuitable to detect (with sufficient accuracy) possible changes in average ion velocities produced from the new VAT designs tested in this study.

3.5.4 Performance summary

In conclusion, the FC probe was shown to be suitable for collecting the ion currents generated by the VAT prototypes in this study. An analysis of secondary electron emission effects, plasma electron repulsion and space-charge-limited current effects shows that the FC probe operates and behaves within acceptable limits. Although the presence of signal dampening made absolute measurements difficult to accomplish, analysis showed that relative comparison of test results across different VAT tests and arc pulse conditions could still be achieved to provide valuable test results. Signals from the FC probe were sufficient to conduct ICDD measurements and therefore obtain a measure of the plasma jet shape of various VAT designs. The probe was used in conjunction with a two-axis rotation system (as described in the next section) to achieve this. The *ion charge ratio* (charge of ion current signal divided by charge of arc current pulse), was introduced in Section 2.3.2 and used in all ICDD studies as a more accurate and robust indicator of ion production.

It was clear that the FC probe design could be significantly improved and optimised to reduce circuit effects, improve ion transmission and absorption and further reduce the possibility of error from any secondary electron emission. For instance, one performance improvement could be achieved by using a grid instead of a single hole in front of the probe of sufficiently small grid hole size (e.g. ~50 μm) to effectively repel incoming plasma electrons. Also, the negative bias plate could be positioned directly in front of the ion collector to reflect secondary electrons back into the collector. The surface area and sizing of the collector could be refined to extend the range of the maximum space-charge-limited current. Finally, the drift length available in the current vacuum chamber setup used for ion velocity measurements could be extended with additional chamber modules installed onto the main chamber.

3.6 Two-axis rotation system

3.6.1 Background

One of the important characteristics of the electric thruster is the distribution or "spread" of the plasma jet as it exits the thruster and expands into the surrounding environment. In particular, the plasma jet distribution influences the level of normal thrust produced and the plasma jet's interaction with surrounding surfaces. For most thrusters, the exhaust jet is composed almost entirely of ions. With VATs, however, a significant portion of eroded cathode material can form macroparticles and neutrals. Fortunately, the situation is simplified by the fact that the momentum of these products have a negligible contribution to thrust for two reasons: (1) most of the macroparticles are ejected at steep radial angles to the cathode surface normal, and (2) they have low average velocities ($\sim$ 400 m/s) (Daalder 1976). Thus, for all intents and purposes, we assume that the thrust plume can be accurately represented by the ion plume and its distribution (commonly referred to as the ion current density distribution or ICDD).

ICDD capture methods

In order to measure the ICDD, a common method is to capture ion current signals from a single or several Faraday probe(s) at various relative angles to the head of the thruster under study (see Table 3.3 for some examples). Within the test domain, the Z axis is generally defined along the centreline of the thruster (or normal thruster axis). Visual inspection of the VAT plume can also be done using high-speed cameras (Pietzka et al. 2011). However, optical methods are especially challenging for studying vacuum arc plasmas since the cathode spot(s) are a strong source of light emission and optical systems are often costly and complex to handle. Thus, for simplicity, feasibility and cost, we adopted the ion collection via probe method. A comparison and analysis of different ICDD measurement rig solutions in Table 3.3 was performed. Method 3 was found to be the most feasible and suitable to achieving the study's objectives within the constraints of the present vacuum chamber setup.

Table 3.3: Comparison of ICDD capture methods using Faraday probes

	Method 1	**Method 2**	**Method 3**
Description	Move a single probe or probe array relative to the fixed thruster in Cartesian co-ordinates	Move a single probe or probe array relative to the fixed thruster in Polar co-ordinates	Move the thruster relative to a fixed single probe in Polar co-ordinates
Example	Zhuang et al. (2009)	Walker (2005)	Sekerak (2005)
Probe config.	Linear array	Curved array	Single
Thruster	Vacuum arc thruster	Hall Thruster	Vacuum arc thruster
Motion	Z axis	Yaw axis	Yaw & Z axis
Advantages	Actuation requirements are less demanding; large, heavy thrusters can be easily tested	Probe always faces thruster; large, heavy thrusters can be easily tested	Mechanically simple; uses least chamber volume
Disadvantages	Decreasing viewing angle of plume as probe array moves further from thruster; large test area needed; inclination of probe face(s) with respect to thruster face must be considered	Large test area needed; mechanically challenging to move probe in more than one rotational axis	Limited thruster sizes and masses

In this study, emphasis was placed on measuring VAT plume ICDDs with greater fidelity than had been previously done before. This was achieved by taking ICDD measurements in two dimensions, thereby allowing the symmetry of the plume to be more accurately assessed. Based on knowledge of the plume shape, the direction of the force (also known as thrust vector) being produced by the VAT can be properly determined. This is an important performance characteristic for VATs, which may not necessarily produce thrust exactly along the centreline of the thruster. Knowledge of the thrust vector gives an indication of the pointing accuracy of a spacecraft and its effects on the spacecraft's attitude (e.g. residual moment forces).

Thrust vector

The thrust vector is defined as the force magnitude and direction comprised of the sum total of all directed ion momentum, taking into account all radial and normally-directed force components. For all cases studied here, this is equivalent to the vector sum of the pitch and yaw components of peak measured ion flow.

Figure 3.28 illustrates the thrust vector diagram and its components. Detailed calculation of the thrust vector is found in Appendix C.1, resulting in the following expressions for the thrust vector (absolute) magnitude C and deviation angle from normal β_T:

$$C \sin \beta_T = \sqrt{A^2 \sin^2 \beta_y + B^2 \sin^2 \beta_p} \tag{3.17}$$

$$\tan^2 \beta_T = \tan^2 \beta_y + \tan^2 \beta_p \tag{3.18}$$

where A and B are the respective yaw and pitch magnitudes and β_y and β_p are the respective yaw and pitch deviation angles of peak ion flow measured in their respective planes.

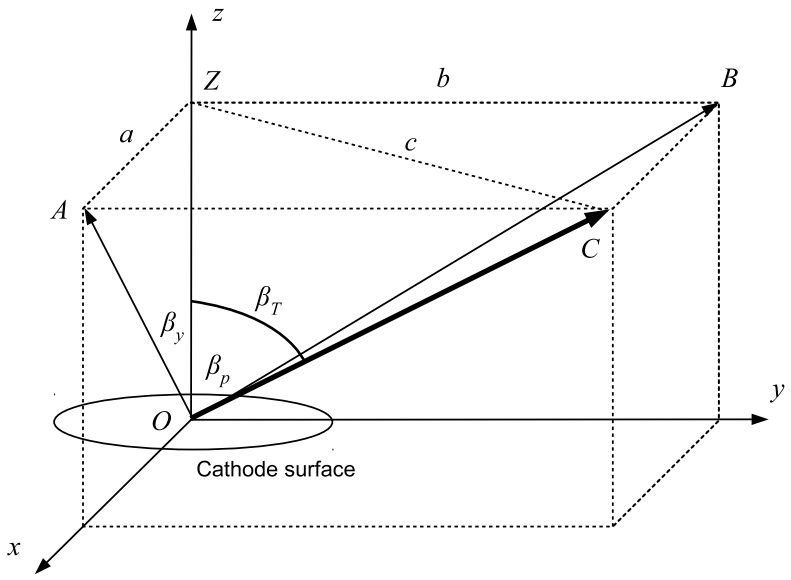

Figure 3.28: Vector diagram of thrust vector comprised of yaw and pitch components.

3.6.2 Description of ICDD capture system

Expanding on Sekerak's (2005) approach and based on the popular use of mechanical stings in aerodynamic wind tunnel testing, a custom-built Two-Axis Rotation System (TARS) based on Method 3 (as defined by Table 3.3) was developed. Figures 3.29 and 3.30 show a photograph and schematic of the TARS and FC probe that comprises the entire ICDD setup within the chamber. The TARS provides full and combined ±90° pitch and yaw motion of a mounted thruster assembly relative to a fixed ion probe in such a way that the point distance between the thruster head centre point and the probe entrance remains constant at all angles of rotation. Appendix C.2 contains details on finding the thruster assembly's true orientation angle. Currently, Z axis positioning of the probe must be performed manually by the user, but the system can easily accommodate future upgrades such that the ion probe can be remotely actuated with a linear mechanical feedthrough or guide. Thus, the ICDD capture system has the potential to perform full three-dimensional plume characterization of single or multiple thruster assemblies.

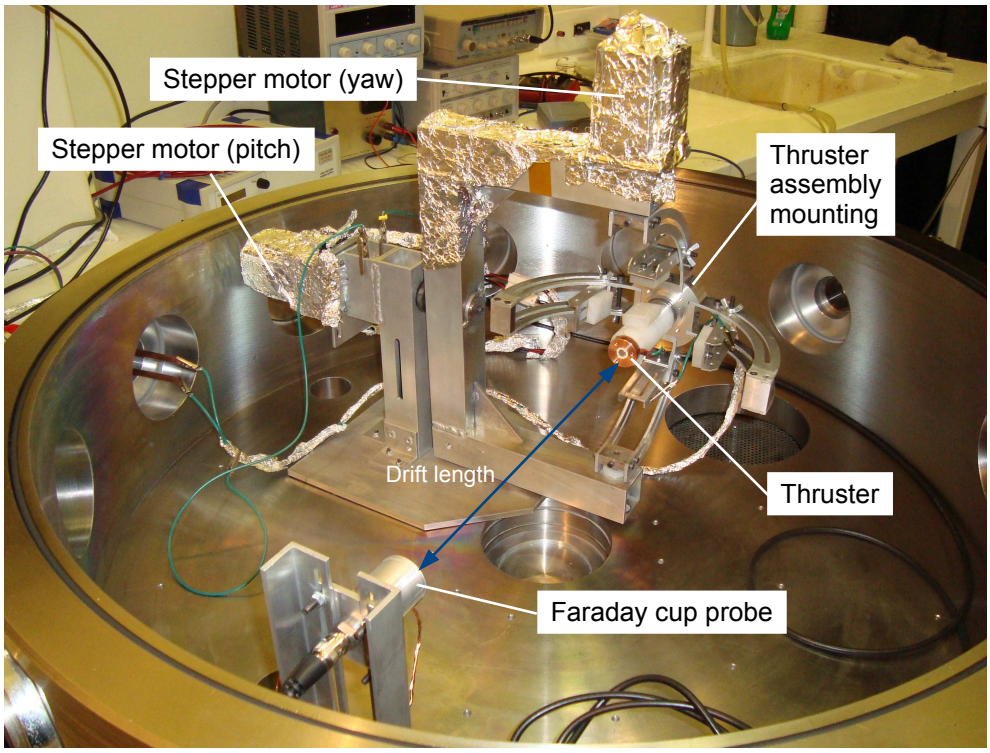

Figure 3.29: Photograph of ICDD capture system with TARS rig and Faraday cup probe. VAT prototype is centrally mounted to TARS frame.

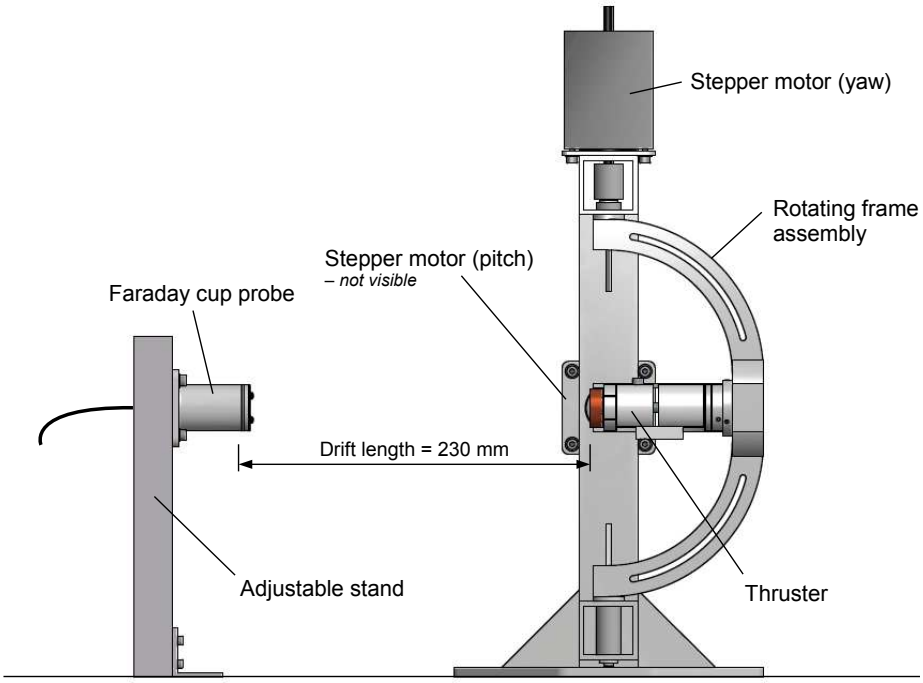

Figure 3.30: Schematic side view of ICDD measuring setup with TARS and Faraday cup probe arrangement as used in this work.

Specific technical challenges encountered whilst designing the system was the ability to remotely provide a high-torque solution with good angular resolution and accuracy, mitigating the negative effects of thruster EMI on the control system, and successfully operating within the volume constraints of the vacuum chamber. The TARS structural frame was made primarily of aluminium, the shaft components made of shaft steel and the bushings made of Vesconite polymer and UHMW-Polyethylene plastic for low rotational friction. The maximum allowable total thruster assembly mass on the frame is 2 kg. Each of the two rotating axes were powered by a Bipolar 4-lead 2.8 A Fulling stepper motor, providing a standalone maximum holding torque of 1.85 Nm and a step resolution of 1.8°. A 7.5 ratio gearbox was attached to the pitch motor to provide additional turning torque required for the frame. A counterweight was included to balance the frame and reduce torque loads. Each stepper motor was powered by an actively-cooled modified 2.8 A dual H-bridge driver circuit from Rugged Circuits LLC, which in turn was controlled by an Arduino MEGA 2560 micro-controller connected via USB to a control PC.

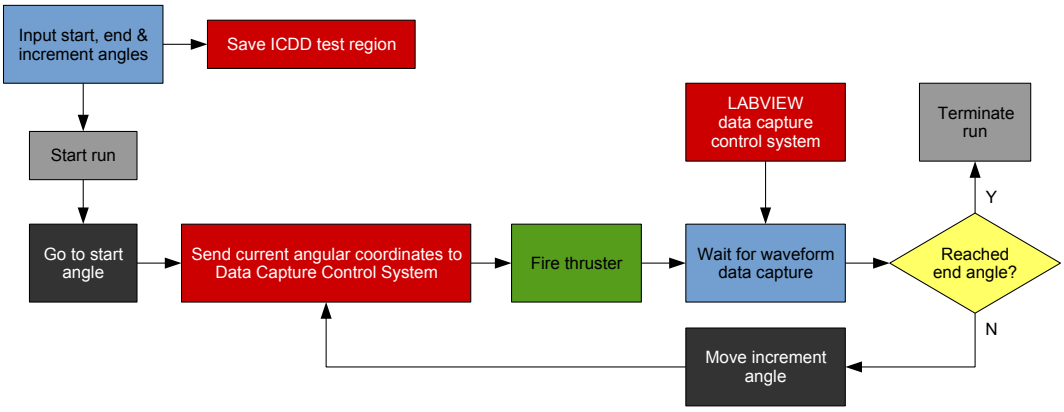

Figure 3.31: Process flow chart of TARS stepper motor control system

A standalone motor control application was developed in Microsoft Visual Studio to provide a convenient means of manually or automatically controlling the orientation of the thruster assembly for data capture (process flow chart in Figure 3.31). Starting and ending locations can be independently specified as well as the increment of angle rotations. For simplicity of control, angular increments were set to a fixed multiple of a complete 4-stage rotation of each stepper motor, i.e. for yaw, $1 \times 4(1.8) = 7.2°$ or $2 \times 4(1.8) = 14.4°$ and for pitch, $10 \times 4(1.8/7.5) = 9.6°$ or $20 \times 4(1.8/7.5) = 19.2°$. This approach always ensured that the thruster assembly's position did not go out of phase with its tare position.

A feedback checking subroutine was also put in place to prevent any TARS motion until the thruster firing sequence and FC probe data collection by the LABVIEW data capture program had been completed for a particular position. A functional diagram of the ICDD measurement system is illustrated in Figure 3.32.

Finally, it was found at times that EMI caused by the VAT and its pulse circuit could affect the TARS actuation and control system and cause the controller and data-acquisition programs to crash mid-test. Hence, analogue common mode filters were installed throughout the system to successfully attenuate high frequency noise.

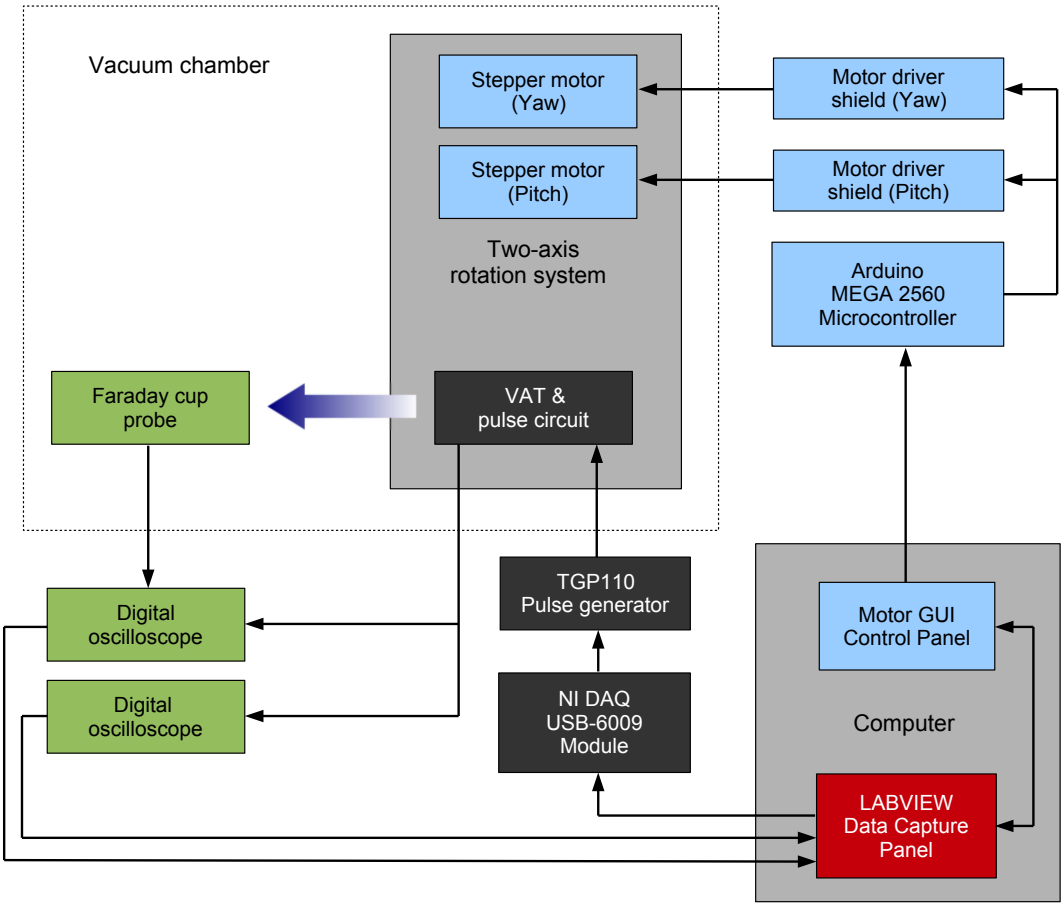

Figure 3.32: Functional diagram of ICDD measuring system

3.6.3 Commissioning & verification

Thruster Positioning

A verification test for each motor was performed in order to determine the positioning accuracy of the system. The angular position of the thruster arm frame was measured using a digital level (accuracy ±0.1°) for a range of yaw and pitch angles at two different worst-case loading scenarios. All load cases include a single thruster installed at the frame's central mounting position and the motors operating conservatively at about 70% torque capacity (the current-carrying capacity of the driver circuits limits the motor torque to approximately 90% of its maximum rating).

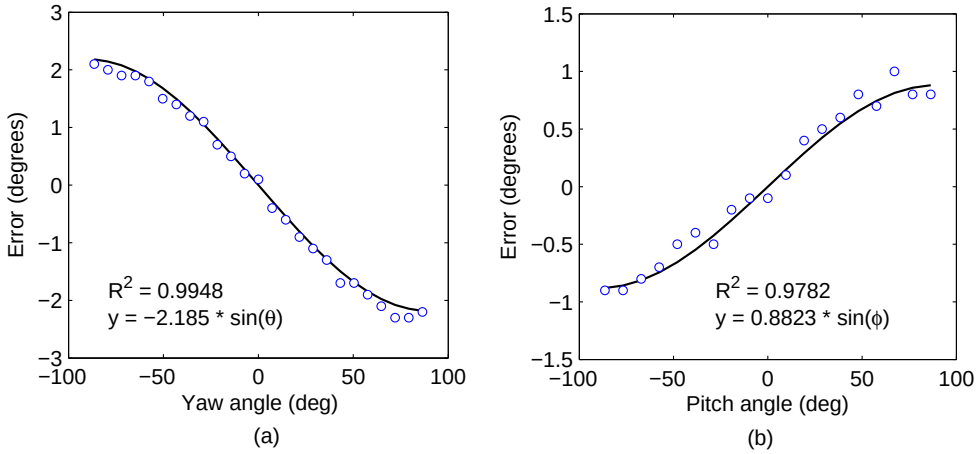

Figure 3.33: Range of alignment errors over (a) yaw and (b) pitch angles for worse-case scenario TARS thruster assembly positions. Data curves best fit to sinusoidal function. Pitch error due to gearbox teeth play is not shown here.

The first load case was performed where the yaw motor experiences the greatest moment arm due to the thruster and arm frame, that is, when the system is pitched at −90° (+90° will also produce the same loading scenario). Figure 3.33a presents the error measured between the desired and actual yaw angles. Error behaviour can be explained by the fact that the weight of the thruster and arm frame produces a moment arm on the yaw motor shaft, which is only constrained to rotate by the magnetic field in the motor coils. Thus, the greater the moment arm, the more the shaft angular position will shift out of alignment. Further evidence for this is given by the sinusoidal nature of the errors, which is precisely expected for a static weight whose moment arm varies with inclina-

tion according to basic vector geometry. According to manufacturer specifications, the stepper motor is able to provide an angular tolerance of 0.1° with no load. With the load case included, the yaw angle error range extends up to 2.2° maximum.

The second load case was performed where the pitch motor experiences the greatest moment arm due to the thruster and arm frame, that is, when the arc frame is at zero yaw position. Figure 3.33b presents the error measured between the desired and actual pitch angles. The pitch error also follows the yaw error in a similar sinusoidal fashion. However, the gearbox on the pitch motor contributes a larger overall error as well as a bias error due to play between gear teeth in the pitch motor's gearbox. This bias error comes into effect whenever a change in pitch direction occurs. Thus, a conservative pitch error of 1.6° was assigned for all pitch angles including a shift of −2.5° to account for the bias error occurring during the ICDD capture procedure's pitch manoeuvre.

Probe positioning

As shown in Figure 3.30, the ICDD capture system was arranged such that the Faraday cup probe was located at a fixed distance from the thruster head. The probe distance had to be carefully chosen to ensure that an ion signal of sufficient magnitude could be received by the probe at all test angles. This was done so that background noise or equipment resolution limits did not become significant for the smallest signals. In addition, a limitation was also placed on how large an expected signal could be received so that the voltage drop across the terminating resistor remained no more than 15% of the negative bias of the ion collector. Thus, the probe was placed at least 200 mm away to allow a maximum voltage signal of no more than 18 V. This probe distance also ensured that the probe's presence did not significantly distort the plasma jet emitted and influence test results.

The probe position used for ICDD tests was nominally set at 230±0.5 mm, which was defined as the distance from the tip of the VAT to the tip of the ion collector housed within the FC probe. Alignment of the probe with respect to the zero position of the thruster was performed manually using a ruler as guide with an estimated pointing angle accuracy of

$\sim 0.25°$. These probe positioning errors were considered small enough to be excluded from the ICDD analysis.

3.6.4 ICDD data capture & analysis

Data collection & processing

ICDD data was typically captured over a pitch angle range of $\pm 76.8°$ in increments of $9.6°$, and yaw angle range of $\pm 86.4°$ in increments of $7.2°$ or $14.4°$. At each angular position, 10–20 samples for arc current, arc voltage and ion current were captured and processed. This relatively modest number of samples was chosen to limit the amount of cathode erosion taking place such that changes to cathode geometry did not adversely affect the captured ICDD. Ion charge ratio values were calculated and aggregated into a single representative mean value (with 95% confidence level bounds) for each position. To remove any outliers, Peirce's Criterion was applied to each $\bar{J}$ data set.

Surface fitting

A least squares method was used to find the best type of distribution to surface fit the plume data. For data sets with only one pitch or yaw range captured, a curve fit algorithm was implemented instead. Due to the non-linear nature of the data fit, the Levenberg-Marquardt regression fit solver was used in this study. Test data was normalized for a probe distance $z = l = 1$ and for an arc current $J.dA = 1$. This generalized the data such that the distribution fit could be applied for all probe distances and arc current values.

Four types of distributions were assessed to fit $\bar{J}$ test data in each axis in the following manner:

For an Exponential distribution,

$$\bar{J} = \frac{2}{\sqrt{\pi} l^2 k \operatorname{erf}(2\pi/k)} \exp\left(-\left[2\pi\left(1-\cos\left(\phi-\phi_e\right)\right)\right]^2/k^2\right) \tag{3.19}$$

For a Cosine distribution,

$$\bar{J} = \frac{\cos\left(\phi-\phi_e\right)}{\pi l^2} \tag{3.20}$$

For a Gaussian distribution,

$$\bar{J} = \frac{1}{\pi l^2} \exp\left(-\frac{\left(\phi-\phi_e\right)^2}{2w^2}\right) \tag{3.21}$$

For a Parabolic distribution,

$$\bar{J} = \frac{1}{\pi l^2}\left(1-\left|\phi-\phi_e\right|\right)^{\gamma_1/\gamma_2} \tag{3.22}$$

where k, w, γ_1 and γ_2 are distribution-specific parameters or spread factors describing the shape of that distribution, ϕ is the divergence angle (in pitch or yaw) and ϕ_e is the deviation angle of ϕ to the normal axis, i.e. centreline of the thruster head.

Cosine is the most efficient and ideal plume spatial distribution with the ions travelling with equal rates uniformly in all directions. However, other distributions like Exponential and Gaussian are considered in order to take into account observations in literature and this work that some ion flux is present at high angles ($> 80°$) to the cathode surface normal (e.g. see Polk et al. (2008)) and that the cathode spots move around on the cathode surface (i.e. the ion source is not a perfectly small and stationary point).

Figure 3.34 provides an example of average $\bar{J}$ values over the test range of ICDD capture with various distribution surface fits for comparison. Each fit assessment produced a set of goodness-of-fit results comparing each fit to test data (see Table 3.4). The two statistical indicators used for comparisons were the R^2 value and Root Mean Square Error

(RMSE). The best fit is the one with an R^2 value closest to one and a RMSE closest to zero.

Table 3.4: Surface fitting results for the example shown in Figure3.34. Spread factors, pitch and yaw absolute deviation angles, and goodness-of-fit indicators for each distribution type are listed. The Gaussian distribution is shown to be the best fit in this example (highlighted in grey).

Fit	**Spread factor(s)**	β_p (deg)	β_y (deg)	R^2	**RMSE**
Exponential	4.066 ±0.210	3.3 ±3.2	0.8 ±3.8	0.929	0.023
Cosine	–	2.9 ±2.5	0.3 ±2.7	0.954	0.019
Gaussian	1.197 ±0.032	4.6 ±1.9	0.7 ±2.2	0.982	0.012
Parabolic	1.316 ±0.112, 2.068 ±0.081	4.0 ±2.1	0.6 ±2.3	0.975	0.013

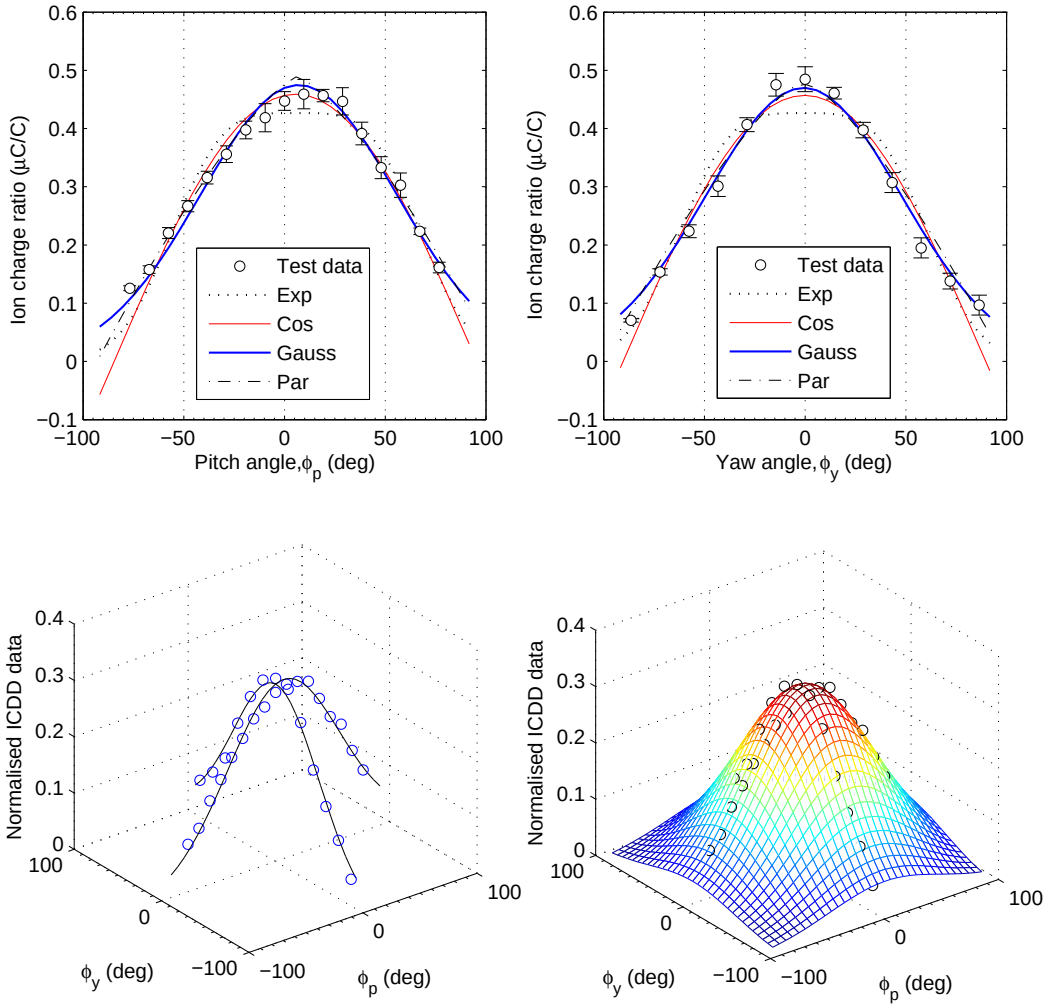

Figure 3.34: Surface fit of ICDD test data with various distribution fits shown for comparison. Test data shown here is for a baseline VAT operating with a Fe cathode (50 A pk, 2.7 ms, 3 Hz, 7.5 W) and a FC probe distance of z = 230 mm. Twenty samples per pitch and yaw angle were taken. Best fit is a Gaussian distribution of spread factor w = 1.197 ±0.032 (R^2 = 0.982, RMSE = 0.012).

Thrust correction factor

The thrust correction factor C_T considers the effect that the ICDD and electrode geometry have on normally-directed thrust. This is because the divergence of the plume and any interference of the electrode surfaces to the ejected ions causes a reduction in thrust. Hence, the larger the value of C_T, the greater the thrust level produced by the VAT. An alternative approach to Sekerak's (2005) derivation of the thrust correction factor was developed in this study and is described in Appendix B. The assumption is made that the average ion charge state and the average ion velocity of the plasma jet plume are spatially uniform. Therefore, only the ion mass flow is considered to affect C_T. Figure 3.35 defines the C_T problem domain based on the VAT electrode geometry. The resulting generalised expression of C_T for any arbitrary $\bar{J}$ distribution is as follows:

$$C_T = \frac{\bar{L}^2}{\pi} \int_0^{2\pi} \int_0^{2\pi} \int_0^{\bar{r}_a} \int_0^{1} \bar{J} \frac{1}{\bar{l}^2} \, dA_1 \, dA_2 \tag{3.23}$$

where

$$\bar{L} = L/r_c \tag{3.24}$$

$$\bar{r}_a = r_a/r_c \tag{3.25}$$

$$\bar{l}^2 = \bar{L}^2 + \bar{r}_1^2 + \bar{r}_2^2 - 2\bar{r}_1\bar{r}_2\cos(\theta_1 - \theta_2) \tag{3.26}$$

$$dA_1\,dA_2 = \bar{r}_1\bar{r}_2 d\bar{r}_1 d\bar{r}_2 d\theta_1 d\theta_2 \tag{3.27}$$

and $\bar{r}_1, \bar{r}_2$ are radial vectors along the cathode surface and anode exit surface as shown in Figure 3.35.

The value of C_T was numerically solved using a combination of Adaptive Simpson quadrature and trapezoidal integration (implemented in MATLAB), where inputs of thruster geometry and the ICDD fit parameters were used (for the example in Figure 3.34, r_c = 6.35 mm, $\bar{r}_a$ = 1.58 and $\bar{L}$ = 0.16). However, finding the uncertainty of C_T was not straightforward, given that C_T depended on an analytical expression of the ICDD via a complex

quadruple integral. Sources of uncertainty originated from (1) pitch and yaw angular positions, (2) noisy arc behaviour, which influenced $\bar{J}$ and (3) uncertainty of the ICDD distribution-specific spread factor. Thus, a numerical solution was sought.

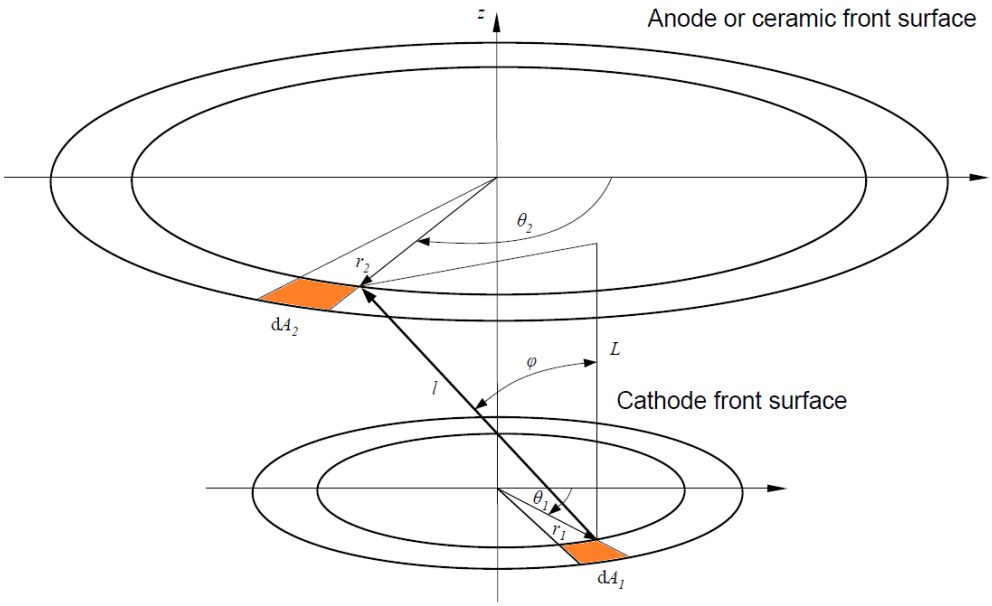

Figure 3.35: Problem geometry and variable definitions used for calculating C_T. Adapted from Sekerak (2005).

The Monte Carlo simulation technique was used to determine the effect of all uncertainties on C_T and the thrust vector by generating pseudo-random $\bar{J}$ data (mean value and angle position) that followed the same assumed statistical behaviour of the actual experimental data measured, i.e. a Normal distribution. A total of 251 random test runs were generated and fitted, resulting in a simulated uncertainty of the ICDD spread factor and deviation angles from actual test data measurement uncertainties and test sampling limits. A comparison between simulated and actual uncertainties were made, with the larger of the two values being the final uncertainty for the relevant parameter. The worst-case ICDD spread factor uncertainty was subsequently used to calculate the final uncertainty of C_T. The worst-case combination of pitch and yaw deviation angles (positive or negative) were used to find the final thrust vector deviation angle uncertainty. Thus, for the example shown in Figure 3.34, a final result of $C_T = 0.637 \pm 0.0132$ and $\beta_T = 4.7° \pm 1.7°$ was produced. Typical uncertainties for C_T in this study were 5% when only axis was measured and 1–2% when two axes were measured. Uncertainties for β_T typically ranged from $\pm 1.5°$ to $\pm 6°$.

3.6.5 Performance summary

A suitable ICDD capture technique was developed for this work, where a TARS actuation system was designed, built and tested to provide acceptable range (±90°) and accuracy (≤ ±2.2°) for all thruster assembly load cases. Used in conjunction with the FC probe, the ICDD of VAT plasma plumes could be automatically captured and processed with various control systems and data processing techniques with higher fidelity than previously accomplished. Resulting thrust correction factors were obtained with good accuracy for this work (2–5%). However, thrust vector deviation angle accuracy was moderate (±1.5–6°) due to the limited accuracy of the TARS' stepper motors (especially the pitch motor) and the limited number of test samples that could be captured.

3.7 Ion collector

3.7.1 Background

The ion collector is simply an electrically conductive metal enclosure that receives the ion flux travelling outward from the thruster, with the goal of determining the total ion current emitted by the VAT. Based on the same working principle as the FC probe, the captured ions induce current flow within the ion collector circuit, which is subsequently measured across a terminating resistor. The ion collector is negatively biased to repel the incoming plasma electron flux. The ion collector in various forms has been widely used in literature (e.g. Kimblin (1971), Anders et al. (2005)).

3.7.2 Description

Design specifications for the ion collector as depicted in Figure 3.36, are as follows:

- The collector's circular walls and dome were made of 0.9 mm thick aluminium sheeting. Sections were joined together with conductive copper foil and Kapton tape.
- The ion collector was negatively biased to −60 V with a standard DC power supply to repel plasma electrons.
- The ion collector was sized in order to mitigate the possibility of discharges between the thruster and the collector. Thus, the collector walls were designed to be at least 220 mm away from the thruster head, which was located at the centre of the collector cavity.
- BNC cabling and connectors were used to connect various portions of the ion collector and its circuitry.

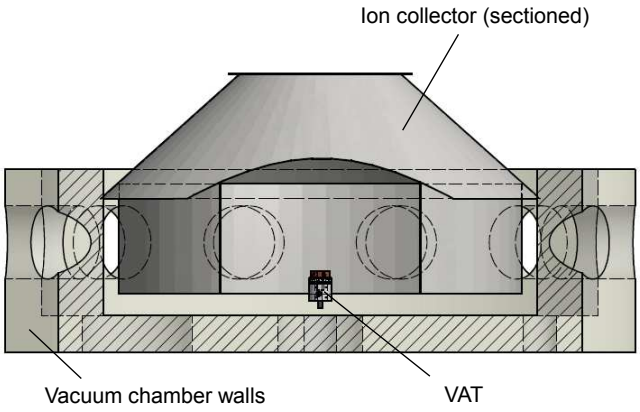

Figure 3.36: Sectioned view of ion collector enclosure for measuring total ion-to-arc current ratio. Enclosure is suspended and isolated from vacuum chamber with plastic blocks (not shown here). Thrusters are positioned in the centre of the enclosure to ensure total and uniform collection.

3.7.3 Signal measurement and verification

As explained in Chapter 2.3.1, the ion-to-arc current ratio is roughly 10% for most cathode materials across a wide range of arc currents. Thus, for a peak arc current of 50 A, a total ion current peak of ~ 5 A was expected to be detected by the ion collector. A terminating resistor value of 2.65 ±0.01 Ω was used to ensure a reasonable voltage drop of roughly 10 V across the resistor. Figure 3.37 shows ion-to-arc current ratio measurements obtained at various bias voltages (from −60 V to +20 V). A bias voltage of −60 V is

shown to achieve full repulsion of plasma electrons. To account for the stochastic nature of ion production, forty samples of ion current were taken for each test and aggregated to produce a smoothed result. Since the ion-to-arc current ratio ϵ was the final parameter desired, the total charge delivered to the VAT and detected by the collector was used to find this value (see discussion of ion charge ratio in Section 2.3.2).

3.8 Erosion rate measurement

3.8.1 Background

Fuel consumption of the VAT is generally defined as the rate at which cathode material is eroded during thruster operation. The most common means of measurement in literature is the cathode weight loss method. Boxman et al. (1995, p. 122–124) also discuss other methods such as measuring the total ion current and ion charge number to find the ion erosion rate, imaging and calculating the volume of craters left on the cathode surface, or measuring changes to the cathode geometry. The weight loss method is a more conservative and robust means of determining the cathode erosion rate because it takes into account the full range of particles (ions, neutrals and macroparticles) emitted from the fuel rod itself. However, long test times or many pulse firings are required to gener-

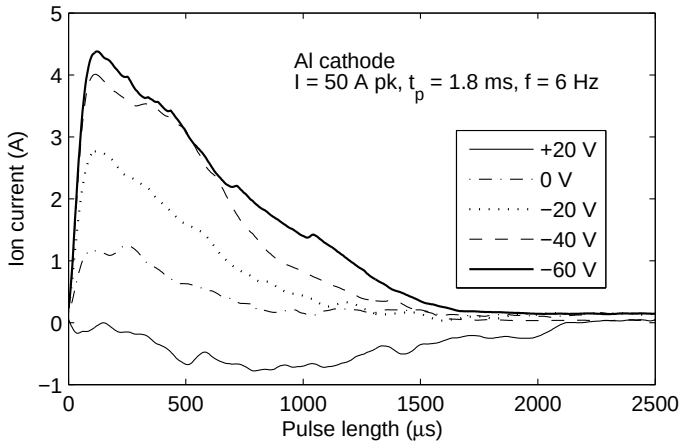

Figure 3.37: Measurement of ion current signal emitted from a baseline VAT taken at various ion collector bias voltages from −60 V to +20 V. Negative ion current signal at +20 V clearly depicts non-repulsion of plasma electrons.

ate an accurate result and the erosion rate values are time-averaged. Measurement error due to deposition of particles on nearby thruster components and surfaces is avoided by weighing only the cathode and not the entire thruster.

In the weight loss method, the difference in cathode mass Δm before and after a set period of thruster operation is measured. In addition, the total cumulative amount of pulse charge $\sum Q$ that is delivered to the thruster during the test is also recorded. Using both sets of measured values, the cathode erosion rate can be formulated as

$$E_r = \frac{\Delta m}{\sum Q} \tag{3.28}$$

which was introduced earlier in Chapter 2 as Equation 2.4. The parameter E_r (normally in units of μg/C) is a convenient way for comparing the erosion rate of the cathode across different thruster pulsed operating conditions of arc current, pulse length, pulse frequency and average power level.

The total cumulative pulse charge is

$$\sum Q = \bar{I} t_p f \Delta t \tag{3.29}$$

where Δt is the total operating time of the thruster (or test time). Finally, the mass flow rate of the VAT (in kg/s) can also be found by simply multiplying E_r with the average pulse arc current and thruster duty cycle:

$$\dot{m} = E_r \bar{I} \left(t_p f \right) \tag{3.30}$$

3.8.2 Description of erosion measurement technique

A typical erosion test in this study consisted of the following features:

- Before an erosion test, each thruster and its cathode rod was prepared and reset to "new" thruster conditions.
- Cathode mass measurements were performed with an analytical mass balance (Pioneer PA214, ±0.1 mg resolution) before and after each erosion test. Care was taken to ensure a clean cathode rod was carefully inserted into the VAT assembly prior to testing and gently removed from the VAT assembly at the end of the test. This ensured as small mass errors as possible due to cathode handling.
- All tests were conducted with thrusters initially at room temperature (roughly 20° C).
- The VAT was sometimes initially fired for 30–200 pulses depending on the cathode material to "burn-in" the thruster and ensure proper initiation of the thruster. This initial amount of released charge contributed a small but insignificant error to the total value of $\sum Q$ ($\leq$ 0.5–1%).
- The VAT was operated continuously for several thousand pulses – sometimes for as much as 100 C of total pulse charge delivered. This ensured that enough material was eroded for good test accuracy and the thruster operated with realistic and steady heating conditions for an extended period of time. Cathode erosion was also limited such that the changing cathode geometry did not affect the overall thruster geometry and operating conditions in a significant manner. For example, the locally-eroding portion of the cathode surface began to recede into the thruster head after 80–100 C.
- Between 100–300 pulse waveform samples were captured in a single test, appropriately consolidated and weight-averaged to find the total cumulative pulse charge $\sum Q$. Since the present test method made a time-averaged calculation of E_r, only average values of I and t_p were used to find E_r. Thus, only the uncertainties of f, Δt and Δm were considered in the final uncertainty analysis of E_r (typically 2–4% error). The nominal ranges of uncertainty for each parameter in this study is listed in Table 3.5 below.

Table 3.5: Range of typical values and uncertainties for f, Δt and Δm in this work's erosion studies and their effect on final E_r uncertainty

Parameter	**Nom. values**	**Uncertainty**	**Effect on E_r uncertainty**
Mass loss, Δm (mg)	2–100	±0.1	Strong
Pulse frequency, f (Hz)	2–10	±0.1–0.001	Medium
Total test time, Δt (s)	250–3000	±1–5	Weak

Chapter 4

Thruster design, behaviour & performance evaluation

4.1 Introduction

Detailed descriptions of the baseline VAT's design, development, verification and evaluation are presented here. Key lifetime tests are conducted on VAT prototypes with three different cathode materials to study and characterise the behaviour and performance of the baseline VAT design and assess its suitability as a reference thruster. Various equipment, methods and analyses are used to demonstrate and achieve testing of the baseline VATs, thereby establishing suitable application towards later studies.

4.2 Thruster description

4.2.1 Electrode design

The basic vacuum arc thruster design is comprised of an anode, cathode, insulator and

arc initiation mechanism and arc driving mechanism (pulsed power circuit). VAT thrusters have traditionally adopted a coaxial design with a central cathode rod surrounded by a ceramic tube and an outer anode ring or cylinder, e.g. Gilmour & Lockwood (1972), Schein et al. (2002a) and Polk et al. (2008). Other electrode configurations tested include planar block (Lun 2009) and annular tube (Zhuang et al. 2009) designs. Figure 4.1 illustrates some of the electrode configurations available in coaxial and planar geometries. Each design type possesses characteristic strengths and weaknesses. For example, rod and tube designs as shown in Figures 4.1a–b are easier to manufacture, but cannot incorporate a cathode feeding mechanism as easily as the annular design shown in Figure 4.1c. On the other hand, the annular design suffers from lower thrust values due to the cathode being receded into the thruster body. It was decided early on in the project that the baseline thruster should follow a design that could be easily compared to existing experimental and theoretical VAT models. Thus, the standard coaxial rod electrode design which has been extensively studied and characterised in literature, was implemented. In addition, the symmetrical nature of a coaxial design along the thruster centreline simplifies analysis of the jet plume.

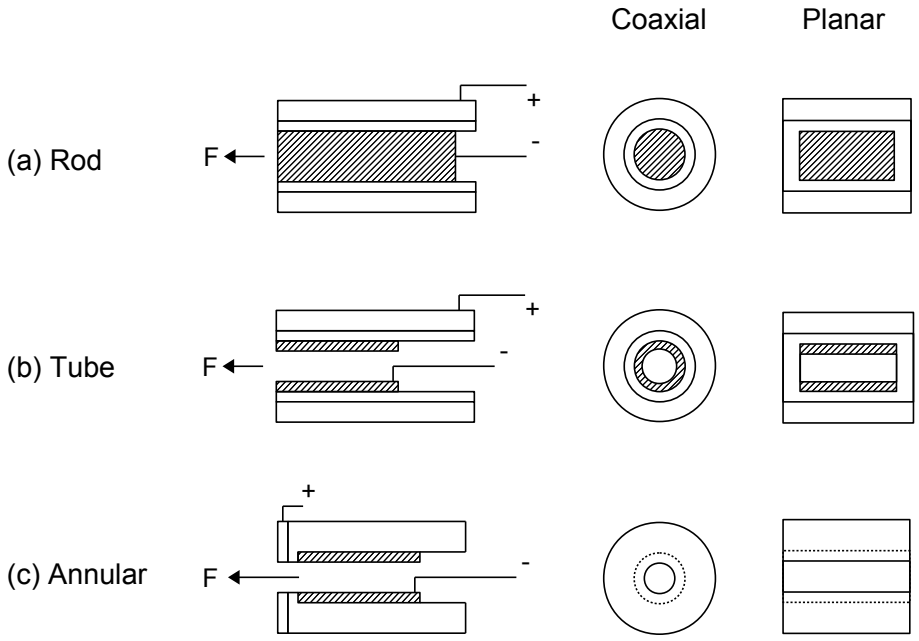

Figure 4.1: Illustrated matrix of (a) rod, (b) tube and (c) annular VAT electrode designs in both coaxial and planar format (based on Lun (2009)).

The main requirements of the thruster design were simple and repeatable manufacture, use of low-cost, commercially available, high-vacuum compatible materials and use of standard sizes (see Table 4.1). The main drivers of the thruster size were found to be the

commercial availability of compatible cathode material rod sizes and insulator tube diameters as well as repeatable and accurate manufacture of thruster components. Larger-sized cathodes (e.g. 6 mm diameter) enable different cathode shapes to be practically made and tested as well as allow the VATs to experience a wider range of heat power levels compared to the earlier and more common cathode diameter of 3.18 mm. For simplicity, no cathode feeding mechanism was implemented in this work. All prototypes were constructed by the workshop at the School of Mechanical, Industrial and Aeronautical Engineering.

Table 4.1: Major VAT design requirements and constraints

Requirement/constraint	**Description**
Mass and size	Should be of a size not too dissimilar to actual flight hardware, but large enough for easy handling and modification
Modularity	Should easily accommodate different anode designs and insulator tube sizes
Safety	Must not pose a health or operational hazard to personnel and nearby equipment
Systems integration	Must be simple to mount onto diagnostic equipment in a variety of orientations
Cost	Should be of relatively low cost to allow several prototypes to be built
Manufacture and materials	Limited to commercially available products and local manufacturing capabilities; simple to repair and modify

After a number of design iterations and preliminary tests, the final form of the reference VAT as shown in Figure 4.2 was finalised to the following material and size specifications:

- All cathodes were rods of 6 or 6.35 mm diameter and an initial length of 50 mm.
- The anode is comprised of a 25 mm OD, 10 mm ID, 8 mm long copper cylinder to help absorb and dissipate the thermal load. The anode can be located flush or slightly protruded at the front of the thruster. In all test cases in this work, the anode was normally situated 0.5 mm above the cathode surface unless otherwise stated.
- The insulator is made of an alumina tube of 10 mm OD, 6 or 6.35 mm ID and 25 mm length. Alumina ceramic has become the standard material of choice for use

in vacuum arc research given its exceptional thermal-resistance and electric insulation strength. Unless otherwise stated, all tests in this work had the insulator tube mounted 0–0.25 mm below the cathode to ensure good contact of the conducting film with the cathode.

- The thruster housing is made of ultra-high molecular weight polyethylene (UHMW-PE), which is easy to machine, vacuum-friendly, of low cost and has a higher mechanical strength than many other vacuum-compatible plastics. Allowance was made for convenient mounting of the VATs to a flat surface or plate and easy replacement of individual thruster components. The housing also offers high electrical insulation between any relevant electrically-conducting parts.
- Overall, the VAT baseline design occupies a volume of 30 mm dia × 50 mm length, with an approximate mass of 60 grams.

4.2.2 Arc initiation mechanism

A vacuum arc pulse can be initiated between the anode and cathode by several means. A common method is to create a high voltage spike between the electrodes, creating a conductive bridge for the arc current to flow. Unfortunately, the dielectric breakdown limit is very high (10's of kV) for high vacuum conditions and can require costly and sizeable HV power units. To address this, alternative techniques for arc triggering including mechanical triggering, laser ablation and gas ignition have been explored (Anders et al. 1998). These methods are either complex to implement or produce too few pulses ($\sim 10^3$) suitable for regular VAT operation and testing ($\geq 10^4$).

Eventually, Gilmour & Lockwood (1972) and Anders et al. (1998) developed a novel vacuum arc initiation technique that applied a thin conducting film on the ceramic surface between the anode and cathode electrodes. This "triggerless" arc initiation technique has the effect of creating a very small gap which can be traversed by a lower voltage spike or, in some cases, even short-circuit the electrodes. Given a sufficiently high initial arc current, microscopic portions of the film experience high field emission and Ohmic or Joule heating to vapourise. The vapourised material provides an initial conducting

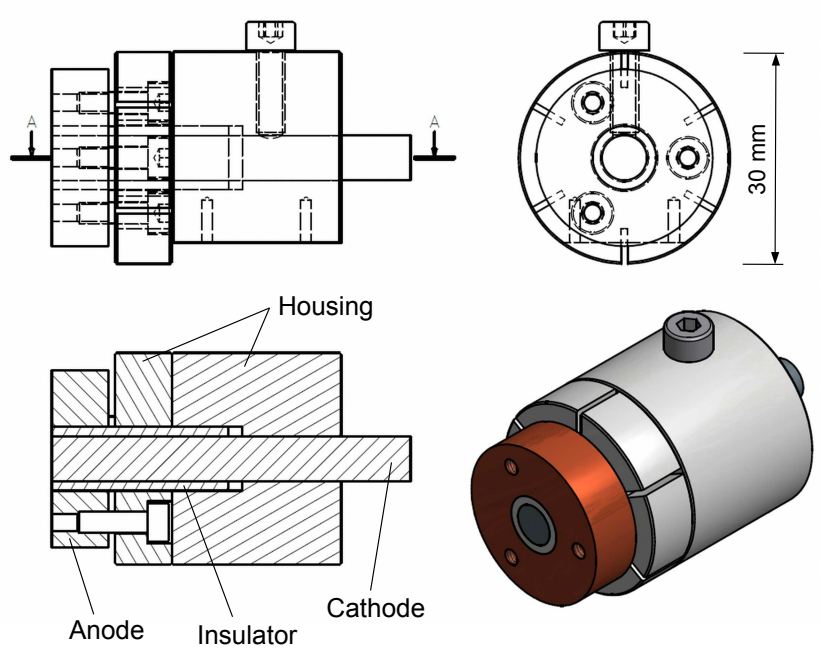

(a)



(b)

Figure 4.2: (a) Engineering model drawings and (b) photographs of baseline/reference VAT design.

bridge between the electrodes for the rest of the arc current to flow and the vacuum arc is ignited. Each time the arc pulse fires, the conducting film will partially dissipate due to the localised thermal load and the explosive nature of the arc. However, the erosion of the cathode causes some ejected molten particles to deposit back onto the insulator. This replenishes and maintains the film for subsequent pulse firings. Graphite or metal powder is typically used as a suitable film material. In this work, a number of film materials and film manufacturing techniques were tested.

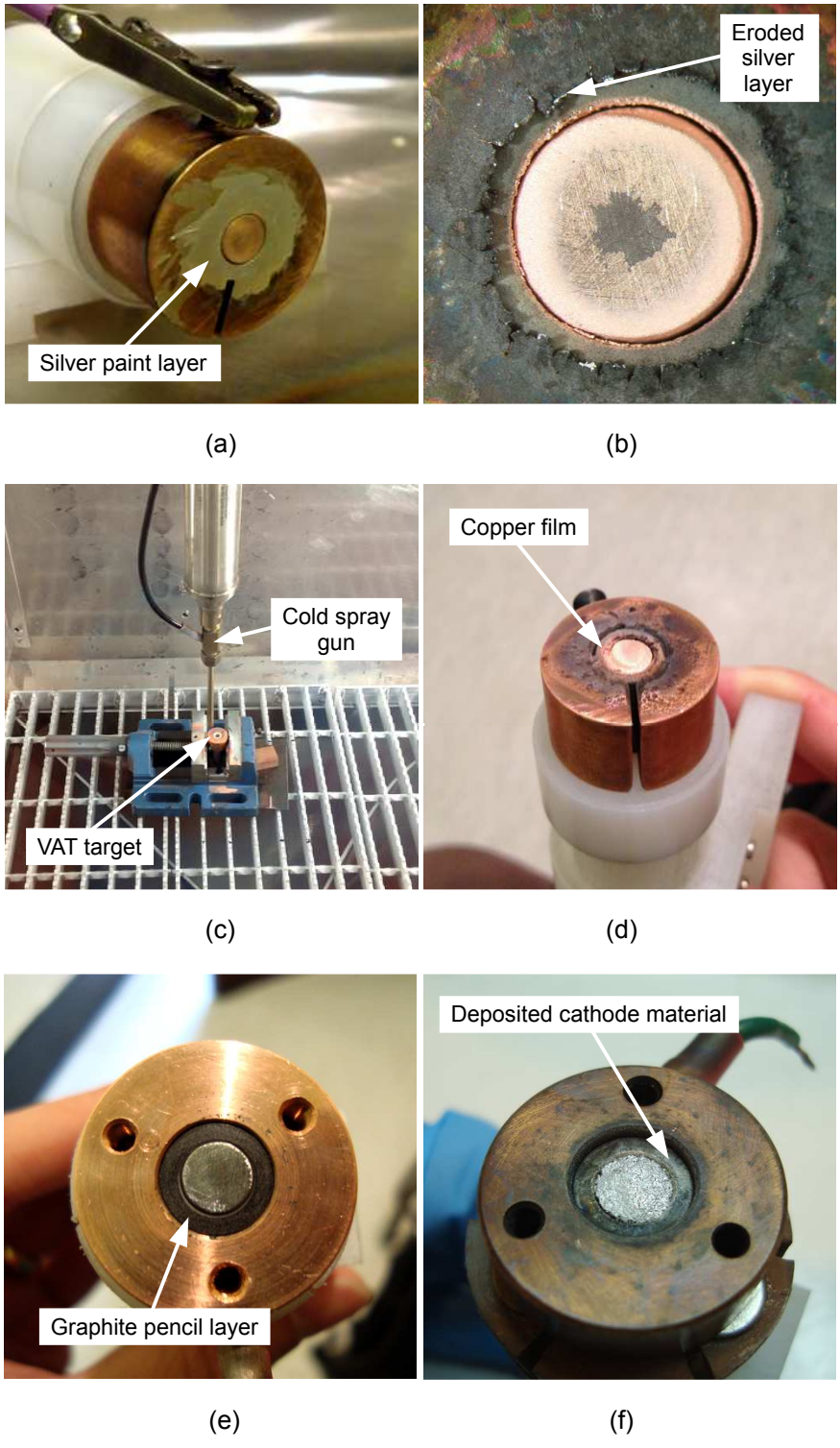

Figure 4.3: Exploration of different film manufacturing techniques such as (a) & (b) silver paint, (c) & (d) cold spray copper films, and (e) & (f) graphite coatings used to manufacture the thin conducting film for triggerless arc initiation.

1. The first attempt was to apply a graphite coating drawn on the ceramic face using an ordinary lead pencil. However, there was difficulty in accomplishing reliable thruster firings since the graphite would either short-circuit the thruster or dissipate too quickly.

2. The second attempt was to apply silver conductive paint as depicted in Figure 4.3a. However, even after curing, the coating quickly eroded away after low-energy pulsing and was found to significantly reduce thrust production (Figure 4.3b). This was attributed to the low melting point of the silver paint. Molten droplets of silver as well as combusted solvent particulates were also found to block and absorb ions ejecting out of the thruster's front end. High resolution microscopy of the cathode and a target deposition plate revealed evidence of this effect.

3. The third attempt was to adopt the cold-spray deposition technique. A thin film of copper was deposited on the thruster face (Figure 4.3c) and filed down to a suitable thickness. Arc initiation was easier to attain with this method, but several weaknesses with this approach made it impractical. Firstly, it was difficult to generate very thin coatings in a repeatable manner on the face. Coatings tended to be thick and highly porous, both of which are undesirable (Figure 4.3d). Secondly, a long setup and preparation time is required for the deposition process and many VAT tests were expected to be made. Thirdly, the high speed of the copper particles caused high thermal shock to the ceramic, causing it to crack and erode more easily than before. Further work is needed before cold spray deposition can be made a viable technique.

4. The fourth and final attempt to create a simple-to-prepare, reliable thin conducting film was to return to the first attempt of applying graphite with the additional step of dissolving the graphite in solvent such as acetone. This caused the graphite particulates to break up and smoothly cover the ceramic face (Figure 4.3e). Graphite conducting paint spray was also shown to be suitable. Arc initiation was successfully demonstrated (Figure 4.3f) and the presence of the film was sustained provided the pulse energy was roughly greater than 0.2 J. The initial resistance of the film could easily be controlled by the location and amount of applied graphite, and was usually set between 0.1–20 kΩ. Pulses of up to 10^4 were regularly accomplished with ease. Thus, a suitable arc initiation technique for the level of testing

expected in this study was found.

4.2.3 Choice of reference cathode materials

Although nearly any solid conducting element can be used as fuel, pure metallic elements are the most common cathode materials to be used in VATs. Metal aluminium (Al), iron (Fe), bismuth (Bi) and copper (Cu) cathode rods were chosen as primary baseline cathode materials for this study due to their wide range of thermophysical and vacuum arc properties, thrust production, and availability of predicted thruster performance (Polk et al. 2008, Lun et al. 2010). One particularly important feature of each chosen material was their ability to generate different amounts of cathode spots for a given amount of arc current depending on the element's thermophysical properties (discussed in Chapter 1, see Table 1.1). Thus, for the arc current range studied here, Bi is expected to have many cathode spots present on the surface during an arc pulse, whilst other materials such as Al or Cu are expected to only produce a single cathode spot. Table 4.2 lists some physical properties of the cathode materials used in this study.

Additionally, this work provided an opportunity to experimentally validate predicted VAT performance for these cathode materials (which has not been published in full to date) as well as to help validate and verify thruster operation and test diagnostic equipment. Finally, the varying characteristics of these materials may help to explain observed vacuum arc behaviour across different studies performed in this work.

Table 4.2: Material properties of Al, Fe, Cu and Bi cathode samples used in this study. Thermophysical data from Incropera & DeWitt (2002).

Property	**Al**	**Fe**	**Cu**	**Bi**
Purity	2N*	3N5	2N5*	5N
Atomic mass (AMU)	26.3	55.9	63.5	209
Density ($\times 10^3$ kg/m^3)	2.70	7.87	8.93	9.78
Boiling point (K)	2792	3134	2835	1837
Melting point (K)	933	1810	1358	545
Thermal cond. (W/mK), *molten*	218	32	339	7
Thermal cond. (W/mK), *room*	237	80	401	8

* Commercially pure

4.3 Thruster characterisation, validation and verification

4.3.1 General operation of VAT prototypes

Thruster preparation and initiation

Before any test measurements were made on a VAT prototype (baseline or new), the end face of its cathode rod was prepared and cleaned with a metal file to ensure a relatively smooth surface texture. Also, the VAT was initially"burned-in" by repeated firing by up to a few hundred pulses or a few Coulombs of delivered arc charge to remove cathode surface oxides, residual gases embedded within the cathode and excess graphite on the front face of the thruster. This ensured as consistent operation as possible across thruster prototypes.

Visual observation of VAT exhaust jet

Figure 4.4 shows a close-up of baseline VAT prototypes firing inside the chamber with the characteristic glowing plasma plume and sporadic emission of incandescent macroparticles. Each cathode material plasma was observed to give off a specific colour emission, corresponding to the ionisation energy of its atoms. For example, Al plasma is purple, Fe plasma is blue, Bi plasma is turquoise, Cu plasma is green, and Carbon plasma is white.

4.3.2 Thruster performance tests

Test configuration

Lifetime thrust tests for three individual baseline VAT thrusters were performed for Al, Fe and Bi cathode materials. The electrode configuration for each thruster was such that the cathode was located flush to the anode and the insulator recessed into thruster by

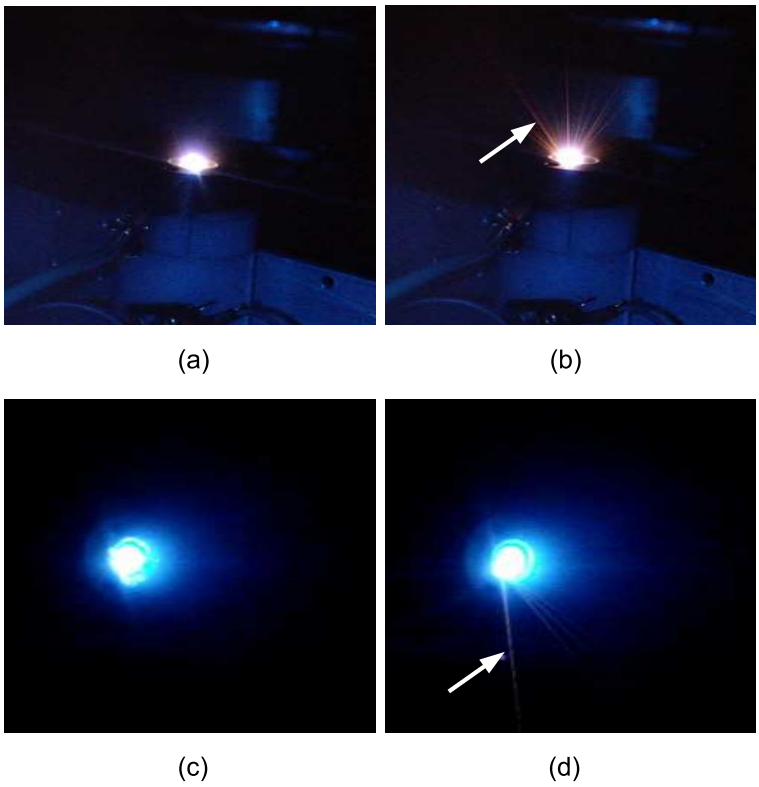

Figure 4.4: Close-up views of Al and Fe VAT prototypes firing inside the vacuum chamber with visible plasma jet plume emanating outward from the cathode surface – (a) Al plasma generally exhibits a purple glow, whilst (c) Fe plasma exhibits a blue glow. Macroparticle emission in each respective VAT is observed in (b) and (d) as radiating incandescent particles from the cathode region (highlighted with arrows).

0.5 mm. All three thrusters were mounted on the thrust measurement stand (see Section 3.4) as shown in Figure 4.5 and tested in a single vacuum run with only one calibration procedure needed for the setup. Measurements of mass erosion rate for each cathode material were conducted simultaneously in each test case, the results of which were later verified with additional erosion tests.

Pulse characteristics

The same inductor coil size was used for each test case to generate VAT arc pulses, where each thruster was fired with triangular-shaped pulses of approximately 50 A peak arc current and with a short, medium or long weight-averaged median pulse length between 200–2000 μs. Table 4.3 summarises the weight-averaged arc pulse characteristics (arc

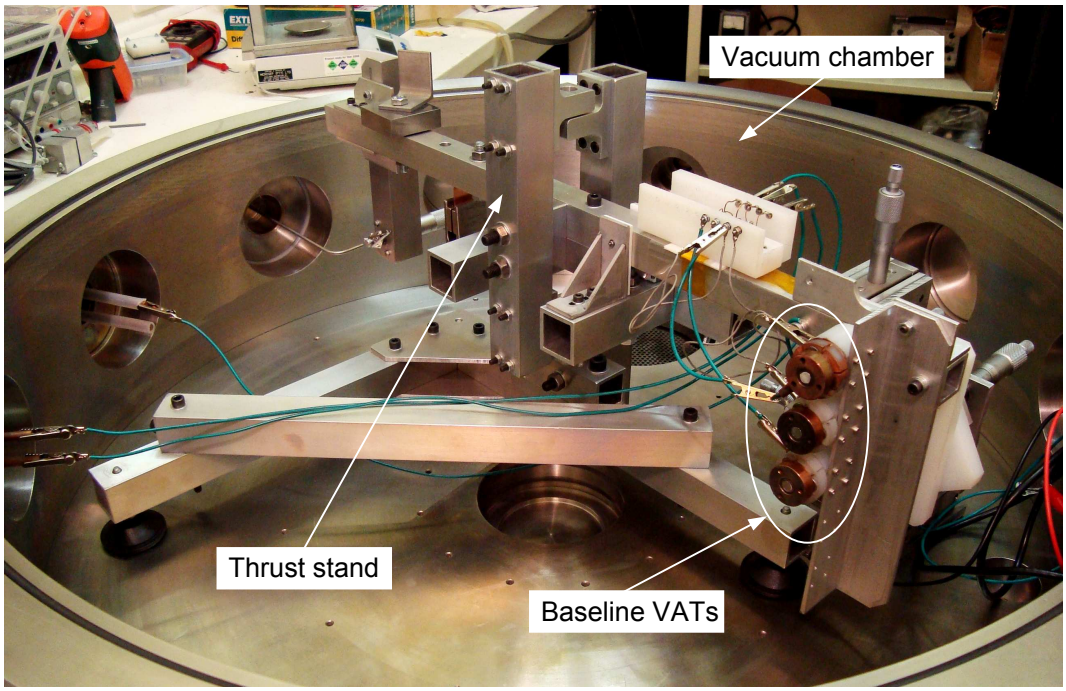

Figure 4.5: Thrust stand setup with three VATs mounted for lifetime testing. Cathode materials used were Al, Fe and Bi. Lifetime test duration of 1–5 $\times 10^4$ pulses.

current, arc voltage, average arc power, median pulse length, pulse frequency, pulse energy, pulse charge) and accumulated lifetime data (cumulative arc pulse charge delivered, total number of pulses fired) over the duration of each material lifetime thrust test. Since each cathode material was expected to possess different levels of thrust production ability, different pulse frequencies (5–50 Hz) for each material were chosen in order to generate a large enough beam displacement to obtain a thrust measurement with acceptable accuracy. Each VAT was operated for roughly $n = 1\text{–}5 \times 10^4$ pulses to assess thrust production capability over time.

Table 4.3: Summary of total weighted-averaged arc pulse characteristics, total charge transferred and total pulse firings for baseline VAT lifetime tests for Al, Fe and Bi cathode materials

	Weight-averaged values							**Total**	
	I (A)	V (V)	P (W)	t_p (μs)	f (Hz)	E_j (J)	Q (mC)	$\sum Q$ (C)	n
Al	26.9	36.9	8.1	156	50.1	0.13	4.3	183	42 714
Fe	23.3	21.1	3.4	658	10.1	0.33	15.1	772	50 975
Bi	12.6	11.8	1.5	1962	5.0	0.29	24.7	250	10 049

Figure 4.6 displays the typical arc charge and discharge current and voltage waveforms observed for each cathode material tested. Prior to the beginning of a vacuum arc pulse

(time $t < 0$), the pulse circuit builds up current in the inductor coil for a period of several hundred microseconds. The rate of current rise is different for each cathode material, most likely dependant on the material electrical conductivity. A fast current rise indicates a cathode with high conductivity (e.g. Al), whilst a decaying current rise indicates a cathode with poor conductivity (e.g. Bi). Once having reached the desired peak arc current level (50 A in this case), the current is switched to flow into the thruster. At this stage, the arc initiates by the triggerless arc initiating mechanism ($t = 0$) and the VAT fires. For a given inductor size, the length of the arc pulse also correlates with the choice of cathode material, or rather the cathode arc voltage. The lower the arc voltage required by the cathode, the longer a vacuum arc pulse can be generated. This can be linked to the material-specific minimum arc current level (chopping current limit) needed to develop a vacuum arc.

Cathode erosion

Table 4.4 compares measured erosion rate data for the baseline thruster design. Measured results for Al and Fe show generally good agreement with literature. In the case of Fe, its erosion rate value was measured as roughly midway between literature results for short (250 μs) and long pulses (0.52 s). This can be expected given that Fe's pulse length value (and hence, heating time of the surface) was in-between those tests in literature. The predicted ion erosion rates are expected to be lower than the values of E_r since macroparticle production is ignored in the calculation. With this knowledge, 32 % and 46% of Al and Fe cathode mass loss respectively can be assumed to take the form of neutrals and macroparticles (MP's). Low-melting point materials like Bi are estimated to have a significant portion of its mass loss in the form of neutrals and MP's (83%).

Observation of the erosion patterns on the three thrusters at the end of the lifetime test as shown in Figure 4.7 revealed how differently each cathode behaved. Al (t_p= 156 μs) and Fe (t_p= 658 μs) showed erosion mostly at the outer circumference of the cathode rod (roughly 0.5 and 1 mm respectively), whilst Bi (t_p= 1962 μs) had an almost uniform erosion of the cathode surface and some recession of the cathode into the thruster. Longer pulses appeared to produce better erosion characteristics because the cathode spots had

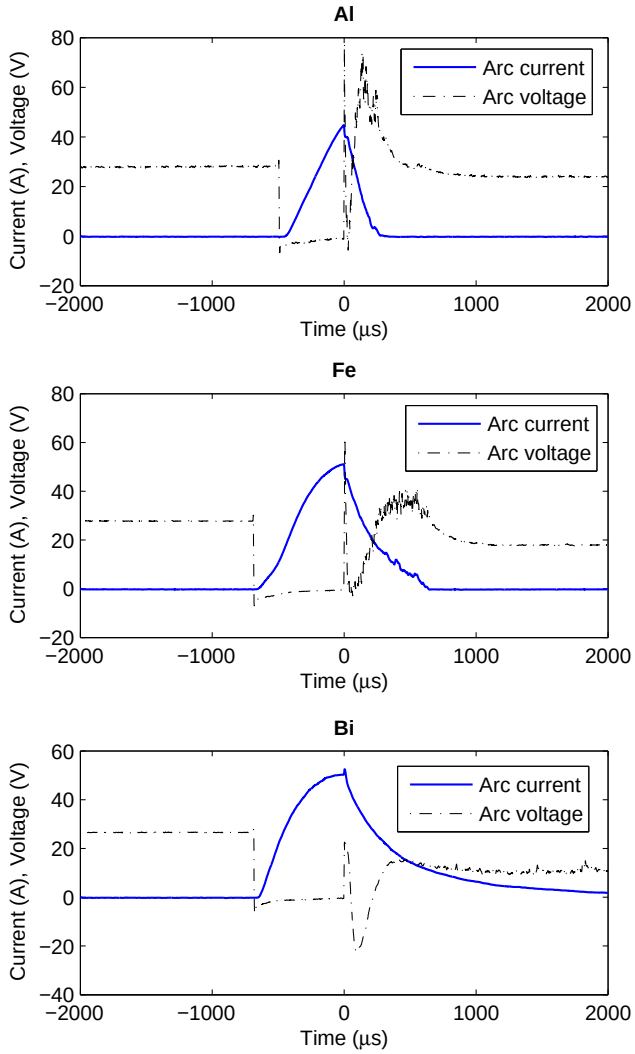

Figure 4.6: Typical averaged arc current and arc voltage pulse waveforms for Al, Fe and Bi during lifetime thrust tests. Data shown here after n = 3000–4000 pulse firings.

a longer time to "walk" over the surface and erode it. The number of cathode spots may have also played a role in cathode erosion, where a large number of spots (in the case of Bi, ≥ 10) enables uniform erosion, whilst only 1–2 spots (Al and Fe) exhibits localised surface erosion. Thus, the choice of arc pulse characteristics and cathode material plays an important role in manner of cathode erosion. Significant deposition of cathode material on the interelectrode insulator surfaces of all thrusters was also seen, which facilitates continued triggering of the thruster.

Table 4.4: Comparison of measured and predicted erosion rates of baseline VATs with published literature. Measured cathode mass loss in brackets.

		Erosion rate, E_r (μg/C)		
Type	**Description**	**Al**	**Fe**	**Bi**
	This work			
Exp	Total mass loss, Δm (mg)	(5.7 ±0.1)	(43.7 ±0.1)	(51.9 ±0.1)*
	50 A pk, 150–2000 μs	31.2 ±0.6	56.6 ±0.6	1267.4 ±3.6*
Exp[a]	100 A, 250 μs	28	48	
Exp[b]	200 A, 0.52 s		73	
Calc[c]	Ion erosion only	19	26	211

* Results for Bi were obtained from an additional erosion rate test (Q = 41 C) due to a measurement error in the lifetime test.
[a] Brown & Shiraishi (1990)
[b] Kimblin (1973)
[c] Lun et al. (2010)

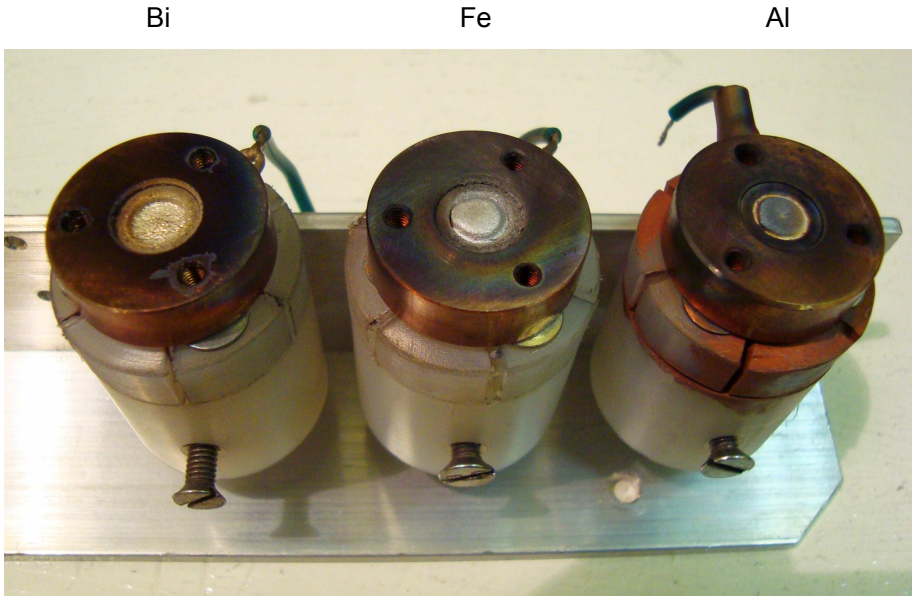

Figure 4.7: Used thrusters after lifetime and verification thrust tests. Note the differences in cathode erosion patterns for each thruster.

Arc pulse behaviour

Figure 4.8 depicts arc pulse characteristics over the course of the lifetime test for all materials. Each data point is a snapshot in time, representing 15–20 waveform and test samples taken at that moment in the test. It is important to note that the error bars in the figure (and subsequent ones) are also indicative of the fluctuations and noisy behaviour typical of vacuum arc behaviour (as previously discussed in Section 3.3.2) and do not only represent measurement uncertainty, which is generally much smaller than

the final uncertainties shown here.

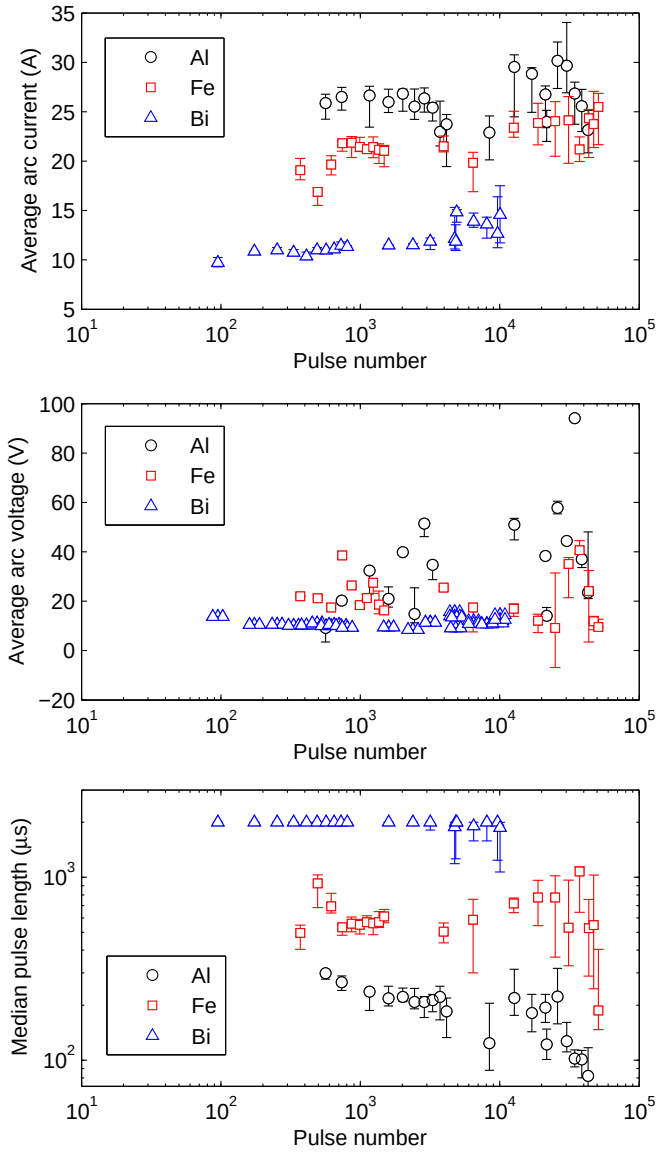

Figure 4.8: Measured arc pulse current, voltage and median pulse length over duration of lifetime test on baseline VATs with Al, Fe, and Bi cathodes. Data fluctuation and error bars are indicative of the noisy behaviour of the vacuum arc pulses. Lifetime test duration is expressed in terms of number of pulses fired.

Relatively stable arc pulse characteristics were observed in the 10^3–10^4 pulse range. This indicated that a stable thruster operating condition was established during that time. Although the average pulse charge remained overall constant over the course of the lifetime tests, a gradual shortening of the pulse length was observed, especially beyond 10^4 pulses. A corresponding growth in arc voltage and increasing instability of the arc (as depicted by increasing magnitude of data error bars) near the end of the tests was also seen.

For example, Figure 4.9 illustrates the growth of Fe's median pulse length error bounds from an initial 10% nominal to up to 50% nominal as the test progressed.

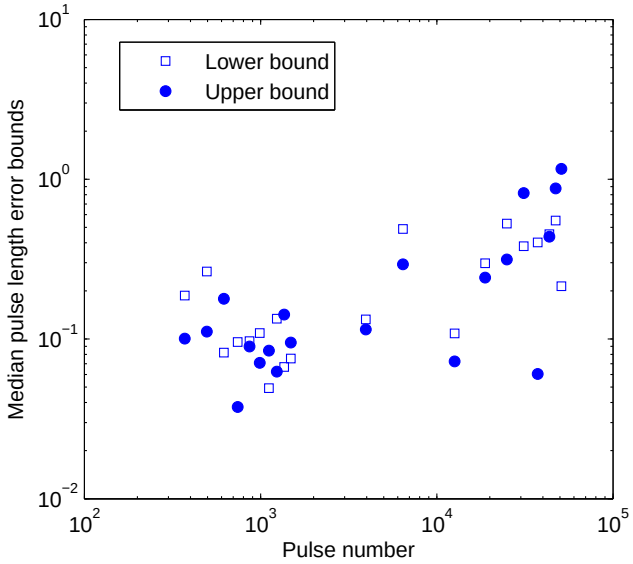

Figure 4.9: Growth of median pulse length error bound values over time for Fe cathode lifetime test. Vertical axis represents the lower and upper bound values as a percentage of the median pulse length value.

All these observations are indicative of the onset of degradation of the conducting path for the vacuum arc pulse, which occurs at different points in the test depending on the cathode material. The conducting path was found to be affected by two possible failure modes. The first mode, due to the absence of a cathode feeding mechanism, is the recession of the eroding cathode fuel rod into the thruster, which widens the gap between the electrodes. This was illustrated by the Bi cathode, which melted considerably during the test. The second mode is the erosion of the conducting film on the insulator. This type of failure was experienced with the use of Fe and Al, which have significantly lower erosion rates than Bi. This makes these materials less capable of replenishing the portions of the conducting film that eroded after being subjected to arc triggering and the accompanying high thermal load. Similar lifetime issues were experienced by Pietzka et al. (2013) when operating at the 1–20 W low power range. Although work by Anders et al. (1998) showed that the triggerless method was successful up to 10^6 pulses, this may be because of the higher arc currents and pulse lengths that were used (200 A, 5 ms), which would have produced a larger amount of film deposition on the insulator than was seen here. Although this present study was unable to attain the long operating lifetimes achieved by Anders et al. (1998), firing VAT prototypes up to 10^4 pulses was at least shown to be

sufficient for reaching and establishing a sizeable duration of relatively stable nominal thruster behaviour and performance as well as generating significant amounts of data on prototype operation.

Thrust generation

Tests confirmed the linear dependency of thrust on arc current as shown in Figure 4.10a. Plotting thrust per average arc current in Figure 4.10b also shows that the thrust production mechanism is relatively stable for most of the test duration. However, lower initial T/I values were seen for Al and Fe due to some outstanding oxide layers and ex-

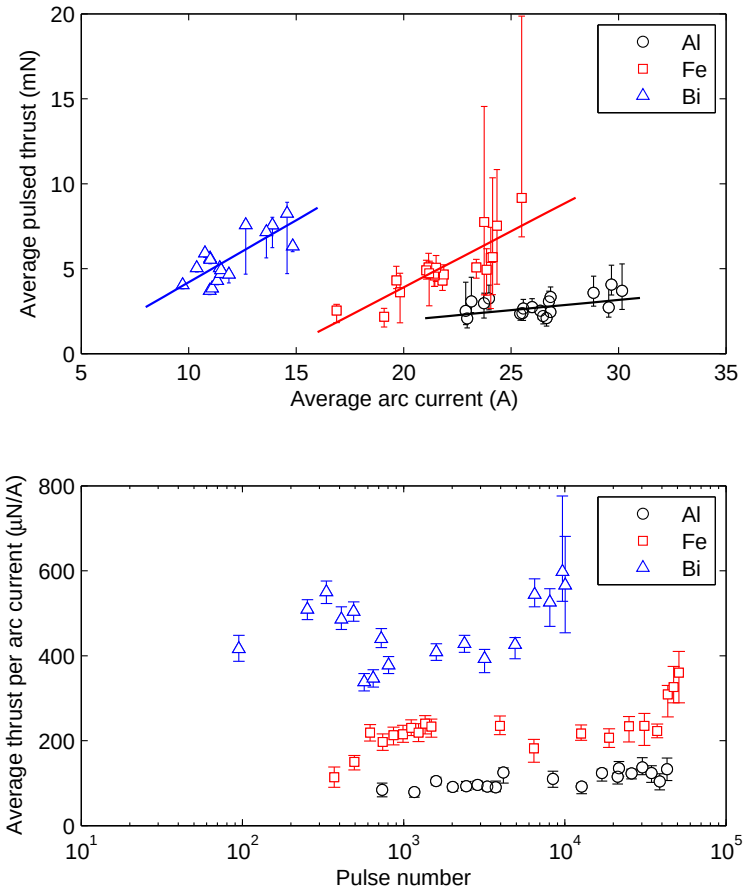

Figure 4.10: (a) Measured thrust against arc current for baseline VATs with Al, Fe, and Bi cathodes with observed linear trends of thrust against current; (b) shows change in thrust production per input arc current over thruster lifetime.

cess graphite film remaining despite the initial burn-in phase. The transition to nominal thrust production occurs at different times depending on the cathode material. For example, Al and Fe took up to several hundred pulses to reach nominal thrust production, whilst Bi had almost no initial thrust transition. This behaviour of Bi is most likely due to its high erosion rate, which would very quickly remove oxide layers and residual gas within the cathode surface. Near the end of the lifetime tests, a significant increase in thrust scatter and aberrant thrust values were observed for all test cases. This was due to the approaching failure of the thruster as discussed earlier, which caused unstable thruster behaviour and skewed thrust measurement.

Figure 4.10b demonstrates the wide range of thrust production levels possible with low-powered VAT thrusters. At one extreme, Bi produced the largest nominal average thrust per arc current (502 μN/A), whilst Al produced the smallest (117 μN/A). Fe represented mid-ranged thrust production values typically seen by most metal cathodes (221 μN/A) as shown by Polk et al. (2008). General scatter in thrust data, also reported by Ziemer (2001), is indicative of the variable and "noisy" thrust generation properties of a standard VAT design. There are a number of causes for this. The first cause is the ever-changing surface conditions of the interelectrode gap in the VAT, which influences vacuum arc plasma production and thrust generation. The second cause is the varying location of the cathode spots on the cathode surface from which the plasma jet is emitted over the course of the VAT's lifetime. This can have a small but measurable effect on the thrust vector. The third cause is the random variation in the arc pulse waveform profile at every pulse firing, which is a feature of the vacuum arc as well as the limitations of the present pulse circuit design.

Overall thruster performance

A plot of average thrust against average thruster power in Figure 4.11a shows the generally increasing trend of thrust with power. Bi produced the largest average thrust-to-power ratio (42.5 μN/W), whilst Al produced the smallest (3.2 μN/W). Fe produced an average thrust-to-power ratio of 10.5 μN/W, a nominal VAT performance value widely reported in VAT literature. The diverse range of impulse bits generated by the VAT thrusters

in Figure 4.11b also illustrates the flexibility of the thruster to produce a variety of performance levels as desired. Once again, Bi produced the largest nominal impulse bit size (10 μNs), whilst Al produced the smallest (0.5 μNs). Fe produced a nominal impulse bit size of 3 μNs in the 0.2–0.4 J range – comparable to measured impulse values by Ziemer (2001) for a Titanium cathode, which delivered 2–10 μNs impulse bits at pulse energy levels of 1–2 J.

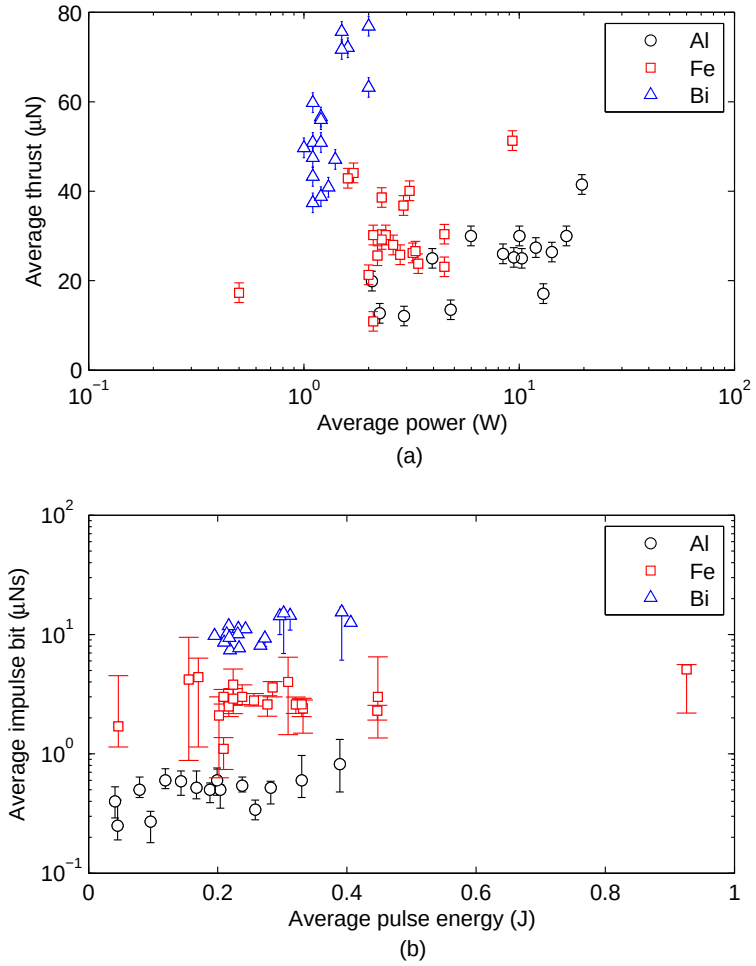

Figure 4.11: (a) Measured average thrust against average arc power and (b) average impulse bits against average pulse energy for baseline VAT tests using Al, Fe, and Bi cathodes. A wide range of thrust and impulse production performance across all materials is demonstrated. General increases in thrust and impulse with increasing thruster power and energy levels are also observed.

A summary of overall baseline VAT performance is given in Table 4.5. Average thrust-to-arc current ratio values for Al, Fe and Bi (ranging from 117 to 502 μN/A) are sufficiently varied to illustrate the wide range of thrust production capabilities possible within VATs depending on the choice of cathode fuel material. Specific impulse calculations were obtained by combination of average T/I and E_r data for each cathode material, resulting

in I_{sp} values of 382 s, 398 s and 40 s for Al, Fe and Bi respectively. Thruster efficiencies were also calculated to be 0.6%, 2.0% and 0.8% for Al, Fe and Bi respectively.

Table 4.5: Overall performance results of baseline VAT tests with Al, Fe and Bi cathodes. Values of T/I and T/P are averaged over the entire data set for each cathode material.

Performance metric	**Al**	**Fe**	**Bi**
Thrust per arc current, T/I ($\mu N/A$)	117	221	502
Thrust-to-power ratio, T/P ($\mu N/W$)	3.2	10.5	42.5
Erosion rate, E_r (μg/C)	31.2	56.6	1267.4
Specific impulse, I_{sp} (s)	382	398	40
Efficiency, η (%)	0.6	2.0	0.8

The variety of performance levels across cathode materials is such that VATs can be tailored to suit the propulsive needs of the satellite mission. Missions requiring high thrust and thrust-to-power ratio at the sacrifice of specific impulse, can employ a heavy, low-melting point material such as Bi. Missions relying more critically on fuel efficiency, at the expense of lower thrust and thrust-to-power ratios, could employ a higher but still modest specific impulse material such as Al or Fe. Practical trade-offs in fuel selection may also include the storage volume of the fuel (influenced by material density), the ease of arc triggering (effectiveness of insulator film replacement) and risk of MP contamination on surrounding satellite subsystems (e.g. solar panels).

4.3.3 VAT plume distribution

The plume distribution of the VAT's plasma jet was verified by mapping the ion current emitted by the baseline VATs along two principle axes. Measurements were taken with a Faraday Cup probe fixed at drift lengths ranging from 223–234 mm from the central thruster assembly head. Each thruster was rotated along the pitch and yaw axes over the $\pm 90^\circ$ range of angles in increments of 9.6° and 14.4° respectively. An example of the resulting ICDD maps for Al, Fe and Bi are shown in Figure 4.12, where each data point represents the mean value of 10–20 data samples captured at a specific yaw or pitch angle.

A best surface fit algorithm was implemented to map and extrapolate each set of cap-

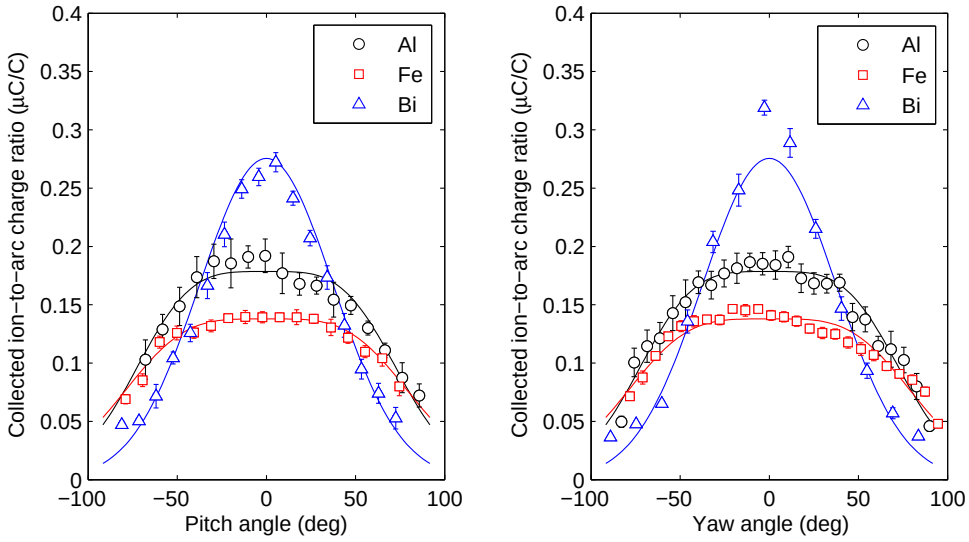

Figure 4.12: Ion current plume distributions along (a) pitch and (b) yaw axes for baseline VATs using Al, Fe and Bi cathodes. I = 50 A pk and average pulse lengths for Al, Fe and Bi are 309, 506 and 3421 μs respectively. Measured deviation angles along pitch and yaw axes have been corrected to produce centred ICDDs for comparison purposes. Vertical axis is the ion charge collected by the Faraday cup probe divided by the arc pulse charge.

tured ion plume data to a known distribution (Gaussian, Exponential, etc.). Al and Fe ICDDs were found to fit an Exponential distribution, whilst Bi's ICDD followed a Gaussian distribution. Results of each fit are listed in Table 4.6 with its distribution-specific spread factor and goodness-of-fit indicators (R^2 and root mean square error (RMSE)). The thrust vector was generally found on average to deviate no more than $\beta_T \leq 10°$ from the normal thrust axis. This meant that normally-directed thrust was expected to decrease no more than $1 - \cos(10°) = 1.5\%$, a small margin of error.

Thrust vector deviation angles appeared to decrease with longer arc pulses and higher cathode spot numbers, e.g. compare Al and Bi results. This result is expected since the prolonged presence as well as greater distribution of spots on the cathode surface should result in more stable and uniform generation of the VAT plasma jet. Therefore, consideration should be made when operating VATs at short pulses ($\leq$ 1 ms) or with a small number of cathode spots and their effects on the thrust vector.

Thrust correction factors were calculated for each test case using the method described in Section 3.6.4, where fitted parameters of the measured plume distributions and specified thruster geometry served as inputs. Resulting C_T values listed in Table 4.6 show

reasonable agreement to Polk et al.'s (2008) prediction of C_T = 0.64 assuming an Exponential distribution. However, all measured C_T values are lower than this predicted value with differences of 7.8% (Al), 11.2% (Fe) and 21.1% (Bi). For Al and Fe, this could be due to non-uniform (and initially asymmetrical) erosion of the cathode surface, a behaviour not properly considered in the theoretical analysis of C_T. The resulting Exponential distribution is an inherent feature of edge-triggered VAT designs and short arc pulses, where gradual "rounding" of the cathode rod at its edges eventually recedes the location of the cathode spot(s), reducing the amount of ions being emitted from the thruster.

Table 4.6: Specifications of fitted plume distributions (type, spread factor, goodness-of-fit indicators) and thrust vector deviation angles for baseline VAT designs with Al, Fe and Bi cathodes. Resulting thrust correction factors for each case are also listed.

	Plume distribution specifications					
	Fit	**Spread factor**	R^2	**RMSE**	β_T (deg)	C_T
Al	Exponential	5.596 ±0.200	0.948	0.012	9.6 ±3.4	0.590 ±0.008
Fe	Exponential	6.636 ±0.267	0.934	0.010	8.5 ±2.5	0.564 ±0.006
Bi	Gaussian	0.926 ±0.037	0.969	0.018	4.6 ±3.1	0.505 ±0.022

Surprisingly, Bi's ICDD results show a much narrower distribution compared to Al and Fe, despite experiencing relatively uniform cathode erosion (Gaussian distribution). The reason for this may be attributed to the high MP content generated by a low-melting point cathode material like Bi. Macroparticles are known to be generally emitted at shallow ejection angles to the cathode surface (Daalder 1976). The absorption of ions by MPs at these ejection angles may offer an explanation for the narrower ICDD of Bi. Thus, the presence of MPs may in fact negatively affect thruster performance by reducing the value of C_T and that broadly assigning C_T = 0.6–0.64 to a baseline VAT design may only be valid for materials with relatively low to medium erosion rates, i.e. low to moderate levels of MP production.

4.3.4 Comparison with empirical performance model

A basic empirical model of VAT performance can be made using Equation 2.1 and substituting variables with experimentally measured data from literature (see Table 4.7). This approach is identical to Polk et al. (2008), except for the use of updated values of C_T, ϵ

and v_i. Table 4.8 compares empirical model predictions against nominal VAT lifetime test performance. Predicted Fe performance shows excellent agreement to measured results. The biggest contrast between measured and predicted results occurred with Al and Bi. This was due to the higher arc voltages that were experienced with Al and the significantly higher erosion rate for Bi. The low thrust result for the Al test could be due to its very short pulse length, which was expected to produce plasma with a higher-than-usual average ion charge state, which would in turn produce a lower thrust overall. This conclusion was later confirmed with subsequent tests on Al cathodes operating at longer pulses in this study.

Table 4.7: Empirical values used for predicting baseline VAT performance of Al, Fe and Bi cathodes

Parameter	Al	Fe	Bi	Source
Ion-to-arc current ratio	0.112	0.080	0.102	Anders et al. (2005), Kimblin (1973)
Average Ion charge state	1.73	1.82	1.17	Anders (2001)
Average ion velocity (km/s)	15.4	12.6	4.7	Anders & Yushkov (2002*b*)
Thrust correction factor	0.590	0.564	0.505	Calc. in this work (see Table 4.6)
Arc voltage	23.6	22.7	15.6	Anders et al. (2001)
Erosion rate (μg/C)	28	48	211*	Brown & Shiraishi (1990)

* Erosion rate for Bi are from predicted ion erosion only (Lun et al. 2010).

Table 4.8: Comparison of weight-averaged measured and empirically predicted performance results for baseline VAT tests using Al, Fe and Bi cathodes. Predicted results are in brackets.

Performance metric	Al		Fe		Bi	
Thrust per arc current, T/I ($\mu N/A$)	117	(161)	221	(181)	502	(449)
Thrust-to-power ratio, T/P ($\mu N/W$)	3.2	(6.8)	10.5	(8.0)	42.5	(28.8)
Specific impulse, I_{sp} (s)	382	(584)	398	(385)	40	(217)
Efficiency, η (%)	0.6	(1.9)	2.0	(1.5)	0.8	(3.1)

Both Al and Fe demonstrated specific impulses lower than that predicted by Polk et al. (2008) and Lun et al. (2010) primarily due to differences in erosion rate values and assumed ion-to-arc current ratios of $\epsilon = 0.1$. Despite its high thrust production, the specific impulse of Bi is very low (40 s). This is largely due to its high erosion rate. Finally, average thruster efficiencies were found to vary with cathode material and were situated in the correct order of magnitude predicted by thruster models. The reason VATs in general have low efficiencies ($\eta \leq 10\%$) is because most of the pulse energy is devoted to merely ionising the material (Schein et al. 2002a). It is therefore of great importance that efforts towards improving VAT efficiency place focus on increasing thrust production ($\eta \propto T^2$),

and reducing power and fuel consumption ($\eta \propto 1/E_r, 1/P$).

4.4 Summary

A number of vacuum arc thruster prototypes were shown to be successfully and repeatedly constructed and tested. Equally important, thruster tests also assisted in the validation and verification of the operation and performance capabilities of various measurement systems and techniques developed in this study. The use of different cathode fuels, which represented the diverse range of possible cathode materials available for use, confirmed the wide range of performance levels that can be delivered by VATs. The effects of material properties and the manner of cathode erosion on thruster behaviour was also observed in some initial detail. The material-specific transition period to nominal thruster operation after VAT initiation and burn-in was observed and considered in subsequent performance measurements in the project.

Acceptable thruster power levels, thruster lifetimes and general pulse operational conditions were identified and demonstrated. Nominal thruster behaviour produced a range of performance levels comparable to reported literature and empirical modelling. An important finding was the specific impulse of mid-performance Al and Fe VAT prototypes, which delivered more realistic values on the order of 400 s. This approach acknowledges the sensitivity of VAT performance to the arc voltage and erosion rate (MP's included), both of which can vary significantly depending on the choice of cathode material, thruster's design, pulse characteristics and operating conditions.

Limitations of the baseline design were identified and the onset of failure modes assessed. For example, the duration or number of fired pulses within an individual VAT test was practically limited to 10^4 pulses in this study to (a) minimise the effects of an absent feeding mechanism on cathode erosion behaviour and plume divergence, and (b) avoid the onset of thruster failure, which produced erratic vacuum arc behaviour and large measurement errors. Thus, subsequent thruster test measurements in this study were taken for at least up to 10^3–10^4 pulses to adequately capture sufficient durations of

stable thruster behaviour.

In conclusion, the successful development of a baseline VAT design has provided the necessary foundation for a more generalised study of VATs and the exploration of various design improvement techniques as presented in subsequent chapters.

Chapter 5

Pulse length study

5.1 Introduction

This chapter considers the effect of arc pulse length on VAT performance and behaviour with particular attention given to millisecond-long pulse lengths, an operational condition largely ignored in VAT literature. An understanding of the relationship between arc pulse length and cathode surface erosion is initially established. This aspect of VAT design sets the tone for a broad and systematic exploration of the consequences of such a relationship on plasma jet behaviour, ion production and potential implications for VAT design philosophy and performance.

5.2 Method

Thruster prototypes following the baseline VAT design with Al, Fe, Cu and Bi cathode fuel rods were used in this study. Numerous prototypes were prepared and operated such that each VAT was test fired with a desired median pulse length within the range of 150–4500 μs long. The pulse length was roughly controlled by modifying and tuning the inductive energy storage pulse circuit for each thruster test to achieve the desired arc pulse

waveform characteristics (see circuit description in Section 3.3). Peak arc currents of 25, 50 and 100 A were selected for study, where the majority of tests were run at 50 A peak arc current. Thruster firing rates ranged from 1 to 10 Hz in order to (a) control average power level and (b) generate sufficient levels of average thrust for accurate thrust measurement. Detailed thrust, ICDD, ion current and erosion rate measurements were undertaken on each VAT prototype to characterise their behaviour and performance. The typical test procedures, methods and analysis for each measurement type is described in Chapter 3.

5.3 Results & discussion

5.3.1 Erosion tests

Thruster prototypes operating at long pulse lengths (≥ 1000 μs) tended to produce more uniform erosion of the cathode rod face, where there was sufficient time for the cathode spots to travel over the surface area to erode it before the arc pulse extinguished. Figure 5.1 shows examples of erosion patterns on Bi and Al cathodes operating with short and long arc pulse lengths. Long pulses (2–3 ms) showed very uniform erosion of the cathode surface compared to the use of short pulses (250–500 μs), where erosion only took place up to $\sim$ 1 mm from the cathode edge. In the case of Al, erosion was initially restricted along one side of the cathode rod, but would be expected to eventually erode the entire cathode edge after an extended period of time (as seen with Bi).

Thus, the arc pulse length played a critical role in how the cathode eroded depending on the size of the cathode surface area. Generally stated, a larger-sized cathode (e.g. 6 mm dia.) requires a much longer pulse length than would be required for a smaller cathode (e.g. 3 mm dia.) to achieve uniform erosion (e.g. 500 μs vs. 2 ms). This finding is in agreement with Pietzka et al.'s (2013) encounters with VAT design discussed earlier in Section 1.3.4.

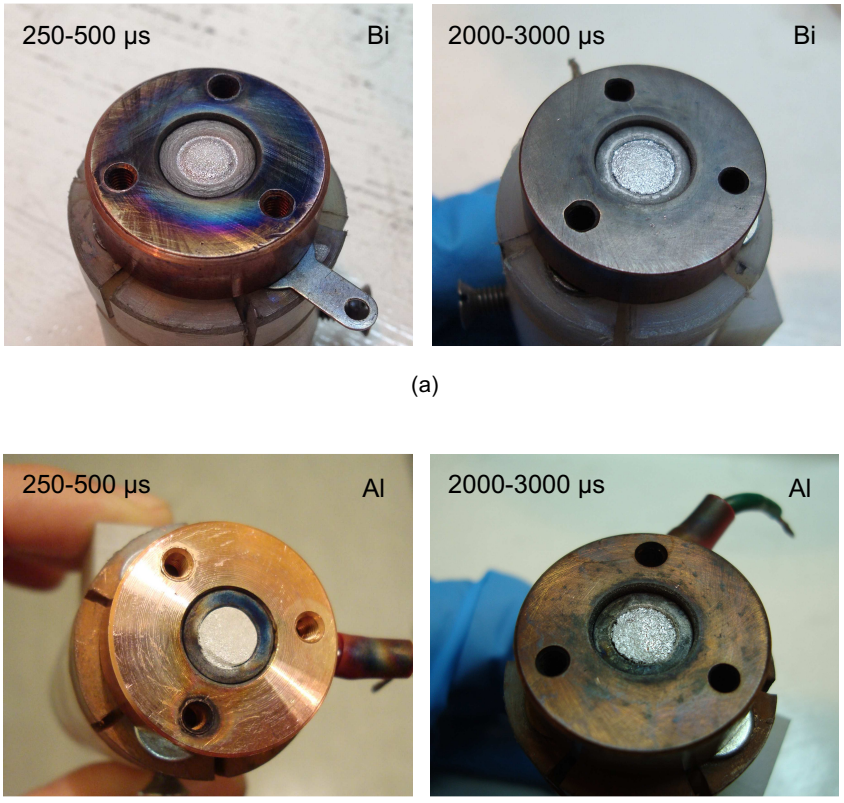

Figure 5.1: Comparison of erosion uniformity between short (250–500 μs) and long (2000–3000 μs) pulses on (a) Bi and (b) Al cathodes. Majority of erosion extends up to 1 mm from cathode edge when using short pulses, whilst long pulses produce near-uniform erosion. Peak arc current $I = 50$ A.

Table 5.1: Comparison of selected erosion rate results for Al, Fe, Cu and Bi cathode materials in a baseline VAT design operating with long and short pulses. Peak arc current is $I = 50$ A.

	Pulse type	t_p (μs)	P (W)	f (Hz)	E_r (μg/C)	**Diff.**
Al	Long	1906	15.7	7	31.9 ±0.6	+2.2%
	Short	156	8.1	50	31.2 ±0.6	
Fe	Long	2213	5.4	3	75.5 ±1.1	+71.6%
	Long	2366	0.4	0.25	76.5 ±2.0	+73.9%
	Short	236	1.6	20	44.0 ±1.1	
Cu	Long	1420	5.5	2	83.5 ±2.1	+72.5%
	Short	166	3.0	20	48.4 ±1.7	
Bi	Long	2130	0.8	2	1267.4 ±3.6	+34.0%
	Short	185	0.6	5	945.5 ±12.0	

Table 5.1 compares selected erosion rate test results for both short- and long-pulsed operation using a variety of cathode materials run at I = 50 A peak arc current. In each material case (with the exception of Al), operating VATs with longer arc pulse lengths was found to increase the cathode erosion rate due to the greater heat load imposed on the cathode rod. These results are in agreement with work by Daalder (1975) and Shalev et al. (1986), who found that increases in arc current levels, pulse length and overall cathode temperature for various cathode materials had an exponential effect in increasing the erosion rate. In essence, all materials will eventually experience large increases in erosion rate given sufficient input heat load. The operating point at which this begins to occur will vary depending on the material and electrode size. Al (which has a high thermal conductivity) did not increase in this case simply because the input heat load in this particular test was below the materialâĂŹs threshold of excess melting.

With reference to the listed material properties in Table 4.2, cathode materials with a combination of high thermal conductivity and high melting point were noted to generally produce lower erosion rates. However, an exception in the behaviour of Cu was seen, which showed a significant increase in E_r compared to Al, whose E_r values were highly resilient to increases in pulse length. This is puzzling given that Cu possesses a higher thermal conductivity and melting point compared to Al. This disparity cannot be sufficiently explained at this time.

An important finding of this erosion study was that the pulse length plays a much greater role than the average power level in determining the cathode erosion rate. Examples include: (1) Fe producing the near-identical erosion rate result (~76 μg/C) during long-pulsed operation irrespective of average power level (0.4 W vs. 5.4 W), and (2) Bi producing a 34% increase in erosion rate with a longer pulse despite operating with a low average power level ($\leq$ 1 W). These results suggest that it is the local heat conditions near the cathode spot emission sites that are mainly responsible for the cathode erosion.

Average power levels above a certain value are assumed to only begin taking effect once the overall cathode temperature rises to the point of gross melting (dependant on an individual material's thermophysical properties). Interestingly, Fe's erosion rate reached an upper asymptotic limit of $E_r \sim 75$ μg/C at approximately 2500–3000 μs pulse length

(Figure 5.2). This suggests that there may be a limit to the effect of arc pulse length on the erosion rate on a cathode of this size (coincidently, the maximum value of E_r measured here is nearly identical to that measured by Kimblin (1973) on a 25 mm dia. cathode operating at I = 200 A, t_p = 520 ms).

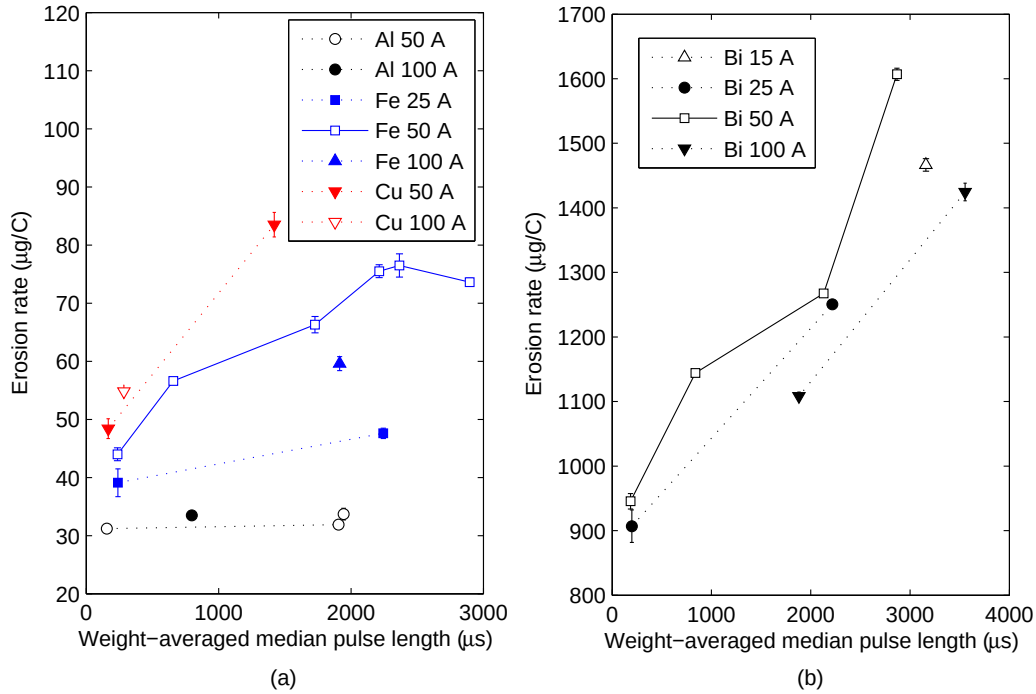

Figure 5.2: Erosion rate results for baseline VATS operating at various pulse lengths for (a) Al, Fe, Cu and (b) Bi cathodes. Peak arc currents in the 15–100 A range are studied.

Figure 5.2 expands Table 5.1's results by plotting erosion rate test data over a wide range of median arc pulse lengths (150–3500 μs) and peak arc currents (I = 15, 25, 50, 100 A) for various cathode materials. As before, cathode erosion rate is generally seen to increase with increasing arc pulse length.

The erosion rate of Al and Cu was shown to be insensitive to the peak arc current in the 50–100 A range, most likely due to the good thermal conduction of these materials. However, a surprising result is that erosion rates for Fe and Bi are higher at 50 A peak arc current than either the 15, 25 or 100 A peak arc currents. As expected, a lower peak arc current causes a lower heat load and hence lower melting. Conversely, a high arc current ought to produce a higher heat load and erosion rate. However, the lower erosion rate values at 100 A peak arc current (higher heat load) in the case of Fe and Bi are counter to this argument. One possible explanation is that operating at a higher arc current was

sufficient to generate additional cathode spots on the surface of Fe and Bi at the beginning of the pulse. These spots are more likely to spread out and cover more surface area, eventually distributing the arc heat load to a level lower than would be experienced at 50 A and resulting in a lower erosion rate. Complementary evidence for this view is given in the situation of Cu, which showed no change in erosion rate with varying arc current at short pulses (50 and 100 A), suggesting that no change in heat distribution on the Cu cathode surface occurred. This result is in agreement with observations by Djakov & Holmes (1971) and Beilis et al. (1997) who found that Cu maintained a single cathode spot for arc currents $I \leq$100 A. In conclusion, the erosion rate is largely influenced by the local heat load, which is a function of not just the peak arc current, but also of the cathode spot distribution, and the interaction of both these factors.

5.3.2 ICDD measurements

Significantly larger ion charge ratio values[1] were observed when baseline VATs were fired at increasingly longer pulses as shown in Figure 5.3. In general, a considerably greater increase in charge emitted was found to occur in front of the thruster than at its outer radial edges, where the largest increases (up to 200% or more) were seen of Al's and Fe's $\bar{J}$ values along the thrust centreline. The behaviour of increasing ion charge ratios also appeared to be consistent for I = 50 and 100 A (at least in the case of Fe). However, there was a limit to this effect for Bi, which showed virtually no change in ion charge ratio values beyond a pulse length of 1500 μs. The slightly higher $\bar{J}$ values at a very short pulse of 132 μs compared to 506 μs in Fe is likely due to the higher average charge state of the ions being produced under the shorter pulse length condition.

The large increases in collected ion charge per given input arc charge during long-pulsed operation is a surprising result. Conventional understanding of vacuum arc behaviour and operation says that ion production rate should be linear to arc charge. As such, there ought be no change in the magnitude of the ion charge ratio collected regardless of delivered arc charge (integral of arc current with respect to arc pulse length). Indeed, a

[1] The ion charge ratio parameter was defined and motivated for use in ICDD measurements in Section 2.3.2.

comparison of Fe's ICDD results at short pulses for both 50 A and 100 A peak arc currents yielded similar levels of peak ion charge ratio along the thruster centreline (ICDD profile shapes of 50 A and 100 A are slightly different because a greater number of cathode spots are present at higher arc currents, which creates a more uniform spread of plasma flux (Gaussian distribution) compared to the Exponential distribution typically generated under low arc current operation).

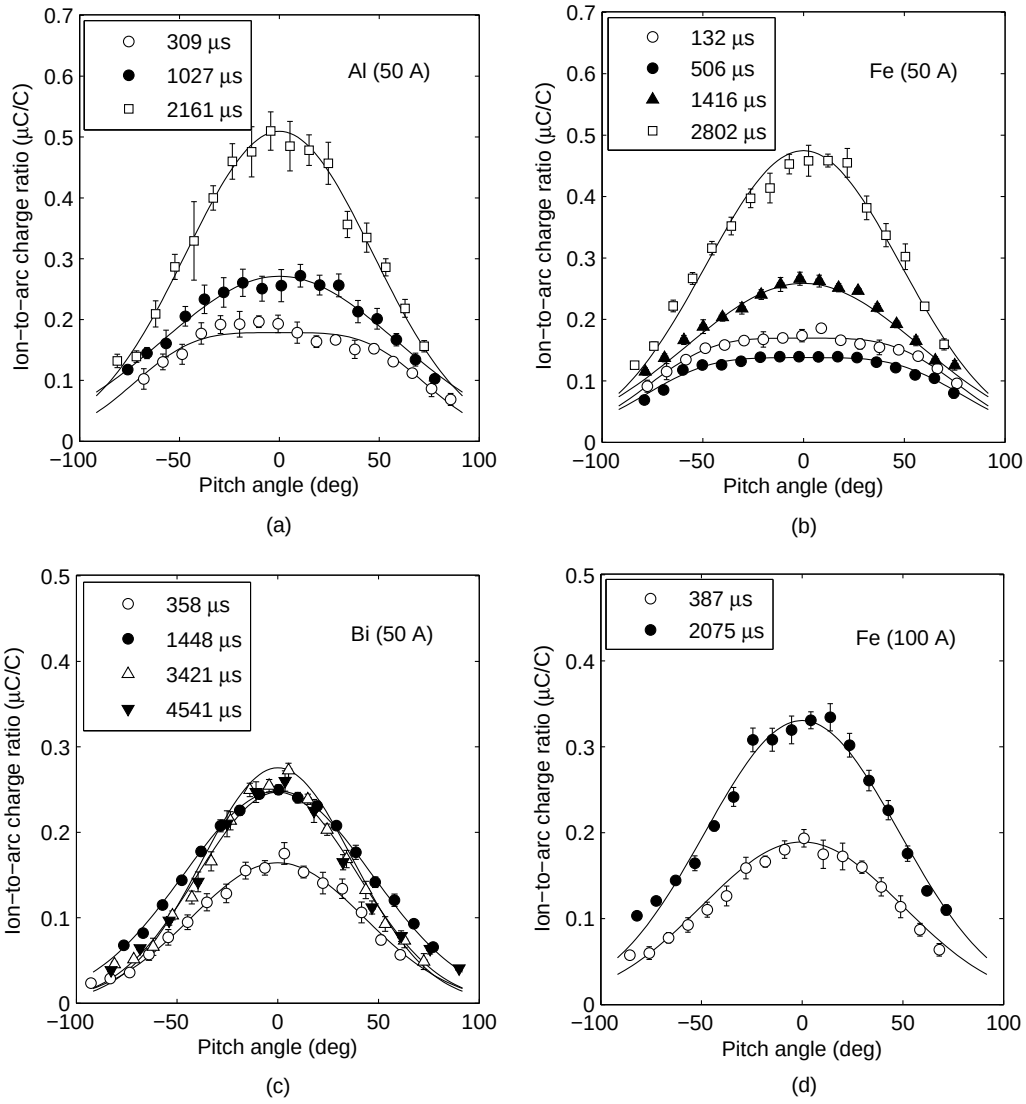

Figure 5.3: ICDD results for baseline VATS operating at various pulse lengths using (a) Al, (b) Fe and (c) Bi cathodes. Peak arc currents I = 50 A for (a)–(c) and I = 100 A for (d). For conciseness, only pitch data is shown in detail here.

There are three possible causes for the increase in measured ion signals:

1. A higher ion charge state can give the appearance of higher ion charge ratio when

detected by the FC probe. However, this is unlikely to be the case here because of Anders's (1998) observed *decrease* of average ion charge state with pulse length. In fact, operating at millisecond-long pulse lengths may have actually decreased the average ion charge state even further than had been previously thought due to increased charge exchange collisions with lesser-charged ions and neutrals (Anders & Yushkov 2007).

2. Charged macroparticles may have been captured by the FC probe and contributed to the total charge signal. Operating for long pulses gives sufficient time (roughly 500 μs) for these macroparticles to travel across the test setup drift length (230 mm) and potentially enter the FC probe. However, macroparticles are mostly ejected at large angles to the normal. This would have caused an increase in collected charge at wide pitch and yaw angles, which was not observed here. In fact, the largest increases in ion signal are observed directly in front of the thruster. Thus, macroparticles are also ruled out as a cause for the increase in ion signal.

3. The final remaining possibility is the generation of additional ions in the near-cathode spot region(s) or in front of the VAT. This can occur as a result of increased charge exchange (CEX) collisions between ions and neutrals (or even small MP's) to produce a surplus of (lower-charged) ions within the plasma flux. The highest growth rate of $\bar{J}$ seen along the thruster centreline suggests that most of the CEX takes place within the centrally-located region of the plasma jet.

A good question to ask is whether there is a sufficient amount of eroded cathode material in the form of neutrals or small macroparticles that could be converted into additional ions. With reference to published estimates and measurements of ion and total erosion rates under "standard conditions" as shown in Table 4.4, it can be seen that at least 30–50% of eroded material is available for additional ionisation. Thus, reported increases in ion production rates at longer pulses are within possible limits of available cathode material.

Using data from Figure 5.3, a plot of peak ion charge ratios emitted along the thruster centreline with respect to the arc pulse length reveals different growth rates of $\bar{J}$ depending on the cathode material, shown in Figure 5.4. All materials show similar near-linear

increases in peak $\bar{J}$ up to 1–1.5 ms, but then diverge at different rates as the pulse length is extended further. Least-squares fit trend lines through test data in Figure 5.4 indicate that Al has a quadratically increasing peak $\bar{J}$ with t_p, Fe maintains a linear increase in peak $\bar{J}$ and Bi has a quadratically-decreasing $\bar{J}$ with t_p (trend line parameters are listed in Table 5.2).

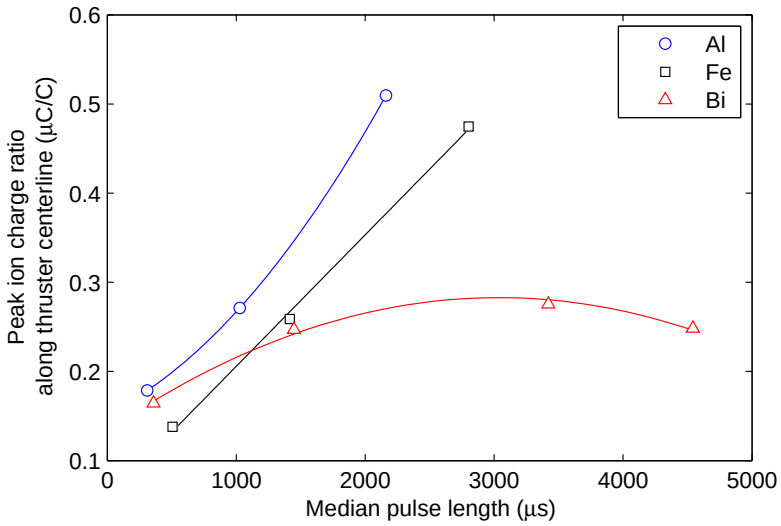

Figure 5.4: Growth of peak ion charge ratios along thruster centreline with pulse length. Cathode materials Al, Fe and Bi each show different growth behaviour. Peak ICDD test data taken from Figure 5.3 (a)–(c) where peak I = 50 A.

Table 5.2: Trend fit specifications for peak ion charge ratios $\bar{J}$ (μC/C) against median pulse length t_p (μs) as shown in Figure 5.4.

	Fit type	**Fit equation**	**Coefficients**			**RSME**
			a	b	c	
Al	Quad.	$\bar{J} = at_p^2 + bt_p + c$	4.383×10^{-8}	7.041×10^{-5}	0.153	0.000
Fe	Linear	$\bar{J} = bt_p + c$		14.75×10^{-5}	0.058	0.010
Bi	Quad.	$\bar{J} = at_p^2 + bt_p + c$	-1.619×10^{-8}	9.826×10^{-5}	0.134	0.008

One interpretation of this behaviour is that all materials initially experience exponentially increasing ion flux production rates with increasing arc pulse length. However, the material's thermal properties ultimately limit the level and rate of flux growth by increased melting and gradual increase of MP presence in the plasma jet (observed as an increase in erosion rate as previously discussed in Section 5.3.1). At some point, increased heating and melting at ever-longer pulses is sufficient to completely halt the growth of ion flux and possibly reduce it to lower levels (as seen with Bi).

Techniques or design approaches to limit the growth of MP's may allow further growth in ion production rates, e.g. using larger cathodes or increased spot motion. Thus, this work proposes that a given cathode design will have a unique maximum ion flux production rate per input arc current, which depends on the arc pulse characteristics, spot behaviour, cathode size and cathode material. These findings highlight the careful trade-off that must be made by the designer between the generation of ions and MP's when developing VAT and vacuum arc ion sources.

Table 5.3 lists the resulting ICDD parameters against pulse length for Al, Fe and Bi cathodes. Results indicate that operating at longer pulse lengths causes the ICDD to transition from an Exponential distribution to a Gaussian distribution. This occurs because there is a greater amount of time for the cathode spots to traverse the cathode surface and uniformly emit plasma instead of being locally restricted to the cathode edge. Thus, in the case of arc currents as low as 50 A peak, operating with long pulse lengths improves the average momentum transfer of ions in the normal direction by influencing the ICDD.

Table 5.3: Test parameters and results (distribution type, spread, goodness-of-fit, thrust correction factor) for ICDD measurements at various arc pulse lengths. Data from Figure 5.3 is included.

	Pulse characteristics			**ICDD parameters**			
	I (A)	f (Hz)	t_p (μs)	**Dist.**	**Spread**	R^2	C_T
Al	50	10	309	Exp	5.596	0.948	0.590
	50	6	1027	Gauss	1.453	0.969	0.723
	50	6	2161	Gauss	1.154	0.985	0.619
	100	10	1150	Gauss	1.139	0.937	0.613
Fe	50	10	132	Exp	6.300	0.961	0.571
	50	10	506	Exp	6.636	0.934	0.564
	50	10	1416	Gauss	1.431	0.977	0.717
	50	3	2802	Gauss	1.197	0.982	0.637
	120	10	387	Gauss	1.232	0.966	0.651
	100	10	2075	Gauss	1.191	0.977	0.635
Bi	50	2	358	Gauss	1.065	0.986	0.579
	50	2	1448	Gauss	1.154	0.992	0.619
	50	1	3421	Gauss	0.926	0.969	0.505
	50	10	4541	Gauss	0.986	0.978	0.538
	100	10	3282	Gauss	0.879	0.985	0.477

A plot of thrust correction factors[2] shows a more detailed picture of its relation to arc

[2] See Section 2.3.1 for definition.

pulse length. For example, Figure 5.5 reveals what appears to be an optimum C_T region occurring in the t_p = 1000–1500 μs range for all materials tested at I = 50 A peak (as high as 0.72 for Al and Fe, spread w ~1.4). This may have to do with the previously-mentioned ICDD shape transition from an Exponential to a widely-spread Gaussian distribution. As the pulse length increases further, the ICDD becomes narrower, resulting in a lower C_T value until the cathode is saturated with cathode spots, approximating a cathode surface with uniform emission of ions (e.g. see Bi results).

Testing Fe at higher arc currents (I = 100 A peak) as indicated in Figure 5.5 showed that a higher C_T value can occur at short pulses. This is attributed to the increased number and distribution of cathode spots that tends to produce a Gaussian-shaped ICDD. However, this condition appears to keep C_T relatively constant at 0.64–0.65 throughout the arc pulse length range.

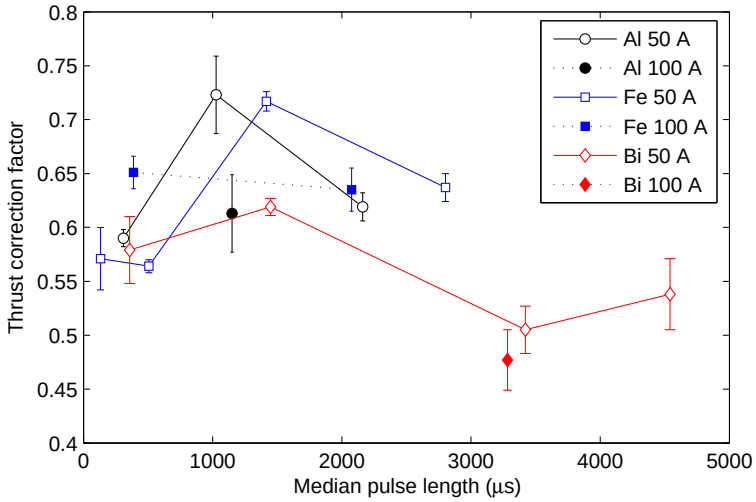

Figure 5.5: Thrust correction factor results for baseline VATS operating at various pulse lengths using (a) Al, (b) Fe and (c) Bi cathodes. Peak arc currents of 50 A and 100 A are studied.

No significant changes in C_T were seen for Bi operating at I = 100 A. This is most likely due to Bi already having a large number of cathode spots present in either case of I = 50 A or 100 A. The lower C_T value in Al at I = 100 A remains unexplained. It may have to do with a poorer-shaped Gaussian distribution fit (R^2 = 0.937) compared to the rest of the ICDD data set (typ. R^2 = 0.97–0.99) or it may provide further evidence that operating the VATs at I = 50 A is a special case as was initially observed in the erosion rate data of Figure 5.2.

The behaviour of the thrust correction factor also indicates some material dependence. Although all materials exhibit similar C_T values under an Exponential distribution, operating at longer arc pulses resulted in some material differences. Both Fe and Al continue to follow similar behaviour in C_T, whilst Bi produces lower increases of C_T and then further decreases in the 3–5 ms pulse length range. Thus, Bi at 3–5 ms represents a special case where two effects are *doubly* reducing the value of C_T. The first is the growth restriction of ion production rate as seen in Figure 5.4 and the second is the narrowing of the ICDD. Both effects can be attributed to the extraneous release of MP's, which impedes the ion flux (see also discussion in Section 4.3.3).

5.3.3 Ion current

Measurements of ion-to-arc current ratios for baseline VATs operating in both short and long pulses under the same single test setup are shown in Table 5.4. Increases of 10.4–16.6% in ϵ were seen across all materials tested, with greater increases for materials with a higher thermal conductivity and boiling point. This result further verifies that operating VATs at longer arc pulse lengths increases the rate of ion production.

Table 5.4: Comparison of averaged ion-to-arc current ratio results for Al, Fe and Bi cathode materials in a baseline VAT design operating with long and short pulses. Peak arc current is I = 50 A.

	Pulse type	t_p (μs)	f (Hz)	ϵ (%)	**Diff.**
Al	Long	1610	10	8.86 ±0.28	+16.6%
	Short	117	6	7.60 ±0.22	
Fe	Long	2156	6	9.25 ±0.12	+12.7%
	Short	228	5	8.21 ±0.12	
Bi	Long	2492	2	6.17 ±0.11	+10.4%
	Short	256	5	5.59 ±0.15	

Ion-to-arc current values for Al and Bi are somewhat lower (32–45%) than that measured by Anders et al. (2005) and Kimblin (1973), whilst Fe shows excellent agreement (3%) with literature (see Table 4.7). Potential causes for this discrepancy may have partially to do with the recession of the cathode within the thruster over the course of the tests, where the electrode configuration of the baseline VAT in this study was such that the cathode and insulator were receded 0.5 mm from the anode face. However, this configuration

was expected to produce no more than 5–10% lower ion current compared to the flush electrode designs used in literature. Further study is required to explain these lower-than-expected values.

5.3.4 Thrust tests

To further investigate the effect that long pulses have on VAT behaviour and performance, thrust measurements were conducted on baseline VATs over a wide range of pulse lengths and cathode materials (Al, Fe, Cu and Bi). Figure 5.6 presents consolidated thrust data for all cathode materials taken from multiple thrust datasets measured over a period of several months. Data shows an increasing trend in thrust production rates (represented here as the ratio of pulsed thrust per average arc current or T/I) with increasing median pulse lengths across all materials tested at I = 50 A peak. Average thrust per arc current values at t_p = 2000 μs were shown to be 11.0–24.9% higher (depending on the cathode material) compared to T/I values measured at t_p = 500 μs. These thrust results run counter to conventional understanding of VATs, which assumes that the thrust production rate should remain constant and relatively independent of arc current levels and pulse duration (within Region E of Figure 1.3).

The cause of the enhanced thrust production effect is not immediately clear. The observed rise in T/I against t_p across different materials operating at the same arc current level suggests that the number of cathode spots present on the surface does not play a significant role here. The arc currents used in this study are also considered too low for appreciable spot interaction (e.g. due to self-magnetic fields) to take place. Increases in T/I could be explained by both the measured ~10% increase in total ion current and ~10% increase in C_T when operating VATs with long arc pulses – giving a ~20% total increase in thrust. However, the significant increases in $\bar{J}$ values observed in the ICDD tests (up to 100–200% increases along thruster centreline) do not fit this explanation. Future measurements of ion charge state distributions and ion energies within long-pulsed vacuum arc plasmas may help shed further light on this mystery.

Additional thrust tests may provide more insight into the mechanism of enhanced thrust

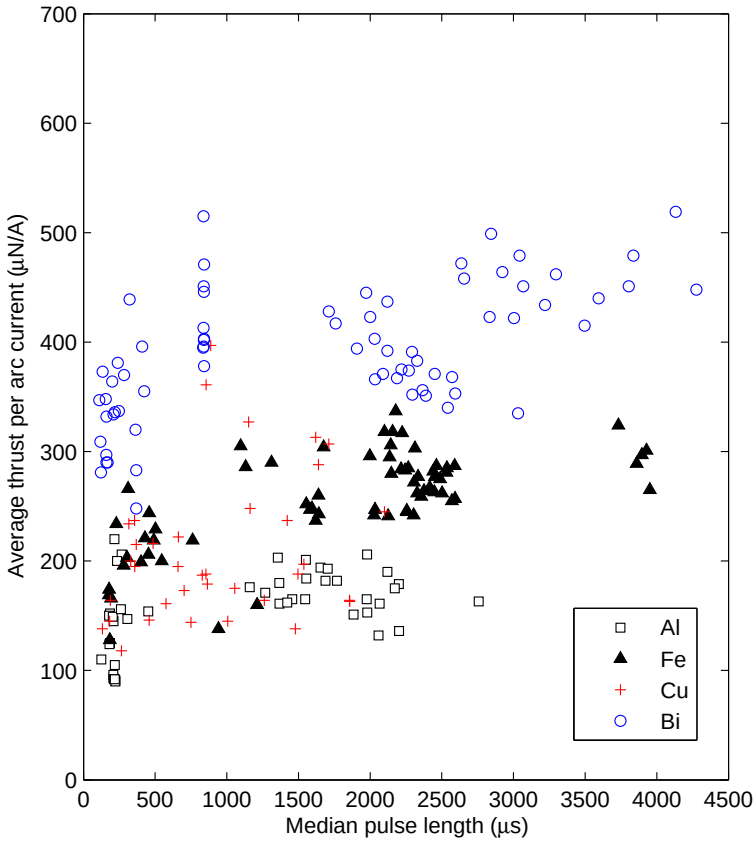

Figure 5.6: Average thrust per current results for baseline VATs using Al, Fe, Cu and Bi cathodes operating at 50 A peak arc current at various pulse lengths. All thrust data here is shown for VATs firing up to no more than a total cumulative arc pulse charge of ~80 C. Error bars have been omitted for visual clarity.

production. For instance, detailed thrust results for Fe presented in Figure 5.7 show that long-pulsed thrust tests running at 25 A and 100 A peak arc current produced differences in thrust production behaviour compared to the 50 A peak tests. Whilst T/I values for Fe running at I = 25 and 100 A peak appeared to also follow an increasing trend with pulse length, both datasets were *below* the 50 A average trend line. This observation suggests that, at least for the case of Fe, operating the baseline VAT at I = 50 A peak represents a special case of VAT operation – a trend consistent with erosion and ICDD results presented earlier. Indeed, test observations showing that the baseline Fe VAT delivers both its largest increase in thrust production (21.3% incr. in T/I to 262 μN/A, t_p = 2000 μs) as well as its largest increase in erosion rate (71.6% incr. in E_r to 75.5 μg/C, t_p = 2213 μs) when operating at I = 50 A and ~2 ms long arc pulses, suggesting a correlation between the two effects.

Thrust tests results on other cathode materials show some agreement with this argument (see Figures D.1 and D.3 in Appendix D). For example, Al showed no observable difference in T/I values for I = 50 and 100 A peak, whilst Bi at I = 100 A peak produced lower T/I values compared to 50 A. This behaviour of Bi could be attributed to the presence of additional neutrals or MP's in the plasma plume when operating the VAT at such a high cathode heat load, thus reducing the ion flux. This issue would be absent in Al, which has a higher capacity to absorb the heat load at high arc currents. Thus, a connection exists between the thermal load present during millisecond-long arc pulses and the production of ions (and thrust).

It should be noted that the thermal load at which the enhanced thrust effect becomes most significant is also governed by the size or surface area of the cathode being used. The broader implication is that long-pulsed VATs utilising cathodes of a certain size will be required to operate with a specific set of arc pulse characteristics (arc current level and pulse length) to experience the maximum effect of this enhanced thrust production mode. In this study, the maximum observed thrust benefit was attained within an oper-

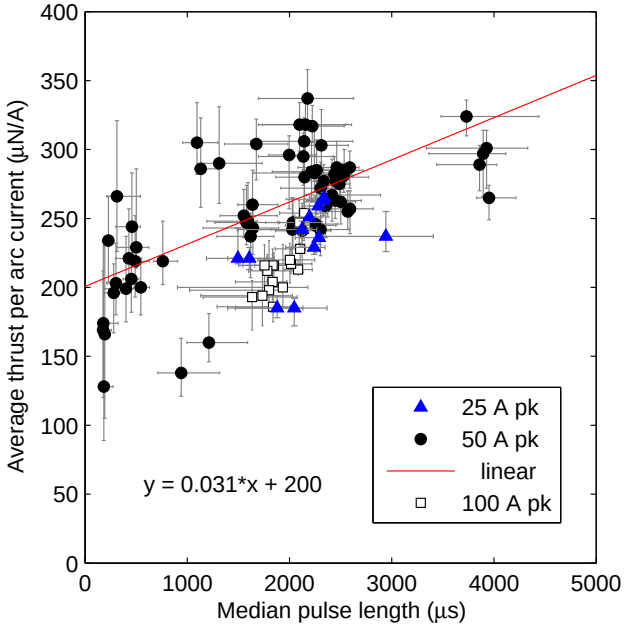

Figure 5.7: Average thruster per current results for baseline VAT with Fe cathode operating at 50 A peak arc current at various pulse lengths. A linear fit (for visual purposes and appropriate within the range and scope of study) through 50 A data shows an increase in average thrust production with increasing pulse length from 216 μN/A at 500 μs to 262 μN/A at 2000 μs (21.3% increase).

ating region of I = 50 A peak arc current, t_p = 2000–4000 μs on a cathode rod of 6.35 mm diameter.

5.3.5 Proposed mechanism for enhanced ion and thrust production rates

Vacuum arcs emit significant amounts of neutral particles. This occurs not only from currently-active cathode spot emission sites, but also from previously-formed sites or craters long after the cathode spot has moved to a different location. This is because these sites are still sufficiently hot from the intense local heating by the vacuum arc to evaporate neutral particles. When the vacuum arc pulse exists up to a certain duration, there may be sufficient time for these excess neutrals to leave the surface, subsequently collide with and become ionised by surrounding plasma emitted from new spot emission sites. The result is an increase in the amount of ions available to provide additional plasma jet momentum. Since all cathode materials emit neutrals, this could explain why all cathode materials tested experienced an improvement in thrust production regardless of their vacuum arc plasma properties.

It is also assumed that increased CEX between ions of high and low charge states occurs during longer arc pulses as hinted at by Anders et al. (2007*b*). This has the effect of lowering both the average ion charge state and energy of the plasma (see Section 1.3.3 and Equation 2.1). Unfortunately, the degree of additional CEX that might be occurring cannot easily be measured with the present method of testing. This is because changes in the average charge state of ions cannot be detected by the FC probe and ion collector since the total charge of the plume remains preserved during capture. It is only the contribution of additional charge by CEX between ions and zero-charge neutrals (introducing "new" momentum-contributing particles into the plasma) that is being detected by the probes.

There are likely to be limits to which thrust production is enhanced under long-pulsed VAT operation. For example, operating at very long pulses (e.g. ≥5–10 ms) could result in an excess of neutrals and MP's due to increased heating of the cathode, potentially reducing ion production as suggested by the arrested growth of peak $\bar{J}$ in Bi ICDD data (Fig-

ure 5.4). Excess neutrals may also significantly reduce the average ion energy (Anders & Yushkov 2007) such that the net momentum of the ions is reduced rather than enhanced. The effect that operating VATs at long arc pulses lengths has on average ion velocity remains unknown at this stage. Finally, excessive cathode heating can lead to accelerated growth of the erosion rate, which is detrimental to the VAT's specific impulse. In conclusion, this study shows that a more nuanced relationship exists between thrust, neutral production and MPs than was previously acknowledged.

5.3.6 Overall performance

An overall view of the typical specific impulse performance of baseline VATs operating with long pulses is given in Table 5.5. For comparison, VATs operating with short pulses are also provided. Average erosion rate data was taken from Table 5.1, whilst average T/I data was obtained by interpolating against the average linear trend lines of Figure 5.7 and other figures in Appendix D. Specific impulse values for each thruster are calculated using Equation 2.3. For example, in the case of Al (t_p = 156 μs), I_{sp} = (133.3/31.2)/9.81 × 10^3 = 436 s.

Table 5.5: Comparison of thruster performance for selected baseline VAT designs for Al, Fe, Cu and Bi cathodes operating with short and long pulses. Peak arc current at I = 50 A.

	t_p (μs)	T/I (μN/A)†	E_r (μg/C)	I_{sp} (s)	**Diff.**
Al	156	133.3	31.2	436	+24.5%
	1906	170.0	31.9	543	
Fe	236	207.3	44.0	480	-24.4%
	2213	268.6	75.5	363	
Cu	166	185.5	48.4	391	-29.2%
	1420	226.9	83.5	277	
Bi	185	355.0	945.5	38	-13.2%
	2130	407.5	1267.4	33	

† Estimated by linear interpolation of T/I trend line in Figure 5.7.

In most cases, operating the baseline VATs with long arc pulse lengths did not guarantee an improvement in the specific impulse efficiency of the thruster. Although long-pulsed VATs generated appreciably higher thrust per arc current values (11.0–24.%), their erosion rates were also significantly higher (typ. 34.0–73.%) compared to short-pulsed VATs.

The net result is that despite the thrust improvement, the long-pulsed VATs were found to have 13.2–29.2% lower I_{sp} values.

An exception is made of Al, which was able to maintain a stable erosion rate for both short and long arc pulse lengths. This meant that the baseline Al VAT was able to achieve a 24.5% increase in specific impulse (543 s) when operated with long pulses. This result is important because it shows that a greater erosion rate is not a prerequisite for a higher thrust production rate, i.e. the additional ion flux originates from neutrals that could already be present during "standard" VAT operating conditions (short pulses). This implies that any means of reducing the excess erosion rate due to the increased thermal load on the cathode surface could potentially allow a long-pulsed VAT to accomplish gains in both thrust production *and* specific impulse.

5.3.7 Comments on surface contaminants and gas absorption

Studies by Yushkov & Anders (1998) found that the pulse repetition rate can affect the composition and ion CSDs of metallic vacuum arc plasmas. By operating at "standard" vacuum arc conditions (50–300 A, 250 μs) and low pulse frequencies (e.g. $\leq$ 1–5 Hz), the plasma composition was found to tend towards a lower average ion charge state because of the absorption of residual gases and formation of oxide monolayers by the cathode surface between pulses. Vacuum levels were also shown to influence the formation time of monolayers, with poorer vacuums generating monolayers at shorter times. Vacuum test pressures used place monolayer formation time on the order of 0.3–0.5 s, i.e. 2–3 Hz for this work, which was close to the operating conditions experienced in a number of long-pulsed VAT thrust tests. Thus, surface contaminants could possibly result in lower average ion charge states, which may not be evident at higher vacuum levels (e.g. 10^{-7} Torr).

However, a comparison of several long-pulsed ICDD and thrust datasets operating either in this transitional pulse frequency region or at higher frequencies (e.g. 10 Hz) failed to show any detectable differences in ion production or thrust from one another, or showed behaviour contrary to what was expected of surface contamination effects. Addition-

ally, lower average ion charge states would have resulted in a shift of ICDD data across all capture angles, which was not observed here. Thus, despite operating at low pulse frequencies, the performance of long-pulsed vacuum arcs did not appear to be significantly affected by the possible presence of residual gases and surface contaminants in this work. Further study, especially at very high vacuum levels will help verify the presence and extent of this possible but unlikely influence.

5.4 Summary

This study has presented experimental performance data of long-pulsed VATs operating in a different manner to that seen in traditional short-pulsed VATs. New erosion rate, ICDD and thrust data on baseline VATs operating in the 150–4500 μs range of pulse lengths was obtained, extending available literature on the performance and behaviour of cathode materials under different pulse conditions. The previously untested VAT operating region was found to cause enhanced rates of ion and thrust production during millisecond-long arc pulse lengths, challenging conventional understanding of VAT operation and vacuum arc behaviour.

In agreement with literature, cathode erosion rates were found to increase (significantly, in the case of Fe, Cu and Bi) with longer pulse lengths due to the increased cathode heat load. The study also showed that the erosion rate was largely governed by local heating of the cathode (pulse length) rather than average heat distribution (average arc power). The number of cathode spots present on the surface was also surmised to influence the cathode erosion rate in a way that higher arc currents (≥100 A) can sometimes lead to a lower erosion rate due to better spot distribution and motion.

ICDD measurements showed significant increases in captured ion charge of up 200% along the thruster centreline when operating with long arc pulses, indicating enhanced ion production. However, total ion current measurements found only up to a 16.6% increase during long-pulsed operation. The discrepancy between these ion data must be further explored.

The previously assumed "standard" thrust correction factor range of 0.64 by Polk et al. (2008) serves only as a rough guideline in the design of VATs . In reality, the value of C_T was found to rely on a host of factors, such as the cathode material, the arc pulse length and the arc current. Other influences such as the manner of cathode spot distribution, erosion coverage on the cathode surface as well as interference from macroparticles were also indicated. The highest-value thrust correction factor of $C_T = 0.72$ was found to exist for Al and Fe operating at 50 A peak arc current and 1–1.5 ms pulse length, delivering a Gaussian-shaped ICDD with a spread factor of $w \sim 1.4$. Further study on MP production in long-pulsed VATs is also needed to better understand its effects on the VAT plasma jet and thrust performance.

Improvements in average thrust per arc current ranged from 11.0–24.9% depending on the cathodes material at $I = 50$ A peak. Charge-exchange collisions between ions and neutrals within the plasma are put forward as the most plausible explanation of the observed increases in ion and thrust production, where the average ion charge state is lowered and neutrals are ionised to contribute additional ion flux to the plasma jet. Further measurements of the ion properties such as the charge state distribution and energy levels should be done to help verify and expand on this hypothesis.

Improvements in the thruster specific impulse were not guaranteed. The significant increases in erosion rate for many of the cathode materials due to the increased thermal load present during long arc pulses was sufficient to overcome the thrust production gains and actually reduce the I_{sp} by as much as 29.2%. However, the performance of Al shows that I_{sp} gains are possible if the thermal load can be successfully managed.

A region of maximum specific impulse operation likely exists for each cathode of a certain size (thermal capacity), material composition and arc pulse characteristics (current, pulse shape, length). The particular example found here was the use of arc pulses consisting of $I = 50$ A peak and $t_p \approx 2000$ μs, which was found to be a distinct test case across all types of measurements on the baseline VAT design, where the common denominator was a cathode of diameter 6.35 mm.

Chapter 6

Cathode shape study

6.1 Introduction

This chapter explores the use of conical surfaces as an alternative cathode geometry to the flat profile of traditional cathode designs used in VATs. Experimental observations and theoretical modelling within related disciplines of laser ablation and nuclear fusion have shown that the ablation of conical surface geometry and convergent plasma flows can produce a significantly different plasma jet emission compared to that from a single or planar plasma jet source. This work presents preliminary studies on the effect of cathode surface shape on the VAT plasma jet's behaviour and thruster performance.

6.2 Method

6.2.1 Cathode design

Due to practical design and time constraints, only one cathode diameter size (6.35 mm) was investigated. Al, Fe and Bi metals were chosen as test cathode materials based on

the wide range of density and thermophysical properties these elements possess. Three concave conical profiles with cone angles of $\alpha = 90°$, $120°$ and $135°$ were each machined out of the baseline cathode rods for each material (Figure 6.1b). The flat cathode profile of the baseline VAT design ($\alpha = 180°$) was also tested to act as a reference cathode design for results comparison (Figure 6.1a). Each conical cathode was mounted flush to the insulator to ensure good edge contact at the thruster front face. The anode electrode was installed 0.5 mm above the insulator tube and cathode to ensure a good line of sight with the cathode for improving the average travel path of electrons flowing across the interelectrode gap.

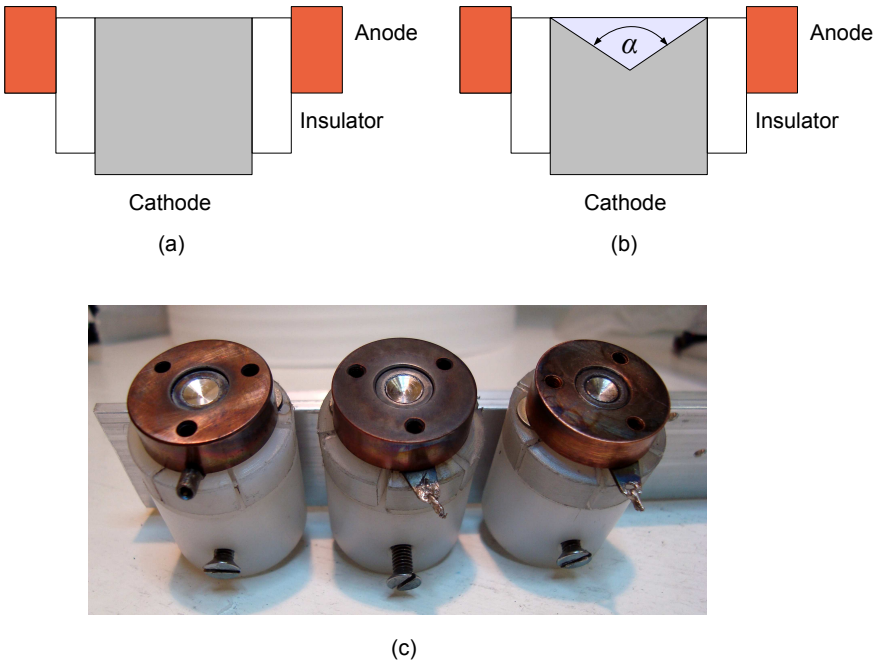

Figure 6.1: Illustration of thruster geometry used in this study with (a) flat and (b) concave cathode surface profile defined by cone angle α. VATs with conical cathodes prepared for testing are shown in (c).

6.2.2 Choice of arc pulse characteristics

Although operating the VAT at much higher arc currents (100 A to kA range) assists in spot coverage (e.g. see Neumann et al. (2009)), the small-sized cathode rods in this study tended to experience significant heating at peak arc currents of 100 A and above. This resulted in poor erosion performance of the conical cathodes rods, which in turn produced poor ICDD and thrust data. Operating at high pulse frequencies ($\geq$ 10 Hz) also tended to

easily overheat the long-pulsed VATs and generate poor or erratic results. Thus, conical Al, Fe and Bi VATs in this shape study were limited to operating at 50 A peak arc current and pulse frequencies of 6, 3 and 1 Hz respectively. The resulting average thruster power levels were kept as low as practically possible at 15–20 W for Al, 5–10 W for Fe, and 1 W for Bi.

Arc pulse lengths used in this shape study were in the millisecond range. Although VAT pulses of 250–500 μs long have traditionally been used, a reasonably long pulse was required in this study to ensure as uniform erosion of the cathode as possible. This behaviour was necessary to ensure that the cathode profile geometry could be maintained for as long as possible during a test. Testing with short pulses generally resulted in only the cathode rod edge being eroded, with little/no erosion at the cathode centre. By using a sufficiently long arc pulse time, cathode spots were able to reach the centre of the cathode rod face and ensure that the full effect of the cathode electrode shape could be utilised and observed. Initial results suggested that the effect of arc pulse length on performance needed to be examined more closely.

6.2.3 Test setup

Analysis of arc pulse behaviour, erosion rates and behaviour, ICDD profiles and thrust from conical cathode VATs was extensively undertaken. ICDD tests were prepared in the same fashion as described in Section 3.6 and conducted with a FC probe distance of 230 mm from the TARS central thruster head assembly. To minimise the effect of setup or thruster build variation on ICDD measurements, thrusters were tested in random order of conical designs and cathode materials. Thrust measurements were conducted with the direct thrust stand (see Section 3.4) and were also randomised by mounting 2 or 3 thrusters with a different combination of conical design and/or cathode material on the thrust stand for any one set of tests.

6.3 Results & discussion

6.3.1 Arc pulse behaviour

Figures 6.2 and 6.3 display measured average arc voltage and pulse lengths for various cathode materials operating with various cone angles. Visual observation of VAT operation showed increasing instability of the arc as narrower cone angles were tested. This generally resulted in a rise of the average arc voltage with cone angle. In addition, difficulty was experienced in generating sufficiently long pulses for tests on 90° cone angles, especially for Al. Both sets of behaviour can be explained by considering the geometric differences between the baseline VAT and the conical VAT as previously illustrated in Figure 6.1. In general, the more recessed the cathode surface is, the greater the interelectrode gap becomes and the higher the arc voltage needs to be to sustain the vacuum arc pulse. Beyond a certain gap distance, the vacuum arc is unable to sustain itself and the arc extinguishes before the arc chopping limit is normally reached. Due to this effect, the shorter pulse lengths present in conical cathode tests were appropriately acknowledged and considered where possible during evaluation of test data in this part of the study.

An exception to this behaviour was Bi, which did not show appreciable drops in average arc voltage or median pulse length with varying cone angle. This may have to do with the low-melting point of Bi, which caused the cathode to generate a large amount of neutrals during the vacuum arc, thus providing a highly conductive medium for sufficient electron flow to occur within the interelectrode gap. This result shows that the production of neutrals and MP's may be considered as one of the many number of feedback mechanisms[1] within the vacuum arc that determines the VAT's operating condition.

[1] Briefly mentioned in Section 2.1.2, feedback mechanisms within the vacuum arc may include interactions between adjacent cathode spots, nearby surfaces (especially the cathode surface) and the near-cathode plasma. An excellent illustration of vacuum arc feedback processes is given by Hantzsche (1983, p. 89).

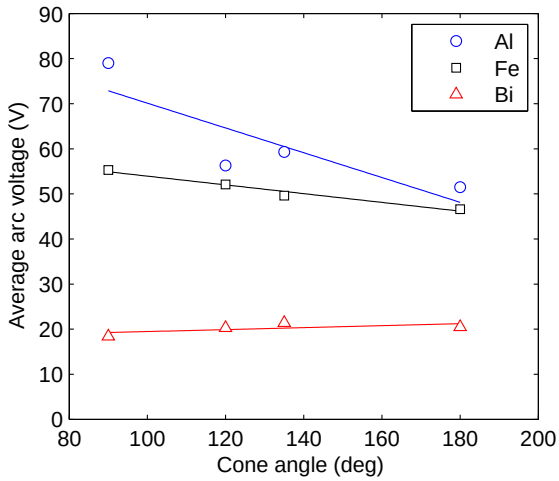

Figure 6.2: Growth of average arc voltage for decreasing cone angle α. Each data point represents combined average of arc voltage test data.

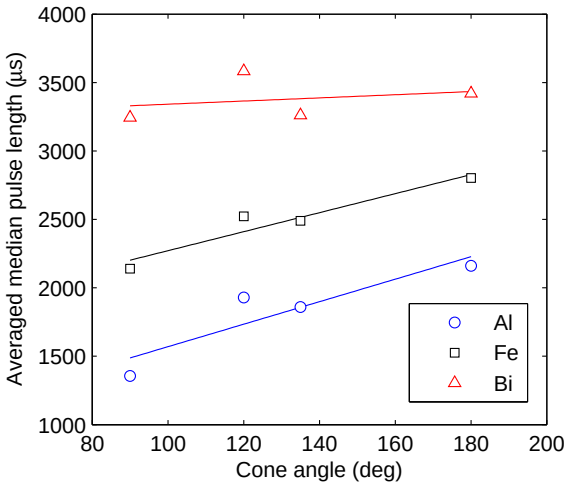

Figure 6.3: Shortening of arc pulse with decreasing cone angle α. Each data point represents combined average of median arc pulse length.

6.3.2 Erosion rate

Erosion rate measurements were made for each material across selected cathode cone angles (α = 180°, 120° and 90°), as shown in Table 6.1 (baseline flat cathode results were obtained from Section 5.3.1). A surprising result was that conical cathodes produced lower cathode erosion rates as the cone angle became narrower. This effect was observed across all materials tested. Generally more uniform cathode spot coverage and erosion was also observed in tests with conical cathodes. Thus, implementing a conical cathode design in a VAT was successful in counteracting the high erosion rates expected with the

use of long arc pulse lengths as discussed in Chapter 5.

Table 6.1: Comparison of average erosion rates of baseline (180°) and conical VATs for selected cone angles (120° and 90°). For additional context, weight-averaged pulse lengths (in milliseconds) during each E_r measurement are included in brackets.

	Erosion rate, E_r (μg/C)					
Cone angle, α (deg)	**Al**		**Fe**		**Bi**	
180° (flat)	33.7 ±1.0	(1.9)	75.5 ±1.1	(2.2)	1606.9 ±9.4	(2.9)
120°	29.5 ±1.1	(1.3)	50.5 ±1.1	(2.2)	952.6 ±1.7	(2.8)
90°	24.9 ±0.9	(1.4)	49.6 ±0.8	(2.6)	938.7 ±3.8	(3.1)

A number of arguments can be made to explain this effect. Firstly, the surface area of the cathode subjected to vacuum arc processes increases with decreasing cone angle. This means that the overall heat load (and hence, temperature) of the cathode per given surface area is reduced since there is more surface available to absorb the thermal load of the arc. For example, 90° and 120° conical cathodes have 41.4% and 15.5% more surface area respectively when compared to the flat cathode (see Figure 6.4). With the exception of Al, more than 15% additional surface area did not appear to cause further reductions in the erosion rates of Fe and Bi. This limit could be linked to the interelectrode gap problem mentioned in the previous section. However, a note should also be made that the slightly longer pulse lengths experienced by the 90° conical cathodes may have biased the E_r data to higher rates than would have been experienced otherwise.

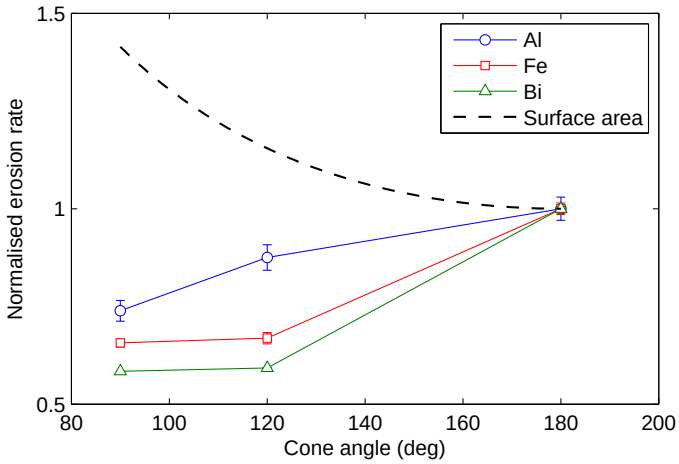

Figure 6.4: Measured cathode erosion rates at selected cone angles of α = 180°, 120° and 90°. Results are normalised to flat cathode result (baseline). Normalised surface area of cathode rod head against cone angle is also included for comparison.

Secondly, the inclined inner surface of the conical cathode was observed to encourage

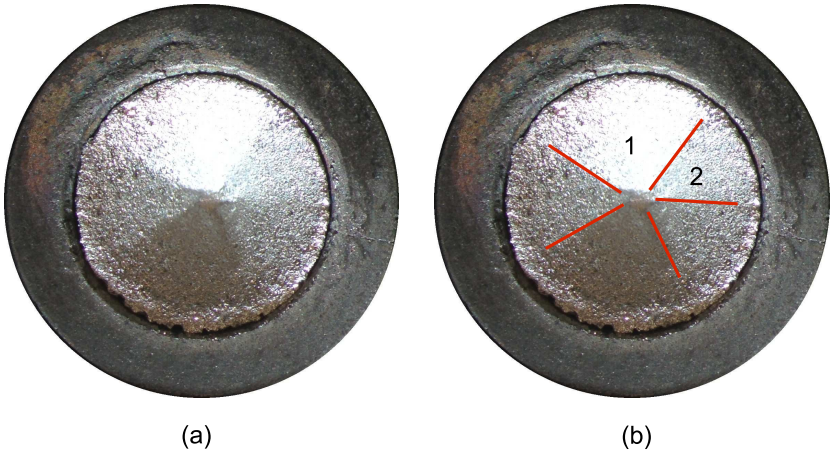

Figure 6.5: View of eroded conical Fe cathode (α = 120°) in (a) unaltered and (b) highlighted views. Radial grooves or "spokes" are highlighted with red lines. Grooves in segment 1 are spaced roughly 80° apart, whilst grooves in segment 2 are spaced roughly 60° apart.

cathode spot motion away from the triggered edge towards the cathode centre. This would have likely resulted in increased spot velocities, a behaviour which could explain the reduced erosion rate. Some supporting evidence is shown in a magnified image of an eroded Fe cathode (120°) in Figure 6.5, which reveals radial grooves or "spokes" in the cathode surface spaced apart in roughly equal fashion. This indicates preferential motion of spots towards the cathode centre, especially along the grooves. What is puzzling, however, is how the grooves are formed and why the grooves are spaced at roughly the same angular distances apart (60°–80°). This may have to do with the ignition probability of new spots being influenced by the surface's exposure to the plasma jet, which expands into the cavity of the conical cathode shape.

Thirdly, the recessed geometry of the conical profile is able to more easily re-capture a portion of MP's and neutrals generated by the vacuum arc spots, re-solidifying them back into the bulk cathode for ionisation a short time later. Thus, on average, less eroded material would be ejected as waste material, resulting in a lower total cathode erosion rate. Future studies are required to further characterise MP behaviour and distribution arising from the use of conical cathodes.

6.3.3 ICDD and thrust correction factors

Figure 6.6 presents ICDD data for all conical cathode designs and materials tested in both pitch (±76.8° range, 9.6° increments) and yaw (±86.4° range, 14.4° increments) axes. Each data point represents an average of twenty $\bar{J}$ measurements taken at a particular position along the pitch or yaw axis, with uncertainty bounds indicative of the degree of scatter within each set of measurements. Of all three materials tested here, Bi ICDD data in Figure 6.6a contained the smallest uncertainty bounds, whilst Al ICDD data in 6.6c contained the largest uncertainty bounds. The ICDD values obtained for Bi were roughly half the magnitude when compared to the ICDD values for Fe and Al, likely corresponding to the lower average ion charge state of Bi. As was argued in Section 4.3, these bounds may be related to how the different number of spots present on each type of cathode material influences erosion, and the plasma jet distribution during each vacuum arc pulse; i.e. the greater the number of active cathode spots on the cathode surface, the smoother the overall plasma jet behaviour becomes.

In all cases, the best surface distribution fit was found to be Gaussian (w_1 = 0.93–1.35, R^2 = 0.92–0.99, RMSE = 0.011–0.023). Measured thrust vector deviations were found to be generally small[2] at $\beta_T \leq 10°$. Figure 6.6 shows that all materials exhibited similar changes in ICDD profiles with varying cone angles. However, Al showed a large decrease in $\bar{J}$ values at $\alpha = 90°$, influenced mostly by the shorter pulse length used there. Peak $\bar{J}$ values showed a general decrease with decreasing cone angle as expected since a more recessed cathode should emit less ions. However, at wide ejection angles, $\bar{J}$ values remained unchanged across all cathode shapes and materials tested. This resulted in a "flattening" of the ICDD profiles with decreasing cone angle.

Figure 6.7 compares thrust correction factors for conical and baseline VAT cathode designs with the median pulse length of each ICDD test included (in brackets, milliseconds). Baseline C_T values shown here were approximated by linear interpolation of data in Table 5.3 according to the equivalent median pulse length[3]. To allow accurate and

[2] Some larger deviations were observed in a number of Fe cathode tests (Figure 6.6b). This was found to be due to insulator edge erosion. This effect did not significantly influence subsequent ICDD and C_T analysis.

[3] An exception is made for the Bi baseline C_T at 5.1 ms. This value was taken from an ICDD test with a

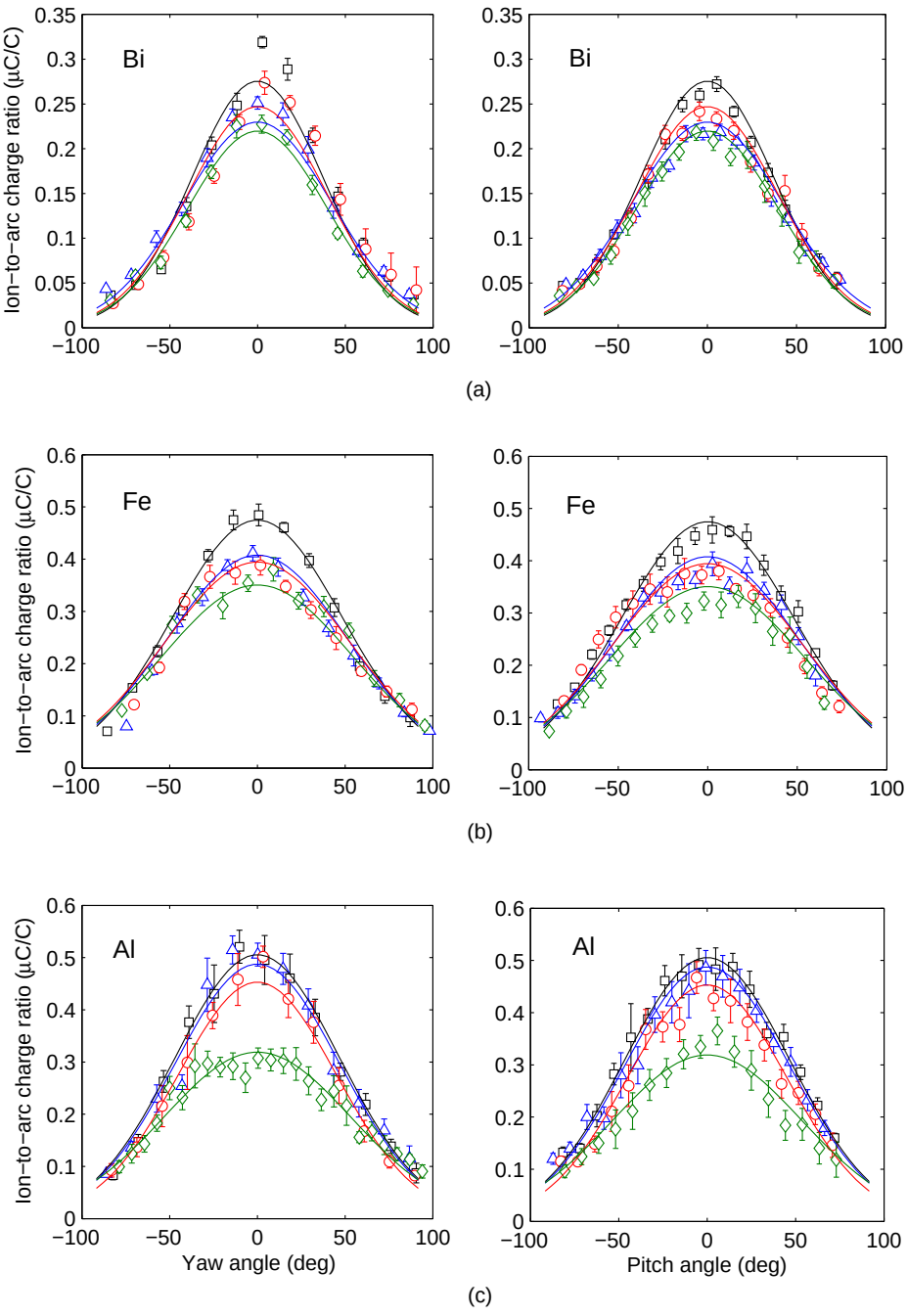

Figure 6.6: Ion current density distribution results for (a) Bi, (b) Fe and (c) Al cathodes at $\alpha = 180°$ (□), 135° (△), 120° (○), and 90° (◇) cone angles along pitch and yaw axes. Data corrected for thrust vector deviation in both pitch and yaw to aid visual comparison.

direct comparison of conical cathodes to the baseline cathode design, "virtual" thrust correction factors were calculated for all conical test cases by mathematically treating each cathode as if it were a flat cathode profile, i.e. identical values of L, r_c and r_a as for the flat reference cathode design. This approach is valid because all designs were

median pulse length of 4541 μs (maximum pulse length measured for baseline Bi VAT in Chapter 5).

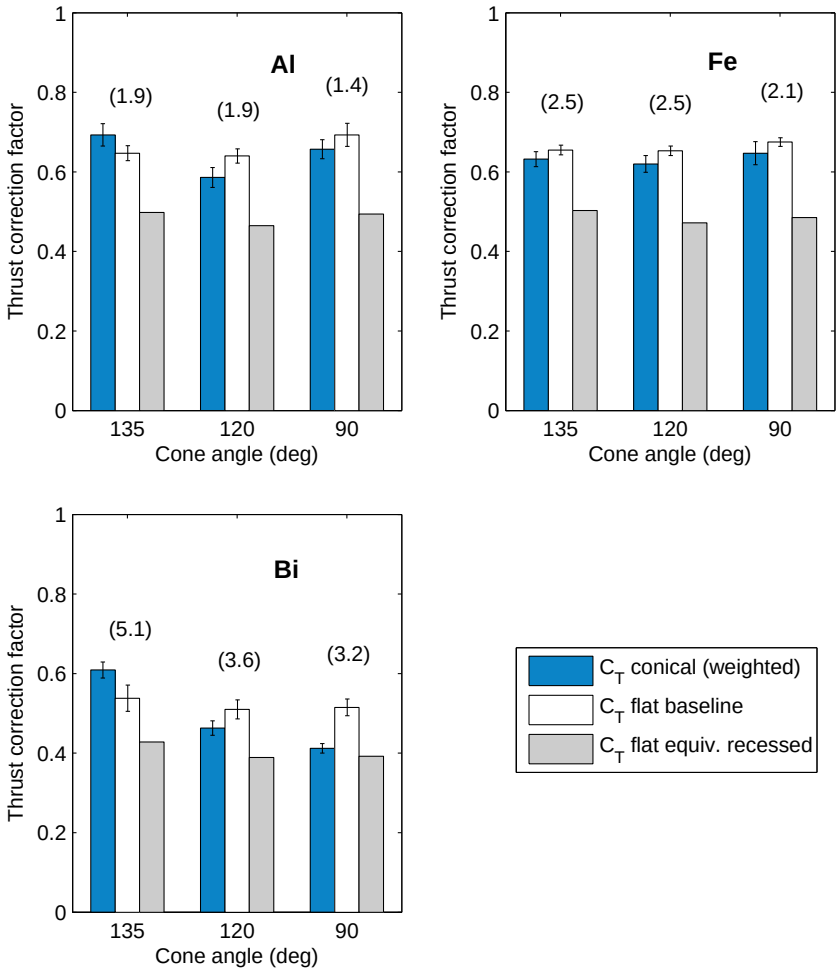

Figure 6.7: Comparison of weighted C_T' values for a conical cathode design against approximated C_T values for a flat cathode design at the same arc pulse length (number in brackets, milliseconds). Flat cathode designs being compared are baseline (0.5 mm recessed) and equivalently recessed to the same depth as a conical cathode design (135° → 0.65 mm, 120° → 0.91 mm, 90° → 1.58 mm).

tested with the same anode electrode, ceramic geometry and ICDD test setup. Additionally, each conical cathode $C_{T,\alpha}$ result was weighted with respect to the reference cathode through comparison of their peak $\bar{J}$ values, thus taking into account both the changes in ICDD spread and magnitude of the conical cathode shape, i.e.

$$C'_{T,\alpha} = \frac{\max\left(\bar{J}_\alpha\right)}{\max\left(\bar{J}_{180}\right)} C_{T,\alpha} \tag{6.1}$$

where $\max\left(\bar{J}_{180}\right)$ was obtained by using the fitted equations of Table 5.2 at the equivalent median pulse length.

Most conical cathode shapes generated average C'_T values similar those of their flat cathode counterparts (5–10% lower than baseline). Notable deviations were Al and Bi at 135°, which generated 7% and 13% higher C'_T values over their baselines respectively and Bi at 90°, which generated a 20% lower C'_T value over the baseline (see Figure 6.8).

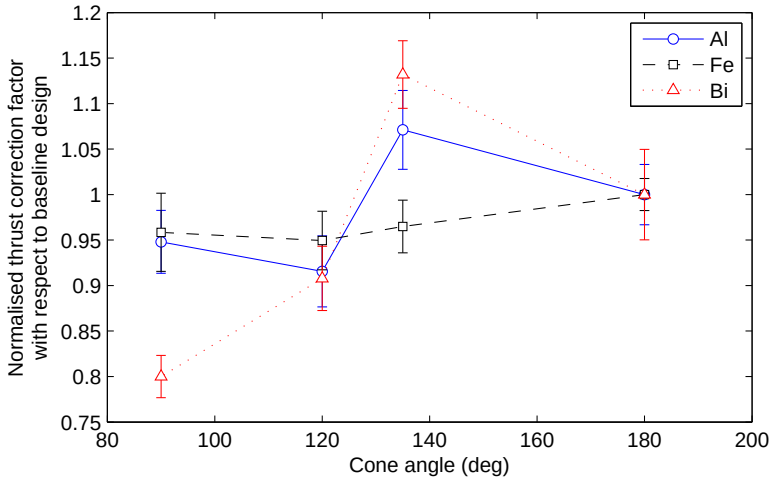

Figure 6.8: Thrust correction factors for conical cathode designs normalised against baseline flat cathode design (α = 180°). Test data taken from Figure 6.7. Pulse lengths used are in the 1.4–5.1 ms range.

Further comparison of conical cathodes against flat cathodes recessed at the same average depths (135° → 0.65 mm, 120° → 0.91 mm, 90° → 1.58 mm) reveals that the conical cathode design produces 15–40% greater momentum in the normal direction. This is most likely due to the angled surfaces of the conical profile, which allows more ions to escape through the VAT front face, even at wide ejection angles. This is consistent with the observed increase in the spread of measured ICDD profiles with decreasing cone angles in Figure 6.6.

However, an exception is made of Bi at 90°, which produced a thrust correction factor nearly identical to that of an equivalently-recessed flat cathode. This result may be due to poor erosion behaviour experienced by Bi, whose melting point is much lower than the other metals tested.

6.3.4 Thrust production

Figure 6.9 presents thrust per arc current results for Al, Fe and Bi cathodes for various cone angles. A normalised version of these results are given in Figure 6.10. Each data point represents an average of 16 individual thrust tests taken for each thruster type operated up to a total pulse charge of roughly $\sum Q = 50$ C. Linear solid lines represent the average T/I values for each cathode material operating in a baseline VAT across a range of pulse lengths (obtained from Figures D.1–5.7 and D.3.).

A significant number of conical cathode designs across all materials were shown to generate enhanced thrust production over the baseline (typically 10–30% higher, see Figure 6.10). A few exceptions included some test cases for Al and Fe, which generated no thrust

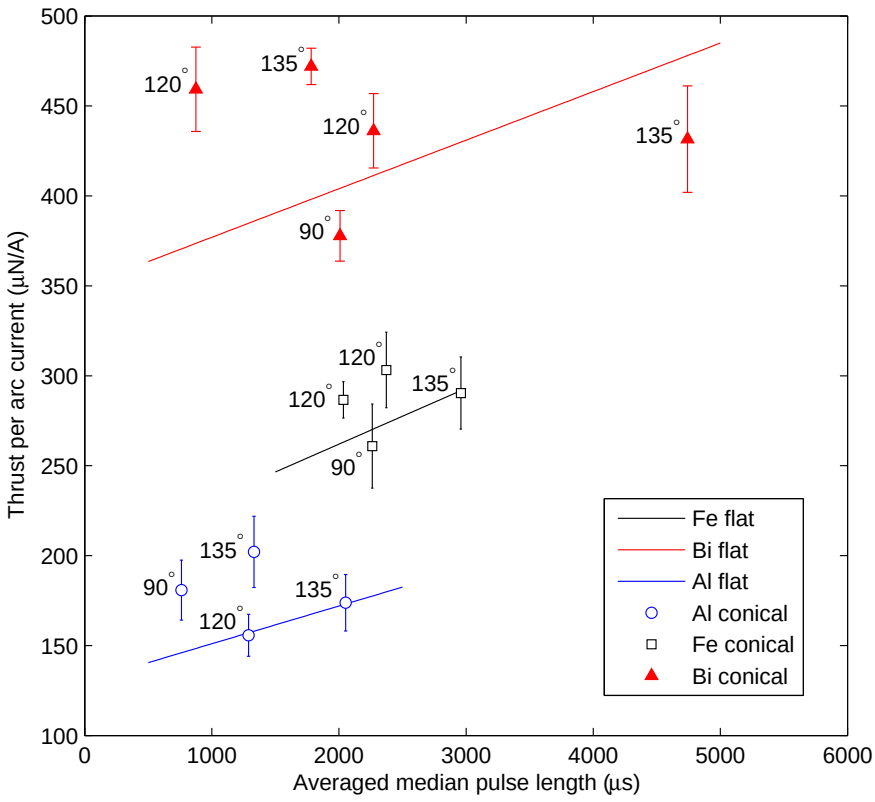

Figure 6.9: Thrust measurements (T/I) measured at various cathode cone angles ($\alpha = 90°$, 120° and 135°). Each data point is an average of 16 thrust tests run up to $\sum Q \approx 50$ C. Trend lines shown represent average thrust per arc current for baseline flat cathodes tested in this study as presented in Figures D.1–5.7 and D.3.

improvement, whilst the 90° and one 135° test case for Bi produced 5–10% lower thrust production rate. At first glance of the data in Figure 6.9, no discernible relationship appears visible between thrust production and cone angle within a specified cathode material. In each material tested, the same conical design can produce different changes in thrust production depending on the median pulse length that was used (e.g. Al 135°, Bi 135° and 120°). Part of the problem lies in the inherent coupling of pulse length and thrust within the test data, a relationship previously established in Chapter 5.

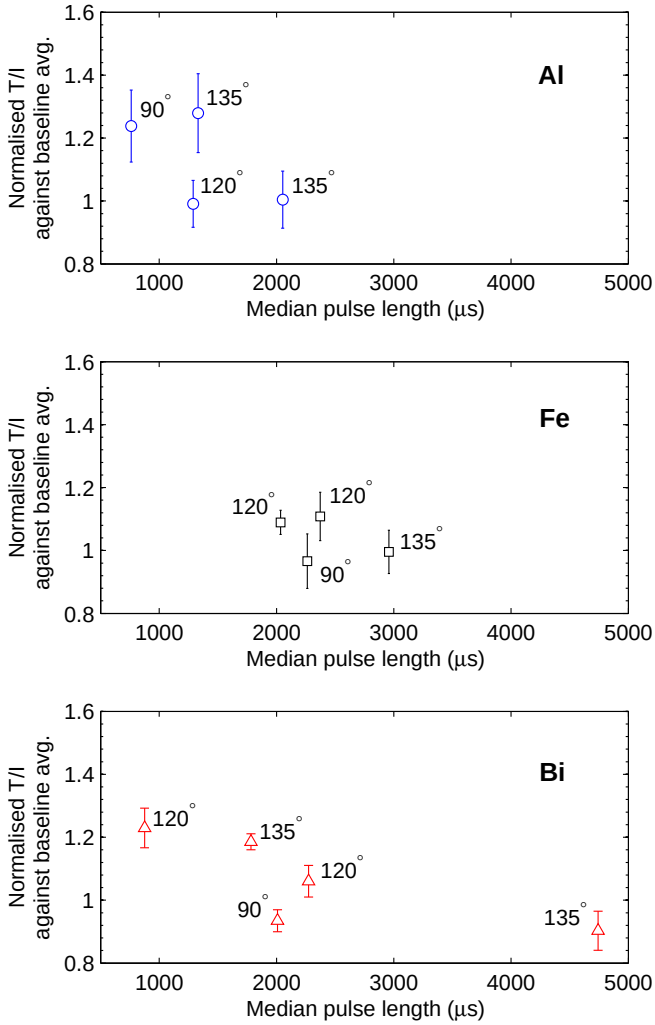

Figure 6.10: Measured thrust per arc current for various cathode cone angles ($\alpha = 90°$, 120° and 135°) normalised against baseline average thrust trend lines. Test data taken from Figure 6.9.

However, consolidating Figure 6.10's normalised data for all cathode materials against pulse length, may offer some insights. This approach assumes that the choice of cathode material exerts a weak influence on thrust production as seen by the similar levels

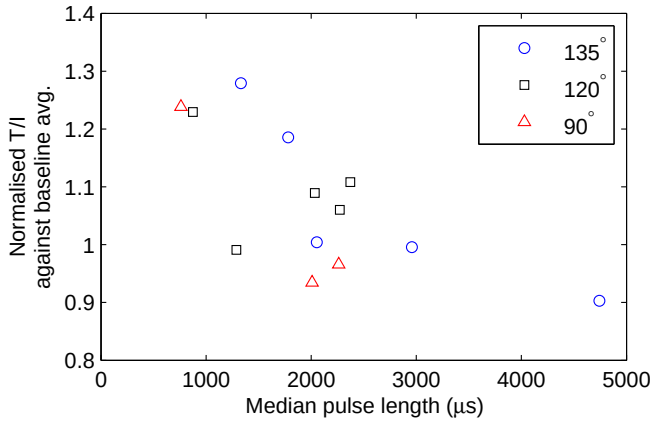

Figure 6.11: Consolidated average T/I values for various cathode cone angles ($\alpha = 90°$, 120° and 135°) and materials normalised against baseline average thrust trend lines. Test data taken from Figure 6.10.

of relative thrust changes experienced across all materials used in this study. The consolidated data plot shown in Figure 6.11 suggests a number of interesting relationships. Firstly, it appears that the relative change in thrust production ($\Delta T/I$) due to the cathode conical shape exhibits a pulse length dependence. The highest gains (20–27%) in $\Delta T/I$ initially occur in the t_p = 1–1.5 ms range, eventually declining to the lowest (or negative) gains (-5–10%) as the pulse length extends into the t_p = 2–5 ms range. Secondly, changes in thrust production appear just as sensitive, if not more so, to the arc pulse length than to the actual cone angle being used. Thirdly, nearly all results for cone angles 135° and 120° deliver similar trends in $\Delta T/I$, whilst similar levels of $\Delta T/I$ for cone angle 90° are roughly shifted to lower pulse lengths. Given that the thrust-to-pulse length relation (as found in Chapter 5) has already been taken into account by means of data normalisation, these observations bear a second relation to the pulse length or rather, the time duration over which the arc spots have travelled across the cathode surface profile. A possible explanation for this behaviour is given below.

It was observed in this work that once arc initiation took place, the cathode spot generally tended to travel away from the triggered edge and over the exposed bulk cathode surface. In the case of a conical profile, the spot encounters the inclined inner surface of the cathode, causing its motion to increase (Section 6.3.2) and become more recessed into the cathode as it moves towards the cathode centre. The rate and extent to which the spot recedes into the cathode will depend on the cathode cone angle and the arc pulse

length, where a narrower cone angle results in faster spot motion, whilst a longer pulse length results in further spot travel. The net effect is that a deeply-recessed spot will produce lower thrust than a spot closer to the thruster front face. This is consistent with observations in Figure 6.11. In other words, short pulses and wide cone angles result in the largest increases in $\Delta T/I$, whilst long pulses and narrow cone angles result in small or even reduced $\Delta T/I$. A simplified four-outcome summary of these effects are shown in grid form in Figure 6.12.

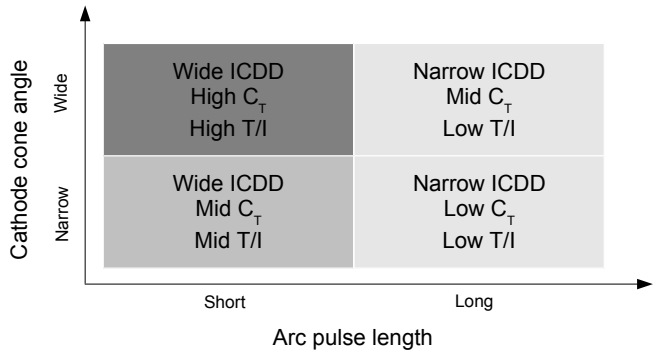

Figure 6.12: Simplified four-quadrant outcome on plasma jet shape and thrust production as a function of cathode cone angle and arc pulse length.

In conclusion, the conical profile of the cathode (6.35 mm diameter) is most effective in enhancing thrust production by up to $\Delta T/I$ = 27% when operating with wider cone angles (120°–135°) and pulse lengths of $t_p \leq 1.5$ ms, equal to and even surpassing T/I values obtained at much longer arc pulse lengths. A further extension of these findings is that there likely exists an optimum cone angle for a fixed pulse length that produces a maximum thrust production rate and/or thrust correction factor, which can be roughly assumed to be within the range $135° \leq \alpha < 180°$ for the VATs used in this study.

6.3.5 Overall performance

Table 6.2 compares key performance metrics for selected conical designs against baseline VATs with significant increases in I_{sp} across all example test cases (34.7–67.9% improvement). Test cases with cone angles 120° and 135° demonstrated the best overall performance features with up to a 20–28% increase in thrust per arc current, a 26–42% decrease in erosion rate, and with a penalty of only a few volts rise in average arc voltage (Figure 6.2). Thus, conical cathodes have been successfully demonstrated to significantly

improve VAT performance by simultaneously increasing thrust production and reducing fuel consumption to achieve a compounded improvement in thruster specific impulse. Furthermore, a design trade-off can be made to obtain the best I_{sp} value of a particular VAT design by deciding on a careful balance of interacting factors such as cathode size, cathode cone angle and arc pulse length.

Table 6.2: Comparison of VAT performance for selected conical and equivalent baseline VAT designs operating with Al, Fe and Bi cathodes at I = 50 A. Thrust and erosion rate data taken at similar millisecond-range pulse lengths for each case pair.

	Cathode design	t_p (ms)	T/I (μN/A)	E_r (μg/C)	I_{sp} (s)	**Diff.**
Al	Baseline flat	1.3	158.0	31.6†	510	+34.7%
	135° cone		202.1	30.0*	687	
Fe	Baseline flat	2.2	273.6	75.5	369	+65.9%
	120° cone		303.2	50.5	612	
Bi	Baseline flat	2.3–2.8	411.4	1483.6†	28	+67.9%
	120° cone		436.2	952.6	47	

† Estimated by linear interpolation of E_r values in Figure 5.2.
* Estimated by linear interpolation of E_r values for cone angles α = 120° and 180°.

6.3.6 Possible explanations for enhanced thrust

Recalling the expression for VAT thrust from Equation 2.1,

$$T = C_T \left(m_i \frac{I_i}{e\bar{Z}} \right) \bar{v}_i \tag{6.2}$$

the observed thrust increases in this cathode shape study could be attributed to changes in the plasma jet shape (thrust correction factor), average ion charge state, total ion current and/or average ion velocity. In the complex environment of the vacuum arc, the thrust changes observed are likely to be due to a combination of all these effects to varying degrees, given that they are not necessarily independent of one other.

Observed changes in the thrust correction factor did not always result in a corresponding change in thrust production. While a few ICDD test cases did show matching behaviour (e.g. Fe 135°, 2.5–3 ms; Fe 90°, 2.1–2.3 ms), other cases did not (e.g. Al 135°, 1.9–2.1 ms; Fe 120°, 2.4–2.5 ms; Bi 135°, 4.7–5.1 ms). This variability could be attributed to the limited sample size and pulse length range of the ICDD data. Unfortunately, no strong

correlation between changes in C_T and corresponding changes in T/I for pulse lengths $\geq$ 2 ms can be definitively stated based on this.

A study of T/I data in the t_p = 1–1.5 ms range, however, could be attributed to changes in C_T. As was previously established in Section 6.3.3, conical cathode profiles produced a more spread out ICDD than a flat cathode due to its inclined surface. As was observed in erosion tests in the pulse length study in Chapter 5, Section 5.3.1, it was also found in this study that preliminary conical cathode tests using shorter arc pulses ($\leq$1 ms) produced cathode spots less recessed within the conical profile, which in turn would be expected to also increase the spread of the overall ICDD. Lastly, data in Section 5.3.2 showed that "flatter" ICDD's produced higher C_T values, particularly in the 1–1.5 ms range. With all these observations in mind, could the largest $\Delta T/I$ values observed here for conically-shaped cathodes operating at t_p = 1–1.5 ms be entirely attributed to a highly spread out ICDD and an increase in C_T alone?

A quick check against the largest measured test case suggests otherwise. For example, consider the case of Al 135° at t_p = 1.3–1.4 ms with an estimated baseline C_T value of 0.693 (Figure 6.7) and a relative average thrust increase over the baseline T/I of 27.9% (Figure 6.10). If the total gain in thrust production was due to an increase in C_T alone, that would imply that C_T would have increased from 0.693 to 0.886, i.e. 88.6% of the total ion momentum contributes thrust in the normal direction. Although theoretically possible, such a scenario seems unlikely. A more realistic situation is that the change in plasma jet shape produces a limited increase in the value of C_T, providing only a partial contribution to the overall thrust gain seen in conical cathode designs. In addition, the effect of C_T on the overall T/I of the conical cathode design is highly dependant on the pulse length. Thus, other (and potentially more dominant) influences apart from the change in C_T must also play a role to account for the improved thrust production seen here.

Additional evidence for influences other than C_T on final thrust can be shown in the test cases of Fe 120° tested within the 2–2.5 ms range. Figures 6.7 and 6.8 show that the thrust correction factor for a Fe 120° conical design is 5% lower than its flat baseline value. However, Figures 6.9 and 6.10 report that the same Fe cathode design experienced

a 10% *increase* in T/I above its flat baseline result. This meant that Fe 120° conical design achieved a greater T/I than the flat baseline despite almost no change in the thrust correction factor.

Other possible influences could include an additional increase in CEX between neutrals and ions. The geometry of a conical cathode is such that the trajectories of emitted particles have greater likelihood of crossing paths and hence increase ionisation for greater ion flux. Unfortunately, this is only speculation at this point. Further in-depth studies on plasma properties of conical cathodes is required.

Another possible contribution may include plasma acceleration, where the conical cathode geometry shapes and accelerates the exiting plasma jet with the creation of a localized region of high pressure just in front of the cathode. Such a pressure region has been observed in recent laser ablation experiments (Luna et al. 2007, Yeates et al. 2011, Gambino et al. 2013), where a stagnation region was observed to form between two pulsed plasma jets, lasting for much longer than the jet pulse themselves. This higher pressure region of plasma in front of the cathode may serve to increase plasma diffusion away from the thruster and thus enhance thrust. However, this proposed behaviour requires confirmation in future plume studies.

As a side note, Lebedev et al. (2002) showed that the ion mass had an influence on the focusing effect in conically convergent plasma flows. Materials with a high mass were seen to produce narrower and faster jets due to their higher radiative cooling properties. Unfortunately, similar levels and behaviour in relative thrust production experienced across all the cathode materials in this study was insufficient to show (at least for now) that a material dependence exists for the plasma jets created by conical cathode profiles.

In conclusion, the exact cause of the thrust increases observed for a number of conical cathode designs in this study remains unknown. The change in the shape of the plasma jet can be considered a partial contributor, but other influences such as CEX and plasma acceleration need to be explored.

6.4 Summary

This study has shown that a simple change to the shape of the cathode electrode may affect VAT performance in a number of ways. Measurements of erosion rate, ICDDs and thrust of various conical cathode shapes using different cathode materials were performed and showed that, in some cases, a greater amount of thrust and lower levels of erosion rate were achieved compared to the baseline VAT design under the same arc conditions. This resulted in significant increases in the specific impulse of conical cathode designs – as high as 67.9% above the baseline result and achieving values approaching 700 s on what are generally considered medium-performance cathode materials. Further testing on additional materials with typically high performance (e.g. Mg, Ti, Cr, Zr, see Appendix A.1) may yield similar improvements in specific impulse, easily breaking the I_{sp} = 1000 s mark.

The cause and mechanism of the thrust increase experienced with conical cathode profiles can only be partially explained and required further investigation. Evidence indicates that at least two design factors made a significant influence on thrust production, namely the arc pulse length and the cathode cone angle. Both factors dictated how widely-spread out the plasma jet's ICDD became, which in turn determines the level of ion momentum that is normally-directed (wider cone angles and shorter pulses in the 1 ms range tend to result in large thrust gains). The complex relationship between spot motion and cathode profile geometry was also recognised and outlined within this study, leading to a greater understanding towards optimisation of VAT performance. However, many aspects of conical cathode behaviour remain not yet fully understood and must be further investigated.

Consolidation of thrust data found that the cathode material had a weaker influence over relative thrust gains than initially expected. This may be due to the limited sample size of captured data as well as in the limited control of the manner in which cathode material was eroded and ionised. Another factor might be that the operational conditions of the VATs were outside the region in which material effects became evident. Further testing with additional materials and different-sized cathodes is also recommended.

Finally, maintaining a stable conical profile geometry over long periods of thruster operation remains a technical challenge. The present thruster design limits the use of conical cathodes due to its edge-triggered arc initiation mechanism, which flattens the cathode profile as the surface erodes away (spots travel outside → in). This limited test durations to only several thousand pulses before the conical profile geometry underwent appreciable change. A better solution is to incorporate a centrally-triggered mechanism, which will help to maintain the conical profile of the cathode (spots travel inside → out). Central triggering will also help ensure uniform and consistent spot coverage, which may aid in the accuracy of future testing.

Chapter 7

Carbon cathode study

7.1 Introduction

Carbon possesses different material properties and structural characteristics from metals, posing unique engineering challenges and scientifically interesting behaviour as a cathode material. This chapter examines the novel use of carbon graphite and graphite compounds as cathode fuels for VATs. An assessment of erosion behaviour, ion current production and thruster performance was made on various carbon cathodes installed on the baseline VAT design.

7.2 Method

7.2.1 Material list

Several carbon-based cathode material candidates were explored, covering a variety of physical properties, microstructure and composition. Table 7.1 lists the various grades and properties of the 6 and 6.35 mm dia. × 50 mm long carbon rods tested in this

study. These rods were mostly sourced from suppliers of EDM-grade electrodes (EDM = Electric Discharge Machining), which are prepared specifically for arc-related industrial applications. In particular, POCO electrodes were chosen for their highly isotropic nature and lower porosity (< 0.1 μm) over traditional graphites. Graphite compounds were also initially explored by testing copper-impregnated graphite compounds, which are comprised of a homogeneous mixture of copper and graphite micro-particles (estimated 15% Cu by volume according to the final sample material's density). Finally, Glassy (or vitreous carbon) exhibits unique structural and thermophysical features compared to graphite, with noticeable features such as extreme hardness, zero porosity, impermeability to liquids and gases as well as being composed of nano-sized structures (fullerene).

Table 7.1: List of grades and properties of carbon rod materials tested in this study (data obtained from suppliers' websites). Carbon materials are grouped according to their composition, namely that of (1) pure carbon and (2) copper-impregnated graphite compounds. Materials are arranged in order of increasing average particle size.

Name & grade	**Supplier**	**Avg. particle size** (μm)	**Density** (g/cm^3)	**Electrical resistivity** ($\mu\Omega$.cm)
Pure carbon				
GC (G series)*	HTW	< 0.01	1.42	114
AF-5	POCO	1	1.80	1727
EDM-3	POCO	5	1.81	1372
EDM-200	POCO	10	1.82	1219
Copper-impregnated graphite†				
TTK-4C	Toyo Tanso	4	2.90	254
EDM-C3	POCO	5	3.05	305
EDM-C200	POCO	10	3.00	178

* Glassy carbon
† Estimated 15% Cu by volume

7.2.2 Operating conditions and performance tests

Arc pulses of 50 A peak were exclusively applied to all carbon VAT tests. This was mostly because of ensuring restricted thermal loading on the cathode as well as a limitation of the pulse circuit components, which experienced difficulty in generating higher peak arc currents due to the higher resistance of carbon cathodes. Testing at arc currents lower than 50 A were deemed to be of little value, given that carbon experiences only a single spot for arc currents ≤ 200 A (Boxman et al. 1995). This meant that, apart from thermal considerations, vacuum arc cathode spot behaviour and features were not expected to

significantly change within the I = 10–200 A range. Additionally, generating pulses with peak arc currents above 200 A becomes more technically challenging to accomplish, especially in the context of a small and safe VAT design for small satellites like the CubeSat. Further exploration will be needed to expand on the limited test conditions of the carbon cathode study presented in this work.

Various VAT performance tests were conducted on each carbon or graphite cathode sample, capturing detailed measurements of thrust, erosion rate, total ion current and plume distribution (C-3 only). Thrust and most erosion tests were combined in a single test run, where the VATs were initially fired for up to approximately $\sum Q$ = 20 C with 10 short pulse measurements ($\leq$ 500 μs) and then up to $\sum Q$ = 60–100 C with 20-30 long pulse measurements (~2 ms). This was done to assess if any change in thrust production against arc pulse length was present. Visual inspection of cathode erosion behaviour on each sample was also performed.

7.3 Results & discussion

7.3.1 Overall behaviour and thrust production

Pure carbon cathodes

Figure 7.1 displays erosion patterns for pure carbon and graphite samples resulting from the combined thrust and erosion tests. The erosion pattern on all graphite cathodes were observed to consist of deep craters (on the order of 0.5–1 mm) concentrated at the triggering edge of the cathode rod and tended not to extend further than roughly 1 mm from the insulator inner edge. The eroded surface roughness of GC was different to that of the other graphite cathodes. Apart from being largely restricted to the rod edge, its eroded surface was considerably finer, most likely due to the nano-sized structures and superior hardness of GC. Carbon cathode erosion behaviour was in stark contrast to the more uniform and distributed erosion of metal cathodes. This can be explained by consid-

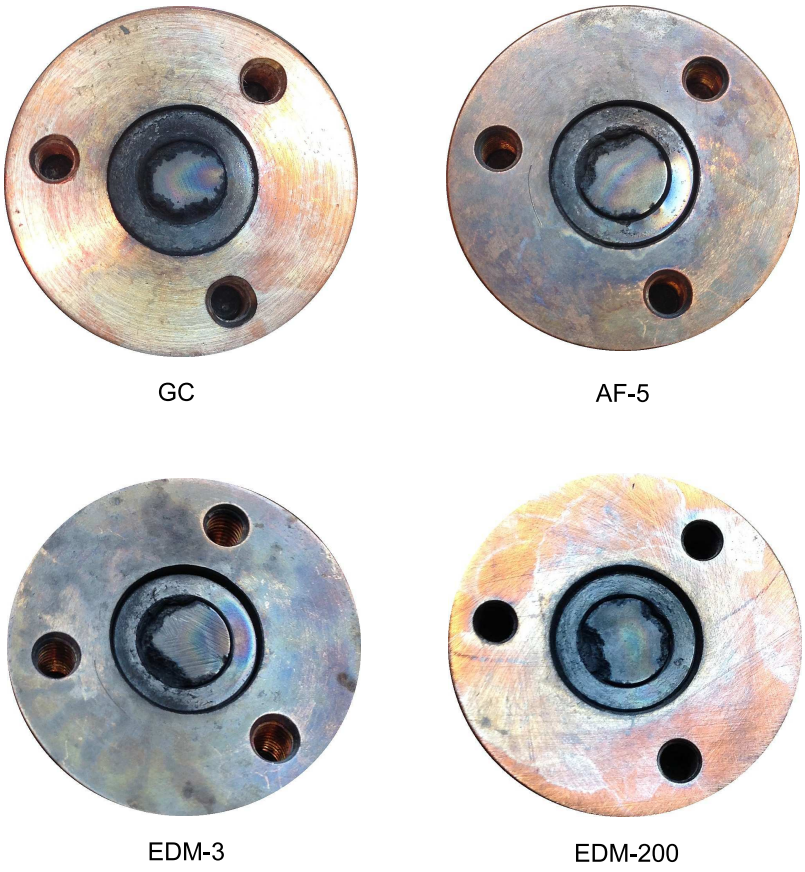

Figure 7.1: Photographs of cathode erosion for Glassy carbon (GC) and AF-5, EDM-3 and EDM-200 pure carbon graphite rods.

ering the following:– firstly, temperature has a unique effect on the resistivity of carbon graphite, which behaves in a manner *opposite* to metals, i.e. graphite becomes more electrically conductive the hotter it gets. The result is that cathode spots are discouraged from moving away from their locations and tend to "burrow" themselves into the bulk cathode body. Secondly, spot motion is also discouraged by the typically low thermal conductivity levels (30–45 W/mK[1]) locally experienced by graphite material heated up by the high temperature cathode spots. This means that surface conditions for subsequent cathode spot generation are most suitable close to the previously extinguished hot crater site and least suitable far away on the colder bulk body surface. Thirdly, graphite does not melt, but instead sublimates. In metals, the molten state of freshly-made craters causes the surrounding metal to flow, spread out and blend back into the bulk cathode surface. This material behaviour is absent in graphite. Finally, the formation of deep craters widens the gap between the cathode and insulator, further isolating the central

[1] Supplier's website – `http://www.poco.com`

core of the cathode body from stable vacuum arc processes.

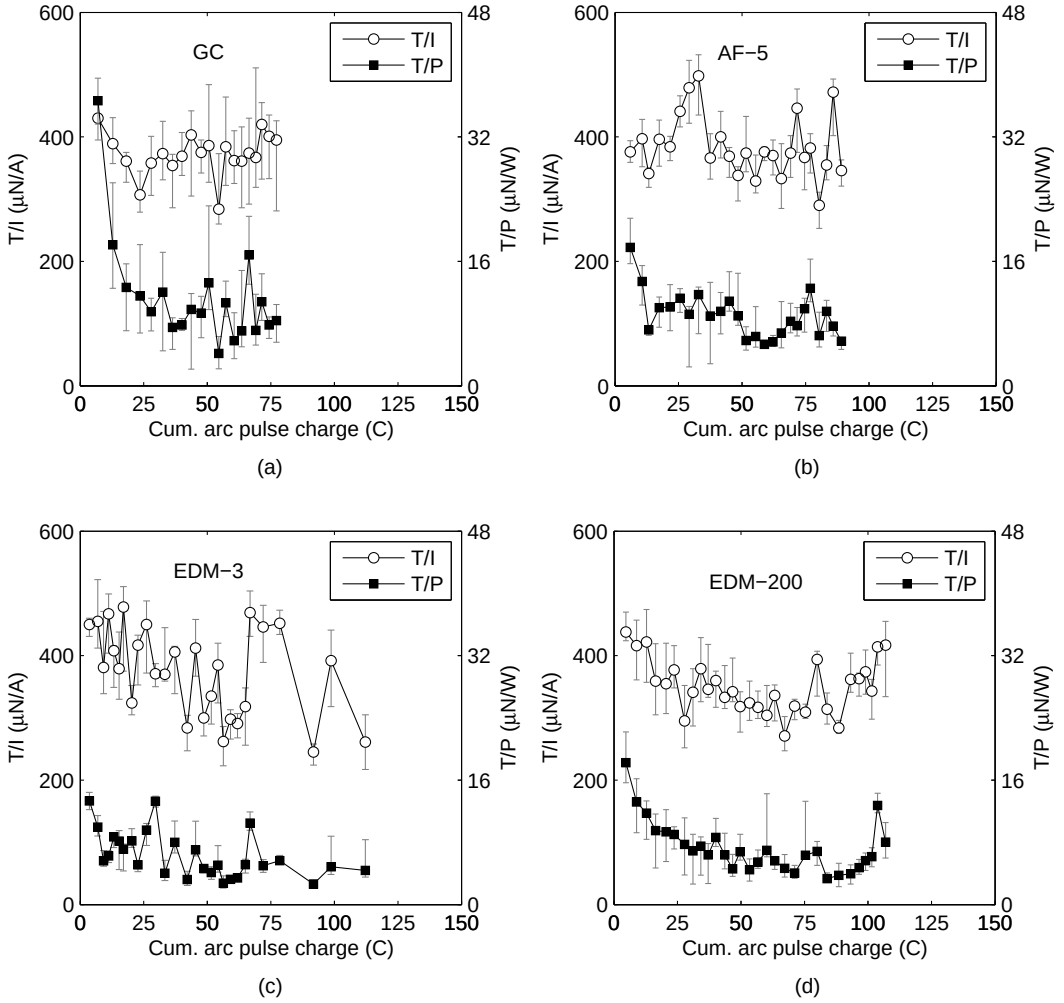

Figure 7.2: Measured thrust per arc current (left vertical axis) and thrust-to-power ratios (right vertical axis) over test duration for pure carbon cathodes. Materials include (a) GC, (b) AF-5, (c) EDM-3 and (d) EDM-200. Total cumulative pulse charges range from 80 to 120 C. Lines through data points are for visual aid only.

Figure 7.2 displays thrust measurements for the pure carbon materials tested in terms of thrust per arc current T/I and thrust-to-power ratio T/P for typically 6000 pulses. For much of the test, thrust production of GC and AF-5 remained relatively constant at 380 μN/A with a few intermittent "spikes" of high and low values. This was in contrast to EDM-3 and EDM-200, which showed a decline of thrust per current levels (450 μN/A $\rightarrow$ 300 μN/A) as the total number of pulses increased. Additionally, EDM-3 results were more erratic and EDM-200 thrust production showed a gradual increase near the end of its test (80–110 C). Thrust-to-power levels were initially very high (up to 36 μN/W for GC, $\sim$ 16 μN/W for the rest of the group) and showed a rapid decline to 5–8 μN/W at the end

of the test run.

In contrast to metallic cathodes in Chapter 5, no discernible changes in carbon's thrust production was observed between short- and long-pulsed operation. However, this difference could be partially obscured by the effect of the fast-receding cathode. Nevertheless, these results support the view put forward in Chapter 5 that increased thrust production at long pulses is due to greater amounts of CEX between ions and neutrals reducing the average ion charge state. This is because C ions from a pulse vacuum arc were previously measured in literature to be almost entirely singly charged, i.e. $\bar{Z} = 1$ (Yushkov & Anders 1998, Brown 1994). Thus, further lowering of $\bar{Z}$ using longer arc pulses is not possible in this case, with the expected result that thrust production remains constant regardless of arc pulse length.

The negative effects of deep crater erosion on the emission of plasma flux and arc voltage was evident in Figure 7.2, where thrust production of EDM-3 and EDM-200 underwent a decline over time as the cathode spot became more receded into the cathode body. This effect is further exasperated by the low density of graphite rods. Eventually, a relatively stable thrust value was approached, likely due to the depth limit of the craters being reached. Intermittent bursts of high thrust values can be explained by the cathode spots travelling back to the top of the cathode surface and generating more plasma, before eroding part of the surface away and quickly receding into deep craters again. Erosion uniformity is obviously affected by the size of the cathode. For example, a smaller cathode would experience better erosion characteristics since the erosion "zone" would occur over much large portion of the cathode surface. However, cathode recession would also occur at a higher rate, not to mention increased thermal loading on the smaller cathode body. Thus, design trade-offs and a suitable electrode design must be carefully considered for carbon-based cathodes to address its unique erosion behaviour.

Copper-graphite compound cathodes

Figure 7.3 displays erosion patterns on copper-graphite compounds cathode resulting from the combined thrust and erosion tests. Erosion behaviour of copper-graphite ma-

terials exhibited a blend of metal and graphite erosion characteristics. Although each material developed a large shallow crater (3–4 mm in length and 1–2 mm in breadth) on one side of the cathode, spot coverage was seen over the entire surface area with significantly greater uniformity than that of the pure carbon samples. The surface of C-3 possessed fine erosion structures likely due to its smaller particle sizes (compared to C-200) and lower porosity (compared to TTK-4C). The inclusion of Cu micro-particles was therefore shown to improve the thermal characteristics of the cathode compound such that spot coverage was visibly increased, leading to better erosion characteristics.



Figure 7.3: Photographs of cathode erosion for TTK-4C, C-3 and C-200 copper-impregnated carbon graphite rods.

It is speculated that melting of copper micro-particles within copper-graphite compounds by the heating action of the cathode spot(s) may help to bind surrounding carbon particles together, mitigating thermal shock and rod cracking. The fact that the bulk cathode body is comprised entirely of microscopically-sized particles may also assist in limiting the emission of large macroparticles. A detailed MP collection and analysis study in the future is required to verify this potential benefit of metal-graphite compound cathodes.

Figure 7.4 displays measured thrust results for copper-impregnated graphite compounds also in terms of T/I and T/P. As with pure cathodes, no discernible changes in thrust production were observed between short- and long-pulsed operating regimes. However, thrust production values and behaviour were different compared to pure carbon cathodes, following similar thrust trends over time to pure metal cathodes (see Figure 4.10b). For example, thrust production of TTK-4C remained almost steady at an average value of 267 μN/A, which was more than 40% lower than average thrust production values of GC and AF-5. Although TTK-4C's thrust-to-power declined in a similar manner to pure graphite cathodes (8 μN/W $\rightarrow$ 4 μN/W, especially after $\sum Q$ = 60 C), thrust-to-power ratios for C-3 and C-200 remained relatively stable at roughly 6 μN/W, a behaviour not seen in the pure carbon graphite cathodes.

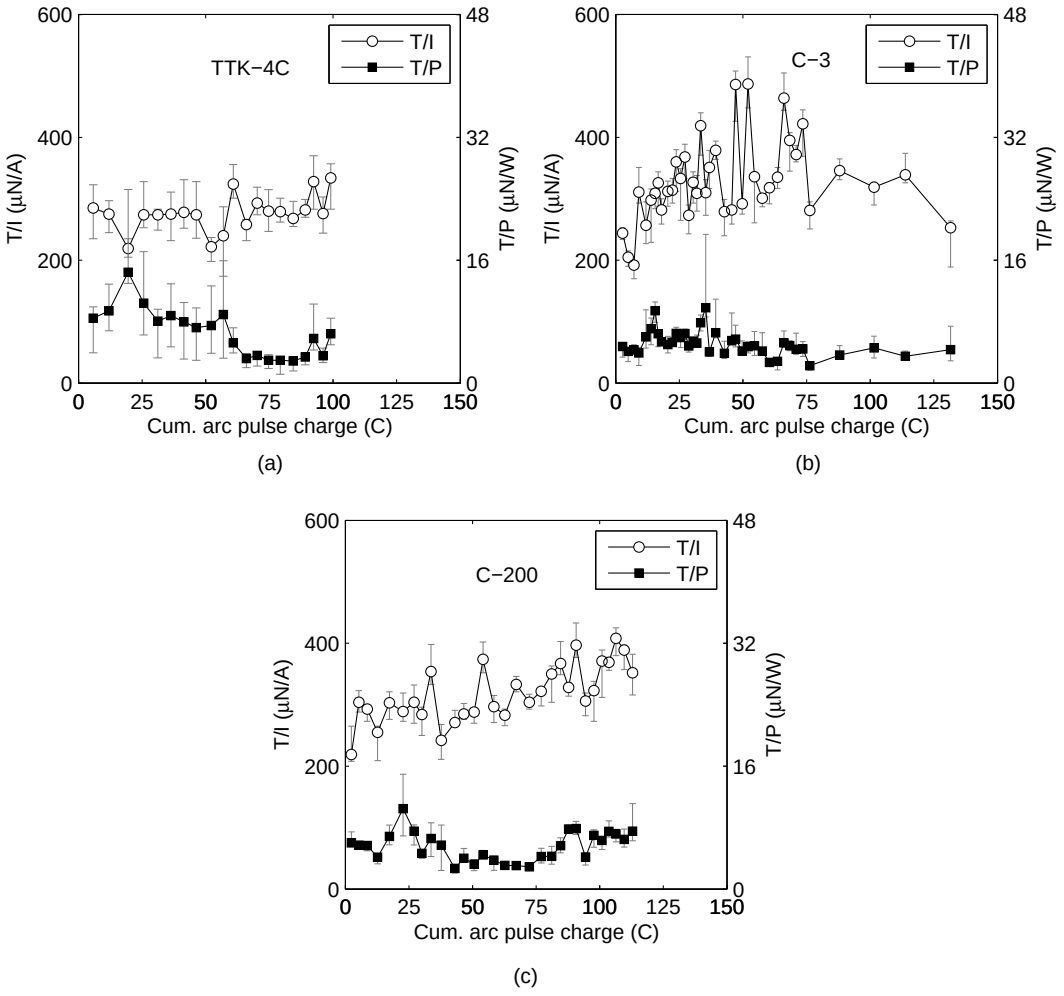

Figure 7.4: Measured thrust per arc current (left vertical axis) and thrust-to-power ratios (right vertical axis) over test duration for copper-impregnated carbon cathodes. Materials include (a) TTK-4C, (b) C-3, and (c) C-200. Total cumulative pulse charges range from 80 to 120 C. Lines through data points are for visual aid only.

Another difference in thrust behaviour between pure and metal-compound graphite cathodes was observed with samples C-3 and C-200, which both initially generated low thrust values close to 200 μN/A. Over time, both materials showed a gradual increase in thrust production, reaching intermittent values in excess of 400 μN/A. To further illustrate this, Figure 7.5 compares thrust production over time for both EDM-3 and EDM-200 cathodes and their respective copper-impregnated counterparts (C-3 and C-200). Each material test began with different starting levels of thrust, but appeared to converge to similar thrust production levels by $\sum Q$= 50 C. Thus, it is shown that the presence of Cu does not negatively affect thrust production within carbon graphite cathodes over long-term VAT operation.

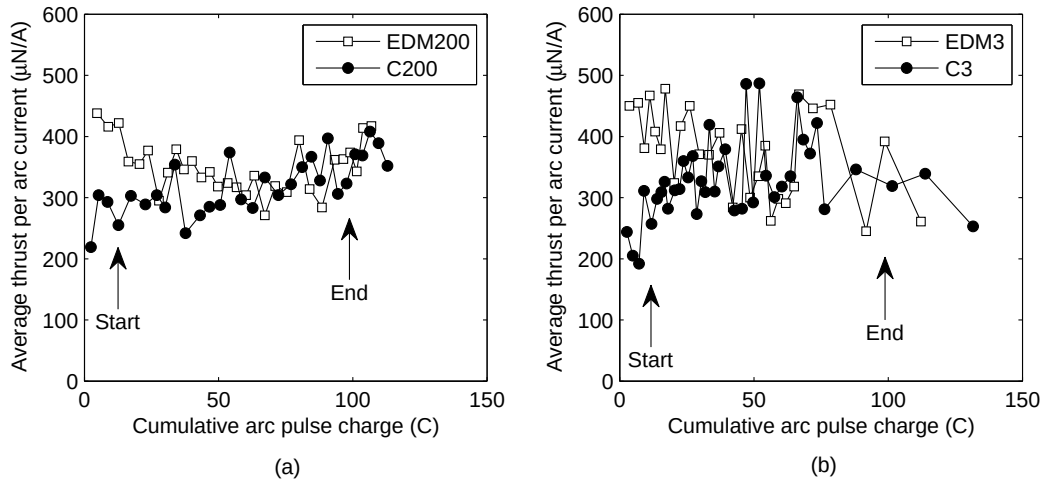

Figure 7.5: Comparison of thrust per arc current behaviour over test duration for pure graphite and copper-impregnated carbon graphite compounds. Materials shown are paired as (a) EDM-200 and C-200, and (b) EDM-3 and C-3. Differences in starting thrust levels and converged thrust levels at the end of the test are highlighted with arrows.

The presence of a compound mixture of elements within a cathode might provide synergistic benefits. Recently, Zhirkov et al. (2013) found that the presence of a high cohesive energy material such as C within a Ti-C compound cathode resulted in plasma with higher average and peak ion energies than the native ion energies of the two elements alone and independent of the ion mass. This was explained by plasma quasineutrality and higher pressure gradient generated within the plasma. Thus, it is possible that the Cu ions in C-3 and C-200 are accelerated to higher velocities than seen in pure Cu cathodes (which have lower thrust production compared to pure graphite), allowing C-3 and C-200 to achieve equal or higher final thrust per arc current values over the pure graphite cathodes.

7.3.2 Erosion rate

Figure 7.6 presents erosion results for all carbon samples tested over a range of pulse lengths. It should be noted that all long-pulsed results (≥500 μs) presented here (except for C-3) are weight-averaged from carbon thrust tests, which used both short and long pulses. Three distinct groupings of results can be made. The first group are the majority of pure graphite cathodes, which possessed average E_r values close to ~42 μg/C. This shows that the particle size (1–10 μm) within the pure carbon cathodes has a weak influence over the erosion rate. A unique feature of the graphite cathodes was their relatively constant erosion rates over the tested range of pulse lengths. This meant that these cathodes were relatively insensitive to the increased heat load at longer pulse lengths and hence did not generate more MP content because no additional melting of the bulk cathode occurred[2]. The second group is GC's results, which contain the highest set of values of all the carbon cathodes tested here (average of 46.2 μg/C). A small increasing trend of erosion rate with pulse length was observed, a behaviour similar to metals, but opposite to that of the rest of the carbon samples. The third group are the copper-graphite compounds, which delivered the lowest erosion rates in the long-pulse regime (33.4–39.3

[2]Carbon cathodes still produce MP's despite sublimating, most likely resulting from various-sized pieces of cooler solid material being released by the explosive and violent nature of the vacuum arc.

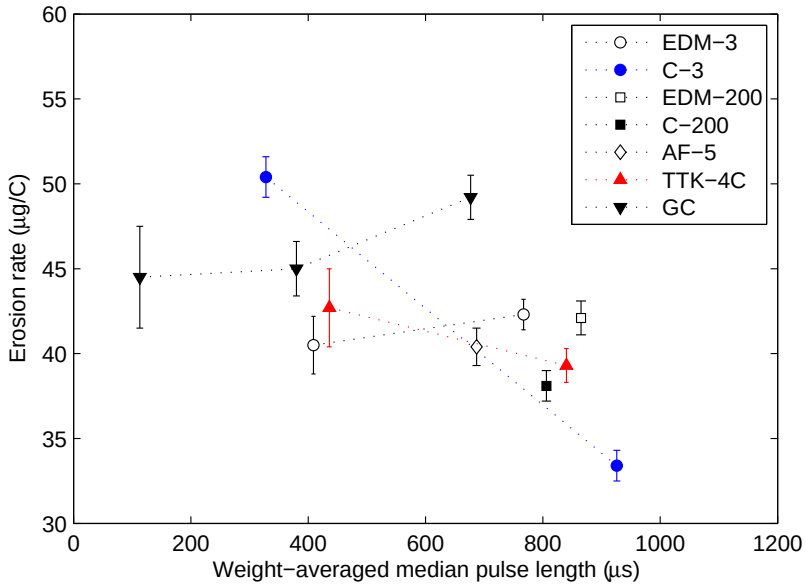

Figure 7.6: Measured erosion rate results for carbon cathodes in this study. Typical pulse characteristics used are I = 50 A peak, f = 10–20 Hz, $\bar{P}$ = 2–10 W.

μg/C). However, these compound cathodes showed increases in erosion rate when operated at short pulses (8.7% increase for TTK-4C and 50.9% increase for C-3). Further analysis is needed to help explain this behaviour.

Figure 7.7 plots various carbon cathode samples in relation to their properties (average particle size, electrical resistivity) and resulting long-pulsed erosion rates. Data reveals that E_r experiences small reductions in both sets of pure and copper-impregnated graphite rods (4 and 12.3% respectively) as the material's electrical conductivity (opposite to resistivity) and average particle size decreases. This result is in agreement with Kandah & Meunier (1996, p. 525) who found that factors such as porosity and grain size can influence cathode spot motion and velocity over the cathode surface, where larger

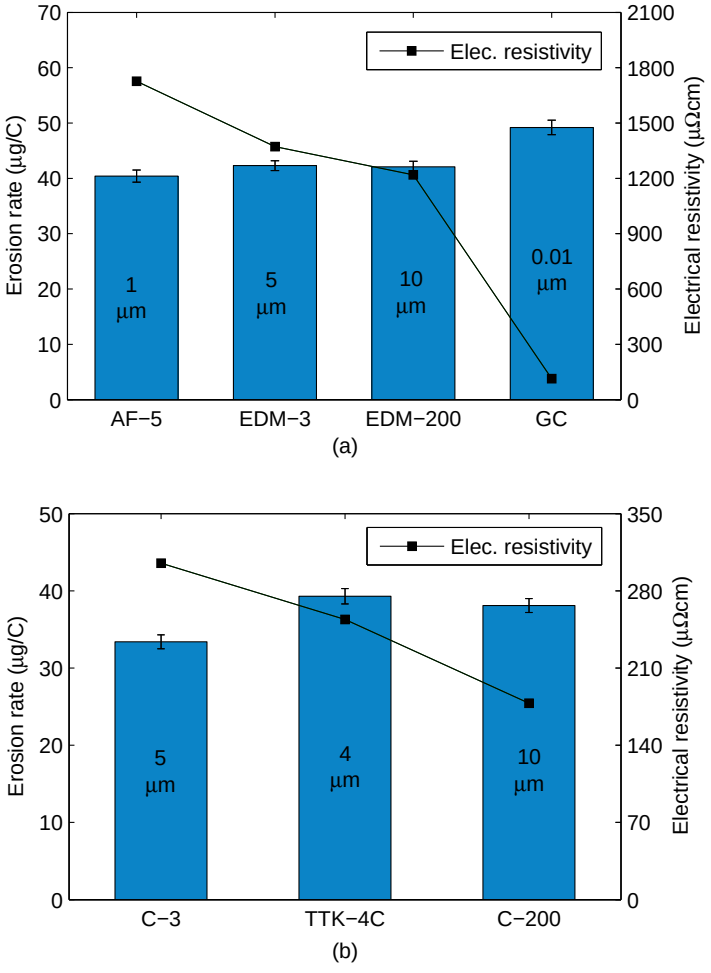

Figure 7.7: Relationship between material properties and (long-pulsed) erosion rates for (a) pure carbon and (b) copper-impregnated graphite cathodes. Average particle size and electrical resistivity of each material is indicated.

pore sizes can result in slower spot velocities, resulting in higher erosion rates.

Further evidence for the effect of microstructure on erosion rate was seen in a comparison between the compositions of C-3 and C-200, where C-3 contained micro-sized particles of Cu and C closer to or smaller than the characteristic cathode spot size normally seen on carbon. The presence of a small-sized cathode surface microstructure may produce the effect of appearing homogeneous to the cathode spot, "fooling" it into behaving as if it were on a conventional "smooth" metallic cathode. This can result in higher spot velocities and hence a lower erosion rate. This argument was made by Wang et al. (2003) when testing nano-crystalline CuCr cathodes, which generated higher spot velocities due to its finer microstructure compared to traditional CuCr alloys. The higher erosion rate of TTK-4C is suspected to be due to different quality of porosity or particle isotropy between the Toyo Tanso and POCO samples. Unfortunately, detailed material properties for TTK-4C were difficult to obtain, limiting any further analysis and conclusions up to this point.

An exception is made of GC, which has a different structural form (fullerene) compared to graphite (polycrystalline). This structural difference can significantly influence the thermal properties of the material. For example, despite its low resistivity and sub-micron structures, GC has a very low thermal conductivity[3] (6.3 W/mK at room temperature) compared to EDM graphites[4] (69–121 W/mK at room temperature; 30–45 W/mK at 2000 K). Coupled with the highly localised erosion seen at the triggered cathode edge (Figure 7.1), intense thermal conditions are considered to be the most likely cause of GC's higher erosion rates.

7.3.3 ICDD measurement

A significant challenge in using graphite cathodes was in its poor erosion characteristics, which rapidly changed the geometry of the cathode surface during thruster operation, forming deep craters at the cathode edge. This meant that an ICDD test on a typical pure

[3] Supplier's website – `http://www.htw-gmbh.de`
[4] Supplier's website – `http://www.poco.com`

carbon cathode could not generate a symmetrical and well-defined jet distribution. As a compromise, an ICDD test was done on a copper-graphite compound sample, which produced improved uniform erosion that would make a ICDD fit possible. Test material C-3 was chosen and its ICDD measured as shown in Figure 7.8. Test results revealed a Gaussian distribution, but also showed significant scatter in data points, possibly due to the variable properties of each Cu and C ion species. Only $\bar{J}$ along the yaw axis was measured due to large scatter and shortening of the pulse length during the ICDD test. On average, a high thrust correction value of $C_T = 0.757$ was obtained, albeit with a large uncertainty of ±0.197. Thus, a carbon-based cathode material was shown to produce a relatively widely-spread plasma plume that resulted in a thrust correction factor only slightly higher than measured for a typical metal cathode under the same pulse length (see Table 5.3).

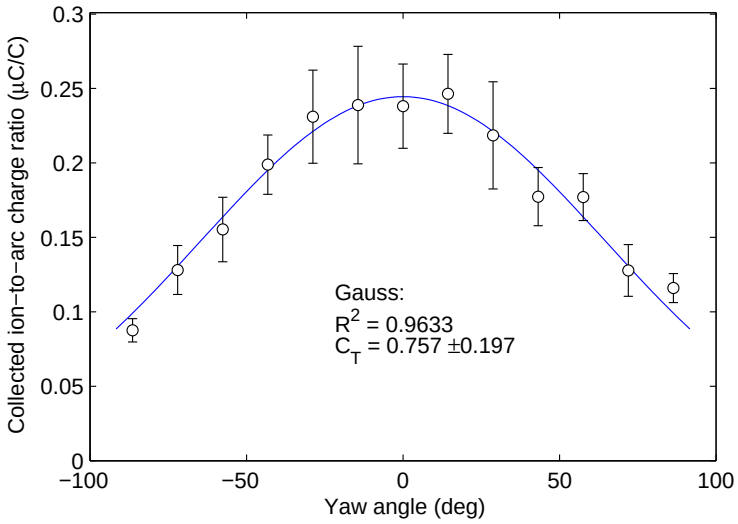

Figure 7.8: Measured ICDD of cathode material C-3 in a baseline VAT. Typical pulse conditions are $I = 50$ A peak, $t_p = 1.4$ ms, $f = 2$ Hz.

7.3.4 Overall performance

A summary of VAT thrust and erosion rate results (long-pulse) provided in Table 7.2 reveals that carbon cathodes produced high average thrust per arc current values (267–383 μN/A) and similar or better erosion rates (33.4–49.2 μg/C) compared to metal cathodes. Thrust-to-power ratios (4.9–12.8 μN/W) and thruster efficiencies (1.7–4.8 %) were on the order of or better than that measured for a mid-performance metal like Fe (see also Table

4.8). Specific impulse values of I_{sp} = 693–998 s for carbon materials were calculated to be in the order of 50–250% higher than a typical baseline metal cathode as measured in this study. This finding shows that carbon-based cathodes are amongst the highest performing fuels that can be used in a VAT. More importantly, material C-3, which delivered the highest I_{sp} value of any other cathode material in this work, also achieved the highest experimentally-verified I_{sp} value of any VAT fuel ever reported in literature.

Table 7.2: Summarised performance test results for long-pulsed baseline VATs with carbon-based cathodes. Thrust per arc current, thrust-to-power ratio and impulse per pulse energy results are weight-averaged against delivered charge per test sample for a total population sample from $\sum Q$ = 0 to 80 C. Fe baseline performance as measured in Chapter 4 is provided for comparison.

	E_r (μg/C)	T/I (μN/A)	T/P (μN/W)	I_{sp} (s)	η (%)
GC	49.2	372	12.8	771	4.8
AF-5	40.4	383	9.6	966	4.6
EDM-3	42.3	378	6.6	911	2.9
EDM-200	42.1	350	8.0	847	3.3
TTK-4C	39.3	267	7.7	693	2.6
C-3	33.4	327	5.1	998	2.5
C-200	38.1	298	4.9	797	1.9
Fe (t_p = 658 μs)	56.6	221	10.5	398	2.0

The small differences in average thrust production between pure graphite materials in Table 7.2 suggests that plasma production is weakly affected by the cathode material's structural properties. This is expected given that the plasma composition is identical across all cases (that is, only C ions). However, the cathode microstructure appeared to, if briefly, significantly affect the operating arc voltage of the cathode material. For example, compare the initial thrust-to-power ratios between GC and the pure graphite materials in Figure 7.2. GC, with its nanostructure, showed a very high thrust-to-power ratio (36 μN/W) at the beginning of its thrust test, until cathode erosion increased the VAT's interelectrode gap. On the other hand, AF-5, EDM-3 and EDM-200 produced lower (but still good) initial thrust-to-power ratios (~16 μN/W). These preliminary results hint that a finer cathode microstructure may help to lower the operating arc voltage and improve thruster power consumption.

There is a view that the fine microstructures within materials such as GC enhances field-emission and the arc initiation process (Hosoki et al. 1979). Similar evidence for enhanced field-emission from Pyrolytic carbon, another non-structured fine carbon mate-

rial, was found by Goebel & Schneider (2005). However, significantly more detailed studies are required before any further conclusions can be made on the effects of graphite cathode microstructure on arc voltage. Practical issues such as the receding cathode surface from the interelectrode trigger edge over time will need to be addressed to enable such a study.

In contrast to pure graphite, different grades of graphite compounds produced varying levels of average thrust production. For example, TTK-4C produced only 81.7 % of the thrust generated by C-3, despite having similar average particle sizes. This suggests that some other factor is affecting thrust production. One possibility may be related to the MP production from each material, where TTK-4C produces a 17.7% higher erosion rate than C-3. These additional MP's may impede the outgoing plasma flux, causing a lower thrust value.

7.3.5 Comparison with literature

Despite the extensive use and study of graphite cathodes in vacuum arc research and industry, detailed studies of their performance as fuel in VATs have been largely absent. Recently, Fuchikami et al. (2013) performed some initial impulse measurements of a VAT carbon-fibre reinforced plastic cathode rod. However, many details of their test setup and method remain unspecified, making comparison difficult. An estimate of their results indicates impulse bit production of roughly 5 μNs per Joule of energy ($\equiv$ 5 μN/W), which is similar to what is reported here.

All erosion results measured in this work are in good agreement with Kandah & Meunier (1996), but are significantly higher than when steady or near-continuous arcs are used ($\sim$ 40 μg/C vs. 10–17 μg/C). Meunier et al. (2007) suggested that short pulses on graphite tend to produce higher erosion rates due to the greater amounts of MP's produced from the inherently violent processes of pulsed vacuum arc operation. This could explain the higher erosion rates seen in short-pulsed operation of C-3 and TTK-4C. Thus, the possibility exists for superior erosion performance by up to a factor of two if a carbon cathode were operated at second-long pulse lengths instead of μs- to ms-long pulse lengths. Fur-

ther testing is needed to verify this.

The only available prediction for carbon cathode thruster performance was made by Polk et al. (2008), who broadly assumed an ion-to-arc current ratio of $\epsilon = 0.1$ for all cathode materials. Although this assumption is reasonable for many materials, this does not necessarily hold true for carbon. Experiments by Anders et al. (2005) showed that the ion-to-arc current ratio for carbon (unspecified type or grade) could be as high as $\epsilon = 0.19$.

Results within this study are in sharp contrast to these findings (summarised in Table 7.3), where measured ion-to-arc current ratio for AF-5 and C-3 in this study is significantly lower than that previously reported within literature for carbon (ϵ = 0.06–0.07 compared to 0.1 or 0.19). Further mystery is added when considering all the carbon materials measured in this work, which generated between 33.6–46.2 % *greater* average thrust values than that generously predicted by the empirical model ($\epsilon = 0.19$). By this interpretation, these results imply that the carbon materials used in this study produced

Table 7.3: Comparison of averaged measured carbon VAT thrust and erosion performance against empirical model and published literature. Note that model assumes $\epsilon = 0.19$ (in brackets). EDM-200's lowest measured thrust per arc current level (occurring at $\sum Q = 67$ C) is included in brackets directly underneath the total test average. Ion-to-arc current ratios for AF-5 and C-3 are averaged over 200 samples taken at $I = 50$ A peak, $t_p = 1.5$–2 ms, $f = 2$ Hz.

Type	**Description**	**Ion-to-arc current** ϵ	**Thrust** T/I (μN/A)	**Erosion rate** E_r (μg/C)
	This work			
Calc.[a]	See Equation 2.1	(0.19)	262	
Exp.	(50 A pk, 250–2500 μs)			
	C-3	0.065 ± 0.005	327	33.4
	AF-5	0.067 ± 0.007	383	40.4
	EDM-200		350	42.1
	EDM-200 ($\sum Q = 67$ C)		(271)	
Exp.[b]	70 A, 2.5–5 ms			40–124
Exp.[c]	100 A, 1.5 s	0.10		17
Exp.[d]	70 A, 60–960 s			11.4
Exp.[e]	60–300 A, 500 μs	0.19		

[a] Empirical model with assumed values of $\epsilon = 0.19$ (Anders et al. 2005), $v_i = 17.3$ km/s (Anders & Yushkov 2002*b*), $\bar{Z} = 1$ (Brown 1994) and $C_T = 0.64$ (Polk et al. 2008).
[b] Kandah & Meunier (1996) – results are for various grades of carbon (ZXF-5Q, AXF-5Q, PS and PYROID) under no magnetic field.
[c] Kimblin (1973)
[d] Lefort et al. (1993)
[e] Anders et al. (2005)

less than three times the amount of ions than expected, yet accomplished nearly 50% better thrust production than predicted!

A number of possible scenarios may be entertained to account for these apparent anomalous ion and thrust values. First, ignoring differences in material properties and assuming the ion collection result is correct, the average ion velocities must be much higher than previously reported to reach the correct thrust values. This would require the average ion velocity to be some 3.5 times higher than previously measured (17.3 → 60 km/s), which seems highly improbable. Second, the thrust correction factor is higher than the assumed value of C_T = 0.64 (Polk et al. 2008). Some supporting evidence for this comes from the measured ICDD for C-3, which resulted in C_T = 0.757 (18.3% higher than assumed). However, this is far too small an effect to explain such high thrust production.

A third possibility is that a portion of the emitted carbon ions may have been neutralised by plasma electrons before reaching the ion collector, indicating a lower total ion current than actually emitted by the VAT. This behaviour is surprising given that the vacuum arc plasma no longer becomes collision-dominated after travelling a short distance (mm scale) from the cathode surface (Anders 2008). Additionally, the identical ion collector setup was used to include repeated measurement of ϵ for Fe, which were in general agreement with reported literature. No apparent plasma neutralisation was observed in those measurements.

Partial agreement of thrust results with literature could be found once significant erosion of the carbon cathode occurred. For example, thrust results for EDM-200 (the lowest thrust-producing material) showed a gradual reduction in thrust production after some time ($\sum Q$ = 67 C) to as low as 271 μN/A – a value very close to empirically predicted thrust (only 3.4% difference in thrust, assuming Anders et al.'s (2005) measurement of ϵ = 0.19). This suggests that the ion current results presented here need to be independently verified and the measurement technique should be re-evaluated for future studies of carbon cathode fuels. In conclusion, no explanation can be currently given for the higher-than-expected T/I values produced in all carbon-based cathodes tested in this study.

7.4 Summary

The novel use of glassy carbon, graphite and metal-impregnated graphite compounds as cathode fuel for VATs was successfully demonstrated and their performance characteristics measured. Each type of carbon was shown to possess unique cathode performance and erosion behaviour based on its set of thermal, electrical and micro-structural properties. As such, this work strongly emphasises the importance of reporting detailed specifications on the grade or type of carbon material sample used in vacuum arc and VAT studies.

The erosion behaviour of carbon cathodes is clearly different to those comprised of pure metals. Deep craters were typically seen in pure carbon and graphite samples, whilst the modest inclusion of a highly-conductive metal to graphite (15% by volume) enabled surface erosion characteristics similar to that of metals. By improving the thermal properties of graphite cathodes and increasing spot motion, erosion rates as low as 33.4 μg/C (material C-3) could be accomplished.

The erosion rate of carbon cathodes was generally robust against the arc pulse length and showed general agreement with literature. Surprisingly, E_r trends for copper-impregnated graphite were opposite to that of metals, generating higher E_r at short pulses and lower E_r at long pulses. Interpreting these results in conjunction with previous studies suggests the possibility that operating at even longer pulse lengths (on the order of seconds) may lower cathode erosion rates even further. Detailed MP studies on carbon cathode materials is recommended.

Average thrust production from pure carbon cathodes (350–383 μN/A) was significantly higher than predicted by the empirical model (262 μN/A). Reasons for this are not clear at this stage, where measured improvement in the thrust correction factor of 18.3% to give C_T = 0.757 can only account for roughly half of the enhanced levels of thrust production observed. Additional measurements of ion current and ion energies are therefore needed to investigate this discrepancy. Copper-impregnated graphite cathodes also generated high average thrust production levels (267–327 μN/A), but showed a gradual *increase* in

T/I over the test duration compared to the gradual thrust *decrease* seen in pure carbon cathodes (due to deep crater formation). This places metal-graphite compounds at an advantage over pure-carbon cathodes in maintaining good thruster performance over long operating times.

All carbon-based cathodes generated very high thruster performance, with some producing excellent initial thrust-to-power ratios and specific impulse values amongst the highest seen in VATs (16–36 μN/W, 700–1000 s). It was also argued that material microstructure and composition played a prominent role in determining cathode performance. Materials comprised of a combination of fine microstructure and possessing high electrical resistivity were generally found to deliver high levels of thrust per arc current and low erosion rates.

Further evidence for CEX as the main cause of increased thrust production at longer arc pulse lengths proposed in Chapter 5 was seen in carbon VAT thrust tests, which failed to show any measurable difference in T/I between short- and long-pulsed operation. This was expected since carbon ions from a pulsed vacuum arc were previously found in literature to be almost entirely singly-charged.

Finally, the time-dependence of carbon VAT performance was seen in thrust data, where the arc voltage was noticeably lower, often by more than half, at the beginning of the thrust test and quickly rising as thruster operation progressed. This was likely due to the quick erosion of cathode material away from the triggered edge as well as the formation of deep craters, both of which increased the interelectrode surface gap between the VAT electrodes. It is possible that an improved electrode design incorporating a feeding mechanism may eliminate the unwanted performance degradation seen here, achieving full utilisation and best performance possible from carbon cathodes.

Chapter 8

Discrete anode switching technique

8.1 Introduction

As argued in Chapter 1, increased spot motion causes less local heating and melting of the cathode with the overall result of decreased macroparticle production and erosion rate. This kind of operation is desirable because it means that less propellant is consumed to produce the same amount of thrust, i.e. higher specific impulse values and efficiency. This study explored the use of the discrete anode switching technique in an effort to increase spot motion and hence reduce cathode erosion. The first reported use of this technique was by Vergason et al. (2001), whose aim was to improve the characteristics of thin films in industrial coating applications. By utilising several discrete anodes individually switched in a cyclical fashion, a considerable reduction of cathode surface roughness and macroparticle content was achieved. Although cathode erosion rates were not directly measured, it is safe to assume that the reduced quantity of generated MPs also corresponded to a decrease in cathode erosion.

The test conditions used by Vergason et al. (2001) were for large titanium cathode bars run at 120 A arc current and arc times of 250 ms, 5 s and 120 hours. In contrast, the VATs in this study operated with much smaller-bodied cathodes and at lower arc cur-

rents and pulse lengths. Thus, it was not initially clear if anode switching would be an effective mechanism for improving VAT performance and operation. This study assesses the adaptation of the Discrete Anode Switching (DAS) technique to VATs.

8.2 Description of anode switching setup

8.2.1 Anode design

The anode electrode was modified in a number of ways. Firstly, the standard copper ring anode of the baseline VAT was replaced with a six-segment split anode design as shown in Figure 8.1. Each anode segment was mounted against the side of the insulator tube and could be electrically isolated from one another or paired as desired. Secondly, a manufacturing change to the insulator's conducting film was implemented, where a thick layer of conducting carbon paint was used instead of the usual pencil graphite film. This ensured good mechanical strength between the anode segments and the thin conducting graphite film. Application of carbon paint also allowed much lower contact resistance between the anode and conducting film, reducing the rate of film erosion during VAT operation. A suitable film thickness and junction manufacturing layout was found to ensure good and desired VAT operation as shown in Figure 8.2. Table 8.1 lists the electrical contact resistances typically manufactured at the thruster's various interelectrode junctions.

Table 8.1: Typical electrical resistances of interelectrode junctions of the segmented anode VAT design

Junction	**Resistance** (kΩ)
Anode-graphite film	0.1–0.5
Graphite film-cathode	5–20
Anode-graphite film-anode	> 20–50

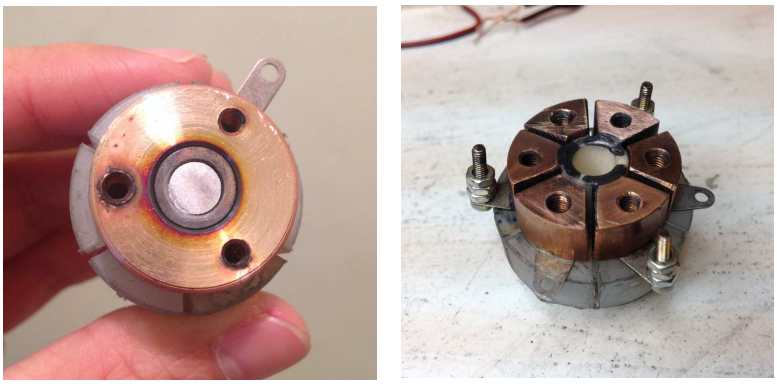

(a) (b)

Figure 8.1: Anode designs used in this study on a baseline VAT: (a) standard ring and (b) six discrete segments.

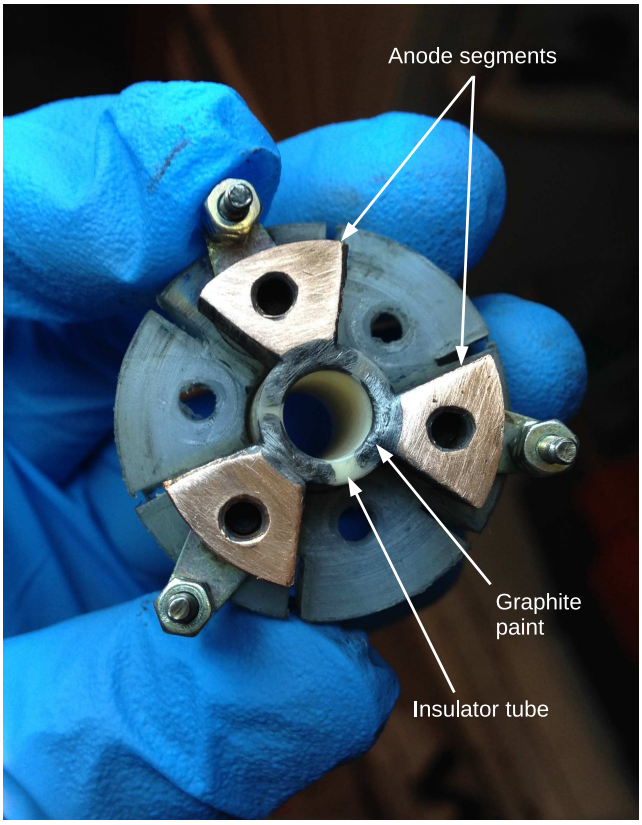

Figure 8.2: Close up of a semi-built segmented anode VAT with graphite film installed on three equally spaced anodes. Once graphite film construction was completed, the cathode rod and remaining anodes were mounted with final film touch up.

8.2.2 Switching patterns and times

Due to a limited number of available power feedthrough electrodes installed on the test vacuum chamber, only three active anodes (or anode pairs) could be independently controlled during thruster firing. Figure 8.3 illustrates two different anode switching patterns that were used in this study.

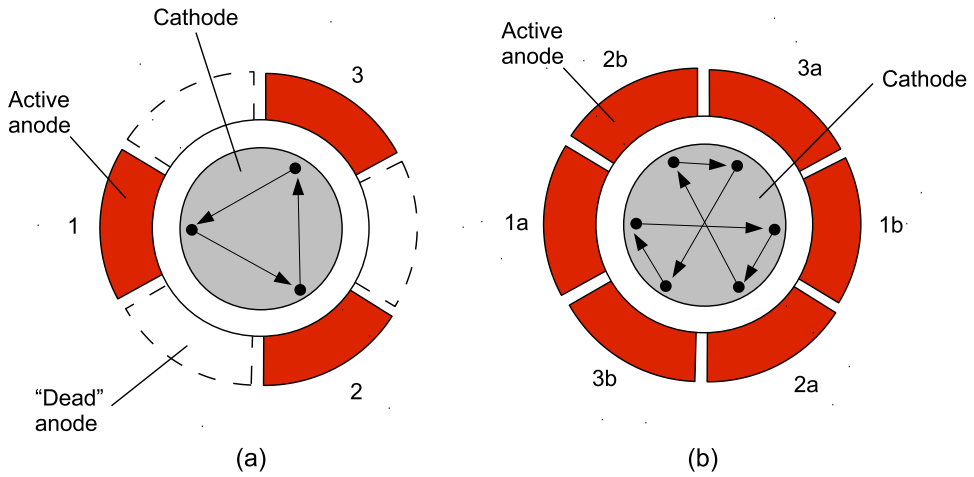

Figure 8.3: Schematic of anode switching patterns. Black dots and arrows represent cathode spot(s) and their expected forced motion over the surface at various stages in the anode switching sequence according to (a) triangular motion with three active and inactive (or "dead") anodes used, or (b) cross-shaped motion with three active anode pairs.

The first anode switching pattern (Figure 8.3a) consisted of activating each of the three anodes spaced equally apart in a repetitive circular sequence. The remaining three anodes were kept inactive (or "dead") and played no role in the vacuum arc other than to restrict plasma from exiting the side of the VAT. The "dead" anodes were not connected to the conducting film or pulse circuit. This mode of operation was observed to cause the spots to move in a typically triangular fashion.

The second anode switching pattern (Figure 8.3b) consisted of three connected pairs of anodes. This configuration allowed all six anode segments to be controlled with only three anode switching commands. By connecting two oppositely-facing anode segments into a pair, the first segment (with conducting film installed) triggered the beginning of the arc pulse. During the arc, plasma filled the near-cathode region and allowed the second segment (with no conducting film installed) to become electrically active as well.

Eventually, the second segment became favoured as the primary current-carrying anode due to the lower electrical resistance between it and the cathode, with the plasma acting as a conducting bridge. Thus, the desired result is to force the arc spot(s) to travel in a crossed-shaped pattern, following each preferred anode segment with each cycle. This technique of using multiple and preferential anode switching operation was inspired by the established use of mechanical triggers in DC vacuum arc sources pioneered by Sablev et al. (1974), plasma torch designs by Schein et al. (2007) and VAT design work by Krishnan (2009).

Switching frequencies of 4–16 Hz were used by Vergason et al. (2001) to ensure that the anode switching time was comparable to or much smaller than the 0.25–5 s arc pulse durations used (1–80 switching operations within a single pulse). This was done in order to encourage the arc spot(s) to "follow" the active anode within a single arc pulse. A similar approach was used in this study, where switching times of $T_1 = 45$, 120, and 520 μs were chosen when running the DAS technique for VATs operating with pulse lengths of 200–2000 μs long.

8.2.3 DAS control system

The DAS switch control system (SCS) was comprised of a set of IGBT transistor switches connected into the VAT pulse circuit to control its power output. A circuit schematic of the SCS is shown in Figure 8.4. Each IGBT (**Q1**, **Q2** and **Q3**) was powered by an electrically floating gate driver (**G1**, **G2** and **G3**) and commands to each gate driver were sent from an Arduino microcontroller (**S1**, **S2** and **S3**). User inputs were sent to the microcontroller via PC to adjust the anode switching times as desired. Optocouplers (**U1**, **U2** and **U3**, model H11L1M-FC) were used to electrically isolate the microcontroller from the SCS. A cache of 9 V batteries (**V1**, **V2** and **V3**) were used as floating voltage sources for the optocouplers and gate drivers. The gate drivers and IGBT components used were the same model types as for the main VAT pulse circuit. Current- and voltage-limiting resistors for the optocouplers and gate drivers are omitted from the schematic for visual clarity. Battery power for each optocoupler is also omitted. Note that the arc voltage being measured here includes the voltage drop across the anode IGBTs. This makes the measured arc

voltage conservatively a few volts higher than the potential drop between the anode and cathode electrodes.

Due to inherent speed restrictions in the microcontroller, a single command to the anodes to switch states took 20 μs to be executed. A lower anode switching limit of 40 μs was therefore dictated by the current switching control system used. To protect the SCS and VAT pulse circuit, a transitional phase was applied between each anode switching step, where both the prior anode and the next anode in the switching sequence were both active for a brief period of T_2 = 20 μs before fully transitioning to only the next anode being active and deactivating the prior anode in the switching sequence. Therefore, each anode (or anode pair) was active on their own for periods of ΔT = 5, 80 and 480 μs.

Figure 8.5 shows the anode signal switching timeline used for both the triangular and cross-shaped patterns where

$$T_1 = T_2 + \Delta T + T_2 \tag{8.1}$$

The SCS was linked to the VAT pulse circuit trigger signal such that it would only begin switching once the VAT circuit began powering the VAT. The SCS was also configured to disconnect the VAT from the pulse circuit after a short period of time to ensure that arc current did not continue flowing through the VAT longer than desired. For example, after firing arc pulses of 500 μs long, the SCS kept the anode side of the circuit open for 250–500 μs for a total VAT closed-circuit duration of 750–1000 μs.

8.3 Test method

Initial tests showed that the cross-shaped anode switching pattern produced better surface coverage and more uniform erosion of the cathode surface. Therefore, the majority of test results presented here made use of the cross-shaped anode switching pattern. The graphite film at the interelectrode interface was rebuilt anew prior to each VAT test to ensure consistent and repeatable thruster operation. Erosion rate tests were performed for a range of switching times (45, 120, 480 μs), cathode materials (Al, Fe, Bi, AF-5, C-3) and

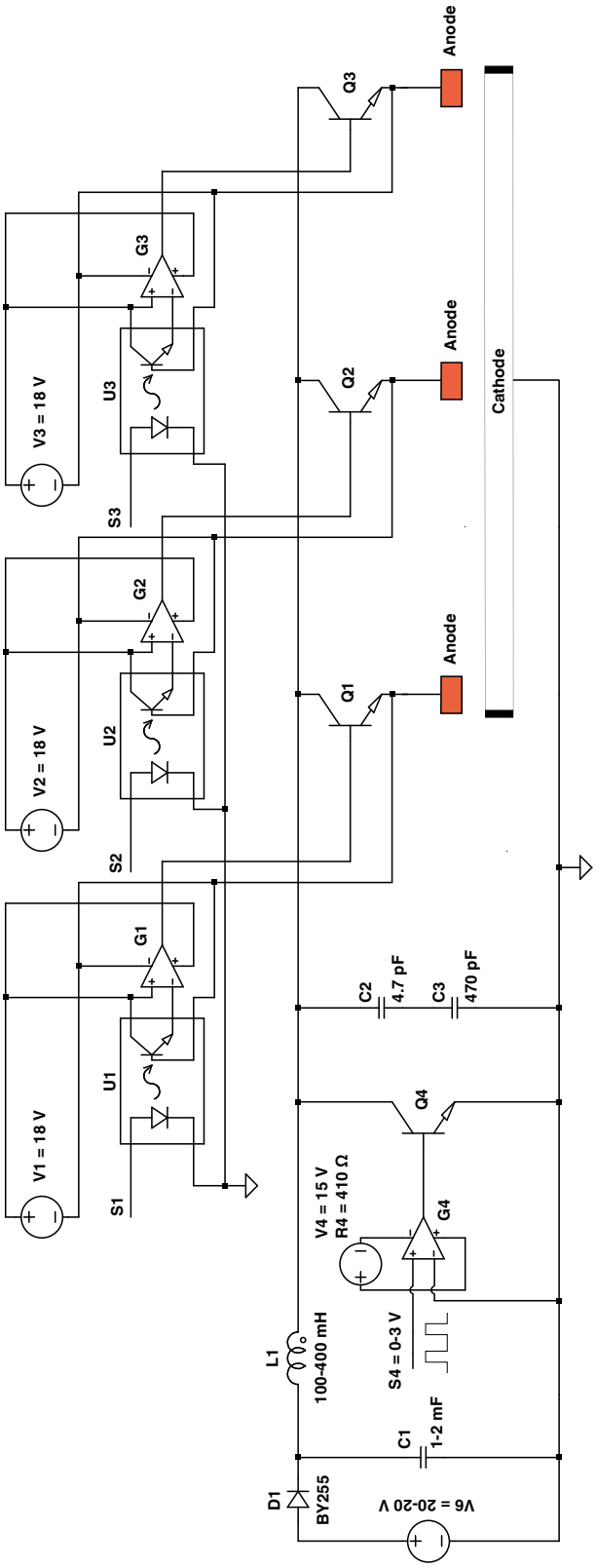

Figure 8.4: Schematic circuit diagram of DAS switch control system comprised of three switching subsystems (one for each anode) incorporated into the VAT pulse circuit. Each subsystem is comprised of an optocoupler to receive Arduino commands, a floating voltage source, a gate driver and a dedicated IGBT switch to control a discrete anode.

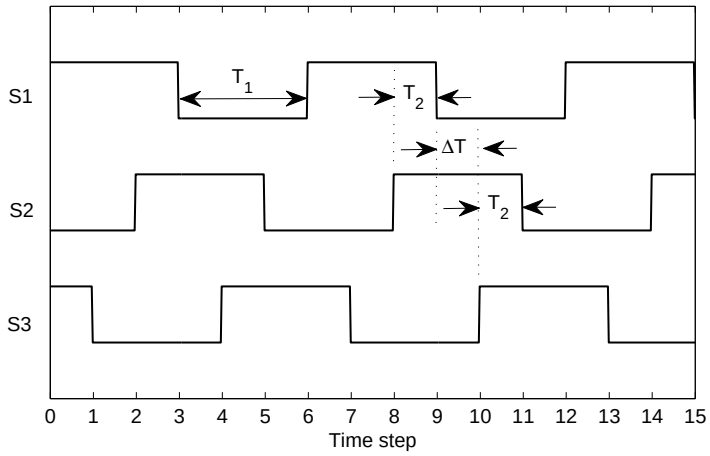

Figure 8.5: Anode signal switching timeline for each anode signal (**S1**, **S2** and **S3**) where T_1 is the anode active switching time (45, 120 and 520 μs), T_2 is the transition time (20 μs) and ΔT is the dedicated anode activation time (5, 80 and 480 μs).

arc pulse currents (25, 50 A) and pulse lengths (200–2000 μs) to characterise the effectiveness and limits of the DAS technique. Finally, a thrust test was performed on one of the discrete anode VAT designs to verify that the DAS technique did not negatively interfere with plasma production.

8.4 Results & discussion

8.4.1 Erosion behaviour across different cathode materials

The DAS technique was tested on a variety of cathode materials to assess its effect on erosion behaviour. Figures 8.6 and 8.7 present erosion patterns on several cathode samples (Al, Fe, Bi, AF-5 and C-3) operating with DAS (120 μs switching time, crossed pattern). Short pulses (300–400 μs, 5 Hz) were especially used to observe the limits of erosion coverage. Each material experienced a net eroded mass loss of 2.4–3.9 mg (except Bi, Δm = 28.5 mg).

Significant differences in erosion behaviour across the range of cathode materials were observed. The level of spot motion and extent to which the spots spread out over the surface could be attributed to the varying thermal conductivities of the materials stud-

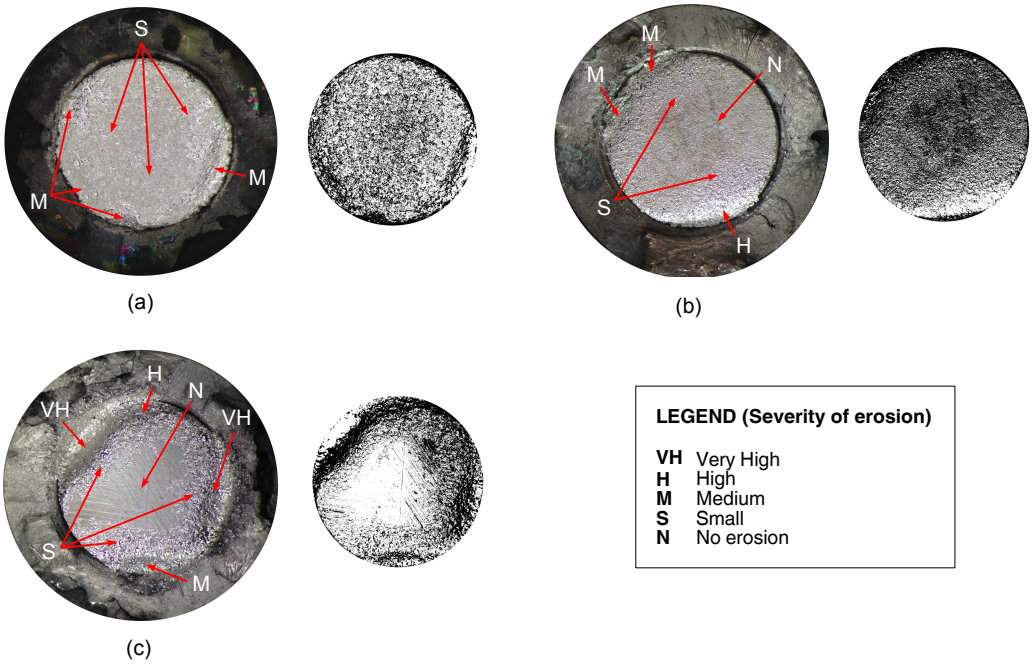

Figure 8.6: Erosion patterns on (a) Al, (b) Fe and (c) Bi cathodes subjected to discrete anode switching (120 μs switching time, crossed pattern). Levels of erosion are labelled according to severity. A high-contrast image of each cathode provides an approximate visual indication of cathode spot erosion coverage. Pulses characteristics are I = 50 A peak and t_p = 300–400 μs long.

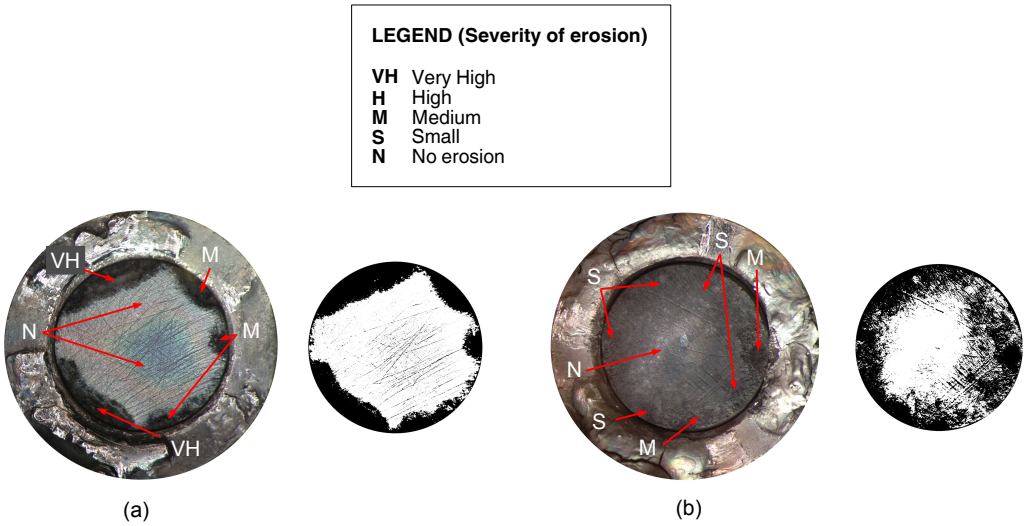

Figure 8.7: Erosion patterns on (a) AF-5 and (b) C-3 graphite cathodes subjected to discrete anode switching (120 μs switching time, crossed pattern). Levels of erosion are labelled according to severity. A high-contrast image of each cathode provides an approximate visual indication of cathode spot erosion coverage. Pulses characteristics are I = 50 A peak and t_p = 300 μs long.

ied. For example, Al (high thermal conductivity, Figure 8.6a) demonstrated very good erosion coverage, whilst Bi and AF-5 (low thermal conductivity, Figures 8.6c and 8.7a respectively) maintained poor coverage with most erosion craters occurring close to the triggered edge. Fe and C-3 (medium-to-low thermal conductivity, Figures 8.6b and 8.7b respectively) showed moderate coverage with an untouched central area of the cathode surface. Thus, the material-dependant "stickiness" or mobility of the cathode spots determined to a large degree the effectiveness of the DAS technique to induce spot motion.

The number of cathode spots present on the surface did not appear to affect coverage. For example, although a large number of spots were present in Bi, the majority of craters appeared closely located. In contrast, Al showed good erosion coverage despite only having a single arc spot. It is surmised that the self-magnetic field within the spots was insufficient to cause spot spreading (as discussed by Boxman et al. (1995)) due to the low arc current level used in these tests (I = 50 A peak). Thus, operating at higher arc currents (e.g. 100–200 A peak) may improve the effectiveness of the DAS technique by forming a greater number of spots and encourage spot spreading on the cathode surface.

8.4.2 Switching limits

A preliminary study was performed to determine some of the operational limits to which the DAS technique would influence the cathode erosion rate. Conservative VAT tests were run on a Fe cathode with low peak arc currents (25 A), short pulses (~250 μs) and low average power levels (1–2 W). A large range of switching times were tested, ranging from as little as 0.5 pulse per switching operation (120 μs) up to 50 pulses per switching operation. For reference, erosion tests were also performed for VATs with (1) all discrete anodes connected as a common anode and (2) the standard ring anode. The results of the tests are presented in Figure 8.8.

Figure 8.8 shows that the manner in which DAS is implemented is important. Operating at fast switching times of 0.5 to 1 switching operation per arc pulse (120 and 520 μs respectively) showed no improvement to the erosion rate compared to the standard VAT design. Thus, results suggest that DAS is ineffective for VATs operating at low arc cur-

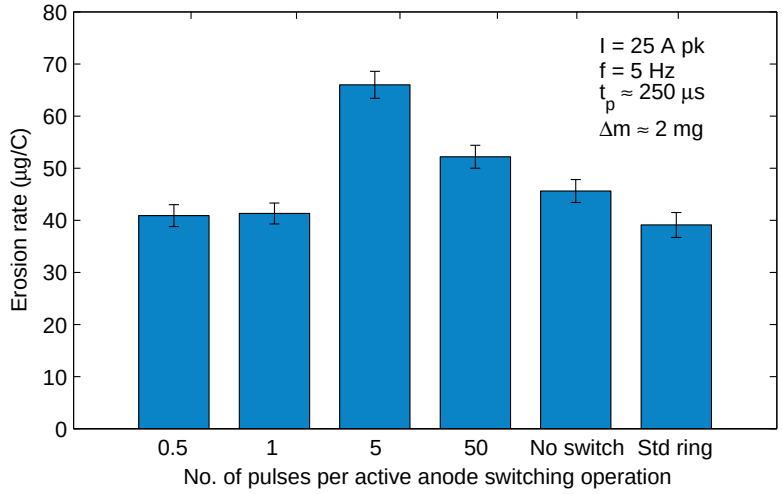

Figure 8.8: Erosion rate results demonstrating lower limits of operation and switching times of DAS technique applied to baseline VAT design with Fe cathode. Pulse characteristics are I = 25 A peak, t_p = 200–330 μs pulse lengths and 1–2 W average thruster power. Anode triangular switching pattern was used.

rents and short pulses. Furthermore, operating with 5–50 pulses or even no switching for each discrete anode produced worse erosion rates over the standard ring design (16.6–68.8% higher). This occurred because spot motion was restricted to a local area of the cathode surface closest to the active anode segment, increasing local temperatures and (likely) MP production. Thus, operating with at least one switching operation per pulse is recommended when implementing the DAS technique in VATs.

8.4.3 Effect of DAS with varying arc pulse length

As was previously established in Chapter 5, the pulse length was found to have a strong influence on cathode erosion rate during nominal VAT operating conditions. With this in mind, a study of different DAS switching times was applied to a Fe cathode operating with peak arc current I = 50 A for a range of pulse lengths. Figure 8.9 provides a map of erosion rate results for 45, 120 and 520 μs switching times at short and long pulse lengths.

Applying the DAS technique at short pulses ($\leq$ 500 μs) did not show any improvement to the erosion rate (DAS results follow the same interpolated line of baseline VAT results). This may be interpreted such that DAS was unable to increase spot motion beyond the

spot mobility limit of the cathode material. However, the DAS technique was successful in achieving reductions in the cathode erosion rate when operating with long pulses (1.5–2 ms). As expected, smaller switching times showed greater reductions in E_r (520 μs → 5%, 120 μs → 11%, 45 μs → 24%, estimated by comparing the interpolated E_r results of the baseline VAT at equivalent pulse lengths). Erosion rate data also suggested that the effectiveness of the DAS technique improved as the pulse length increased, successfully distributing the increased heat load on the cathode surface to a level similar to that present during short pulsed operation. These results support previous evidence in Chapter 5 showing that the erosion rate of a cathode depends more on the heat load within the local spot vicinity than that averaged over the cathode surface. A possible and significant consequence of reduced melting and erosion is the mitigated production and release of MP's. Further study is needed to properly assess this aspect of DAS-enhanced VATs.

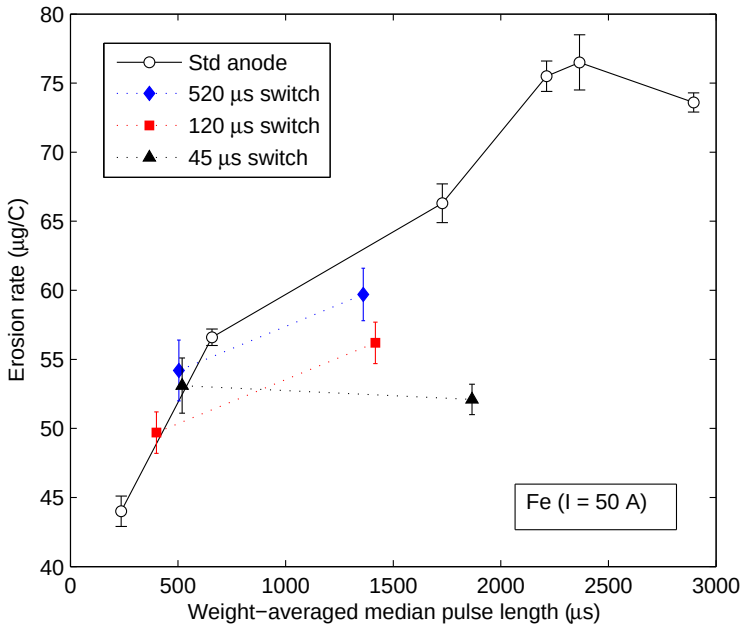

Figure 8.9: Erosion rate results for different switching times as a function of arc pulse length. Tests performed on Fe cathode running at I = 50 A peak. Erosion results for the baseline VAT operating with the standard anode ring is included for comparison.

8.4.4 Thrust

Thrust measurements on a Fe cathode operating with DAS (45 μs switching time) as shown in Figure 8.10 revealed that a DAS-enhanced VAT generated 21.6% higher average levels of thrust production over a baseline VAT operating at the same average pulse length (319 μN/A vs. 262 μN/A at t_p = 1997 μs). This result shows that the thrust-production benefits of long pulsed operation can be sustained and even improved whilst simultaneously mitigating the higher operating heat loads and keeping the erosion rate low (in this test, measured E_r = 53.0 ±1.1 μg/C). The additional increase in average thrust levels could be explained by the reduced production and presence of MP's, which tend to absorb or impede the ion flux.

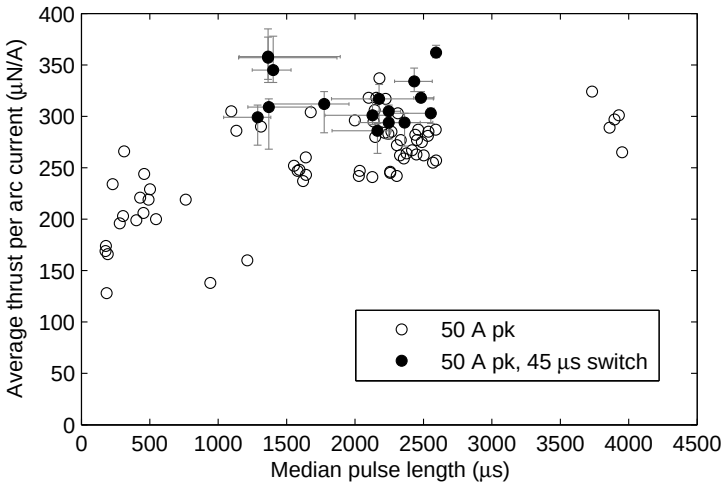

Figure 8.10: Direct thrust measurements for Fe cathode operating in long-pulsed mode with and without DAS implementation. Baseline thrust data was obtained from Figure 5.7 with error bars omitted for visual clarity. DAS-enhanced VAT operating conditions were I = 50 A peak, f = 6 Hz, 45 μs switching time (crossed pattern) run up to a total charge of $\sum Q$ = 92.5 C.

There are two important findings here – (1) the action of increased spot motion (also achieved by conically-shaped cathodes in Chapter 6) has no observable negative effect on thrust production, and (2) it is the additional ionisation of neutrals, and not necessarily the added heating, melting and erosion of the cathode during long arc pulses, that determines the increased production of thrust.

8.4.5 Overall performance

Table 8.2 compares specific impulse performance for (1) short- and (2) long-pulsed baseline VATs as well as for (3) a DAS-enhanced VAT. Average thrust per arc current values for cases (1) and (2) were obtained by interpolating against the average linear trend lines of Figure 5.7, whilst average erosion rate values for case (2) was obtained by linear interpolation of E_r values in Figure 5.2. As expected (and discussed in detail in Chapter 5), the long-pulsed baseline VAT suffers from a 22.1% drop in I_{sp} due to the large increase in E_r when compared to the short-pulsed VAT. However, the DAS-enhanced VAT was successful in achieving a significant overall positive gain in I_{sp} of 614 s – signifying a 27.9% higher specific impulse compared to the short-pulsed baseline design and 50.0% higher specific impulse over the long-pulsed baseline design.

Table 8.2: Comparison of thruster performance for three selected Fe VATs operating with (1) short pulses (baseline design), (2) long pulses (baseline design) and (3) long pulses and DAS implementation. Peak arc current at I = 50 A.

Fe VAT design	t_p (μs)	T/I (μN/A)	E_r (μg/C)	I_{sp} (s)	**Diff.**
Baseline (short)	156	207†	44.0	480	
Baseline (long)	1997	262†	71.4*	374	-22.1%
DAS, 45 μs switch	1997	319	53.0	614	+27.9%

† Estimated by linear interpolation of T/I trend line in Figure 5.7.
* Estimated by linear interpolation of E_r values in Figure 5.2.

It is unknown if an upper limit exists for DAS-induced spot motion and its improvement to overall thruster performance. Under general VAT operating conditions, this limitation is expected to depend (in approximate order of influence) on (1) the cathode material's thermal conductivity, (2) the arc pulse length, (3) the DAS' switching time, (4) the arc current level, (5) the number of cathode spots present and (6) the cathode body's average temperature. In contrast, the influence of magnetic fields to steer cathode spots (as widely reported in literature and used in industry) appear to be of sufficient strength to overcome many of the above-mentioned factors. Future studies on combined use of DAS and magnetic steering may prove to be of scientific interest and practical benefit.

8.5 Summary

The discrete anode switching technique was successfully demonstrated to be a novel and feasible method of controlling the erosion behaviour of a VAT. However, a number of factors limited the effectiveness of DAS implementation. For example, the arc current and anode switching frequency must be sufficiently high to generate appreciable spot motion, and the switching time preferably shorter than the arc pulse duration.

The cathode material's thermal conductivity determined to a large degree the amount of erosion coverage or spot mobility present on the cathode surface. Highly conductive materials such as Al demonstrated excellent spot mobility, whilst low conductive materials such as Bi exhibited poor mobility. The relationship between cathode spot mobility and material thermal conductivity, which was not explicitly characterised in VATs until now, has wider implications for ensuring good cathode erosion behaviour in a VAT design. Although implied, the reduction of MP emission with the DAS technique (an attractive benefit for the VAT) must still be experimentally verified.

A case study on Fe operating at I = 50 A peak and various pulse lengths was performed. Reductions of up to 24% in erosion rate were achieved when DAS was used at long arc pulses, whilst no improvements were observed during short pulses regardless of switching frequency. This suggested that the material's characteristic spot mobility limit had a dominant influence during short-pulsed operation of the VAT.

Thrust tests on the DAS-enhanced Fe VAT confirmed that anode switching or forced spot motion alone does not negatively affect thrust, but can actually improve it by more than 20%. The thrust test also answers a number of questions raised in Chapter 5 about the nature of increased thrust production of VATs under long-pulsed operation and mitigating the negative effects of the inherently higher thermal load on the cathode erosion rate and overall thruster performance. The DAS technique was able to increase the Fe VAT's specific impulse by up to 27.9 % over the short-pulsed baseline design. Further investigation is required to test the limits of DAS on other cathode materials and VAT designs.

Chapter 9

Synthesis

9.1 Overview

Although the intention of each of the four major experimental studies of Chapters 5–8 was to address a specific aspect of VAT design, several overlapping and complementary findings exposed a number of common themes and new insights into the fundamental behaviour and performance of VATs that would not have been obvious otherwise. This short chapter includes: (1) some comments on the roles of arc pulse length and spot motion on VAT design and performance, (2) consolidated test data showing a possible relation between cathode material and the thrust correction factor, (3) a brief exploration on the combined use of DAS and conical cathodes, and (4) for the reader's convenience, an overall summary of performance gains achieved by various VAT designs in this work.

9.2 The use of long arc pulse lengths

This work elevates the importance and utility of arc pulse length in VAT design. Extending arc pulse lengths into the millisecond range was key to achieving useful test results in a number of studies, e.g. on conical cathodes shapes and the discrete anode switching

technique. In both cases, the enhanced thrust performance of long pulses was leveraged, whilst successfully mitigating the unwanted effects of increased local cathode heating by increasing spot motion. Operating long pulses on carbon cathodes was also useful in building supporting evidence that CEX with neutrals is responsible for enhanced ion production in VATs operating with long arc pulses.

The close link between the arc pulse length and the cathode design (size, shape, material) as was widely established across various studies in this work means that VAT performance is governed by an even greater number of critical design elements than was previously appreciated. Significant performance gains can be made by paying considerably closer attention to the cathode's electrode design and operational conditions, designing both elements in concert with one another.

9.3 The key role of cathode spot motion & coverage

Throughout this study, cathode spot motion and coverage over the cathode electrode surface was found to play a pivotal role in the performance of the VAT. In terms of thrust production, the manner in which the cathode spot(s) erodes the cathode will determine the overall plasma jet shape (ICDD) and its ability to direct ion momentum in the normal direction (Chapter 5). In conjunction with the electrode's shape (Chapter 6) and its material properties (Chapter 7), spot motion and coverage also influences the efficacy of ions leaving the thruster.

Many results in this work point to the deep connection between the cathode erosion rate and the range & type of spot motion experienced. Figure 9.1 visually consolidates and connects various aspects and properties of a VAT's design into a simplified network of interactions that ultimately determine the cathode's erosion rate. Cathode spot motion and coverage can be considered a central element in this network.

Outside this core of design parameters, lies a set of "external motivators" that to a large extent, can influence cathode spot motion independently of the cathode's design. These

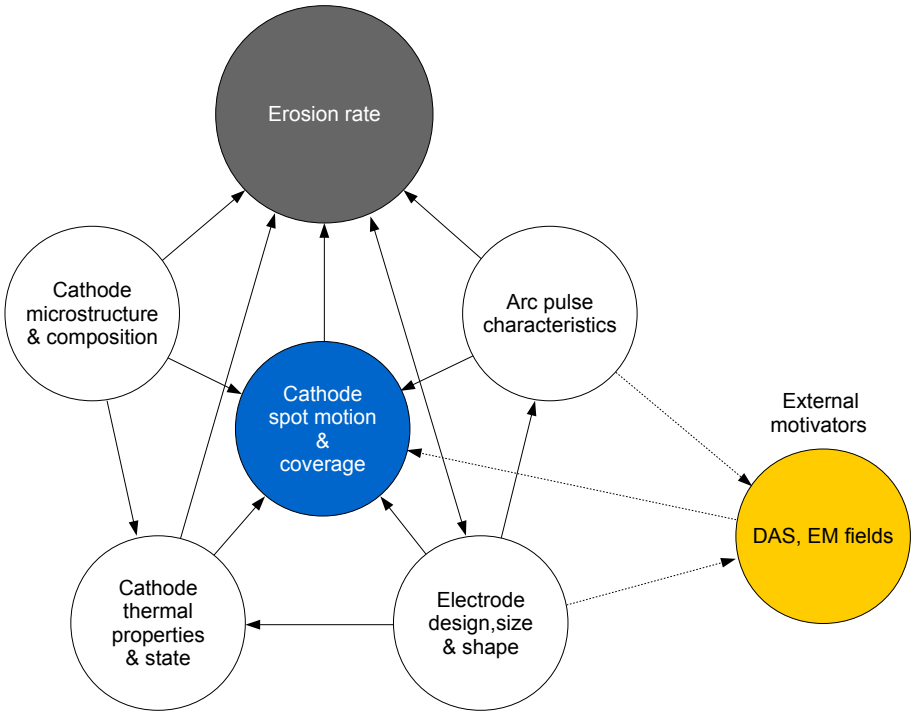

Figure 9.1: Simplified network interaction of factors influencing cathode erosion rate. Spot motion and coverage is seen as a central influence.

"motivators" can include the DAS technique as described in Chapter 8 and electromagnetic fields, which influence and guide the spots via manipulation of the plasma in the near-cathode spot region just above, and are inexorably linked to, the spots on the surface below.

Therefore, with the aid of Figure 9.1, a recommended general strategy towards improving the performance of the VAT should be to direct, manipulate and guide, as much as practically possible, various design features and properties towards a manner of spot motion and coverage that encourages (1) a reduction in cathode erosion rate, and (2) an enhancement of thrust production.

9.4 Effect of cathode material on C_T

Influences on the thrust correction factor may include more than just the arc pulse length. Consolidation of baseline thruster C_T results for various metals (Chapter 5) and C-3 (Chapter 7) in Figure 9.2 suggests that C_T may also follow an increasing trend with the

choice of cathode material (more specifically, the boiling point of the material) when VATs are operated with long pulses. However, no material dependence was seen for VATs operated with short pulses. Additional study is needed to further verify and characterise this interesting behaviour of C_T against cathode material.

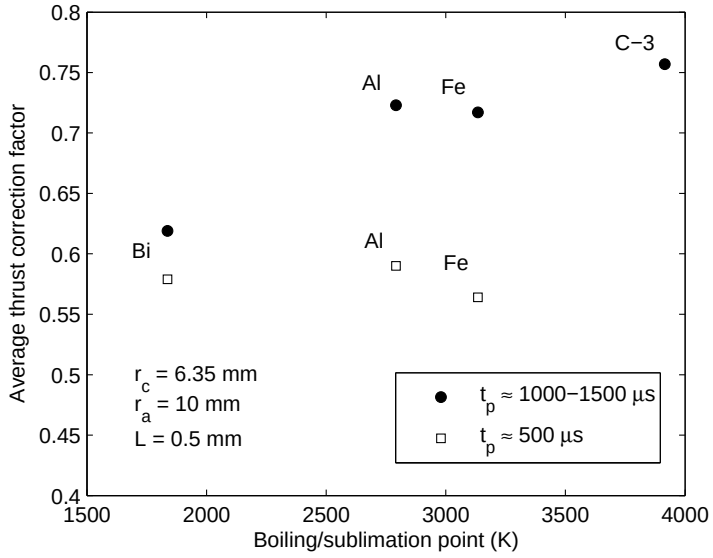

Figure 9.2: Relationship between material boiling point and average thrust correction factor. Data taken from baseline VAT tests operating at I = 50 A peak in both short (500 μs) and long pulses (1000–1500 μs) – see Table 5.3 and Figure 7.8.

9.5 Combined use of DAS and conical cathodes

Earlier in Chapter 6, measurements on conical cathodes revealed that they could experience erosion rates lower than the flat baseline cathode design. This was attributed to the increased surface area and slope of the exposed cathode, which improved its capacity to absorb heat from the arc and encouraged motion of the spot away from the triggered edge towards the cathode's central point. Likewise in Chapter 8, the DAS technique was successful in mitigating the heat load experienced by a cathode operating with long arc pulses by increasing spot motion and redistribution of the thermal load. Could both techniques be used in a single VAT to achieve even lower cathode erosion rates?

The potential for further erosion rate reductions through the combined use of DAS and conical cathodes was briefly assessed with a number of erosion tests on a DAS-enhanced

VAT using a 120° and 135° conical cathodes. Table 9.1 lists E_r measurements for various conical VAT prototypes with and without DAS implementation.

Table 9.1: Comparison of erosion rate results for selected conical and baseline (flat) cathode shapes with and without DAS implementation. Peak arc current I = 50 A. Cathode material is Fe.

Anode design	**Cathode shape**	f (Hz)	t_p (μs)	E_r (μg/C)
Std ring	120° cone	3	2236	50.5 ±1.1
Discrete (45 μs switch)	120° cone	3	1912	50.6 ±1.9
Std ring	Flat	20	236	44.0 ±1.1
Std ring	135° cone	5	331	46.9 ±2.8
Discrete (500 μs switch)	135° cone	5	298	41.8 ±1.1

Results showed that applying DAS to conical cathode designs provided little to no improvement to erosion rate. At long pulses, no change in E_r was measured using a 120° conical cathode. Thus, DAS was unable to improve spot motion and coverage beyond what was already accomplished by the presence of the conical surface. At short pulses, however, a 10.9% reduction in E_r was measured using DAS on a 135° conical cathode. Further insight is given when comparing both short-pulsed conical cathode results to the standard baseline cathode under similar arc conditions. The reason that the conical cathode performed no better or worse[1] than the standard cathode in this scenario was likely due to poorer erosion behaviour. By operating with short pulses, most of the erosion was observed to occur at the outer rim of the conical surface, which contains a thin edge (poorer thermal conduction compared to the bulk cathode body). By encouraging spot motion with DAS, an improvement of at least 5% could be made to the cathode erosion rate over the baseline design. Thus, the DAS technique was shown to be capable of achieving a modest reduction in E_r at short arc pulse lengths, provided the VAT design *also* incorporated a conical cathode shape to improve general spot motion.

Unfortunately, the combination of conically-shaped cathodes and the DAS technique within a VAT was overall unsuccessful in generating appreciable reductions in erosion rate. This showed that the DAS technique, as implemented in this work, was only beneficial under a specific set of scenarios and will require further fine-tuning to be of wider practical use (e.g. higher switching frequencies, different electrode designs and configu-

[1] The overlap of confidence bounds in both results is such that the mean values may not differ with sufficient statistical significance.

rations).

9.6 Overview of VAT specific impulse performance gains

Figure 9.3 summarises the range of I_{sp} values measured for selected VAT prototype designs listed throughout this study. Short-pulse baseline VATs are included to indicate the current typical state-of-the-art in VAT performance. Long-pulsed VATs perform poorer than the baseline due to the increased erosion rate of the cathode under increased thermal loading. The use of Fe as cathode fuel served as a key example throughout the work on various VAT performance changes and improvements. Although the performance of Fe reduced when operating under long pulses, a conical cathode shape and the use of DAS enabled a significant increase in I_{sp} over its baseline design of up to 54%, despite their combined use with long pulse operation.

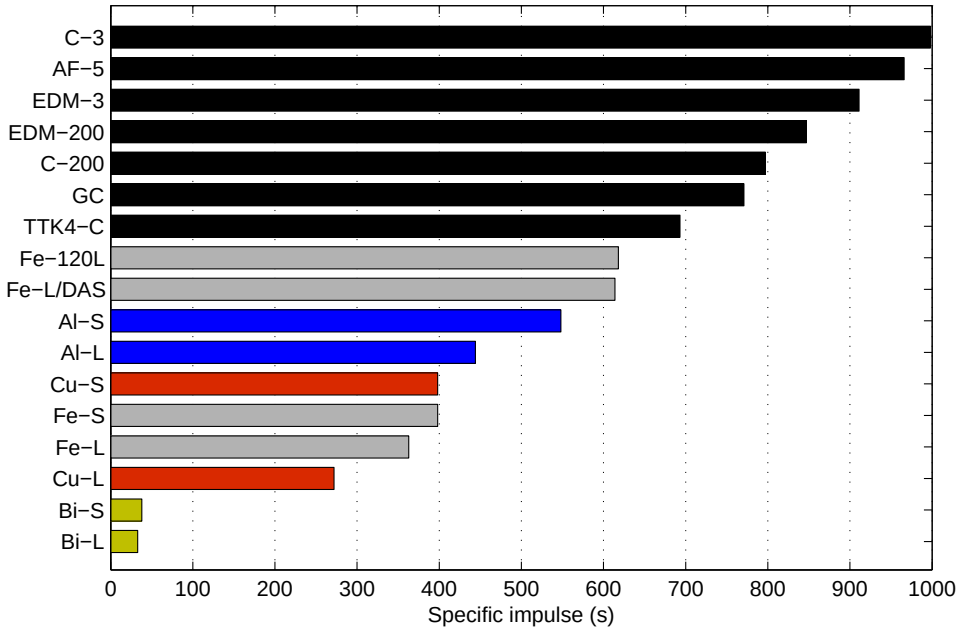

Figure 9.3: Summary and comparison of prototype VAT performance levels (specific impulse) measured within this study. The list includes carbon-based cathode materials and metal cathodes operating in long- (L) and short-pulsed (S) modes. Performance of conical (120°) and DAS-enhanced (45 μs) Fe cathodes are also shown. Each element type is colour-grouped for visual aid.

Carbon-based cathode materials are the highest-performance group of tested cathodes, with 75–250% greater I_{sp} over the baseline Fe VAT illustrated here. The best performing graphite cathode was shown to be EDM material C-3, comprised of 15% Cu and an average particle size of 5 μm. Challenges still remain, however, with the practical use of carbon cathodes – their poorer erosion behaviour compared to metal cathodes will require more careful consideration when designing the electrode arrangement and any feeding mechanisms.

Chapter 10

Conclusion

10.1 Overview

Microthrusters are a key technology needed in the small satellite community and industry for expanding the capability, agility and longevity of satellite missions. Vacuum arc thrusters possess several attractive features that enable it to serve this need by offering a potentially small, simple and safe propulsion solution. However, VATs have relatively limited flight experience and hardware maturity, deliver promising but modest performance levels, and are lacking in several areas of thruster design philosophy and functional understanding. In an effort to address these issues, this work explored a number of design, operational and material aspects, contributing to greater understanding and performance enhancement of vacuum arc thrusters.

To accomplish this work, a high-vacuum facility together with high-fidelity performance diagnostic tools and equipment was designed, built, tested and commissioned. A direct thrust stand, Faraday Cup probe, two-axis rotation system and ion collector were successfully developed to extensively measure the performance of several VAT prototypes powered by pulsed power circuits. The use of baseline thrusters, with comparable performance to literature, were a key and crucial element in the examination of new thruster

designs as well as in the verification and validation of diagnostic equipment. Four main areas of VAT design and operation were undertaken, namely studying the effect of (1) longer arc pulse lengths and (2) conical cathode electrode shapes; (3) the novel use of carbon and graphite compounds as cathode fuels; and (4) the use of heat management techniques such as discrete anode switching. An overview of each study and its findings are given below.

10.1.1 Arc pulse length

Operating VATs with ms-long arc pulse lengths generated a number of distinct operational and performance differences over traditional short-pulsed VATs. The most surprising of all was in the observed increase in ion production rates (10.4–16.6%) and thrust per arc current values (11–24.9%). Charge exchange collisions with neutrals was seen as the most plausible explanation for this effect, but this requires direct verification. The increase in erosion rate with increasing pulse length showed that cathode erosion depends more on local cathode heating processes rather than average heat distribution. The role of macroparticle production in negatively influencing the ion flux was also recognised, but needs further quantification. Finally, the thrust correction factor was shown to be affected by the arc pulse length, which controlled the manner of cathode surface erosion and distribution of ion emission. This suggests that an optimal condition for maximum ion momentum in the normal thrust direction exists.

10.1.2 Cathode shape

The use of conically-profiled cathode shapes in VATs were shown in a majority of cases to deliver superior levels of thrust as well as reduced levels of erosion rate, achieving specific impulse improvements of over 60% compared to baseline thrusters. The conical shape was particularly effective towards increasing cathode spot motion such that higher heat levels present during long-pulsed operation were essentially mitigated. The coupled effect of arc pulse length and cone angle on the plasma jet profile was recognised as an important, but complex factor in conical VATs and requires further attention. Although

changes to the ICDD due to the conical cathode geometry is considered as a possible source of the observed thrust increases, the potential role of plasma acceleration and CEX needs to be examined.

10.1.3 Carbon cathodes

Several cathodes made of carbon, graphite and graphite-compounds were successfully tested and characterised. The performance of carbon was found to be highly dependent on material microstructure and thermal properties, such that each type or grade of carbon could be considered a unique cathode material. The combination of fine microstructure and high electric resistivity of the carbon material was generally found to deliver high levels of average thrust production (350–383 μN/A) and low erosion rates (33.4–49.2 μg/C). In particular, copper-impregnated graphite material C-3 produced the highest specific impulse (998 s) of any cathode material ever tested in a VAT. The inclusion of copper into a graphite compound was significant enough to counteract the poor erosion behaviour of pure graphite (deep craters instead of gradual erosion) by improving its thermal properties and increasing spot motion. Test results also suggested that the erosion rates of copper-impregnated graphite cathodes improved with longer pulses over the 250–1000 μs regime, a behaviour contrary to that of other materials, including metals. The high thrust levels produced by carbon cathodes remains unexplained by present empirical model predictions and can only be partially accounted for by a 18.3% higher measured thrust correction factor of 0.757.

10.1.4 Discrete anode switching

The control of spot motion using the discrete anode switching technique was feasibly demonstrated to improve the erosion characteristics and reduce the erosion rate of the cathode. The DAS technique was found to be most effective at long arc pulse lengths and short anodes switching times (achieving up to 24% lower E_r), but was ineffective at short pulse lengths. The thermal conductivity of the cathode material was shown to have a significant effect on the mobility of the cathode spots and manner of cathode

erosion, an effect not previously considered in VATs. Finally, a DAS-enhanced Fe VAT was demonstrated to suffer no adverse effects on thrust production as a result of modified spot motion and even showed a 21.6% improvement in average thrust production over the baseline design.

10.2 Recommendations

Although extensive measurements of thrust, ICDD and erosion rate were undertaken, additional diagnostic studies are needed to help resolve many of the open-ended results and conjectures arising from this work. Specifically, detailed analyses of MP spatial and size distributions, ion charge state distributions and ion energy distributions should be made. Preliminary total ion current measurements in this study showed significant unexplained discrepancies with literature in a number of test cases, suggesting further review of the ion current test method used.

The test range of peak arc currents and cathode sizes needs to be extended. Heat management in the relatively small cathode (6.35 mm) was an evident issue that limited the pulse firing rate of VAT prototypes and their ability to absorb increased heat from long pulse length operation. Other VAT designs may also reveal additional optimum design points and further the development of a more complete VAT design philosophy.

Performance testing and characterisation of new or underutilised cathode materials is encouraged. Also, the promising results of copper-impregnated graphite compounds opens up the possible use of a wide and never-before-studied range of materials such as carbides, metal-matrix composites and metal-alloy-carbon compounds for use as potential high-performance cathode fuels for VATs. The inclusion of metals other than Cu in customised recipe proportions could be considered as candidates for further improving the thermal properties and performance of carbon-based cathodes.

Tighter control over the arc pulse length is highly desired. Some reduction in the uncertainty of t_p was accomplished by using the SCS circuit in Chapter 8 to limit the maximum

arc pulse length in some later tests, but control still remains limited. The variability of t_p made comparisons between many test results rather difficult, especially for the cathode shape study, which included the coupled effect of cone angle and pulse length on thrust. Better control of the pulse length will also allow more stable thrust in VATs, which is a desirable feature of a micro-propulsion system. Future work should quantify in better detail the repeatability and accuracy of the VAT to perform specific thrust manoeuvres.

Although the present thruster design was flexible enough to easily test a large number of different cathode samples, the electrode design limited the use of conical cathodes in some ways. For example, triggering the arc at the edge of the cathode rod resulted in erosion that made the cathode surface flatter over time instead of maintaining the conical shape being tested. A centrally-located arc triggering mechanism may offer a better design option. The lack of a feeding mechanism also meant that the cathode eventually receded away from the insulator edge, which widened the interelectrode gap and reduced the stability of the vacuum arc over time. This was a particular problem for low density materials such as graphite. Present implementation of the triggerless arc triggering mechanism in VAT prototypes also experienced degradation at longer operating lifetimes. Thus, only a limited number of arc pulses ($\sim 10^4$) could be fired before thruster operation became unstable. Although this lifetime was of sufficient duration for the tests performed in this work, cathode feeding and triggering issues must be addressed in subsequent VAT designs.

Other vital and logical extensions to this work include: (1) long-term performance studies, (2) eliminating thruster failure modes, especially interelectrode gap and insulator failure, (3) exploring and mitigating the potential effect of MP contamination on surrounding surfaces, (4) addressing EMI, pulse circuit design limitations and power efficiency in the VAT, (5) developing the role and design of the anode electrode, and (6) studying the integrated use of magnetic and electric fields with this work's new designs to further enhance VAT performance.

References

AASC (2011), 'Alameda Applied Sciences Corporation micropropulsion webpage', URL: `http://www.aasc.net/micropropulsion`. Cited 05 May 2014.

Anders, A. (1997), 'Ion charge state distributions of vacuum arc plasmas: The origin of species', *Physical Review E* **55**(1).

Anders, A. (1998), 'Ion charge state distributions of pulsed vacuum arcs-interpretation of their temporal development', *IEEE Transactions on Plasma Science* **26**(1), 118–119.

Anders, A. (2001), 'A periodic table of ion charge-state distributions observed in the transition region between vacuum sparks and vacuum arcs', *IEEE Transactions on Plasma Science* **29**(2), 393–398.

Anders, A. (2008), *Cathodic arcs: From fractal spots to energetic condensation*, Vol. 50 of *Springer Series on Atomic, Optical and Plasma Physics*, Springer, New York.

Anders, A., Brown, I. G., MacGill, R. A. & Dickinson, M. R. (1998), ''Triggerless' triggering of vacuum arcs', *Journal of Physics D: Applied Physics* **31**(5), 584–587.

Anders, A., Oks, E. M. & Yushkov, G. Y. (2007*a*), 'Charge-state-resolved ion energy distribution functions of cathodic vacuum arcs: A study involving the plasma potential and biased plasmas', *Journal of Applied Physics* **102**(4), 043303.

Anders, A., Oks, E. M. & Yushkov, G. Y. (2007*b*), 'Production of neutrals and their effects on the ion charge states in cathodic vacuum arc plasmas', *Journal of Applied Physics* **102**(4), 043303.

Anders, A., Oks, E. M., Yushkov, G. Y. & Brown, I. G. (2004), Measurement of total ion flux in vacuum arc discharges, *in* 'Proceedings of the XXIth International Symposium on Discharges & Electrical Insulators in Vacuum', Yalta, Ukraine, pp. 272–275.

Anders, A., Oks, E., Yushkov, G. & Savkin, K. (2005), 'Measurements of the total ion flux from vacuum arc cathode spots', *IEEE Transactions on Plasma Science* **33**(5), 1532–1536.

Anders, A., Yotsombat, B. & Binder, R. (2001), 'Correlation between cathode properties, burning voltage, and plasma parameters of vacuum arcs', *Journal of Applied Physics* **89**(12), 7764.

Anders, A. & Yushkov, G. Y. (2002*a*), 'Angularly resolved measurements of ion energy of vacuum arc plasmas', *Applied Physics Letters* **80**(14), 2457–2459.

Anders, A. & Yushkov, G. Y. (2002*b*), 'Ion flux from vacuum arc cathode spots in the absence and presence of a magnetic field', *Journal of Applied Physics* **91**(8), 4824–4832.

Anders, A. & Yushkov, G. Y. (2007), 'Puzzling differences in bismuth and lead plasmas: Evidence for the significant role of neutrals in cathodic vacuum arcs', *Applied Physics Letters* **91**(9), 091502.

Barengolts, S., Mesyats, G. & Shmelev, D. (2003), 'Structure and time behavior of vacuum arc cathode spots', *IEEE Transactions on Plasma Science* **31**(5), 809–816.

Beilis, I. (1999), 'Application of vacuum arc cathode spot model to graphite cathode', *IEEE Transactions on Plasma Science* **27**(4), 821–826.

Beilis, I. (2008), 'Modeling of a microscale short vacuum arc for a space propulsion thruster', *IEEE Transactions on Plasma Science* **36**(5), 2163–2166.

Beilis, I. (2014), 'Physics of cathode phenomena in a vacuum arc with respect to a plasma thruster application', *IEEE Transactions on Plasma Science* **PP**(99), 1.

Beilis, I., Djakov, B., Juttner, B. & Pursch, H. (1997), 'Structure and dynamics of high-current arc cathode spots in vacuum', *Journal of Physics D: Applied Physics* **30**, 119–130.

Boxman, R., Sanders, D. & Martin, P. (1995), *Handbook of vacuum arc science and technology: Fundamentals and applications*, Noyes Publications, Park Ridge, New Jersey.

Bridges, W., Frey, J. I. & Birdsall, C. K. (1965), 'Limiting stable currents in bounded electron and ion streams', *IEEE Transactions of Electron Devices* **12**, 264–272.

Brown, I. G. (1994), 'Vacuum arc ion sources', *Review of Scientific Instruments* **65**(10), 3061–3081.

Brown, I., Galvin, J., MacGill, R. & Wright, R. (1987), 'Improved time-of-flight ion charge state diagnostic', *Review of Scientific Instruments* **58**(9), 1589–1592.

Brown, I. & Shiraishi, H. (1990), 'Cathode erosion rates in vacuum-arc discharges', *IEEE Transactions on Plasma Science* **18**(1), 170–171.

Bugaev, A. S., Gushenets, V. I., Nikolaev, A. G., Oks, E. M. & Yushkov, G. Y. (2000), 'Study of directed ion velocities in a vacuum arc by an emission method', *Technical Physics* **45**(9), 1135–1140.

Canuto, E. & Rolino, A. (2004), 'Nanobalance : An automated interferometric balance for micro-thrust measurement', *ISA Transactions* **43**, 169–187.

CPUT (2014), 'CPUT F'SATI ZACUBE-1 blog page', URL: `http://www.cput.ac.za/blogs/fsati/zacube-1/`. Cited 05 May 2014.

Cubbin, E. A., Ziemer, J. K., Choueiri, E. Y. & Jahn, R. G. (1997), 'Pulsed thrust measurements using laser interferometry', *Review of Scientific Instruments* **68**(6), 2339–2346.

Daalder, J. E. (1975), 'Erosion and the origin of charged and neutral species in vacuum arcs', *Journal of Physics D: Applied Physics* **8**(14), 1647–1659.

Daalder, J. E. (1976), 'Components of cathode erosion in vacuum arcs', *Journal of Physics D: Applied Physics* **9**(16), 2379–2395.

Dethlefsen, R. (1968), 'Performance measurements on a pulsed vacuum arc thruster', *AIAA Journal* **6**(6), 1197–1199.

Djakov, B. E. & Holmes, R. (1971), 'Cathode spot division in vacuum arcs with solid metal cathodes', *Journal of Physics D: Applied Physics* **4**(4), 504–509.

D'Souza, B. & Ketsdever, A. (2005), 'Development of a nano-impulse balance for micro-propulsion systems', *41st AIAA/ASME/SAE/ASEE Joint Propulsion Conference & Exhibit* .

Ferrer, P. & Tchonang, M. P. (2011), 'Miniaturization of electrostatic ion engines by ionization and acceleration coupling', *Journal of Physics D: Applied Physics* **44**(33), 335204.

Forrester, A. (1988), *Large ion beams*, Wiley, New York.

Fuchikami, S., Nakamoto, M., Toyoda, K. & Cho, M. (2013), Development of vacuum arc thruster for nano satellite, *in* '33rd International Electric Propulsion Conference', Vol. IEPC-2013-264.

Gambino, N., Hayden, P., Mascali, D., Costello, J., Fallon, C., Hough, P., Yeates, P., Anzalone, A., Musumeci, F. & Tudisco, S. (2013), 'Dynamics of colliding aluminium plasmas produced by laser ablation', *Applied Surface Science* **272**, 69–75.

Gamero-Castaño, M. (2003), 'A torsional balance for the characterization of microNewton thrusters', *Review of Scientific Instruments* **74**(10), 4509.

Gessini, P., Sandonato, G., Irita, R., Gonçalves, J. & e Fernandes, G. (2007), A pendulum target balance for ion engine thrust measurement, *in* '30th International Electric Propulsion Conference', Vol. IEPC-2007-149, pp. 1–12.

Gilmour, A. & Lockwood, D. (1972), 'Pulsed metallic-plasma generators', *Proceedings of the IEEE* **60**(8), 977–991.

Goebel, D. M. & Schneider, A. C. (2005), 'High-Voltage breakdown and conditioning of carbon and molybdenum electrodes', *IEEE Transactions on Plasma Science* **33**(4), 1136–1148.

Grubišić, A. N. & Gabriel, S. B. (2010), 'Development of an indirect counterbalanced pendulum optical-lever thrust balance for micro- to millinewton thrust measurement', *Measurement Science and Technology* **21**(10), 105101.

Hantzsche, E. (1983), 'The state of the theory of vacuum arcs', *Contributions from Plasma Physics* **23**(1), 77–94.

Hantzsche, E. (1991), 'Theory of the expanding plasma of vacuum arcs', *Journal of Physics D: Applied Physics* **24**, 1339–1353.

Hantzsche, E. (2003), 'Mysteries of the arc cathode spot: a retrospective glance', *IEEE Transactions on Plasma Science* **31**(5), 799–808.

Haque, S. (2014), Agile development process of flight hardware for a quad-channel Micro-Cathode Arc Thruster (μCAT) subsystem for the 1.5U BRICSat-P cubesat missionS, *in* '11th Annual CubeSat Developers' Workshop', Cal Poly, San Luis Obispo.

Hosoki, S., Yamamoto, S., Futamoto, M. & Fukuhara, S. (1979), 'Field emission characteristics of carbon tips', *Surface Science* **86**, 723–733.

IEPC (2013), 'Private communication with Pietzka, M., Polk, J., Sekerak, M., Shashurin, A. and Zhuang, T.'. International Electric Propulsion Conference, Washington, D.C.

Incropera, F. P. & DeWitt, D. P. (2002), *Introduction to heat transfer*, fourth edn, John Wiley & Sons, New York.

Kandah, M. & Meunier, J. (1996), 'Erosion study on graphite cathodes using pulsed vacuum arcs', *IEEE Transactions on Plasma Science* **24**(2).

Keidar, M., Beilis, I., Boxman, R. & Goldsmith, S. (1997), 'Voltage of the vacuum arc with a ring anode in an axial magnetic field', *IEEE Transactions on Plasma Science* **25**(4), 580–585.

Keidar, M., Beilis, I., Boxman, R. L. & Goldsmith, S. (1996), '2D expansion of the low-density interelectrode vacuum arc plasma jet in an axial magnetic field', *Journal of Physics D: Applied Physics* **29**(7), 1973–1983.

Keidar, M., Haque, S., Zhuang, T., Shashurin, A., Chiu, D., Teel, G., Agasid, E., Tintore, O. & Uribe, E. (2013), Micro-cathode arc thruster for PhoneSat propulsion, *in* '27th Annual AIAA/USU Conference on Small Satellites', Vol. SSC13-VII-9, Logan, Utah.

Keidar, M., Schein, J., Wilson, K., Gerhan, A., Au, M., Tang, B., Idzkowski, L., Krishnan, M. & Beilis, I. I. (2005), 'Magnetically enhanced vacuum arc thruster', *Plasma Sources Science and Technology* **14**(4), 661–669.

Keidar, M., Shashurin, A., Li, J., Volotskova, O., Kundrapu, M. & Zhuang, T. S. (2011), 'Arc plasma synthesis of carbon nanostructures: where is the frontier?', *Journal of Physics D: Applied Physics* **44**(17), 174006.

Kimblin, C. (1971), 'Vacuum arc ion currents and electrode phenomena', *Proceedings of the IEEE* **59**(4), 546–555.

Kimblin, C. (1973), 'Erosion and ionization in the cathode spot regions of vacuum arcs', *Journal of Applied Physics* **44**(7), 3074–3081.

Koizumi, H., Komurasaki, K. & Arakawa, Y. (2004), 'Development of thrust stand for low impulse measurement from microthrusters', *Review of Scientific Instruments* **75**(10), 3185–3190.

Krishnan, M. (2009), 'Vacuum arc plasma thrusters with inductive energy storage driver'. US Patent 7,518,085 B1.

Kronhaus, I., Schilling, K., Jayakumar, S., Kramer, A., Pietzka, M. & Schein, J. (2013), Design of the UWE-4 picosatellite orbit control system using vacuum-arc-thrusters, *in* '33rd International Electric Propulsion Conference', Vol. IEPC-2013-195, Washington, DC.

Lafferty, J. M., ed. (1980), *Vacuum arcs – Theory and applications*, John Wiley & Sons, Inc.

Lafleur, T. (2007), Corona discharge as an ionization mechanism for electrostatic propulsion applications, BSc (Physics) honours project, University of the Witwatersrand, Johannesburg, South Africa.

Lake, J. P., Cavallaro, G., Spanjers, G., Adkison, P. & Dulligan, M. (2003), 'Resonant operation of a micro-newton thrust stand', pp. 1–10.

Lebedev, S. V., Chittenden, J. P., Beg, F. N., Bland, S. N., Ciardi, A., Ampleford, D., Hughes, S., Haines, M. G., Frank, A., Blackman, E. G. & Gardiner, T. (2002), 'Laboratory astrophysics and collimated stellar outflows: The production of radiatively cooled hypersonic plasma jets', *The Astrophysical Journal* **564**, 113–119.

Lefort, A., Parizet, M., El-Fassi, S. & Abbaoui, M. (1993), 'Erosion of graphite electrodes', *Journal of Physics D: Applied Physics* **26**(8), 1239–1243.

Lun, J. (2009), Development of a vacuum arc thruster for nanosatellite propulsion, MSc thesis, University of Stellenbosch, Stellenbosch, South Africa.

Lun, J., Dobson, R. T. & Steyn, W. H. (2010), 'Determining vacuum-arc thruster performance using a cathode-spot model', *Journal of Propulsion and Power* **26**(4), 663–672.

Luna, H., Kavanagh, K. D. & Costello, J. T. (2007), 'Study of a colliding laser-produced plasma by analysis of time- and space-resolved image spectra', *Journal of Applied Physics* **101**, 033302.

Marks, H., Beilis, I. & Boxman, R. (2009), 'Measurement of the vacuum arc plasma force', *IEEE Transactions on Plasma Science* **37**(7), 1332–1337.

Mesyats, G. (1995), 'Ecton mechanism of the vacuum arc cathode spot', *IEEE Transactions on Plasma Science* **23**(6), 879–883.

Meunier, J.-L., Coulombe, S. & Kandah, M. (2007), 'Erosion of carbon arc cathodes operating in the thermo-field electron emission mode', *Plasma Sources Science and Technology* **16**(1), 33–41.

Micci, M. M. & Ketsdever, A., eds (2000), *Micropropulsion for small spacecraft*, Vol. 187 of *AIAA Progress in Aeronautics and Astronautics*, American Institute of Aeronautics and Astronautics.

Miernik, K. & Walkowicz, J. (2000), 'Spatial distribution of microdroplets generated in the cathode spots of vacuum arcs', *Surface and Coatings Technology* **125**(1-3), 161–166.

Mueller, J. (1997), Thruster options for microspacecraft: A review and evaluation of existing hardware and emerging technologies, *in* 'AIAA/ASME/SAE/ASEE 33rd Joint Propulsion Conference and Exhibit', Vol. 97-3058, Seattle, WA, pp. 1–29.

Neumann, P. R. C., Bilek, M. M. M. & McKenzie, D. R. (2012), 'Fuel selection for pulsed cathodic arc thrusters', *Journal of Propulsion and Power* **28**(1), 218–221.

Neumann, P. R. C., Bilek, M. M. M., Tarrant, R. N. & McKenzie, D. R. (2009), 'A pulsed cathodic arc spacecraft propulsion system', *Plasma Sources Science and Technology* **18**(4), 045005.

Pancotti, A. P., Gilpin, M. & Hilario, M. S. (2012), 'Comparison of electrostatic fins with piezoelectric impact hammer techniques to extend impulse calibration range of a torsional thrust stand.', *Review of Scientific Instruments* **83**(3), 035109.

Peirce, B. (1852), 'Criterion for the rejection of doubtful observations', *Astronomical Journal* **2**(45), 161–163.

Pietzka, M., Kirner, S., Kauffeldt, M., Arens, C., Marques-Lopez, J.-L., Forster, G. & Schein, J. (2011), Development of vacuum arc thrusters and diagnostic tools, *in* '31st International Electric Propulsion Conference', Vol. IEPC-2011-080, Wiesbaden, Germany.

Pietzka, M., Kühn-Kauffeldt, M., Schein, J., Kronhaus, I., Schilling, K., Mai, T. & Lebeda, A. (2013), Innovative vacuum arc thruster for CubeSat constellations, *in* '33rd International Electric Propulsion Conference', Vol. IEPC-2013-306, Washington, DC.

Polk, J., Sekerak, M., Ziemer, J., Schein, J. & Anders, A. (2008), 'A theoretical analysis of vacuum arc thruster and vacuum arc ion thruster performance', *IEEE Transactions on Plasma Science* **36**(5), 2167–2179.

Polzin, K. A., Markusic, T. E., Stanojev, B. J., Dehoyos, A. & Spaun, B. (2006), 'Thrust stand for electric propulsion performance evaluation', *Review of Scientific Instruments* **77**(105108).

Qi, N., Gensler, S., Prasad, R., Krishnan, M., Vizir, A. & Brown, I. (1998), A vacuum arc ion thruster for space propulsion, Technical report, Alameda Applied Sciences Corporation. SBIR Phase-I Final Report.

Rocca, S., Menon, C. & Nicolini, D. (2006), 'FEEP micro-thrust balance characterization and testing', *Measurement Science and Technology* **17**(4), 711–718.

Ross, S. (2003), 'Peirce's criterion for the elimination of suspect experimental data', *Journal of Engineering Technology* **20**(2), 38–41.

Rysanek, F. & Burton, R. (2008), 'Charging of macroparticles in a pulsed vacuum arc discharge', *IEEE Transactions on Plasma Science* **36**(5), 2147–2162.

Sablev, L., Dolotov, J., Getman, L., Gorbunov, V., Goldiner, E., Kirshfeld, K. & Usov, V. (1974), 'Apparatus for vacuum-evaporation of metals under the action of an electric arc'. US Patent 3,783,231.

Sanders, D. M. & Anders, A. (2000), 'Review of cathodic arc deposition technology at the start of the new millennium', *Surface and coatings technology* **133-134**, 78–90.

SANSA (2013), 'SANSA strategic plan 2012–2017', URL: `http://www.sansa.org.za/images/resource_centre/publications/SANSA%20Strategic%20Plan.pdf`. Cited 05 May 2014.

Schein, J., Krishnan, M., Ziemer, J. & Polk, J. (2002b), Adding a "throttle" to a clustered vacuum arc thruster, *in* 'NanoTech', Houston, Texas, pp. AIAA 2002–5716.

Schein, J., Qi, N., Binder, R., Krishnan, M., Ziemer, J. K., Polk, J. E. & Anders, A. (2002a), 'Inductive energy storage driven vacuum arc thruster', *Review of Scientific Instruments* **73**(2), 925–927.

Schein, J., Zierhut, J., Dzulko, M., Forster, G. & Landes, K. D. (2007), 'Improved plasma spray torch stability through multi-electrode design', *Contributions to Plasma Physics* **47**(7), 498–504.

Sekerak, M. (2005), Plasma plume characterization of a vacuum arc thruster, M.S. thesis, California Institute of Technology, Pasedena, CA.

Selden, N. P. & Ketsdever, A. D. (2003), 'Comparison of force balance calibration techniques for the nano-Newton range', *Review of Scientific Instruments* **74**(12), 5249.

Shalev, S., Boxman, R. L. & Goldsmith, S. (1986), 'Macroparticle dynamics during multicathode-spot vacuum arcs', *IEEE Transactions on Plasma Science* **14**(1), 59–62.

Smallsat (2014), 'AIAA/USU conference on small satellites webpage', URL: `http://www.smallsat.org`. Cited 05 May 2014.

Sovey, J. S., Carney, L. M. & Knowles, S. C. (1989), 'Electromagnetic emissions experiences using electric propulsion systems – a survey', *Journal of Propulsion and Power* **5**, 534–547.

Statom, T. (2003), Vacuum arc nano-thruster cathode performance for nano-satellites, *in* '34th AIAA Plasmadynamics and Lasers Conference', Vol. AIAA 2003-4291, Orlando, Florida, pp. 9780–9780.

Takker, P. & Dabrowski, M. (2006), 'Ion launch debriefing', `http://www.amsat.org/amsat/archive/amsatbb/200607/msg00444.html`. Cited 31 May 2011.

Tang, B., Idzkowski, L. & Au, M. (2005), Thrust improvement of the magnetically enhanced vacuum arc thruster (MVAT), *in* '29th International Electric Propulsion Conference', Vol. IEPC-2005-304, Princeton University.

Timko, H. (2011), Modelling vacuum arcs: from plasma initiation to surface interactions, PhD thesis, University of Helsinki.

Vergason, G., Lunger, M. & Gaur, S. (2001), Advances in arc spot travel speed to improve film characteristics, *in* 'Society of Vacuum Coaters 44th Annual Technical Conference Proceedings', pp. 136–140.

Walker, M. (2005), Effects of facility backpressure on the performance and plume of a Hall thruster, PhD thesis, University of Michigan.

Wang, Y., Zhang, C., Zhang, H., Ding, B. & Lu, K. (2003), 'Effect of the microstructure of electrode materials on arc cathode spot dynamics', *Journal of Physics D: Applied Physics* **36**(21), 2649–2654.

Weickert, C. (1987), 'A multicomponent theory of the cathodic plasma jet in vacuum arcs', *Contributions from Plasma Physics* **27**(5), 309–330.

Weyer, R. B., Dobson, R. & van der Westhuizen, K. (2004), Development of a liquefied-gas micro-satellite propulsion system, *in* '18th Annual AIAA/USU Conference on Small Satellites', Logan, Utah, pp. 1–10.

Wong, A. R., Toftul, A., Polzin, K. a. & Pearson, J. B. (2012), 'Non-contact thrust stand calibration method for repetitively pulsed electric thrusters.', *Review of Scientific Instruments* **83**(2), 025103.

Xu, K. G. & Walker, M. L. R. (2009), 'High-power, null-type, inverted pendulum thrust stand.', *Review of Scientific Instruments* **80**(5), 055103.

Yeates, P., Fallon, C., Kennedy, E. T. & Costello, J. T. (2011), 'Charge resolved electrostatic diagnostic of colliding copper laser plasma plumes', *Physics of Plasmas* **18**, 103104.

Yushkov, G. & Anders, a. (1998), 'Effect of the pulse repetition rate on the composition and ion charge-state distribution of pulsed vacuum arcs', *IEEE Transactions on Plasma Science* **26**(2), 220–226.

Yushkov, G. Y., Anders, A., Oks, E. M. & Brown, I. G. (2000), 'Ion velocities in vacuum arc plasmas', *Journal of Applied Physics* **88**(10), 5618.

Zhirkov, I., Eriksson, A. & Rosén, J. (2013), 'Ion velocities in direct current arc plasma generated from compound cathodes', *Journal of Applied Physics* **114**, 213302.

Zhuang, T., Shashurin, A., Brieda, L. & Keidar, M. (2009), Development of micro-vacuum arc thruster with extended lifetime, *in* '31st International Electric Propulsion Conference', Ann Arbor, MI, pp. IEPC–2009–192.

Ziemer, J. K. (2001), Performance measurements using a sub-microNewton resolution thrust stand, *in* '27th International Electric Propulsion Conference', Vol. IEPC-01-238, Pasadena, CA.

Appendix A

Empirical VAT performance table

Table A.1 lists various metallic cathode materials and vacuum arc plasma properties as measured under "standard" arc conditions (100–200 A, 250–500 μs) on small diameter cathode rods as well as predicted VAT performance according to Polk et al.'s (2008) empirical model. Parameters such as ion-to-arc current ratio and erosion rates have been updated to reflect latest literature findings and results reported in this work. The ion erosion rate E_i is equivalent to the ion mass flow rate $\dot{m}_i$, which is a function of the ion mass and average charge state and the ion-to-arc current ratio (see Equation 2.1). The ion mass fraction E_i/E_r gives an indication of what proportion of the ejected fuel consists of ions (an E_i/E_r ratio close to 1 means that the plasma is well-ionised).

Table A.1: Empirical VAT properties and performance for various pure metal cathode materials. The top five performing materials in each category of specific impulse I_{sp}, thrust-to-power ratio T/P and efficiency η are highlighted in grey.

	m_i (amu)	ϵ[a] (%)	$\bar{Z}$[b]	v_i[c] (km/s)	E_i (μg/C)	E_r[d] (μg/C)	E_i/E_r	V[e] (V)	$m_i v_i$	C_T[f]	T/I (μN/A)	I_{sp} (s)	T/P (μN/W)	η (%)	ρ[g] (g/cc)	λ_k[g] (W/mK)
Mg	24.3	12.7%	1.5	19.8	21	31	0.69	18.8	481	0.6	254	834	13.5	5.5%	1.74	146
Al	26.3	11.2%	1.73	15.4	18	28	0.63	23.6	405	0.59[h]	161	584	6.8	1.9%	2.70	218
Ti	47.9	9.7%	2.1	15.4	23	30	0.77	21.3	738	0.6	212	721	10.0	3.5%	4.51	25
Cr	52.0	7.5%	2.1	16.3	19	20	0.96	22.9	848	0.6	188	960	8.2	3.9%	7.14	49
Fe	55.9	8.0%	1.82	12.6	25	48	0.53	22.7	704	0.56[h]	181	385	8.0	1.5%	7.87	32
Ni	58.7	7.8%	1.8	11.5	26	47	0.56	20.5	675	0.6	182	395	8.9	1.7%	8.91	83
Co	58.9	9.6%	1.7	12.1	35	44	0.78	22.8	713	0.6	251	580	11.0	3.1%	8.90	43
Cu	63.6	11.4%	2.0	13.2	38	51	0.74	23.4	840	0.6	298	595	12.7	3.7%	8.92	339
Zr	91.2	10.5%	2.6	15.4	38	53	0.72	23.4	1404	0.6	353	679	15.1	5.0%	6.51	33
Ag	107.9	8.0%	2.1	11.1	43	140	0.30	23.6	1198	0.6	284	207	12.0	1.2%	10.49	361
Cd	112.4	12.0%	1.3	6.8	108	620	0.17	16.0	764	0.6	439	72	27.4	1.0%	8.65	95
W	183.9	5.0%	3.1	11.1	31	55	0.56	31.9	2041	0.6	205	380	6.4	1.2%	19.25	31
Pb	207.2	14.3%	1.6	5.8	192	510	0.38	15.5	1202	0.6	669	134	43.1	2.8%	11.34	95
Bi	209.0	10.2%	1.17	4.7	189	950[h]	0.20	15.6	982	0.51[h]	449	48	28.8	0.7%	9.78	7

[a] Anders et al. (2005), except for Cr, Fe and Ag (measured by Kimblin (1973)) and Ni (predicted by Lun et al. (2010)).
[b] Brown (1994)
[c] Anders & Yushkov (2002*b*)
[d] Brown & Shiraishi (1990)
[e] Anders et al. (2001)
[f] Assumed Gaussian distribution (w = 1.1) and same electrode configuration as for this work's baseline VAT.
[g] Incropera & DeWitt (2002), λ_k at molten temperature.
[h] As measured in this work.

Appendix B

Derivation of thrust correction factor

The thrust correction factor is measure of what proportion of momentum from ions leaving the vacuum arc thruster contribute to normal thrust. This factor takes into account the plume divergence of the thrust plume and the spatial interference of the anode electrode to the escaping plume. The assumption is made that the average ion charge state and the average ion velocity of the plasma jet plume are spatially uniform. Therefore, only the ion mass flow is considered to affect the thrust correction factor. This section provides an alternative derivation of the thrust correction factor to that of Sekerak (2005).

One approach to solving this problem is to make a direct analogy to a fundamental problem in basic thermodynamics of defining a view factor for radiation exchange between two surfaces. The following solution is based on the method of Incropera & DeWitt (2002, p. 748). All ions are assumed to be emitted from the cathode surface, represented by a single flat surface i with area dA_i and normal vector n_i. The anode electrode exit plane is represented by a second flat surface j with area dA_j and normal vector n_j. A line of length R connects the two surfaces, forming the polar angles θ_i and θ_j. A schematic of the coaxial thruster geometry with variable definitions in given in Figure B.1.

Considering the rate at which ion emission from dA_i passes through dA_j, the current density (or intensity) J_{ij} is defined as the rate at which current is emitted by along the

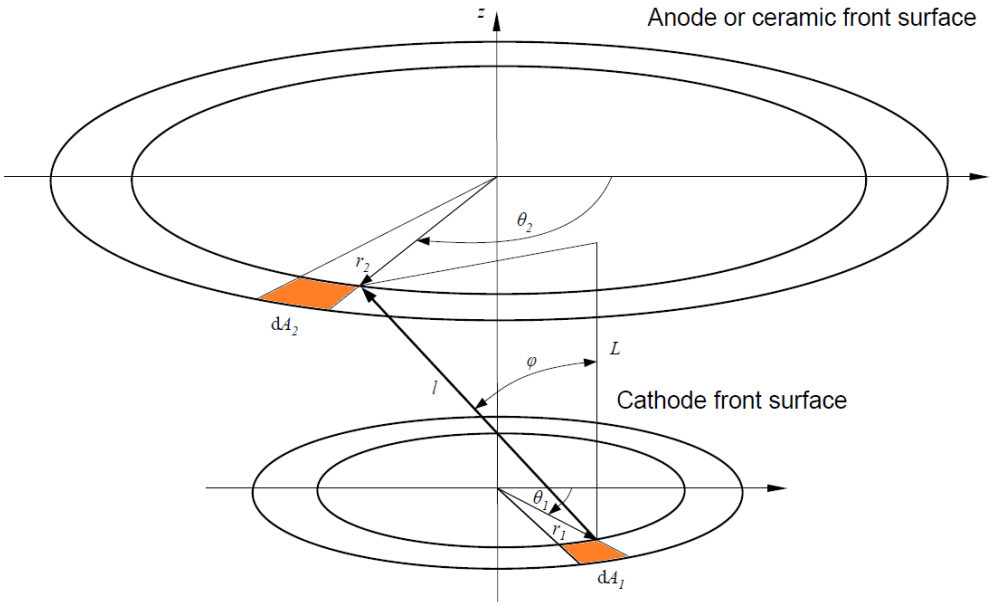

Figure B.1: Problem geometry and variable definitions used for calculating C_T. Adapted from Sekerak (2005).

R direction, per unit area of the emitting surface normal to this direction, per unit solid angle about this direction, i.e.

$$J_{ij} = \frac{dI_{ij}}{dA_i \cos\theta_i d\omega_{ji}} \tag{B.1}$$

where $d\omega_{ji}$ is the unit solid angle subtended by dA_j when viewed from dA_i:

$$d\omega_{ji} = \frac{\cos\theta_j dA_j}{R^2} \tag{B.2}$$

Combining and rearranging the above two equations results in

$$dI_{ij} = J_{ij} \frac{\cos\theta_i \cos\theta_j}{R^2} dA_i dA_j \tag{B.3}$$

Integrating over the two surfaces results in the total rate of emission

$$I_{ij} = \int_{A_i} \int_{A_j} J_{ij} \frac{\cos\theta_i \cos\theta_j}{R^2} dA_i dA_j \tag{B.4}$$

The thrust correction factor (or view factor) is defined as the fraction of current that leaves the cathode (A_i) and is intercepted by the anode plane (A_j):

$$C_T = \frac{I_{ij}}{A_i J_{ic}} \tag{B.5}$$

Note that for this particular case, the two planes i and j are parallel to one another, making $\theta_i = \theta_j$. Normalising for unit drift length $R = 1$ and unit ejected ion current $J_{ic} = 1$, C_T may be rewritten as

$$C_T = \frac{1}{A_i} \int_{A_i} \int_{A_j} J' \cos^2 \theta_i \, dA_i dA_j \tag{B.6}$$

where $J' = J_{ij}/J_{ic}$. Based on the geometry shown in Figure B.1, the following expressions are defined:

$$A_i = \pi r_c^2 \tag{B.7}$$

$$\cos\theta_i = \frac{L}{l} \tag{B.8}$$

Resulting in

$$C_T = \frac{1}{\pi} \int_{A_i} \int_{A_j} J' \frac{L^2}{l^2} \, dA_i dA_j \tag{B.9}$$

Non-dimensionalising the expression for any sized circular geometry results in the following:

$$C_T = \frac{\bar{L}^2}{\pi} \int_0^{2\pi} \int_0^{2\pi} \int_0^{\bar{r}_a} \int_0^{1} \bar{J}' \frac{1}{\bar{l}^2} \, \bar{r}_1 \bar{r}_2 d\bar{r}_1 d\bar{r}_2 d\theta_1 d\theta_2 \tag{B.10}$$

where

$$r_c = 1 \tag{B.11}$$

$$\bar{r_a} = \frac{r_a}{r_c} \tag{B.12}$$

$$\bar{r_1} = \frac{r_1}{r_c} \tag{B.13}$$

$$\bar{r_2} = \frac{r_2}{r_c} \tag{B.14}$$

$$\bar{L} = L/r_c \tag{B.15}$$

$$\bar{l}^2 = \bar{L}^2 + \bar{r}_1^2 + \bar{r}_2^2 - 2\bar{r}_1\bar{r}_2\cos(\theta_1 - \theta_2) \tag{B.16}$$

and J' is any arbitrary current density distribution.

Appendix C

Vector problems in ICDD measurement

C.1 Determining the thrust vector from ICDD data

The thrust vector is defined as the force magnitude and direction comprised of the sum total of all directed ion momentum, taking into account all radial and normally-directed force components. For all cases studied here, this is equivalent to the vector sum of the pitch and yaw components of peak measured ion flow. Figure C.1 illustrates the thrust vector diagram and its components, where A, B and C are the respective yaw, pitch and thrust vector magnitudes and β_y, β_p and β_T are the respective yaw, pitch and thrust vector deviation angles of peak ion flow measured in their respective planes.

Within Figure 3.28, there exist three right-angled triangles, AOZ, BOZ and COZ. Each triangle has the following trigonometric relations:

$$\tan\beta_y = a/Z \tag{C.1}$$

$$\tan\beta_p = b/Z \tag{C.2}$$

$$\tan\beta_T = c/Z \tag{C.3}$$

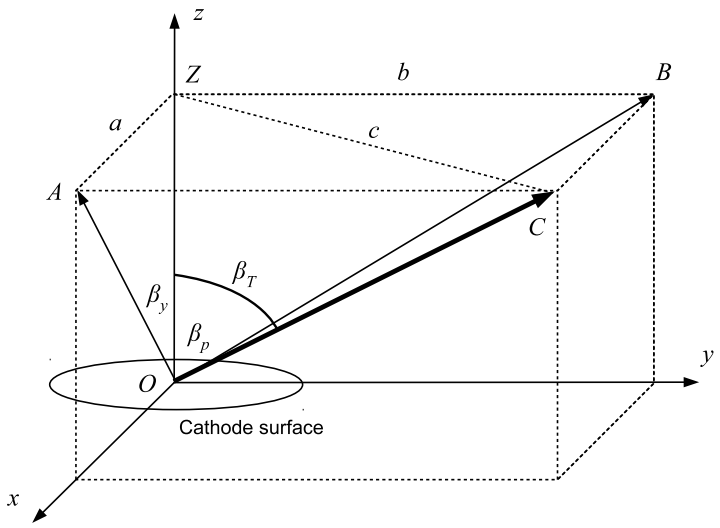

Figure C.1: Vector diagram of thrust vector comprised of yaw and pitch components.

and

$$\sin\beta_y = a/A \tag{C.4}$$

$$\sin\beta_p = b/B \tag{C.5}$$

$$\sin\beta_T = c/C \tag{C.6}$$

Also

$$c^2 = a^2 + b^2 \tag{C.7}$$

Combining Equations C.1–C.3 and C.7 and eliminating the common factor Z, results in an expression of the thrust vector deviation angle in terms of the pitch and yaw deviation angles

$$\tan^2\beta_T = \tan^2\beta_y + \tan^2\beta_p \tag{C.8}$$

Combining Equations C.4–C.6 and C.7, results in an expression of the thrust vector magnitude in terms of the pitch and yaw magnitudes and deviation angles

$$C\sin\beta_T = \sqrt{A^2\sin^2\beta_y + B^2\sin^2\beta_p} \tag{C.9}$$

C.2 Finding the true TARS thruster orientation angle

The problem of finding the true thruster orientation angle within the TARS range of motion is made complicated by the fact that the thruster assembly is oriented in three dimensional space using a combination of two variables – that is, the combined actuation pitch α and yaw β rotation of the thruster assembly. These two positional variables must be combined in order to determine the true thruster orientation angle γ. An elegant geometric solution was conceived by representing γ and pitch and yaw rotations as angles of a tetrahedron, with three of its six edges of equal size r as illustrated in Figure C.2.

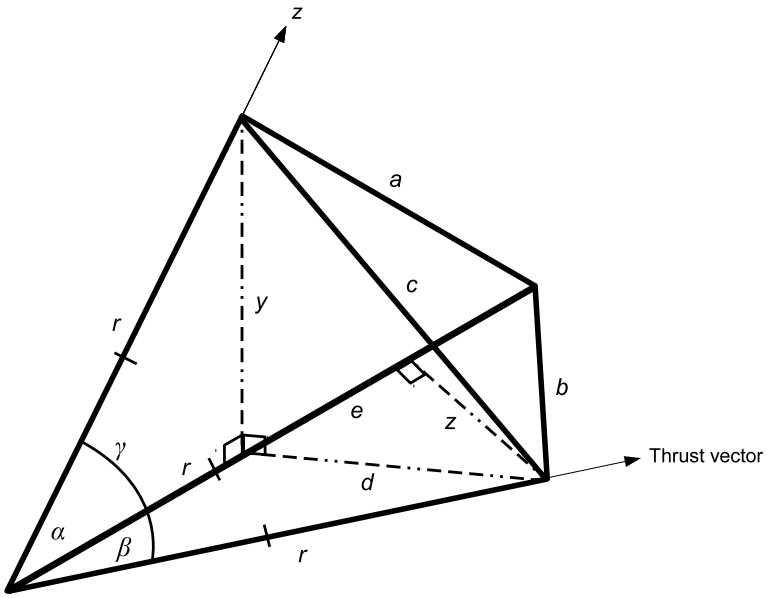

Figure C.2: Geometric representation of thruster orientation angle problem using a tetrahedron

Two smaller right-angles triangles are drawn inside the tetrahedron such that the following Pythagorean relationships can be established:

$$c^2 = y^2 + d^2 \tag{C.10}$$

$$d^2 = z^2 + e^2 \tag{C.11}$$

Rewriting the relevant edges in terms of r, α, β and γ using trigonometric identities:

$$c^2 = 2r^2\left(1-\cos\gamma\right) \tag{C.12}$$

$$e = r\left(\cos\beta-\cos\alpha\right) \tag{C.13}$$

$$y = r\sin\alpha \tag{C.14}$$

$$z = r\sin\beta \tag{C.15}$$

Combining Equations C.10–C.15 results in

$$2r^2\left(1-\cos\gamma\right) = r^2\sin^2\alpha + r^2\sin^2\beta + r^2\left(\cos\beta-\cos\alpha\right)^2 \tag{C.16}$$

Final rearranging leads to the following simple relationship between the true thruster assembly orientation angle and the actuated pitch and yaw rotation angles

$$\cos\gamma = \cos\alpha\cos\beta \tag{C.17}$$

Appendix D

Additional experimental data

D.1 Pulse length study

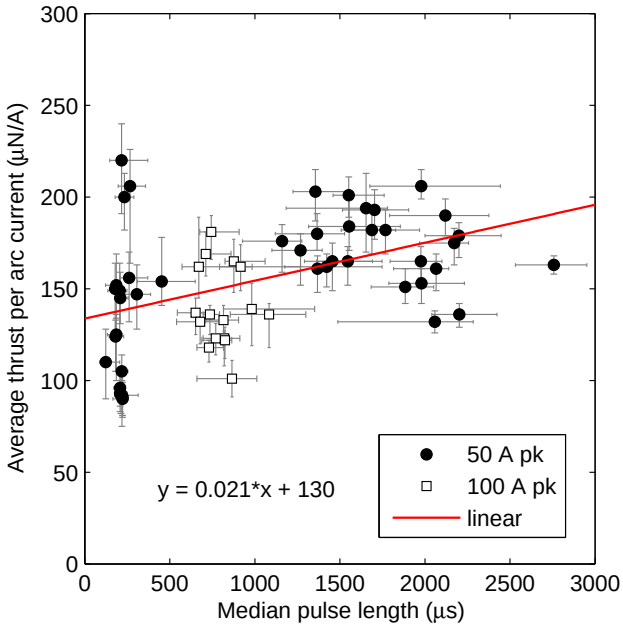

Figure D.1: Average thrust per current results for baseline VAT with Al cathode operating at 50 A and 100 A peak arc current at various pulse lengths. A linear fit through 50 A data shows an increase in average thrust production with increasing pulse length from 141 μN/A at 500 μs to 172 μN/A at 2000 μs (22.0% increase).

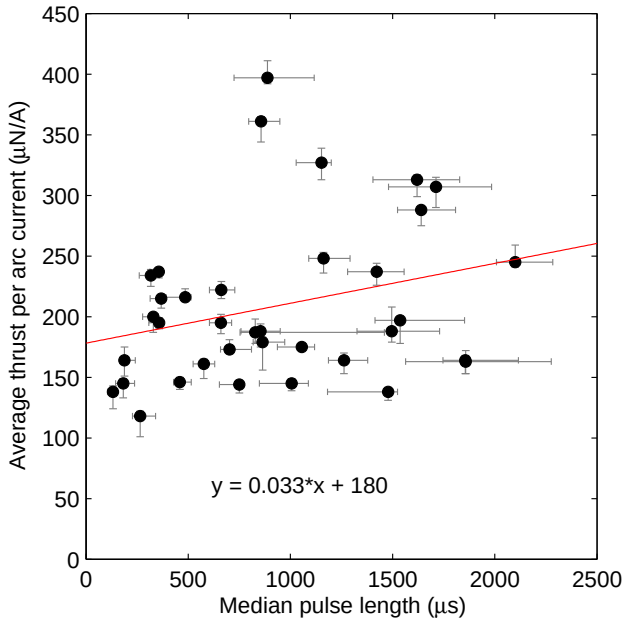

Figure D.2: Average thrust per current results for baseline VAT with Cu cathode operating at 50 A peak arc current at various pulse lengths. A linear fit through 50 A data shows an increase in average thrust production with increasing pulse length from 197 μN/A at 500 μs to 246 μN/A at 2000 μs (24.9% increase).

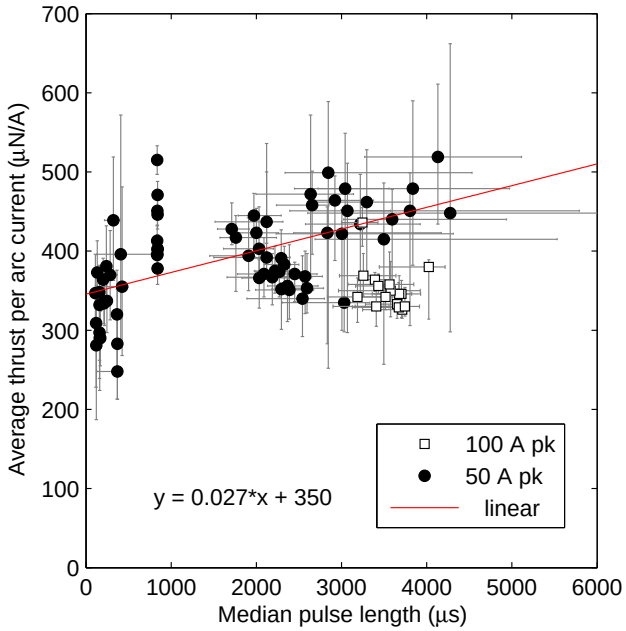

Figure D.3: Average thrust per current results for baseline VAT with Bi cathode operating at 50 A and 100 A peak arc current at various pulse lengths. A linear fit through 50 A data shows an increase in average thrust production with increasing pulse length from 364 μN/A at 500 μs to 404 μN/A at 2000 μs (11.0% increase).